

Gravitational Lensing and Microlensing

Silvia Mollerach & Esteban Roulet

World Scientific

Gravitational Lensing and Microlensing

This page is intentionally left blank

Gravitational Lensing and Microlensing

**Silvia Mollerach
Esteban Roulet**

Centro Atómico Bariloche, Argentina



World Scientific

New Jersey • London • Singapore • Hong Kong

Published by

World Scientific Publishing Co. Pte. Ltd.

P O Box 128, Farrer Road, Singapore 912805

USA office: Suite 1B, 1060 Main Street, River Edge, NJ 07661

UK office: 57 Shelton Street, Covent Garden, London WC2H 9HE

British Library Cataloguing-in-Publication Data

A catalogue record for this book is available from the British Library.

GRAVITATIONAL LENSING AND MICROLENSING

Copyright © 2002 by World Scientific Publishing Co. Pte. Ltd.

All rights reserved. This book, or parts thereof, may not be reproduced in any form or by any means, electronic or mechanical, including photocopying, recording or any information storage and retrieval system now known or to be invented, without written permission from the Publisher.

For photocopying of material in this volume, please pay a copying fee through the Copyright Clearance Center, Inc., 222 Rosewood Drive, Danvers, MA 01923, USA. In this case permission to photocopy is not required from the publisher.

ISBN 981-02-4852-0

To Javier and Nicolás

This page is intentionally left blank

Preface

For many decades gravitational lensing appeared to be just a curiosity associated to the deflection of light predicted by General Relativity. However, in the last twenty years a wide range of lensing phenomena have been discovered, establishing gravitational lensing as one of the most important areas of research in observational astronomy. The activity in this field has been growing at a steady rate, attracting both astrophysicist and cosmologists due to the major implications that these results can have for our understanding of the Universe. The beautiful lensing phenomena can indeed provide crucial information about the geometry of the Universe, its expansion rate and matter content, on the formation of the large scale structures and their distribution at different scales and on the nature of the dark matter. The microlensing searches provide also the possibility to look for non-luminous stellar objects (black holes, neutron stars, faint white dwarfs, brown dwarfs), testing if they are of any relevance to explain part of the dark matter, and even to search for planets orbiting distant stars.

The aim of this book is to provide a self contained pedagogical presentation of the various aspects of gravitational lensing. We hope that this will be useful both to the graduate students and to the researchers interested in this field. It may also be appropriate for a set of lectures on the subject or as part of a more general course on Cosmology. Several specialized review articles and monographs covering the different topics addressed in the book have appeared in recent years and we refer to them at the end of each Chapter as recommended readings. An extensive list of references to the (very large) literature in the field can also be found there, since we generally quoted here only those works which were more relevant to the exposition of

the subject followed. An extensive bibliography on gravitational lensing can be found at http://vela.astro.ulg.be/grav_lens/grav_lens.html.

The structure of the book is as follows: Chapter 1 provides a brief historical introduction to gravitational lensing and presents the most important observational breakthroughs in the field. Chapter 2 contains a basic introduction to General Relativity, providing to the reader the main concepts and tools underlying the lensing phenomena, including the light deflection in a Schwarzschild metric and the gravitational time delays. This Chapter should be useful to the student not familiar with General Relativity and we hope that having a basic approach to this theory through one of its most fascinating manifestations can provide a good starting point to later expand her/his knowledge of the subject. Chapter 3 deals with the theoretical aspects of gravitational lensing, discussing the lens equation, the magnification of the source light, the basic lens models, the formation of multiple images of a source and also the main characteristics of the critical lines and caustics in different lensing systems. Chapter 4 presents the main observational results on lensing by galaxies, clusters and the large scale structures, both in the strong lensing regime, when multiple images are formed, and in the weak lensing regime, when only small distortions of the images result. Chapter 5 presents the theory of microlensing, discussing the magnification light curve, the event duration, the optical depth and the event rate. We also discuss the present status of the observations towards the Magellanic Clouds and the Galactic bulge and confront them with the expectations for different lensing populations. The possibility to obtain more information about the lenses from binary events, parallax and proper motion measurements is discussed in Chapter 6, together with the ability of astrometric microlensing measurements to produce significant advances in this field in a not too far future. Finally, Appendix A contains some basic tools of Cosmology which are used mainly in Chapter 4.

We thank the Editor K. K. Phua for asking us to expand our review article on microlensing into this book, and Suwarno for assistance. Special thanks to D. Harari for comments on the manuscript and to C. Alcock, R. Barkana, M. Bartelmann, W. Colley, W. J. Couch, R. Ellis, W. Hu, L. King, T. Kundic, Y. Mellier, R. Narayan, J. Wambsganss and P. Woźniak for allowing us to reproduce some pictures. We thank Fundación Antorchas and ANPCyT for financial support.

Silvia Mollerach and Esteban Roulet, Bariloche, August 2001.

Contents

Preface	vii
Chapter 1 Historical introduction	1
Chapter 2 The deflection of light	7
2.1 Basics of General Relativity	7
2.1.1 Introduction	7
2.1.2 Tensors in curved spacetimes	9
2.1.3 Motion of particles	13
2.1.4 The spacetime curvature	15
2.1.5 The Einstein equation	17
2.1.6 The Schwarzschild metric	18
2.2 The bending of light	21
2.2.1 Point-like deflector	21
2.2.2 Time delay	24
2.2.3 Extended mass distribution	25
Chapter 3 Gravitational lensing theory	29
3.1 The lens equation	29
3.1.1 Point-like lenses	29
3.1.2 Extended lenses	33
3.2 The surface brightness conservation	34
3.3 Amplification	35
3.4 Caustics and critical lines	41
3.5 Fermat's principle	42

3.6	Galaxy lens models	45
3.6.1	Circularly symmetric lenses	45
3.6.2	Non-circularly symmetric lenses	50
3.7	The folded sky	51
3.8	Folds and cusps	58
3.8.1	Magnification near a fold	60
3.8.2	Magnification near a cusp	62
3.8.3	The binary lens	65
Chapter 4 Macrolensing results		69
4.1	Lensing of quasars	70
4.2	Time delays and H_0	74
4.3	Statistical lensing and cosmological parameters	78
4.4	Strong lensing by clusters	81
4.5	Weak lensing in clusters	84
4.6	Cosmic shear	87
4.7	Quasar-galaxy correlations	94
4.8	Lensing of the Cosmic Microwave Background	94
Chapter 5 Microlensing I: Basics		99
5.1	The Galaxy in brief	100
5.1.1	The thin and thick disks	100
5.1.2	Galactic spheroid and bulge	101
5.1.3	The dark halo	103
5.2	Basic microlensing theoretical tools	105
5.2.1	The light curve	105
5.2.2	Optical depth	107
5.2.3	Event duration distribution	108
5.3	Microlensing of unresolved sources	114
5.4	Observational searches of microlensing	117
5.4.1	Searches towards the Magellanic Clouds	118
5.4.2	Searches towards the bulge	122
Chapter 6 Microlensing II: Beyond the simplest light curve		125
6.1	Binary lenses	126
6.1.1	The complex lens equation	126
6.1.2	Microlensing by binaries	131
6.1.3	Planetary searches	136

6.2	Further determinations of the lensing parameters	139
6.2.1	Proper motion	141
6.2.2	Limb darkening	147
6.2.3	Parallax measurements	148
6.3	Astrometric microlensing	152
6.4	Quasar microlensing	156
Appendix A Cosmology tools		161
A.1	The Friedmann-Robertson-Walker Universe	161
A.2	The distance scales	163
A.3	Large scale structures	166
A.4	Cosmic Microwave Background anisotropies	170
Bibliography		175
Index		189

Chapter 1

Historical introduction

El Aleph? repetí. Si, el lugar donde están, sin confundirse,
todos los lugares del orbe, vistos desde todos los ángulos.

The Aleph? I repeated. Yes, the place where, without confusion,
all the places of the world, seen from every angle coexist.

The Aleph, Jorge Luis Borges.

The bending of light in a gravitational field predicted by General Relativity provided one of the first verifications of Einstein's theory [Dy20]. The value of the deflection angle which results has now been tested at the 0.1% level by observing the change in the apparent position of stars whose light is deflected by the Sun [Le95]. In 1920, Eddington [Ed20] noted that the light deflection by a stellar object would give rise to secondary images of background sources appearing just on the opposite side of the deflector. Chwolson [Ch24] later pointed out that these secondary images could make foreground stars to look like binaries, and that if the alignment were perfect the image of the source would be a ring. In 1936, Einstein [Ei36] published the correct expression for the magnification of the two images of a very distant star, concluding however that the lensing effect of foreground stars was of no practical relevance due to the unresolvably small angular separation of the images and the low probability for a high amplification event to take place.

The following year, Zwicky [Zw37a] showed that, if the deflecting object were a galaxy instead of a single star, the gravitational lensing of the light of a background galaxy would lead to resolvable images. This ‘macrolensing’ effect could provide information about the mass of the intervening galaxy and could make possible the observation of objects at much larger distances due to the magnification of their light, with the lens acting as a natural

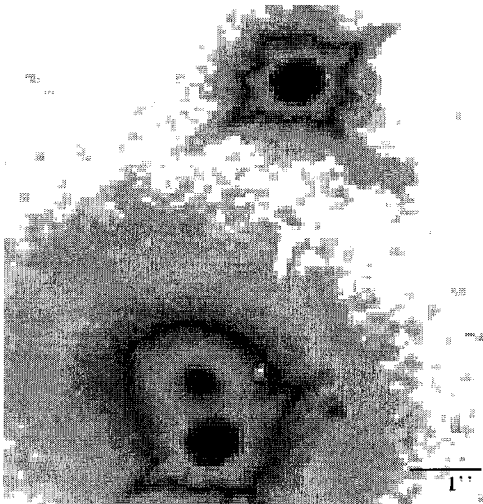


Fig. 1.1 HST picture of the first binary quasar observed, Q0957+561. The angular separation between images is $6.1''$, and the lensing galaxy is close to the image on the bottom (from <http://cfa-www.harvard.edu/glensdata> CfA/Arizona Space Telescope Lens Survey (CASTLES) website, courtesy of C. S. Kochanek, E. E. Falco, C. Impey, J. Lehar, B. Mc Leod and H.-W. Rix).

telescope. Furthermore, in Zwicky's words, the probability that this effect be observed 'becomes practically a certainty' [Zw37b].

It was actually the discovery by Walsh, Carswell and Weymann in 1979 [Wa79] of the multiple imaging of the high redshift quasar Q0957+561, lensed by a foreground galaxy (Figure 1.1), what provided the first observation of gravitational lensing. This discovery opened a new area of research which has now become an extremely active field in astronomy, with the potential of giving also crucial information for cosmology. For instance, the time delay among the multiple images of a quasar allows to measure the Hubble constant once the lens mass has been reconstructed from the location and shape of the images, and this procedure is now becoming a competitive way to determine the expansion rate of the Universe. Also, lensing statistics are sensitive to cosmological parameters, with the frequency of multiple imaging giving constraints on the cosmological constant and the distribution of image splittings probing the amount of structures on galaxy and cluster scales. Gravitational lensing can also affect the observable properties of active galactic nuclei and quasars, and may have to

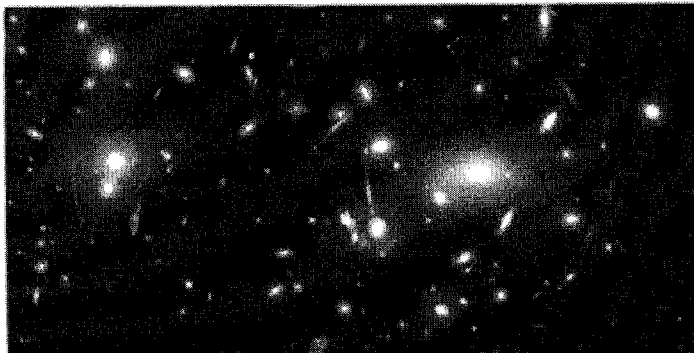


Fig. 1.2 Giant arcs around the cluster Abell 2218, produced by the lensing effect of the cluster mass on background galaxies (credit W. J. Couch (University of New South Wales), R. S. Ellis (Cambridge University) and NASA).

be taken into account when inferring their intrinsic properties.

Another manifestation of gravitational lensing was discovered in 1986 by Lynds and Petrosian [Ly86] and Soucail et al. [So87] in the form of large luminous arcs. These are due to the lensing effects of rich clusters of galaxies on background galaxies, with possible huge tangential magnifications which distort the galaxy shapes into long (giant) arcs around the cluster's cores. One of the nicest examples of this phenomenon is shown in Figure 1.2. Through this kind of observations the central mass of the clusters can be inferred. On the other hand, outside the central region of a cluster, and in general also for clusters which are not massive enough to produce strong lensing effects (i.e. involving multiple image formation), the mass distribution can be reconstructed from the observed shape of the images of thousands of background faint blue galaxies around it. These galaxies look tangentially elongated due to the lensing effect (which in this regime is referred to as weak lensing), and their average ellipticities form a coherent pattern around the cluster encoding the information on the lensing matter distribution [Ty95]. Finally, in empty regions it has been recently possible to measure galaxy ellipticity correlations up to scales of $\sim 10'$, which are induced by the weak lensing due to all the large scale structure along the line of sight to the background galaxies.

Regarding the gravitational lensing by compact objects (e.g. stars), its systematic theoretical study started in the sixties with the work of Liebes [Li64] and Refsdal [Re64], who setup the general formalism and discussed

the lensing of stars in the disk of the Galaxy, in globular clusters and in the Andromeda galaxy.

The lensing effect of individual stars belonging to a galaxy that is itself macrolensing a background source was discussed by Chang and Refsdal [Ch79] soon after the discovery of the binary quasar Q0957+561. When both the lensed source and the intervening galaxy are at cosmological distances, the passage of one of these stars close to the line of sight to one of the images further deflects the source light by an angle which is typically of $\mathcal{O}(\mu\text{arcsec})$. The name ‘microlensing’ then became associated with this process, and is now generally applied to any gravitational lensing effect by a compact object producing unresolvable images of a source and potentially huge magnifications of its light.

Press and Gunn [Pr73] showed in 1973 that a cosmological density of massive compact dark objects could manifest through the microlensing of high redshift sources. In 1981, Gott [Go81] pointed out the possibility of detecting the dark halos of remote galaxies by looking for microlensing of background quasars. It was in 1986 that Paczyński [Pa86a] gave a new face to the field when he noted that, by monitoring the light-curves of millions of stars in the Large Magellanic Cloud (LMC) for more than a year, it would become possible to test whether the halo of our galaxy consisted of compact objects with masses between 10^{-6} and $10^2 M_{\odot}$, i.e. covering most of the range where baryonic dark matter in the form of planets, Jupiters, brown dwarfs or stellar remnants (dead stars, neutron stars or black holes) could lie. It was later realized [Pa91; Gr91b] that the Galactic bulge stars also provided an interesting target to look at, since at least the lensing by faint stars in the disk should grant the observation of microlensing events, and observations towards the bulge could also allow to probe the dark constituency of the Galaxy close to the Galactic plane.

Several groups undertook the observations towards the Magellanic Clouds and the bulge, obtaining the first harvest of microlensing events in 1993 [Al93; Au93; Ud93] (see Figure 1.3). Also follow-up telescope networks have been organized and they are looking for alerted ongoing microlensing events in the search for planetary signals and providing detailed light curves which are used to obtain better information about the lenses. Also the observations of microlensing of unresolved stars in the Andromeda galaxy has started.

As we have seen in this brief introduction, gravitational lensing is an

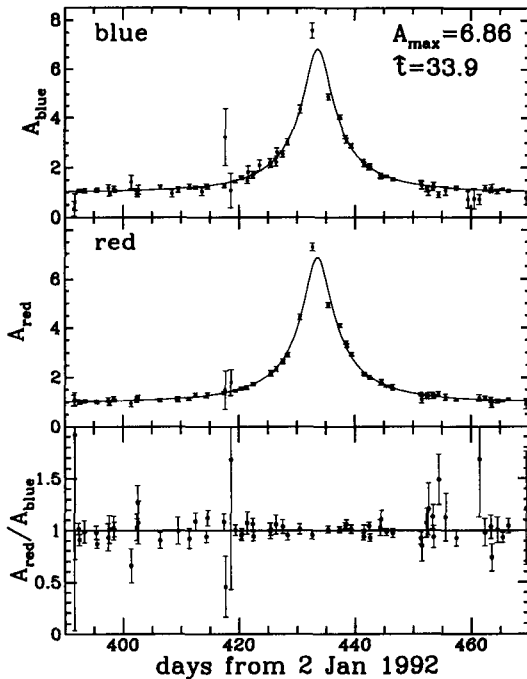


Fig. 1.3 Light-curve of the first microlensing event of a star in the LMC obtained by the MACHO Collaboration. The ratio of the light-curves in two colors is shown in the bottom panel, illustrating the achromaticity of this gravitational effect (courtesy of C. Alcock, reprinted from [Al93] with permission from *Nature*).

ubiquitous phenomenon in the Universe and it has several attractive features. It is a direct manifestation of the deflection of light predicted by General Relativity, giving rise to many beautiful optical effects, such as the multiple imaging, the shape distortion and the magnification of faraway sources. Most importantly, the observation of these effects provides a direct way to measure the amount of matter in the Universe as well as its spatial distribution at different scales, and allows to obtain fundamental information on the cosmological parameters and on the large scale structure distribution in the Universe. On the other hand, microlensing experiments are a powerful tool to search for compact dark objects and faint stars which are otherwise unobservable, and the results obtained at present are already providing crucial insights into the dark matter issue, into the non-luminous contribution to the mass of the different Galactic components and about the

morphology of the inner part of the Galaxy. Microlensing has also applications to stellar astrophysics, allowing to study the binary mass ratios and distribution of separations, to measure the mass of foreground bright stars and even in some special circumstances to resolve the size of the sources.

Chapter 2

The deflection of light

The basic physical process underlying all the gravitational lensing phenomena is the deflection of light by matter. The computation of this deflection has to be done within the theory of General Relativity and hence in this Chapter we start with a brief self-contained introduction to the more relevant aspects of this theory (this may be skipped by those already familiar with it). We derive then the Schwarzschild metric describing the space-time around a massive point-like object and obtain the trajectories of light-rays in that background to infer the induced deflection. We also obtain the gravitational delay affecting the light-rays and generalize the results to the case of an extended lensing distribution.

2.1 Basics of General Relativity

2.1.1 *Introduction*

The universality of gravitation is reflected in the fact that every body feels the attraction effects of all the other bodies and produces also an attractive effect over them. The way we understand the action of gravity has however changed with the theory of General Relativity. It is no longer thought as resulting from the action of a force as in Newtonian physics but instead, since the resulting motion is the same for any object independently of its mass, Einstein postulated that the gravitational effects can actually be ascribed to some intrinsic properties of the spacetime geometry, which gets curved in the presence of matter and through its curvature determines the motion of bodies.

The separate concepts of space and time had already been abandoned with the special theory of relativity. This theory aimed to formulate the laws of physics in such a way that they be valid in all the inertial reference systems, independently of their relative motion. In order that the speed of light be the same for every observer, the measurements of time and distances cannot be absolute, but should depend on the observer's motion. What is independent of the reference system used is the interval between two events. The differential interval ds between nearby events, taking place for example at spacetime coordinates (t, x, y, z) and $(t + dt, x + dx, y + dy, z + dz)$, is defined through

$$ds^2 = c^2 dt^2 - dx^2 - dy^2 - dz^2. \quad (2.1)$$

Another observer, using a different coordinate system (t', x', y', z') will find the same value for the interval between the two events. In particular, the events connected by a light ray have $ds = 0$.

If instead of using the usual Cartesian coordinates as in Eq. (2.1) general curvilinear coordinates are adopted, the squared interval will still be a quadratic function of the displacements, i.e.

$$ds^2 = g_{ik} dx^i dx^k, \quad (2.2)$$

where here and in the following the convention that repeated indices are summed from 0 to 3 is adopted. The metric g_{ik} describes how distances are measured in the spacetime and is taken as symmetric ($g_{ik} = g_{ki}$) since it is contracted with the symmetric product $dx^i dx^k$.

One of the basis of Einstein's theory of gravitation is the weak equivalence principle, which states that in a free falling reference system (as the famous Einstein's lift) an observer experiences no gravitational effects. In other words, by local experiments it is not possible to distinguish between a gravitational field and an accelerated reference system and hence this ensures that all bodies will feel the same acceleration when subject to the action of gravity. This means that it is possible to make, in the neighborhood of any particular point P , a coordinate transformation to the free falling frame in which locally the spacetime reduces to the Minkowski one, i.e. is such that

$$g_{ik}(P) = \eta_{ik} \quad \text{and} \quad \frac{\partial}{\partial x^j} g_{ik}(P) = 0, \quad (2.3)$$

where $\eta_{ik} = \text{diag}(1, -1, -1, -1)$ is the flat metric in Cartesian coordinates used in Eq. (2.1), with $x^0 = ct$.

Contrary to the case of the flat Minkowski spacetime of Special Relativity, in the presence of a gravitational field there exist however no coordinates for which the metric can be reduced globally to the Minkowski form and hence in this case the spacetime is said to be intrinsically curved*.

In General Relativity it is also necessary to abandon the concept of privileged inertial reference systems used in Special Relativity. For instance, it is no longer possible to synchronize clocks at different locations in the presence of gravitational fields (clocks in the basement run slower than clocks in the roof top) and all the physics has then to be defined locally.

The strong form of the equivalence principle allows to describe the effects of non-gravitational forces in a spacetime which is curved by the action of gravity, and it states that locally in a free falling system all the laws of physics take the same form as in the flat Minkowski spacetime of Special Relativity.

2.1.2 *Tensors in curved spacetimes*

The idea in General Relativity is thus that all the physical laws be written in such a way that they take the same form in any reference system, reducing to the Special Relativity expressions in the local free falling frame. In other words, one has to state the physical laws using generally covariant expressions, in order that they retain the same form after a general coordinate transformation.

For a mathematical description of physical phenomena in an arbitrary reference frame some concepts to describe the geometry of four-dimensional spaces in general curvilinear coordinates are needed, and we will discuss here just the most essential ones.

A central role is played by tensors, whose importance lies in the fact that a relation written as an equality among two tensors in a reference frame will also hold in any other reference system.

The simplest tensor is a scalar, which is any function which under a coor-

*Indeed, the curvature of spacetime, which in General Relativity is related to the energy momentum tensor of the matter, will turn out to depend on the second derivatives of the metric. Hence, the presence of matter requires that some of these second derivatives be non-zero, excluding the possibility of finding a coordinate system for which $g_{ik} = \eta_{ik}$ globally.

dinate transformation $(x^0, x^1, x^2, x^3) \rightarrow (x'^0, x'^1, x'^2, x'^3)$ retains its value, $\phi'(x'^i) = \phi(x^i)$.

Next come the vectors, which can be expressed in terms of contravariant or covariant components. The prototype of a contravariant vector is the differential of coordinates, which transforms as

$$dx'^k = \frac{\partial x'^k}{\partial x^i} dx^i. \quad (2.4)$$

In general any set of four quantities A^i transforming as the differential of coordinates, i.e.

$$A'^k = \frac{\partial x'^k}{\partial x^i} A^i, \quad (2.5)$$

constitute the components of a contravariant vector.

The gradient of a scalar transforms instead as

$$\frac{\partial \phi}{\partial x'^k} = \frac{\partial x^i}{\partial x'^k} \frac{\partial \phi}{\partial x^i}, \quad (2.6)$$

and any set of four quantities A_i transforming as Eq. (2.6), i.e.

$$A'_k = \frac{\partial x^i}{\partial x'^k} A_i \quad (2.7)$$

constitute the components of a covariant vector.

Scalars are tensors of rank zero, vectors are tensors of rank one. Tensors of higher order can be defined in an analogous way. For example, a contravariant tensor of rank two is a set of 16 quantities transforming as the product of two contravariant vectors, i.e.

$$A'^{ik} = \frac{\partial x'^i}{\partial x^l} \frac{\partial x'^k}{\partial x^m} A^{lm}. \quad (2.8)$$

It is straightforward to generalize these transformation laws to a tensor with n contravariant indices and m covariant ones: there is a factor $\partial x'^i/\partial x^k$ for each contravariant index and a factor $\partial x^k/\partial x'^i$ for each covariant one. Contravariant vectors transform then with the inverse matrix as respects to the covariant ones, hence their name. This also means that the scalar product of a covariant and a contravariant vector is a scalar, since $A^i B_i = A'^k B'_k$, and in general the contraction of a covariant and a contravariant index in any tensor leads to a smaller rank tensor.

The metric g_{ik} , that contracted with the contravariant tensor $\mathrm{d}x^i \mathrm{d}x^k$ gives the square of the interval (a scalar), is a covariant second rank tensor. A contravariant second rank metric tensor g^{ik} is defined as the inverse of g_{ik}

$$g^{ik} g_{kl} = \delta_l^i \quad (2.9)$$

with δ_l^i the Kronecker delta ($\delta_l^i = 0$ if $i \neq l$ and $\delta_l^i = 1$ if $i = l$). The covariant (contravariant) metric tensor can be used to define an associated covariant (contravariant) vector to a contravariant (covariant) one by $A_i \equiv g_{ik} A^k$ ($A^i \equiv g^{ik} A_k$).

A complication arises when we want to consider derivatives of a vector field $A_i(x^k)$. A simple computation, differentiating Eq. (2.7), shows that the ordinary derivatives of the vector components do not transform as a tensor, since

$$\frac{\partial A'_k}{\partial x'^j} = \frac{\partial x^i}{\partial x'^k} \frac{\partial x^l}{\partial x'^j} \frac{\partial A_i}{\partial x^l} + \frac{\partial^2 x^i}{\partial x'^j \partial x'^k} A_i. \quad (2.10)$$

The underlying reason is that the differentiation process involves the subtraction of vectors at two different neighboring points and, when the transformation coefficients $\partial x^i / \partial x'^k$ are a function of the spacetime point, the difference of the vectors does not transform itself as a vector.

In order to define a differentiation procedure that does transform as a tensor it has to involve the difference of two vectors defined at the same point. Thus, before subtracting the vectors, we have to transport one of them to the neighboring point where the other one is defined. This can be achieved by the so-called parallel transport procedure. The change in the components of a covariant vector when it is transported from the point $x^i + \mathrm{d}x^i$ to the neighboring one x^i will in general be a linear function of the original components and of the displacement between the two points. It can be expressed as

$$\delta A_i = -\Gamma_{ik}^j A_j \mathrm{d}x^k, \quad (2.11)$$

where the coefficients Γ_{ik}^j are called the Christoffel symbols and they describe how the parallel transport is to be performed. With their help the so-called covariant derivative can be defined as

$$A_{i;k} = \frac{\partial A_i}{\partial x^k} - \Gamma_{ik}^j A_j. \quad (2.12)$$

The covariant derivative of a contravariant vector is easy to obtain using the fact that for a scalar the covariant derivative has to be equal to its ordinary partial derivative. Taking the scalar $\phi = A^i B_i$ this gives

$$A_{;k}^i = \frac{\partial A^i}{\partial x^k} + \Gamma_{jk}^i A^j. \quad (2.13)$$

The generalization of the covariant derivatives to higher rank tensors is trivial, for instance for a doubly covariant tensor

$$A_{ij;k} = \frac{\partial A_{ij}}{\partial x^k} - \Gamma_{ik}^l A_{lj} - \Gamma_{jk}^l A_{il}, \quad (2.14)$$

while a plus sign appears in the term with the Christoffel symbol when a contravariant index is involved, as was the case in Eq. (2.13).

Requiring that the covariant derivative transforms as a tensor and that it reduces to the usual partial derivative in Cartesian coordinates in a flat spacetime one can deduce the relation $A_{i;k} = g_{ij} A_{;k}^j$, which is generally valid because it holds in the local free falling frame and it is a proper tensor equation. On the other hand, if we use that

$$A_{i;k} = (g_{ij} A^j)_{;k} = g_{ij} A_{;k}^j + g_{ij;k} A^j, \quad (2.15)$$

we conclude that $g_{ij;k} = 0$. The vanishing of the covariant derivative of the metric implies that

$$\frac{\partial g_{ik}}{\partial x^l} = g_{km} \Gamma_{il}^m + g_{im} \Gamma_{kl}^m, \quad (2.16)$$

and this can be exploited to obtain an explicit expression for the Christoffel symbols in terms of the metric. For this we have to use that the Christoffel symbols are symmetric in the two lower indices[†] to obtain that

$$\frac{\partial g_{ij}}{\partial x^k} + \frac{\partial g_{ik}}{\partial x^j} - \frac{\partial g_{jk}}{\partial x^i} = 2g_{im} \Gamma_{jk}^m, \quad (2.17)$$

and hence one finally gets

$$\Gamma_{kl}^i = \frac{1}{2} g^{im} \left(\frac{\partial g_{mk}}{\partial x^l} + \frac{\partial g_{ml}}{\partial x^k} - \frac{\partial g_{kl}}{\partial x^m} \right). \quad (2.18)$$

[†]This is seen writing explicitly that for a scalar $\phi_{;i;j} = \phi_{;j;i}$, which is true because it is a tensor equation valid in the free falling frame.

2.1.3 Motion of particles

A free particle in the absence of gravity moves in such a way that the action,

$$\mathcal{S} = -mc \int ds, \quad (2.19)$$

is an extreme along its trajectory. As a consequence it follows a uniform and rectilinear motion. In the presence of gravity particles also describe trajectories that are extrema of this action, which is proportional to the interval between the two end-points, but as gravity modifies the geometry of spacetime now ds is a function of the metric. Lines along which the distance between two given points is extremal are called geodesics, and hence particle trajectories are geodesics of spacetime. In the case of propagation of light, since photons are massless the expression Eq. (2.19) is not appropriate, but anyhow the trajectories are extrema of the interval $\int ds$, which actually vanishes for the real paths, meaning that light propagates along null geodesics.

To obtain the equation of motion it is useful to parameterize the trajectories $x^i(\lambda)$ by a parameter λ and find the Euler Lagrange equations for the action $\int (ds/d\lambda)d\lambda$, with $ds/d\lambda = \sqrt{g_{ik}\dot{x}^i\dot{x}^k}$ in terms of the velocities $\dot{x}^i \equiv dx^i/d\lambda$. These are

$$\frac{d}{d\lambda} \frac{\partial}{\partial \dot{x}^k} \left(\frac{ds}{d\lambda} \right) = \frac{\partial}{\partial x^k} \left(\frac{ds}{d\lambda} \right). \quad (2.20)$$

Multiplying the above by $2ds/d\lambda$ one can obtain

$$\frac{d}{d\lambda} \frac{\partial}{\partial \dot{x}^k} \left(\frac{ds}{d\lambda} \right)^2 - 2 \frac{d}{d\lambda} \left(\frac{ds}{d\lambda} \right) \frac{\partial}{\partial \dot{x}^k} \left(\frac{ds}{d\lambda} \right) = \frac{\partial}{\partial x^k} \left(\frac{ds}{d\lambda} \right)^2. \quad (2.21)$$

To simplify this equation we can choose the generic parameter λ in such a way that $ds/d\lambda$ be constant along the trajectory (in this case λ is said to be an affine parameter and the interval measured along the trajectory has a linear dependence on λ). The Euler Lagrange equations reduce then to

$$\frac{d}{d\lambda} \frac{\partial}{\partial \dot{x}^k} (g_{ij}\dot{x}^i\dot{x}^j) = \frac{\partial}{\partial x^k} (g_{ij}\dot{x}^i\dot{x}^j), \quad (2.22)$$

or equivalently

$$\frac{d}{d\lambda} (g_{ik}\dot{x}^i) = \frac{1}{2} \left(\frac{\partial}{\partial x^k} g_{ij} \right) \dot{x}^i \dot{x}^j. \quad (2.23)$$

Expanding the left hand side, contracting with $g^{mk}/2$ and using Eq. (2.18), one gets finally the geodesic equation

$$\frac{d^2x^m}{d\lambda^2} + \Gamma_{kl}^m \frac{dx^k}{d\lambda} \frac{dx^l}{d\lambda} = 0, \quad (2.24)$$

which describes the particle motion for arbitrary coordinates in a curved spacetime.

For a massive particle, the required constancy of $ds/d\lambda$ along the trajectory is usually achieved making the appropriate choice $\lambda = s$, in which case $ds/d\lambda = 1$, i.e.

$$g_{ik} \frac{dx^i}{ds} \frac{dx^k}{ds} = 1 \quad , \quad (m \neq 0). \quad (2.25)$$

This relation actually directly provides a first integral of the geodesic equations.

For a photon, for which $ds = 0$, one has instead

$$g_{ik} \frac{dx^i}{d\lambda} \frac{dx^k}{d\lambda} = 0 \quad , \quad (m = 0). \quad (2.26)$$

In this case, this relation should be considered as a constraint, and the affine parameter is determined actually from the geodesic equations themselves.

The general relativistic equations have of course to reduce to the Newtonian ones in the limit of small velocities and weak gravitational fields. This requirement allows to express in a simple way the metric coefficient g_{00} in the weak field limit in terms of the classical Newtonian gravitational potential φ . To see this let us expand the metric around the Minkowski one, $g_{ik} = \eta_{ik} + h_{ik}$, with $|h_{ik}| \ll 1$, obtaining to leading order in v/c and h_{ik} that $ds \simeq c\sqrt{(1 + h_{00}) - v^2/c^2}dt$. The action in Eq. (2.19) becomes in this limit

$$S \simeq \int \left[-mc^2 + \frac{1}{2}mv^2 - m\frac{h_{00}c^2}{2} \right] dt. \quad (2.27)$$

To reproduce the classical result one must then require $h_{00}c^2/2 = \varphi$, and hence in the weak field approximation one has

$$g_{00} = 1 + \frac{2\varphi}{c^2}. \quad (2.28)$$

2.1.4 The spacetime curvature

As we have mentioned, the effect of gravity is to make spacetime non-flat, and hence to describe this it is essential to discuss the concept of curvature. A direct way to characterize the intrinsic curvature of space is from the fact that when a vector is parallel transported from one point to another in a curved spacetime, different vectors result if the transport is performed along different paths. This can easily be seen in two dimensions by transporting a vector along a triangle on the surface of a sphere, as shown in Figure 2.1. Here the vector \vec{B} obtained from \vec{A} by parallel transport along the great circles from 1 to 2, then to 3 and back to 1 does not coincide anymore with \vec{A} , something which would have never happened on a flat surface.

For higher dimensional spaces, the changes in the vector will depend on the directions along which the transport is performed. For instance, if we first parallel transport a vector A^i a distance Δx along the coordinate x^l and then a distance Δy along a different coordinate x^m , to then go back a distance $-\Delta x$ along x^l and close the loop going $-\Delta y$ along x^m , the overall change in the vector, $\delta A^i \equiv A^i(\text{final}) - A^i$, will be (using that the change

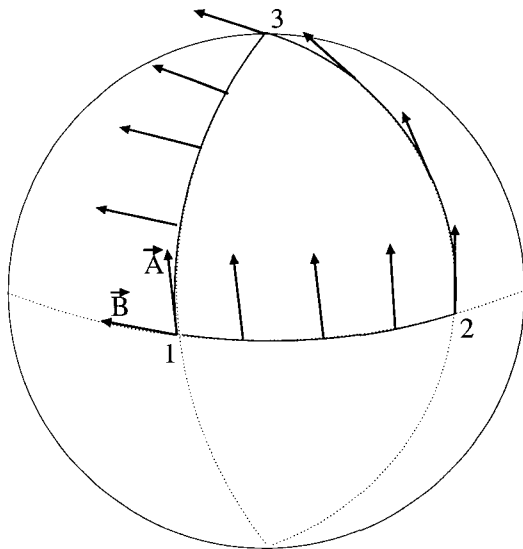


Fig. 2.1 The parallel transport along great circles on the surface of a sphere.

upon the parallel transport is $\partial A^i / \partial x^j = -\Gamma_{jk}^i A^k$)

$$\begin{aligned}\delta A^i &= -\int_{x^l}^{x^l + \Delta x} \left[\Gamma_{jl}^i A^j \right]_{x^m} dx^l - \int_{x^m}^{x^m + \Delta y} \left[\Gamma_{jl}^i A^j \right]_{x^l + \Delta x} dx^m \\ &\quad - \int_{x^l + \Delta x}^{x^l} \left[\Gamma_{jl}^i A^j \right]_{x^m + \Delta y} dx^l - \int_{x^m + \Delta y}^{x^m} \left[\Gamma_{jl}^i A^j \right]_{x^l} dx^m \\ &\simeq \Delta x \Delta y \left[\frac{\partial}{\partial x^m} (\Gamma_{jl}^i A^j) - \frac{\partial}{\partial x^l} (\Gamma_{jm}^i A^j) \right] \\ &= \Delta x \Delta y \left[\frac{\partial}{\partial x^m} \Gamma_{jl}^i - \frac{\partial}{\partial x^l} \Gamma_{jm}^i - \Gamma_{kl}^i \Gamma_{jm}^k + \Gamma_{km}^i \Gamma_{jl}^k \right] A^j.\end{aligned}\quad (2.29)$$

The term in square brackets in the last expression is called the Riemann tensor R_{jml}^i , and if we use the expression for the Christoffel symbols in Eq. (2.18) it can be expressed in terms of the second derivatives of the metric as

$$R_{jml}^i = \frac{1}{2} g^{ik} \left[\frac{\partial^2 g_{kl}}{\partial x^j \partial x^m} - \frac{\partial^2 g_{km}}{\partial x^j \partial x^l} + \frac{\partial^2 g_{jm}}{\partial x^k \partial x^l} - \frac{\partial^2 g_{jl}}{\partial x^k \partial x^m} \right].\quad (2.30)$$

Since $\delta A^i \neq 0$, the parallel transport along two different infinitesimal displacements depends on the order in which they are performed. This also indicates that, unlike what happens with the ordinary derivatives, for the covariant ones (which differ from the ordinary ones by the parallel transport), the second derivatives do not commute. Indeed, direct computation shows that

$$A_{;j;k}^i - A_{;k;j}^i = R_{ljk}^i A^l.\quad (2.31)$$

The fact that the left-hand side of this equation is a tensor implies that R_{ljk}^i must be a tensor. The Riemann tensor is also called the curvature tensor, since it vanishes (independently of the coordinate system adopted) when the spacetime is flat, while a non-vanishing value of it indicates that the spacetime is curved.

Using the covariant components of the curvature tensor, $R_{ijkl} \equiv g_{jm} R_{ikl}^m$, it is easy to verify its symmetry properties

$$R_{ijkl} = -R_{jikl} = -R_{ijlk} = R_{klji}.\quad (2.32)$$

Another important equality satisfied is the Bianchi identity

$$R_{iklm;n} + R_{iknl;m} + R_{ikmn;l} = 0.\quad (2.33)$$

By contraction of two indices in the Riemann tensor, a second rank tensor can be constructed. This construction is unique (up to a sign), since

due to the antisymmetry under the exchange of the first two or the last two indices, the contraction of these would lead to the zero tensor. The contraction between one index in the first couple and another in the second couple is instead non-vanishing, and leads to the so-called Ricci tensor

$$R_{ik} \equiv g^{lm} R_{limk} = R_{imk}^m, \quad (2.34)$$

which is symmetric. Further contracting its indices we obtain the curvature scalar

$$R \equiv g^{ik} R_{ik}. \quad (2.35)$$

By contracting the Bianchi identities, Eq. (2.33), with g^{im} g^{kn} , we obtain the important relation

$$\left(R^{ik} - \frac{1}{2} g^{ik} R \right)_{;k} = 0. \quad (2.36)$$

2.1.5 The Einstein equation

We can now address the crucial point of how matter determines the curved spacetime metric in General Relativity.

In Special Relativity the matter and energy distribution is described by the energy-momentum tensor T_{ik} , and the conservation of energy and momentum reads $\partial T_{ik} / \partial x^k = 0$.

Looking for an equation relating the geometry with the matter, Einstein conjectured that the energy-momentum tensor should act as source for an expression containing the first two derivatives of the metric, since in the non-relativistic and weak gravitational field limit it should reduce to the Poisson equation

$$\nabla^2 \varphi = 4\pi G\rho. \quad (2.37)$$

The fundamental equation he proposed was

$$R_{ik} - \frac{1}{2} g_{ik} R = \kappa T_{ik}. \quad (2.38)$$

Notice that the generalized version of the energy and momentum conservation, $T_{ik}^{;k} = 0$, is insured by Eq. (2.36). On the other hand, with a proper choice of the constant κ the Einstein equation reduces to the Poisson equation in the limit of non relativistic velocities ($v \ll c$), weak gravitational

fields ($g_{ik} \simeq \eta_{ik} + h_{ik}$, with $|h_{ik}| \ll 1$) and fields changing slowly with time ($\partial_t \ll c \partial_x$). Indeed, to first order in h_{ik} the Ricci tensor is

$$R_{ik} \simeq \frac{1}{2} \eta^{lm} (h_{il,mk} + h_{mk,il} - h_{ik,ml} - h_{ml,ik}). \quad (2.39)$$

If one keeps only spatial derivatives, we get for the (0-0) component that $R_{00} \simeq \nabla^2 h_{00}/2$, which looks already like the left hand side of Eq. (2.37) once we take into account that $h_{00} = 2\varphi/c^2$ in terms of the Newtonian potential φ .

Regarding the energy momentum tensor, in the non-relativistic limit its only relevant component is $T_{00} = \rho$, and its trace is also $T \equiv T_i^i \simeq \rho$. If we now contract Eq. (2.38) with g^{ik} , we get that $R = -\kappa T$ and thus the Einstein equation can be rewritten as

$$R_{ik} = \kappa (T_{ik} - \frac{1}{2} g_{ik} T). \quad (2.40)$$

This gives in the weak field limit

$$R_{00} = \frac{1}{c^2} \nabla^2 \varphi = \frac{\kappa}{2} \rho, \quad (2.41)$$

and hence the Poisson Eq. (2.37) is recovered provided that $\kappa = 8\pi G/c^4$.

As in the presence of an homogeneous distribution of matter Eq. (2.38) does not admit static solutions, Einstein added a new term to the equation which allowed for the Universe to remain static, in agreement with the general belief at that time. This is the term involving the famous cosmological constant Λ , so that the complete Einstein equation is

$$R_{ik} - \frac{1}{2} g_{ik} R - \Lambda g_{ik} = \frac{8\pi G}{c^4} T_{ik}. \quad (2.42)$$

After the discovery of the expansion of the Universe the cosmological constant term was abandoned and re-adopted several times. Nowadays it is usually considered as part of the right hand side of the equation, coming from the contribution of a vacuum energy density or of some exotic stress-energy component, and there is actually growing evidence favoring a non-zero value for it.

2.1.6 The Schwarzschild metric

To find exact solutions of the Einstein equations is a difficult task, since they are non-linear in the metric coefficients, and few of them are known to

the present. The first exact solution was obtained by Schwarzschild (setting $\Lambda = 0$, since the effects of a non-zero value would anyhow only be relevant at cosmological distances) and corresponds to the metric outside a spherical distribution of total mass M . It has played a major role in most of the tests of General Relativity and particularly in the determination of the deflection of light by a matter distribution. Since this deflection is at the basis of the gravitational lensing phenomena we are going to present the Schwarzschild solution here in some detail.

The spacetime metric associated to a spherical distribution of mass has to respect the symmetries of the distribution. In particular, it has to take the same value for all the points that are at the same distance from the center. The symmetry of the problem makes it convenient to use spherical spatial coordinates r, θ and ϕ . Let us note however that in the presence of matter the space is not Euclidean, hence this makes the choice of the radial coordinate somewhat arbitrary and in particular there is no choice having all the properties of the Euclidean vector radius, e.g. being equal both to the distance to the center and to the ratio of the length of the circle over 2π .

The most general form of the interval which respects the spherical symmetry is given by

$$ds^2 = C(r, t)dt^2 - A(r, t)dr^2 - B(r, t)(\sin^2 \theta d\phi^2 + d\theta^2) + D(r, t) dr dt. \quad (2.43)$$

Furthermore, any change of coordinate such that $t' = f(r, t)$ and $r' = g(r, t)$ preserves the spherical symmetry and by a convenient choice of these coordinates one can make $D = 0$. We can also choose the radial coordinate such that $B = r^2$, which ensures that circles centered at the origin of coordinates have length equal to $2\pi r$. With these choices, the metric for a spherical symmetric mass distribution takes the form

$$ds^2 = e^{\nu(r, t)}c^2 dt^2 - e^{\lambda(r, t)}dr^2 - r^2(\sin^2 \theta d\phi^2 + d\theta^2). \quad (2.44)$$

The last step is to determine the form of the functions $\lambda(r, t)$ and $\nu(r, t)$ by solving the Einstein equations, which outside the region occupied by the mass distribution take the simple form $R_{ik} = 0$. If we extract the coefficients of the metric g_{ik} from the line element (2.44), then construct the curvature tensor using Eq. (2.30) and from it obtain the Ricci tensor, the resulting equations requiring the vanishing of R_{11} , R_{00} and R_{01} are,

respectively

$$\begin{aligned} -e^{-\lambda} \left(\frac{\nu'}{r} + \frac{1}{r^2} \right) + \frac{1}{r^2} &= 0, \\ e^{-\lambda} \left(\frac{\lambda'}{r} - \frac{1}{r^2} \right) + \frac{1}{r^2} &= 0, \\ \dot{\lambda} &= 0, \end{aligned} \quad (2.45)$$

where a prime denotes derivative with respect to r and a dot derivative with respect to time. From the first two we see that $\nu + \lambda = f(t)$ is a function only of time. We can now exploit that we still have the freedom to rescale the time coordinate in the line element (2.44) so as to absorb $f(t)$ into a new function $\nu(t)$, in such a way that one is lead to $\nu + \lambda = 0$. Combining this with the last equation we see that both λ and ν should be functions only of r , and hence the metric is static. The remaining equation arising from the first two is $(re^\nu)' = 1$, which can be easily integrated to give

$$e^\nu = 1 - \frac{K}{r}. \quad (2.46)$$

The integration constant K is fixed by requiring that at large distances from the mass distribution, where the weak field approximation holds, the Newtonian limit $g_{00} = 1 + 2\varphi/c^2$ be recovered, with the gravitational potential given by $\varphi = -GM/r$ for a total mass M . Then, the constant K takes the value $K = 2GM/c^2$. The metric can then finally be written as

$$ds^2 = \left(1 - \frac{2MG}{rc^2} \right) c^2 dt^2 - \left(1 - \frac{2MG}{rc^2} \right)^{-1} dr^2 - r^2 (\sin^2 \theta d\phi^2 + d\theta^2). \quad (2.47)$$

Notice that the component g_{rr} in the metric of Eq. (2.47) becomes singular at $r = 2MG/c^2 \equiv r_S$, known as the Schwarzschild radius. Anyhow the form of the solution obtained for the metric is valid only in the region $r > r_S$ and we will not discuss the properties of the solutions in the range $r < r_S$, relevant only for the description of black holes[†]. Since the Schwarzschild metric describes the gravitational field outside the mass distribution and the Schwarzschild radius of normal stars and planets is much smaller than their physical size (for example for the Sun it is $r_S = 2.96$ km

[†]Actually, by an appropriate coordinate transformation it is possible to write the metric in such a way that it remains regular at $r = r_S$ (see e.g. [La75]), and hence the singularity encountered is just an artifact of the coordinate system adopted.

and for the Earth it is $r_S = 8.8$ mm), the expression of the metric obtained above will be sufficient for the matters discussed here.

2.2 The bending of light

2.2.1 Point-like deflector

We are now ready to compute in the context of General Relativity the deflection suffered by the light rays passing close to a massive object. The deflection angle can be obtained from the knowledge of the trajectory of the light rays, which correspond to null geodesics and are hence solutions of the geodesic equations (2.24). These equations require the knowledge of the metric, and in the case of a point-like mass describing a compact lens, the metric is spherically symmetric and the line element is thus the Schwarzschild one. Furthermore, we know that the trajectory of the light rays will be contained in the plane defined by the incident light direction and the mass location, and hence it is convenient to choose the coordinates so that the motion is contained in the plane $\theta = \pi/2$. Thus, the trajectory is described by the ϕ and r coordinates and the interval reduces to

$$ds^2 = \left(1 - \frac{2MG}{rc^2}\right) c^2 dt^2 - \left(1 - \frac{2MG}{rc^2}\right)^{-1} dr^2 - r^2 d\phi^2. \quad (2.48)$$

Notice that the metric coefficients do not depend neither on ϕ nor on t . This means that the geodesic equations corresponding to these ‘cyclic’ coordinates will be associated to two integrals of motion

$$\frac{d}{d\lambda} \frac{\partial}{\partial \dot{\phi}} \left(\frac{ds}{d\lambda} \right)^2 = 0 \rightarrow r^2 \dot{\phi} = J, \quad (2.49)$$

$$\frac{d}{d\lambda} \frac{\partial}{\partial \dot{t}} \left(\frac{ds}{d\lambda} \right)^2 = 0 \rightarrow \left(1 - \frac{2MG}{rc^2}\right) c^2 \dot{t} = A, \quad (2.50)$$

where J and A are constants and we denoted by a dot the derivatives with respect to λ .

The additional constraint arising from $ds/d\lambda = 0$ along the trajectory, Eq. (2.26), takes the form

$$\left(1 - \frac{2MG}{rc^2}\right) c^2 \dot{t}^2 - \left(1 - \frac{2MG}{rc^2}\right)^{-1} \dot{r}^2 - r^2 \dot{\phi}^2 = 0. \quad (2.51)$$

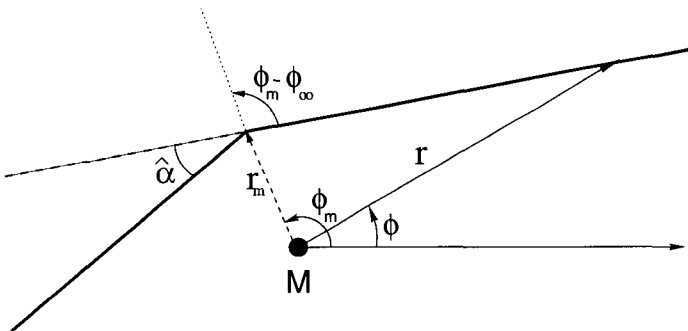


Fig. 2.2 Deflection of a light ray passing close to a mass M .

Without loosing generality we can choose λ (by an appropriate rescaling) so that $A = c^2$ in Eq. (2.50). Replacing Eqs. (2.49) and (2.50) into Eq. (2.51) leads then to

$$\dot{r}^2 = 1 - \frac{J^2}{r^2} \left(1 - \frac{2MG}{rc^2} \right). \quad (2.52)$$

Further combining this result with Eq. (2.49) we get the equation for the trajectory

$$d\phi = \frac{J}{r^2} \frac{dr}{\sqrt{1 - \frac{J^2}{r^2} \left(1 - \frac{2MG}{rc^2} \right)}}, \quad (2.53)$$

which upon integration will give the deflection angle of a light ray passing close to the mass M . Figure 2.2 shows the geometry of the process. At the time of closest approach to M , $\phi = \phi_m$, $r = r_m$ and $dr/d\phi = 0$. From this relation and Eq. (2.53) we obtain for the constant of motion

$$J = \frac{r_m}{\sqrt{1 - \frac{2MG}{r_m c^2}}}. \quad (2.54)$$

Changing now variable to $x = r_m/r$, we obtain from Eq. (2.53) that

$$\phi_m - \phi_\infty = \int_0^1 \frac{dx}{\sqrt{1 - x^2 - \frac{2GM}{r_m c^2} (1 - x^3)}}, \quad (2.55)$$

where ϕ_∞ is the asymptotic value of ϕ very far in the past (the incident direction). An approximate solution, valid when $r_m \gg r_S$ (which holds in

most applications), is readily obtained by direct integration

$$\phi_m - \phi_\infty = \frac{\pi}{2} + \frac{2GM}{r_m c^2}. \quad (2.56)$$

The difference of the two asymptotic directions (approaching and leaving the deflector body) is twice this quantity, and differs from π (no deflection) just by the deflection angle

$$\hat{\alpha} = \frac{4GM}{r_m c^2}. \quad (2.57)$$

Thus, the deflection suffered by light rays passing close to a massive body is proportional to the mass of the object and inversely proportional to the minimum distance of approach to it. Since this result was derived under the assumption that the impact parameter r_m was large compared to the Schwarzschild radius r_S , in this regime the deflection angle $\hat{\alpha} = 2r_S/r_m$ will be small.

The value of the deflection angle predicted by the theory of General Relativity, Eq. (2.57), is actually twice the classical value obtained two centuries ago using Newtonian mechanics by Soldner (1804) [So04] \S . For light rays passing close to the solar limb the relativistic deflection angle amounts to $\hat{\alpha} = 1.75''$. This prediction of Einstein's theory was first confirmed by Eddington looking at the change in the apparent positions of the

\S The classical result is obtained by considering the motion of a particle moving at the speed of light in a central potential $U(r) = -GM/r$. Combining the equations corresponding to angular momentum and energy conservation, the equation for the trajectory is

$$\frac{d\phi}{dr} = \frac{L}{mr^2} \left(\frac{2}{m}(E - U(r)) - \frac{L^2}{m^2 r^2} \right)^{-1/2}.$$

The constant energy is related to the incident velocity $v_0 = c$ through $E = mv_0^2/2$, and since at the point r_m of closest approach one has $dr/d\phi = 0$, we can write $L^2/m^2 = v_0^2 r_m^2 + 2GM r_m$. Integration of the trajectory then gives

$$\phi_m - \phi_\infty = \frac{\pi}{2} + \arcsin \left(1 + \frac{r_m v_0^2}{GM} \right)^{-1}.$$

In the weak field limit, $GM/r_m \ll v_0^2$, this gives for the deflection angle

$$\hat{\alpha} = 2(\phi_m - \phi_\infty) - \pi \simeq \frac{2GM}{r_m c^2}.$$

stars close to the solar limb during a solar eclipse in 1919 [Dy20] and, together with the explanation of the precession of the perihelion of Mercury, allowed the theory of General Relativity to become widely accepted.

2.2.2 Time delay

Besides experimenting a deflection of its trajectory when passing close to a mass distribution, light also suffers a time delay with respect to the travel time in the absence of the gravitational field of the deflector body.

The time delay has two contributions: one is the geometric delay δt_{geom} arising from the fact that the bent trajectory is longer than the straight one, and the other is the gravitational one δt_{grav} (or Shapiro delay [Sh64]) due to the fact that the pace of clocks and distance lengths are affected by the gravitational field of the deflector. To obtain a simple expression for this last, it is convenient to rewrite the Schwarzschild metric with the new radial coordinate R defined through $r = R(1 + GM/2Rc^2)^2$, and then introduce the ‘Cartesian’ coordinates $x = R \sin \theta \cos \phi$, $y = R \sin \theta \sin \phi$ and $z = R \cos \theta$. This leads to

$$ds^2 = \left(\frac{1 - GM/2Rc^2}{1 + GM/2Rc^2} \right)^2 c^2 dt^2 - \left(1 + \frac{GM}{2Rc^2} \right)^4 (dx^2 + dy^2 + dz^2). \quad (2.58)$$

In the weak field limit, this expression can be written as

$$ds^2 = \left(1 + \frac{2\varphi}{c^2} \right) c^2 dt^2 - \left(1 - \frac{2\varphi}{c^2} \right) (dx^2 + dy^2 + dz^2), \quad (2.59)$$

in terms of the Newtonian gravitational potential φ . Notice that very far from the mass distribution, the space becomes asymptotically Euclidean and the time coordinate would just correspond to the proper time measured by an observer. If we consider now the propagation of a light ray ($ds = 0$) between two points A and B , the time elapsed can be computed choosing the z axis along the light-ray trajectory (the geometric effect of the light deflection on the time delay will be included in the next Chapter), to obtain

$$t_B - t_A \simeq \frac{1}{c} \int_{z_A}^{z_B} \left(1 - \frac{2\varphi}{c^2} \right) dz. \quad (2.60)$$

This means that the gravitational time delay is

$$\delta t_{grav} = -\frac{2}{c^3} \int_{z_A}^{z_B} \varphi(z) dz, \quad (2.61)$$

and depends on the gravitational potential integrated along the photon's path. This Shapiro delay has been measured using radar pulses towards the inner planets (Venus or Mercury) that bounce back to the Earth, and provides another classical test of the theory of General Relativity [Re79].

2.2.3 Extended mass distribution

Let us consider now an extended mass distribution $\rho(\vec{x})$ acting as deflector. When the extension of the mass distribution along the light ray direction is small compared to the length of the path of interest, we can make the approximation that the light path consists of two straight lines far from the deflector with a unique deflection taking place at the location of the mass distribution, i.e. the so-called thin lens approximation.

We will denote by $\Sigma(\vec{\xi})$ the surface mass density corresponding to the projection of the mass distribution on a plane passing through its center of mass and orthogonal to the light ray direction,

$$\Sigma(\vec{\xi}) = \int dz \rho(\vec{\xi}, z), \quad (2.62)$$

where $\vec{\xi}$ is the two dimensional vector indicating the positions in the lens plane and z is the coordinate in the orthogonal direction.

The deflection, which can be considered to take place at the point where the light ray crosses the plane, can be obtained as the superposition of the deflections produced by the individual mass differentials

$$\vec{\alpha}(\vec{\xi}) = \frac{4G}{c^2} \int d^2 \xi' \Sigma(\vec{\xi}') \frac{\vec{\xi} - \vec{\xi}'}{|\vec{\xi} - \vec{\xi}'|^2}. \quad (2.63)$$

This is valid because in the weak field limit adopted the non-linear equations of General Relativity get linearized, and hence the superposition principle holds. Notice that the deflection angle has two components, as it has to describe the modulus and the direction of the deflection, while in the case of the point-like mass it was sufficient to consider only its modulus, since it was understood that the deviation was towards the deflector[¶].

[¶]Notice that the angle $\vec{\alpha}$ points *outwards* of the deflector. This convention is generally adopted in order to keep the same signs in the lens equation, to be discussed in the next Chapter, when writing it in a vectorial or a scalar way.

It is useful to write the deflection angle in terms of the projected gravitational potential

$$\psi(\vec{\xi}) \equiv \int dz \varphi(\vec{\xi}, z), \quad (2.64)$$

which using the Poisson equation can be related to the surface mass density distribution (see Eq. (2.37)) through

$$\nabla_{\vec{\xi}}^2 \psi(\vec{\xi}) = 4\pi G \Sigma(\vec{\xi}). \quad (2.65)$$

Furthermore, recalling that the Green function \mathcal{G} for the two-dimensional Laplacian (satisfying $\nabla_{\vec{\xi}}^2 \mathcal{G}(\vec{\xi}, \vec{\xi}') = 2\pi\delta^2(\vec{\xi} - \vec{\xi}')$), is given by $\mathcal{G}(\vec{\xi}, \vec{\xi}') = \ln|\vec{\xi} - \vec{\xi}'|$, the projected potential can be written as

$$\psi(\vec{\xi}) = 2G \int d^2\xi' \Sigma(\vec{\xi}') \ln|\vec{\xi} - \vec{\xi}'|. \quad (2.66)$$

The deflection angle (see Eq. (2.63)) thus turns out to be proportional to the gradient of the projected gravitational potential

$$\vec{\alpha}(\vec{\xi}) = \frac{2}{c^2} \vec{\nabla}_{\vec{\xi}} \psi(\vec{\xi}). \quad (2.67)$$

A particular case of interest in some applications is that in which the mass distribution has spherical symmetry. In this case the surface mass density depends only on the modulus $\xi \equiv |\vec{\xi}|$. Because of the symmetry of the problem the deflection angle takes the same absolute value for all the points at a distance ξ from the center, and is pointed along the radial direction. We can now apply the Gauss theorem for the plane to this case: the integral of the divergence of a field in the surface S_{ξ} enclosed by a circle of radius ξ around the center is equal to the flux of the vector field through the boundary C_{ξ} , i.e.

$$\int_{S_{\xi}} \vec{\nabla} \cdot \vec{\alpha} ds = \oint_{C_{\xi}} \vec{\alpha} \cdot \frac{\vec{\xi}}{\xi} dl. \quad (2.68)$$

Using Eqs. (2.67) and (2.65) we have that $\vec{\nabla} \cdot \vec{\alpha} = 8\pi G \Sigma / c^2$, and hence the modulus of the deflection angle is

$$\hat{\alpha}(\xi) = \frac{4GM(\xi)}{c^2 \xi}, \quad (2.69)$$

with $M(\xi)$ the mass enclosed inside a circle of radius ξ , i.e.

$$M(\xi) = 2\pi \int_0^\xi d\xi' \xi' \Sigma(\xi'). \quad (2.70)$$

Thus, for a spherically symmetric distribution the deflection angle only depends on the total mass enclosed inside the impact parameter ξ but not on its radial profile.

The projected gravitational potential is also useful to express the gravitational time delay caused by a given mass distribution. From Eqs. (2.61) and (2.64), one gets that

$$\delta t_{grav}(\vec{\xi}) = -\frac{2}{c^3} \psi(\vec{\xi}). \quad (2.71)$$

Recommended reading

- L. Landau and E. Lifchitz, Vol. II (1975), “The classical theory of fields” (Pergamon, Oxford).
- S. Weinberg (1972) “Gravitation and cosmology: principles and applications of the general theory of relativity” (John Wiley and Sons, N.Y.).
- B. F. Schutz (1985) “A first course in General Relativity”, (Cambridge University Press).
- C. W. Misner, K. S. Thorne and J. A. Wheeler (1973), “Gravitation”, (W. H. Freeman and Co., San Francisco).

This page is intentionally left blank

Chapter 3

Gravitational lensing theory

The deflection of light by massive bodies studied in the previous Chapter gives rise to many interesting lensing phenomena that can modify the way in which the different sources of radiation in the Universe are seen by an observer. We will now present the lens equation, relating the observed image positions to the actual source position in the presence of deflectors, and study it for different lens models. We will then discuss the main properties of multiple image formation and study the magnification effects which result from the distortion of the solid angle subtended by the source. We will also analyze the critical lines and caustics of the basic lens models, which characterize the image/source positions leading to divergent magnifications, and describe the behavior of the amplification for sources near folds and cusps of the caustic lines.

3.1 The lens equation

3.1.1 *Point-like lenses*

To start studying these effects, we will first consider the simplest situation, corresponding to a point-like mass M (the lens) located close to the line of sight to a source S , as depicted in Figure 3.1. The angle β describes the actual (unobservable) position of the source with respect to the optical axis (chosen for convenience along the lens direction) and θ is the angle of the apparent (observed) position of the source image I . Due to the gravitational field of the lens, the trajectory of the light ray is bent by the

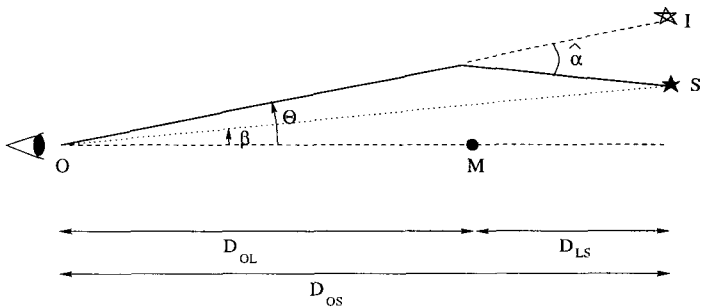


Fig. 3.1 Geometry of a point-like lens system.

angle $\hat{\alpha}$, and from the figure it is clear that

$$\theta D_{OS} = \beta D_{OS} + \hat{\alpha} D_{LS}. \quad (3.1)$$

Introducing the reduced deflection angle

$$\alpha \equiv \hat{\alpha} \frac{D_{LS}}{D_{OS}}, \quad (3.2)$$

Eq. (3.1) can be rewritten as

$$\beta = \theta - \alpha. \quad (3.3)$$

This is the so-called lens equation, which describes the relation between the real and apparent positions of the source.

For the point-like lens, according to Eq. (2.57) and using that the minimal distance of the light ray to the lens is $r_m = \theta D_{OL}$, the reduced deflection angle results

$$\alpha = \frac{D_{LS}}{D_{OS} D_{OL}} \frac{4GM}{c^2 \theta}. \quad (3.4)$$

Hence, in this case the lens equation takes the simple form

$$\theta^2 - \beta \theta - \theta_E^2 = 0, \quad (3.5)$$

where the Einstein angle θ_E is defined as

$$\theta_E \equiv \sqrt{\frac{D_{LS}}{D_{OS} D_{OL}} \frac{4GM}{c^2}}. \quad (3.6)$$

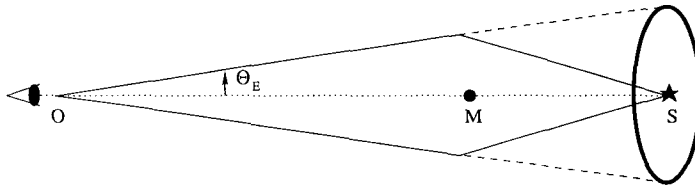


Fig. 3.2 Einstein ring due to the gravitational lensing of a source perfectly aligned with the lens.

Solving the lens equation for any fixed position of the source β , we can obtain the values of θ corresponding to the positions of the images. An interesting result, first noted by Chwolson [Ch24], is that when the lens and the source are perfectly aligned, that is for $\beta = 0$, due to the symmetry of the lens configuration the image is actually a ring of angular radius θ_E , as depicted in Figure 3.2. These kind of images are called Einstein rings, and are also expected whenever an extended lens has spherical symmetry and the background source is aligned on the axis of symmetry. In this case the size of the Einstein angle depends on the total lens mass contained inside the Einstein angle (see Eq. (2.69)).

For a generic position of the source, there will be two images with angular positions

$$\theta_{\pm} = \frac{\beta}{2} \pm \theta_E \sqrt{1 + \frac{\beta^2}{4\theta_E^2}}. \quad (3.7)$$

They lie both along the line in the sky determined by the source and the lens positions and at opposite sides of the lens (one of the solutions of Eq. (3.7) is positive and the other is negative), as shown in Figure 3.3.

The angular separation between the two images is given by

$$\Delta\theta = \theta_+ - \theta_- = 2\theta_E \sqrt{1 + \frac{\beta^2}{4\theta_E^2}}, \quad (3.8)$$

and hence when the source departure from the optical axis is small compared to the Einstein angle, $\beta < \theta_E$, the separation of the images is approximately twice the Einstein angle. To have an estimate for the magnitude

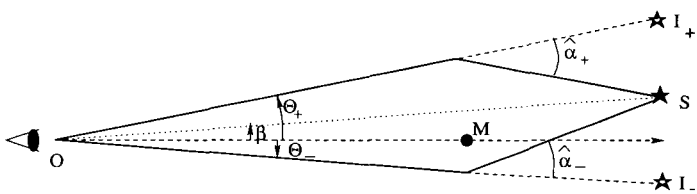


Fig. 3.3 Position of the two images of a point-like lens.

of this separation consider the case of lensing by stars within the Galaxy*. In this case the Einstein angle

$$\theta_E \simeq 0.9 \text{ mas} \sqrt{\frac{D_{LS} 10 \text{ kpc}}{D_{OL} D_{OS}} \frac{M}{M_\odot}} \quad (3.9)$$

is of the order of milliarcseconds, and hence the separation among the images is unresolvable with present optical telescopes (the resolution of the Hubble Space Telescope (HST) is $\sim 0.1''$).

When lensing of quasars by individual stars in foreground galaxies is considered, the distances involved are cosmological (\sim Gpc) and a look at Eq. (3.9) shows that the angular separations become of the order of microarcseconds (μas). This situation is actually what originally gave rise to the name microlensing, which is now generally used to denote lensing processes for which the separation between images is not resolved and hence only a change in the apparent source brightness can be observed.

When a foreground galaxy lenses a background quasar, the Einstein angle is more conveniently expressed as

$$\theta_E \simeq 3'' \sqrt{\frac{D_{LS} 1 \text{ Gpc}}{D_{OL} D_{OS}} \frac{M}{10^{12} M_\odot}}, \quad (3.10)$$

and consequently the typical image separations would be of a few arcsec. This means that, as pointed out initially by Zwicky [Zw37a; Zw37b], when the lens is a galaxy the splittings are large enough for the images to be

*Astronomical distances are usually expressed in parsecs, with $1 \text{ pc} = 3.086 \times 10^{16} \text{ m}$, while masses will be expressed in units of the mass of the Sun, $M_\odot = 1.99 \times 10^{30} \text{ kg}$.

resolved. This fact was actually crucial for the identification of the first examples of gravitational lensing as multiple imaged quasars.

3.1.2 Extended lenses

When the deflector is an extended object, like a galaxy or a cluster, or if it consists of more than one point-like lens, such as in a binary system, the generalized lens equation becomes vectorial. If the extension of the mass distribution along the line of sight is small compared to the distances between the lens and the observer and between the lens and the source, it is a good approximation to consider just the projected mass in a plane (the so-called lens plane) perpendicular to the line of sight and at the location of the lenses. In this case, one can consider that all the deflection takes place on that plane (see Figure 3.4), and the lens equation reads [Bo75]

$$\vec{\beta} = \vec{\theta} - \vec{\alpha}, \quad (3.11)$$

where $\vec{\alpha} \equiv \vec{\alpha} D_{LS}/D_{OS}$, with $\vec{\alpha}$ given by Eq. (2.63), and $\vec{\theta} \equiv \vec{\xi}/D_{OL}$.

Let us now introduce a rescaled projected gravitational potential

$$\Psi \equiv \frac{2}{c^2} \frac{D_{LS}}{D_{OS} D_{OL}} \psi, \quad (3.12)$$

with ψ given in Eq. (2.66). Using Eq. (2.67) one has then that $\vec{\alpha} = \vec{\nabla}_{\theta} \Psi$, where the gradient here is taken with respect to the angular variables, and hence the lens equation becomes

$$\vec{\beta} = \vec{\theta} - \vec{\nabla}_{\theta} \Psi(\vec{\theta}). \quad (3.13)$$

For each image position $\vec{\theta}$ there is clearly a unique source position $\vec{\beta}$. However, since the equation is non-linear in $\vec{\theta}$, for some source positions it might be possible to find multiple solutions of the lens equation. This would correspond to the formation of multiple images, and when this happens one is in the so-called strong lensing regime.

It is important to notice that to derive the lens equation we have used in Eq. (3.1) the relation between the angles and distances known from the usual Euclidean trigonometry. In particular, we wrote the distance between two points in the source plane as the product of the angle they subtend from the observer's location times the distance from the observer to the source plane. In an expanding universe, spatial distances are not uniquely defined and the above mentioned prescription defines the so-called angular

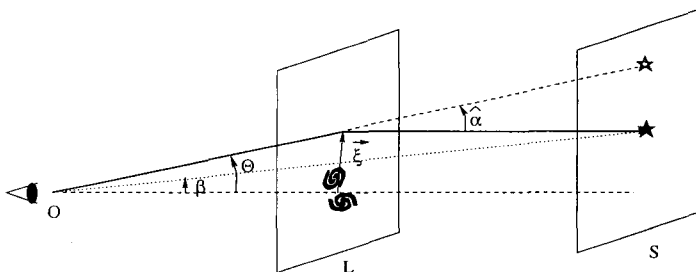


Fig. 3.4 Extended lensing distribution.

diameter distances. Another distance measure which is often encountered is the so-called luminosity distance D_L , defined such that the observed flux \mathcal{F} from an isotropic source with intrinsic luminosity \mathcal{L} is $\mathcal{F} = \mathcal{L}/(4\pi D_L^2)$. The angular and luminosity distances do not coincide in a curved space-time and hence in cosmological applications of gravitational lensing their differences have to be taken into account[†]. In the Appendix A we introduce the Friedman-Robertson-Walker metric describing the expanding homogeneous and isotropic Universe and present the expressions for both distances in terms of the redshift of the object.

3.2 The surface brightness conservation

The deflection of light by matter can produce a change in the apparent luminosity of a source. This is just a consequence of the distortion of the solid angle under which an object is seen because, as we now discuss, the intrinsic surface brightness is not changed by the lensing effects.

To describe the propagation of radiant energy through space, a central concept is that of the surface brightness $I(\nu)$. It is defined as the flux of energy of a certain frequency ν , crossing a unit area perpendicular to the direction of propagation, per unit time, per unit solid angle and per unit frequency interval, i.e.

$$I(\nu) = \frac{dE}{dt dA d\Omega d\nu}. \quad (3.14)$$

Let us now consider the radiation emitted by a source as a flux of

[†]One has to keep in mind also that $D_{OS} \neq D_{OL} + D_{LS}$ when objects at cosmological distances are considered.

photons characterized by a phase-space density $f(\vec{x}, \vec{p}, t)$, which gives the number of photons in a given phase-space volume, i.e.

$$f(\vec{x}, \vec{p}, t) = \frac{dN}{d^3\vec{x} d^3\vec{p}}. \quad (3.15)$$

Using that the beam energy is $dE = E_\gamma dN$, where the individual photon energies satisfy $E_\gamma = h\nu = cp$ (with $p \equiv |\vec{p}|$ the photon momentum), that $d^3\vec{p} = p^2 dp d\Omega$ and that $d^3\vec{x} = dA c dt$, one gets that

$$f(\vec{x}, \vec{p}, t) = \frac{dE}{h c p^3 d\nu d\Omega dA dt} = \frac{I(\nu)}{h c p^3}. \quad (3.16)$$

The Liouville theorem applied to the photon beam requires that the phase-space density f be unchanged during the photon propagation if no absorption or emission of photons takes place [Mi73]. This implies the very important result that $I(\nu)/p^3$ has to be constant along the trajectory, and is hence not affected by the gravitational deflection of light.

If the expansion of the Universe can be neglected, the photon momentum will be conserved as the photon propagates and hence also the surface brightness will be conserved. For cosmological applications, the momentum of the photon p_S emitted by a source at redshift z_S is related to the observed photon momentum p_O through $p_S = (1 + z_S)p_O$. Hence, the surface brightness ‘conservation’ in the expanding Universe takes the form

$$I_O(\nu_O) = \frac{I_S(\nu_S = (1 + z_S)\nu_O)}{(1 + z_S)^3}. \quad (3.17)$$

3.3 Amplification

The flux received from a source is just obtained from the product of its surface brightness times the solid angle it subtends[†]. Since the surface brightness is conserved but the differential deflection of light rays changes the shape and the solid angle that a given source subtends on the sky, the source luminosity will be amplified by the effect of gravitational lensing by

[†]When the brightness changes across the source, as for instance when the darkening near the limb of a star is taken into account, or when the source is an extended object like a galaxy, the integral of the surface brightness across the source has to be done.

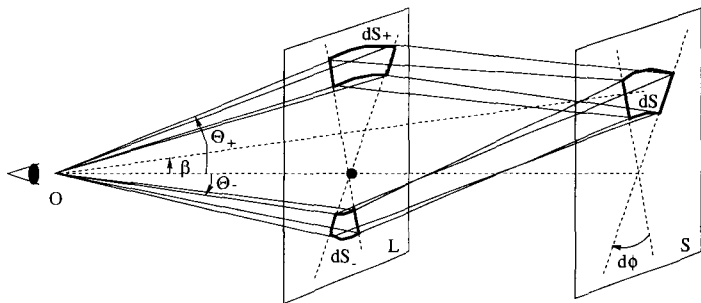


Fig. 3.5 Light ray trajectories from a surface element of the source dS in the presence of a point-like lens. The corresponding surface elements of the images in the lens plane are dS_{\pm} .

an amount

$$A = \frac{d\Omega}{d\Omega_0}, \quad (3.18)$$

where $d\Omega$ is the observed solid angle and $d\Omega_0$ the corresponding one in the absence of lenses.

Let us consider first the case of a point-like lens. A source with angular position $\vec{\beta}$ has two images located at angular positions θ_+ and θ_- given by Eq. (3.7). As illustrated in Figure 3.5, a source element dS , subtending a solid angle $d\Omega_0 = dS/D^2_{OS} = \beta d\phi d\beta$, is observed in the image positions subtending a solid angle $d\Omega_{\pm} = dS_{\pm}/D^2_{OL} = \theta_{\pm} d\phi d\theta_{\pm}$. Hence, the amplification of each of the images can be written as

$$A_{\pm} = \frac{d\Omega_{\pm}}{d\Omega_0} = \frac{\theta_{\pm} d\theta_{\pm}}{\beta d\beta}. \quad (3.19)$$

Using Eq. (3.7) we obtain that

$$A_{\pm} = \frac{1}{2} \pm \frac{\beta^2 + 2\theta_E^2}{2\beta\sqrt{\beta^2 + 4\theta_E^2}}. \quad (3.20)$$

For the image appearing in the opposite side of the lens, at an angle θ_- , the value of $d\Omega_-/d\Omega_0$ is actually negative, meaning that the image is inverted, and hence it is said to have negative parity. When the separation of the images is large enough so that they can be resolved, the relative amplification A_+/A_- of the images can be measured. If on the contrary

the images cannot be resolved, only the total flux received from the source can be observed, and its overall amplification is obtained by adding the absolute values of the magnification of the two images

$$A = A_+ + |A_-| = \frac{\beta^2 + 2\theta_E^2}{\beta\sqrt{\beta^2 + 4\theta_E^2}}. \quad (3.21)$$

To measure this amplification from a single observation is not possible, since generally the original source flux is not known, but if the lens is moving with respect to the line of sight to the source the amplification will change with time and the variation of the luminosity of the images can be measured. This effect was first detected in one of the images of the multiply imaged quasar QSO 2237+0305, and it is also at the basis of the microlensing experiments looking for galactic dark matter in the form of astrophysical compact objects.

In the more general case of an extended lensing mass distribution with no axis of symmetry, the lens equation (3.11) involves the two-dimensional vectorial deflection $\vec{\alpha}$. The vectorial lens equation can be interpreted as a two-dimensional mapping between the positions of the images $\vec{\theta}$ and the actual source positions in the sky $\vec{\beta}$, which would just be the image position in the absence of lenses. Denoting by J the Jacobian of this mapping, i.e.

$$J = \det \frac{\partial \vec{\beta}}{\partial \vec{\theta}}, \quad (3.22)$$

one can relate a differential element of solid angle in the image plane, $d\Omega = d\vec{\theta}_1 \wedge d\vec{\theta}_2$, with the corresponding one in the source plane, $d\Omega_0 = d\vec{\beta}_1 \wedge d\vec{\beta}_2$, through $d\Omega = J^{-1}d\Omega_0$. The magnification of the corresponding image, which is just the ratio of the solid angles, is then given by

$$A = J^{-1}. \quad (3.23)$$

From Eq. (3.13) we can write the matrix of the mapping between the angular coordinates as

$$\mathcal{T}_{ij} \equiv \frac{\partial \beta_i}{\partial \theta_j} = \left(\delta_{ij} - \frac{\partial^2 \Psi}{\partial \theta_i \partial \theta_j} \right). \quad (3.24)$$

It differs from the identity by the Hessian of the rescaled projected gravitational potential Ψ . Recalling that the Laplacian of Ψ is proportional to

the surface density $\Sigma(\vec{\theta})$ (see Eq. (2.65)), we can write

$$\text{Tr} \frac{\partial^2 \Psi}{\partial \theta_i \partial \theta_j} = \nabla_\theta^2 \Psi = 2 \frac{\Sigma(\vec{\theta})}{\Sigma_{cr}} \equiv 2\kappa(\vec{\theta}), \quad (3.25)$$

where we have defined the critical density as

$$\Sigma_{cr} \equiv \frac{c^2 D_{OS}}{4\pi G D_{OL} D_{LS}}, \quad (3.26)$$

and the convergence is $\kappa(\vec{\theta}) \equiv \Sigma(\vec{\theta})/\Sigma_{cr}$.

Two additional independent combinations of the second derivatives of Ψ are necessary to describe the mapping

$$\begin{aligned} \gamma_1 &= \frac{1}{2} \left(\frac{\partial^2 \Psi}{\partial \theta_1^2} - \frac{\partial^2 \Psi}{\partial \theta_2^2} \right), \\ \gamma_2 &= \frac{\partial^2 \Psi}{\partial \theta_1 \partial \theta_2} = \frac{\partial^2 \Psi}{\partial \theta_2 \partial \theta_1}. \end{aligned} \quad (3.27)$$

The matrix of the mapping can then be rewritten as [Yo81]

$$\mathcal{T} = \begin{pmatrix} 1 - \kappa - \gamma_1 & -\gamma_2 \\ -\gamma_2 & 1 - \kappa + \gamma_1 \end{pmatrix}. \quad (3.28)$$

Both γ_1 and γ_2 (as well as κ) are functions of $\vec{\theta}$. The effect of the convergence κ is clearly to change the size of the image of a source without modifying its shape. The part of the matrix formed by the γ_1 and γ_2 terms, called the shear, is the one responsible for the distortions in the image shape. Since the matrix \mathcal{T} is symmetric, there is however no rotation of the image. The amplification is given by

$$A = (\det \mathcal{T})^{-1} = \frac{1}{(1 - \kappa)^2 - \gamma^2}, \quad (3.29)$$

where we have introduced the modulus of the shear $\gamma \equiv \sqrt{\gamma_1^2 + \gamma_2^2}$. The amplification has then a contribution coming from an isotropic focusing due to the local matter density in the lens plane, described by κ , and an anisotropic focusing due to the tidal gravitational effects, described by γ .

The mapping matrix has eigenvalues $1 - \kappa - \gamma$ and $1 - \kappa + \gamma$. In a coordinate system coinciding with the principal axes of the shear at $\vec{\theta}$, the

mapping \mathcal{T} is diagonal and has these eigenvalues in the diagonal[§]. Thus, the image is stretched by a factor $(1 - \kappa - \gamma)^{-1}$ in one direction and by $(1 - \kappa + \gamma)^{-1}$ in the other. A negative value of one of the factors (negative partial parity) means that the image is inverted in that direction. When both eigenvalues are negative, the total parity of the image is positive and hence it will not be inverted, but just appear as if rotated by 180° .

There is a very simple theorem stating that the amplification for images having both partial parities positive is larger than one. Indeed, for these images we know that $1 > 1 - \kappa > \gamma$ (since both κ and γ are positive), and then $1 > (1 - \kappa)^2 - \gamma^2 > 0$, which implies that $A > 1$. As there is always at least one image for which both partial parities are positive, there is always one image with $A > 1$ [Sc84][¶].

One can also infer that the light from the images for which both partial parities are negative have passed through a region with $\Sigma > \Sigma_{cr}$. Indeed, for them $1 - \kappa < -\gamma < 0$ and hence $\kappa > 1$.

When multiple images of the source appear, at least one of them has a negative parity (it is inverted). Then, a sufficient condition in order that a lensing distribution be able to produce multiple images is that the surface density $\Sigma(\vec{\theta})$ exceeds the critical value Σ_{cr} (i.e. $\kappa(\vec{\theta}) > 1$) at some point in the lens plane. However, this condition is not actually a necessary one [Su86], since for the lens to be capable of forming multiple images it is enough that $\kappa > 1 - \gamma$. To have a quantitative idea of the matter column density required to produce multiple images, notice that

$$\Sigma_{cr} \left(\frac{D_{OL} D_{LS}}{\text{Gpc } D_{OS}} \right) = 1.66 \times 10^3 \frac{M_\odot}{\text{pc}^2} = 0.35 \frac{\text{g}}{\text{cm}^2}. \quad (3.30)$$

For a circularly symmetric system, it is convenient to use polar coordinates with the origin in the symmetry axis of the lens. According to

[§]The principal axes of the shear are obtained by rotating the original ones by an angle ϕ , where $\tan 2\phi = \gamma_2/\gamma_1$.

[¶]This result may seem to lead to a paradox: if one considers a sphere around the source and a lens inside it, the fact that $A > 1$ for observers on the sphere suggests that the total flux through the sphere should increase with respect to the case in which the lens is absent, even if the source luminosity is unchanged. The point is that the presence of the lens affects the metric, reducing the area of the observer's sphere and keeping constant the total flux across it (see e.g. Ref. [Ja97a]).

Eq. (2.69) the deflection angle is in this case

$$\beta = \theta - \frac{M(\theta)}{\pi D_{OL}^2 \theta \Sigma_{cr}}. \quad (3.31)$$

Notice that the Einstein angle θ_E specifying the radius of the circular image of a source at $\beta = 0$ has to satisfy

$$M(\theta_E) = \pi (D_{OL} \theta_E)^2 \Sigma_{cr}, \quad (3.32)$$

so that the average surface density inside the Einstein ring is just the critical density Σ_{cr} . If the density is monotonically decreasing from the center, the condition in order that the formation of the Einstein ring be possible in the circularly symmetric potential (and hence also that multiple images could be formed) is then that the density in the center should exceed the critical density.

The mapping matrix for the symmetric lens is $\mathcal{T} = \text{diag}(\text{d}\beta/\text{d}\theta, \beta/\theta)$, i.e.

$$\mathcal{T} = \begin{pmatrix} 1 - \frac{1}{\pi D_{OL}^2 \Sigma_{cr}} \frac{\partial}{\partial \theta} \left[\frac{M(\theta)}{\theta} \right] & 0 \\ 0 & 1 - \frac{M(\theta)}{\pi D_{OL}^2 \Sigma_{cr} \theta^2} \end{pmatrix}. \quad (3.33)$$

The factor $A_r \equiv (\text{d}\beta/\text{d}\theta)^{-1}$ describes the change in the radial dimension of the source due to the lensing (the image of a source with size $\delta\beta$ in the radial direction will appear with $\delta\theta = (\text{d}\theta/\text{d}\beta)\delta\beta$), while the factor $A_t \equiv (\beta/\theta)^{-1}$ describes the tangential magnification of the image, as a tangential length of the source $\beta\delta\phi$ is stretched in the image to $\theta\delta\phi$. The total amplification of the image is just

$$A = A_r A_t = \frac{\theta}{\beta} \frac{\text{d}\theta}{\text{d}\beta}. \quad (3.34)$$

Notice that for a point-like lens, one has $\partial M/\partial\theta = 0$, and hence the mapping matrix reduces to $\mathcal{T} = \text{diag}(1 - \gamma, 1 + \gamma)$, with the shear being $\gamma = -M/(\pi D_{OL}^2 \Sigma_{cr} \theta^2)$. Thus, a point-like lens is a pure shear system outside the central singular point, since being the space around it empty the convergence vanishes.

3.4 Caustics and critical lines

For a given distribution of lenses, the amplification may be divergent for some source positions. The directions in the source plane along which the amplification diverges are called the caustics. The images of the caustics, i.e. the directions in the observer's sky along which a source would be seen infinitely magnified, are known as the critical lines.

Actually, for real sources the amplification does not diverge when they cross a caustic. This is because real sources are extended objects so that the overall amplification is given by an average (weighted by the surface brightness) of the amplification across its surface, and this is finite as it will be discussed later on.

As an example, for the point-like lens the amplification diverges when the source is perfectly aligned with the lens (see Eq. (3.20)). Hence, the caustic is the single point $\vec{\beta} = 0$, while the critical line corresponds in this case to the Einstein ring. Point-like caustics arise only for the very particular case of circularly symmetric lenses. In the general case caustics and critical lines are closed curves. They are determined by the values of $\vec{\beta}$, or respectively $\vec{\theta}$, for which the Jacobian J of the lens mapping vanishes.

Caustics and critical lines have important properties regarding the number and parity of the images. For instance, if we consider a source far away from the line of sight to the lensing distribution, there will be just one image of the source if the lenses are non-singular. However, if we were to displace the background source towards the center of the lensing distribution, additional images will appear in pairs whenever the source crosses a caustic. Hence, the total number of images produced by transparent lenses (so that no images are obscured) has to be odd, a result known as Burke's theorem [Bu81].

For the observer the two new images appear in the same direction in the sky, at a point belonging to a critical line, and having divergent magnifications. Furthermore, always one of the new images has positive parity while the other has negative parity. If the source is displaced from the caustic, these images move apart, one to each side of the critical line. Critical lines hence always divide regions of the sky where images have opposite parities and consequently these lines should form closed contours delimiting regions in which the images have a given definite parity.

When the lens is singular (a very important case including the compact lenses relevant for microlensing as well as some basic galaxy models such

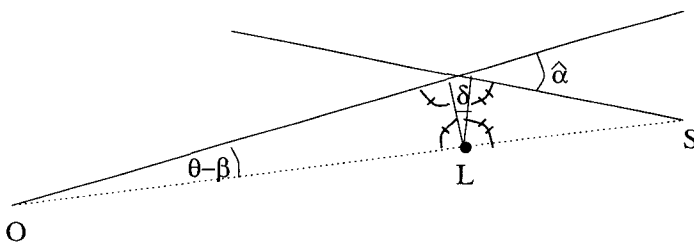


Fig. 3.6 Excess path-length giving rise to the geometrical time delay.

as the singular isothermal sphere) Burke's theorem does not necessarily hold. For instance, for the point-like lens there are always two images, with opposite parities, for any source position. Moreover, for non-singular lenses it is usually very hard to observe all the images, because generally one of them appears very demagnified and it is located near the center of the lensing distribution where a galaxy typically lies. This demagnified central image is actually the one that would be missing in the limit in which the lensing potential becomes singular.

A simple way to understand all these properties associated to the caustics and critical lines will be presented in Section 3.7.

3.5 Fermat's principle

The path followed by the light in the presence of masses acting as lenses can also be understood as a consequence of Fermat's principle [Sc85; Bl86]. In order to see this, let us write the lens equation (2.67) as

$$\vec{\theta} - \vec{\beta} - \vec{\nabla}_{\theta} \Psi = \vec{\nabla}_{\theta} \left(\frac{1}{2} (\vec{\theta} - \vec{\beta})^2 - \Psi \right) = 0. \quad (3.35)$$

According to Eq. (2.71), the second term in the parenthesis is proportional to the gravitational time delay. With the help of Figure 3.6 it is easy to compute the geometrical time delay coming from the increment in the path length of the deflected ray with respect to the straight path that it would have followed in the absence of lenses. This is given as $\delta t_{geom} \simeq (\theta - \beta) D_{OL} \delta / c$, and using basic trigonometric relations it can be seen that $\delta = \hat{\alpha}/2$. This implies that

$$\delta t_{geom} = \frac{D_{OS} D_{OL}}{2c D_{LS}} (\vec{\theta} - \vec{\beta})^2. \quad (3.36)$$

The total time delay will be given by the sum of the geometrical and gravitational delays. Notice that both of them are produced in the neighborhood of the lens and hence when the distance to the lens is large (i.e. when its redshift is sizeable), one has to take into account that during the photon travel from the lens to the Earth the Universe has expanded by a factor $(1 + z_L)$. The delay measured by an observer will then be stretched by the same factor, and from Eqs. (2.71), (3.12) and (3.36) is

$$\delta t = (1 + z_L) \frac{D_{OS} D_{OL}}{c D_{LS}} \left(\frac{1}{2} (\vec{\theta} - \vec{\beta})^2 - \Psi \right). \quad (3.37)$$

Comparing with Eq. (3.35) we see that the lens equation can then be written as

$$\vec{\nabla}_{\theta}(\delta t) = 0, \quad (3.38)$$

This means that for a fixed source position $\vec{\beta}$, the images will appear along those directions $\vec{\theta}$ for which the time delay has an extreme, and hence the geometrical optics approach used so far is actually equivalent to Fermat's principle.

The time delay function $\delta t(\vec{\theta})$ defines a two-dimensional surface which is parameterized by the image coordinates $\vec{\theta}$. The geometrical contribution δt_{geom} tends to give to this surface the overall shape of a paraboloid centered on the source position, and the gravitational potential adds some additional features to the surface. In the absence of any mass distribution acting as lens, this last contribution vanishes and the only extreme of the surface would be the minimum at $\vec{\theta} = \vec{\beta}$, i.e. there is no deflection. When lenses are present, the minimum is generally displaced and other extrema of the surface can also appear.

In terms of second derivatives of the time delay function, one can rewrite the mapping matrix as

$$\mathcal{T}_{ij} = \frac{\partial \beta_i}{\partial \theta_j} = \frac{c D_{LS}}{D_{OS} D_{OL}} \frac{\partial^2 \delta t}{\partial \theta_i \partial \theta_j}. \quad (3.39)$$

We see that the sign of the second partial derivatives of δt will be related to the parities of the corresponding images. Images with both partial

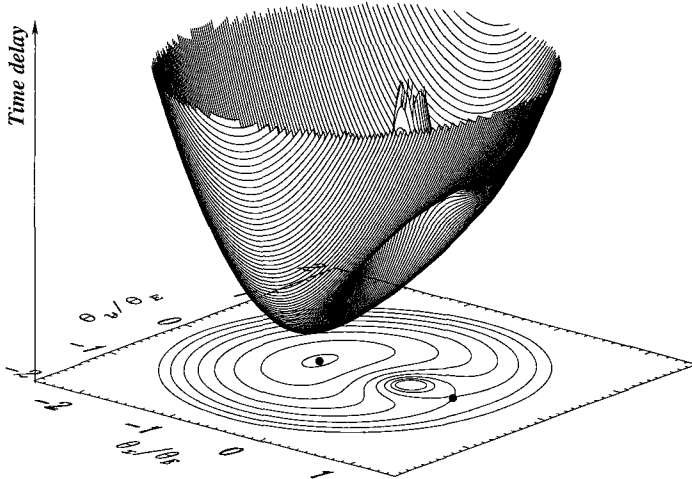


Fig. 3.7 Time delay surface for a point-like lens not perfectly aligned with the source ($\beta \neq 0$). Contour levels are shown in the bottom plane and the dots indicate the location of the two images.

parities positive correspond then to minima of the time delay function. Images with one positive and one negative partial parity correspond to saddle points, while those in which both partial parities are negative correspond to maxima of the time delay. Clearly the image with smaller δt is always a minimum and hence there is always an image with positive parity. Pairs of images appearing or disappearing together when the source is at a caustic have opposite parities and consist of a minimum and a saddle point or a maximum and a saddle point of δt , and their time delays become equal as they merge.

As a simple example, the reduced projected gravitational potential of a point-like lens is given by $\Psi = \theta_E^2 \ln |\vec{\theta}/\theta_E|$ (since $\vec{\alpha} = \vec{\theta}\theta_E^2/\theta^2 = \vec{\nabla}_\theta \Psi$), and hence

$$\delta t \propto \frac{1}{2}(\vec{\theta} - \vec{\beta})^2 - \theta_E^2 \ln \left| \frac{\vec{\theta}}{\theta_E} \right|. \quad (3.40)$$

Thus, for $\vec{\beta} = 0$ (perfect alignment) the total time delay function has the shape of a bottle bottom and has a logarithmic divergence at the center, related to the point-like character of the lens. It has a minimum along the

circle corresponding to the Einstein ring. For $\vec{\beta} \neq 0$, the bottom gets a tilt, as is shown in Figure 3.7. Two extremal points result (shown with a dot in the Figure), a minimum corresponding to the principal image and a saddle point corresponding to the secondary image, which is inverted.

When multiple images are formed, the light travel time for each image is in general different. Thus, variations in the source intensity would arrive to the observer at different times and these time delays are in principle measurable. Moreover, they are quite important in some cosmological applications of gravitational lensing, since they can be exploited to infer the expansion rate of the Universe.

3.6 Galaxy lens models

3.6.1 Circularly symmetric lenses

When the object acting as lens is a galaxy or a cluster, the extended nature of the mass distribution has to be taken into account, and different models have been proposed to describe this situation. A simple and widely used one, which reproduces the flat rotation curves of galaxies, is the singular isothermal sphere. It has a mass distribution given by

$$\rho(r) = \frac{\sigma^2}{2\pi Gr^2}. \quad (3.41)$$

Here σ is the one-dimensional velocity dispersion, which is related to the circular velocity by $\sigma = v_c/\sqrt{2}$. Integrating the mass density along the line of sight we obtain the surface density,

$$\Sigma(\theta) = \frac{\sigma^2}{2GD_{OL}\theta}, \quad (3.42)$$

and the mass enclosed inside a circle of angular radius θ is then $M(\theta) = \pi\sigma^2 D_{OL}\theta/G$. The deflection angle is given, according to Eq. (2.69), by

$$\hat{\alpha}(\theta) = \frac{4\pi\sigma^2}{c^2}, \quad (3.43)$$

which is independent of θ . Then, the lens equation can be written as

$$\vec{\beta} = \vec{\theta} \left(1 - \frac{\theta_E}{\theta} \right), \quad (3.44)$$

where the Einstein angle for this system is

$$\theta_E = \frac{4\pi\sigma^2 D_{LS}}{c^2 D_{OS}}. \quad (3.45)$$

A source located at an angular separation from the center of the distribution smaller than the Einstein angle has two images, located at $\theta_{\pm} = \beta \pm \theta_E$, and otherwise it has only one located at θ_+ . Computing the reduced projected potential for this lens one obtains

$$\Psi(\vec{\theta}) = \theta_E |\vec{\theta}|. \quad (3.46)$$

The time delay function, Eq. (3.37), has then a minimum and a saddle point when $\beta < \theta_E$ while only a minimum if $\beta > \theta_E$.

The amplification of the images is given by

$$A_{\pm} = \frac{\theta_{\pm}}{\beta} = 1 \pm \frac{\theta_E}{\beta}. \quad (3.47)$$

The secondary image, appearing at θ_- , is inverted ($A_- < 0$). Due to the spherical symmetry, this lens model has (as the point-like lens) a point-like caustic at $\beta = 0$, with critical line given by the Einstein ring. Notice that since the deflection angle is constant in this model, one has $A_r = 1$, so that there will be no change in the radial dimension of the source and the magnification is all due to the tangential deformation of the solid angle. One consequence of this is that radially elongated images (radial arcs) can only appear for the singular isothermal lenses as a result of a large tangential demagnification of the source ($A_t \ll 1$) and would then be extremely faint in this model.

The central singularity in the mass density distribution in Eq. (3.41) can be smeared out introducing a core region with finite density. A simple model achieving this is the softened isothermal sphere, with a mass distribution given by

$$\rho(r) = \frac{\sigma^2}{2\pi G(r^2 + r_c^2)}. \quad (3.48)$$

This model is commonly used to fit cluster profiles and decays as r^{-2} at distances much larger than the core radius r_c . Integrating along the line of sight, the surface density results

$$\Sigma(\theta) = \frac{\sigma^2}{2GD_{OL}} \frac{1}{\sqrt{\theta^2 + \theta_c^2}}, \quad (3.49)$$

where $\theta_c \equiv r_c/D_{OL}$. Then, the mass enclosed inside a circle of radius θ is given by

$$M(\theta) = \frac{\pi\sigma^2 D_{OL}}{G} \left(\sqrt{\theta^2 + \theta_c^2} - \theta_c \right). \quad (3.50)$$

The lens equation can be written in this case as

$$\vec{\beta} = \vec{\theta} \left(1 - \frac{\theta_0}{\theta^2} \left(\sqrt{\theta^2 + \theta_c^2} - \theta_c \right) \right), \quad (3.51)$$

where the angle $\theta_0 \equiv 4\pi\sigma^2 D_{LS}/(c^2 D_{OS})$ would correspond to the Einstein angle in the limit of negligible core radius, see Eq. (3.45).

As discussed in the last Section, critical lines are present whenever multiple images can form. One critical line corresponds to the Einstein ring, having an angular radius

$$\theta_E = \theta_0 \sqrt{1 - \frac{2\theta_c}{\theta_0}}, \quad (3.52)$$

and being the image of a source located at the point-like caustic at $\beta = 0$. Another critical line forms when $d\beta/d\theta = 0$, and has angular radius

$$\theta_R = \sqrt{\theta_0 \theta_c} \left[1 - \frac{\theta_c}{2\theta_0} \left(1 + \sqrt{1 + \frac{4\theta_0}{\theta_c}} \right) \right]^{1/2}, \quad (3.53)$$

which is smaller than the Einstein radius. The corresponding caustic is a circle with angular radius $\beta_R = \beta(\theta_R)$. The condition for the existence of both critical lines is clearly that the central surface density be larger than the critical density. The position of the images is obtained by solving the lens equation (3.51), which can be rewritten as a cubic equation

$$\theta^3 - 2\beta\theta^2 + (\beta^2 - \theta_0(\theta_0 - 2\theta_c))\theta - 2\beta\theta_0\theta_c = 0. \quad (3.54)$$

This equation has one or three solutions (images) depending on the location of the source^{||}. Sources located outside the circular caustic ($\beta > \beta_R$) have just one image while those located inside have three images. It is important

^{||}The solutions are easily obtained in terms of $\gamma \equiv \theta - \frac{2}{3}\beta$, so that the lens equation becomes $\gamma^3 - 3p\gamma + 2q = 0$, with $3p = \theta_0^2(1 - 2\theta_c/\theta_0) + \beta^2/3$ and $3q = \beta^3/9 - \theta_0^2(1 + \theta_c/\theta_0)\beta$. Defining $Q \equiv q^2 - p^3$ one has that for $Q \geq 0$ there is one image located at

$$\theta = \frac{2}{3}\beta + \left(-q + \sqrt{Q} \right)^{1/3} + \left(-q - \sqrt{Q} \right)^{1/3},$$

that the additional images of extended sources located in the vicinity of this caustic will look elongated in the radial direction, since being $d\beta/d\theta \simeq 0$ in this case means that the radial extent of the image is much larger than that of the source, and this is why this caustic is named the ‘radial caustic’. On the other hand, images of sources close to the origin, i.e. near the point-like caustic, appear tangentially elongated, i.e. forming large arcs near the location of the Einstein ring. This is illustrated in Figure 3.8, where the shapes of the image(s) of a circular source are drawn for different source positions.

If a lensing distribution (e.g. a cluster) can be modeled as a softened isothermal sphere and radial arcs are observed, their location with respect to the center of the mass distribution, which correspond to $\theta \simeq \theta_R$, can be used to estimate the size of the core θ_c , as can be seen from Eq. (3.53), with θ_0 being estimated from the tangential arcs. In the limit of small core radius all the results of the singular model are recovered. Indeed, one has $\theta_E \rightarrow \theta_0$ in this limit, so that the Einstein angle approaches the value of the singular model in Eq. (3.45). At the same time, the radial critical line collapses to a point according to $\theta_R \simeq \sqrt{\theta_E \theta_c}$, and hence for small core radii the third image is lost, leaving only two images for $\beta < \beta_R \simeq \theta_E$.

The reduced projected gravitational potential in the softened isothermal sphere model is given by

$$\Psi(\vec{\theta}) = \theta_0 \left[\sqrt{\theta^2 + \theta_c^2} - \theta_c \ln \left(\sqrt{\theta^2 + \theta_c^2} + \theta_c \right) \right]. \quad (3.55)$$

It can be checked that the time delay function in Eq. (3.37) will have a minimum, a maximum and a saddle point when $\beta < \beta_R$ while only a minimum otherwise. In this example, the mass distribution has no singularities and the number of images is odd, as expected from Burke’s theorem.

Let us finally mention that another class of spherically symmetric models discussed in the literature is given by

$$\rho(r) = \frac{\rho_s}{(r/r_s)^a (1+r/r_s)^{3-a}}, \quad (3.56)$$

where r_s is the scale radius, such that $\rho \propto r^{-3}$ for $r \gg r_s$ (and hence the total mass is finite) while for $Q < 0$ there are three images ($k = 0, 1, 2$), corresponding to

$$\theta^{(k)} = \frac{2}{3}\beta + \sqrt{4p} \cos \left(\frac{a+2k\pi}{3} \right),$$

where $\cos a = -q/p^{3/2}$.

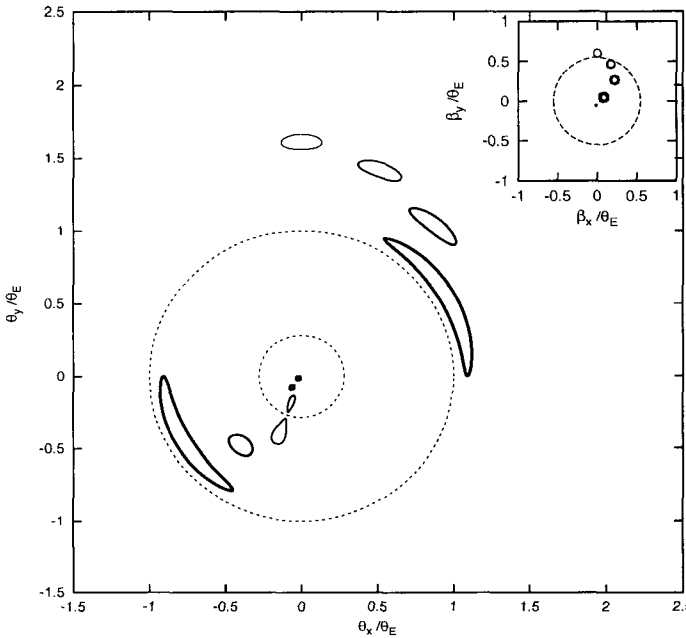


Fig. 3.8 Images of a circular source lensed by a non-singular isothermal sphere, for four different source locations, indicated in the smaller panel. The source in the vertical is just outside the caustic (indicated with dashed lines) and it has one image, also appearing along the vertical. The other sources have three images. The one just inside the caustic has two new images radially elongated, which are close to the radial critical line (smaller circle in the main panel). As the source approaches the origin (the point-like caustic) two of the images become very elongated tangentially around the location of the Einstein ring (the bigger circle), while the third image is near the center and very demagnified.

tal mass of the lens is finite, contrary to the case of the isothermal models). The parameter a governs the density profile near the origin, with $a = 2$ corresponding to a singular isothermal-like profile, while $a = 1$ corresponds to the so-called universal Navarro, Frenk and White profile, which has been obtained as the outcome of numerical simulations of structure formation with dissipationless cold dark matter [Na97]. The density distribution in Eq. (3.56) is hence called generalized NFW profile, and it is a good exercise to write down the lens equation for it. These models are also useful to illustrate the fact that the condition for Burke's theorem to hold is actually not that the mass density be non-singular, but rather that the deflection angle be continuous across the lens (and in particular at the origin in this

case). Since $\vec{\alpha} = \vec{\nabla}\Psi$, with $\nabla^2\Psi = 2\Sigma/\Sigma_{cr}$, and near the origin one has for the density in Eq. (3.56) that $\Sigma \propto r^{-a+1}$, we see that Burke's theorem will hold provided that $a < 2$. Hence, in these generalized NFW profiles a radial caustic is present when $a < 2$, dividing the regions leading to one or three images.

3.6.2 Non-circularly symmetric lenses

A more realistic model for galaxies and clusters has to take into account the ellipticity of the system, and there are several ways in which this can be done. One possibility is to use a surface density with elliptic isodensity contours. A natural model is the smoothed isothermal elliptical one, with

$$\Sigma(\theta_1, \theta_2) = \frac{\Sigma_0 \theta_c}{\sqrt{(1-\epsilon)\theta_1^2 + (1+\epsilon)\theta_2^2 + \theta_c^2}}, \quad (3.57)$$

which provides a good description of galaxy profiles with ellipticity ϵ . At large distances from the center it has the r^{-1} behavior that describes well the dynamics of gas and stars in galaxies.

Another possibility is to consider directly a projected potential with elliptical isopotential lines. The dynamical constraints require $\Psi \propto \theta$ far from the center and hence a convenient parametrisation is

$$\Psi(\theta_1, \theta_2) = \frac{\Psi_0}{\theta_c} \sqrt{(1-\epsilon)\theta_1^2 + (1+\epsilon)\theta_2^2 + \theta_c^2}. \quad (3.58)$$

The advantage of working with the elliptical potential is that it leads to simpler expressions for the deflection and magnification. For small values of the ellipticity this potential form provides a good approximation to the potential associated to an elliptical mass distribution, but however for values of ϵ larger than ~ 0.2 the elliptical potential leads, through the Poisson equation, to a mass distribution with peanut shaped isodensity contours, and thus it no longer provides a reasonable galactic model [Ka93b; Bl87a].

Even if the lensing galaxy were circularly symmetric, the effects of the environment (e.g. if the galaxy belongs to a cluster) will generally lead to a non-symmetric contribution to the total potential. This can be described by adding to the projected gravitational potential the terms

$$\Psi(\theta_1, \theta_2) = \frac{\kappa}{2} (\theta_1^2 + \theta_2^2) + \frac{\gamma_1}{2} (\theta_1^2 - \theta_2^2) + \gamma_2 \theta_1 \theta_2, \quad (3.59)$$

which correspond to including an external convergence κ and shear $\gamma_{1,2}$. This could also be used to take into account the effects of additional perturbations along the line of sight. We should also mention that a circular lens with the addition of an external constant shear can provide a simple model to approximate an elliptical potential.

Caustics and critical lines are more complex for elliptical lenses than for circularly symmetric ones [Ko87]. The central point-like caustic, typical of systems with circular symmetry, is replaced by a four cusp caustic, while the circular caustic associated to radially elongated images is deformed. Each time that a source crosses one of these caustic lines from outside to inside a couple of additional images is formed. Thus, there are regions with one, three and five images.

Figure 3.9 depicts the formation of images in an elliptical potential lens. The panels on the right show the position of the caustics and those on the left the critical lines. The outer critical line is the image of the astroid (diamond shaped) caustic while the inner one is the image of the elliptical caustic. Since the images appearing near the outer critical line are tangentially elongated, this one is called the tangential critical line (and the astroid is the tangential caustic), while the inner critical line is the radial one. Notice also that the images that form in the region between the two critical lines are always inverted, while on the rest of the image plane they have positive parities.

3.7 The folded sky

In this Section we will describe a graphical representation of the lens mapping allowing a simple visualization of many of the gravitational lensing properties previously discussed in this Chapter [Mo00].

We have seen that the lens equation relates the angular position of a source to the angular positions of its images. The mapping from the image to the source plane is clearly single valued, since each image direction corresponds to a unique position in the source plane. On the other hand, the mapping from the source plane to the image plane becomes multiply valued when multiple images of a source are formed. To better visualize the properties of multiply imaged systems, let us consider the observer's sky (image plane) as if it were a deformable sheet, hereafter referred to as the 'sky sheet'. Within this picture, the mapping from the image plane to

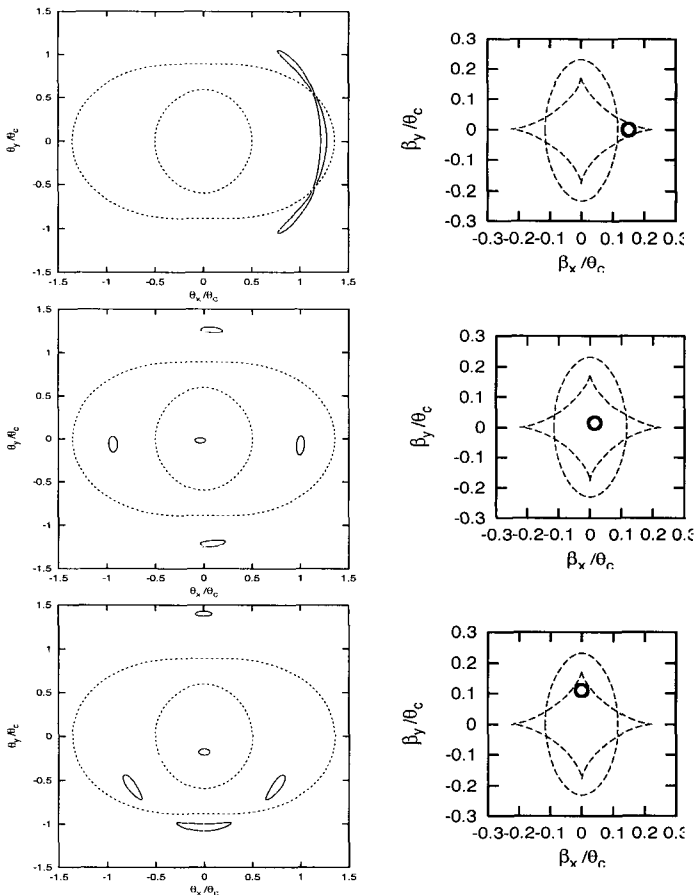


Fig. 3.9 Images of a circular source lensed by a non-singular elliptical potential model ($\epsilon = 0.09$, $\Psi_0/\theta_c^2 = 1.5$), for three different source locations, indicated in the panels on the right. Dotted and dashed lines correspond to critical lines and caustics respectively.

the source plane will just transform this sheet, stretching and eventually (if multiple imaging occurs) folding it, but as long as the lenses are non-singular, without tearing it. This is illustrated in a one dimensional example in Figure 3.10. With this in mind Burke's theorem is trivially understood, since for a given source position $\vec{\beta}$, the number of times the sky sheet is folded on top of the source location will determine the number of images of the source. If no folds are present, just one image will be seen, while every

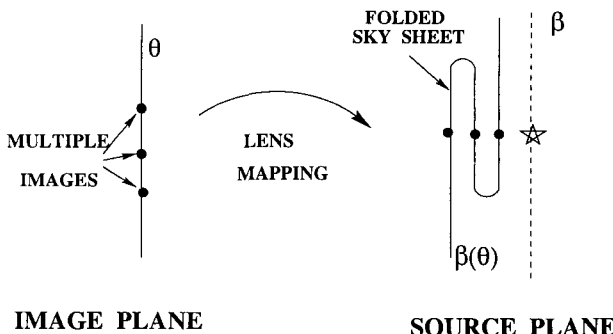


Fig. 3.10 Folded sheet representing the observer's sky (image plane) projected back into the source plane in a strong lensing situation.

fold will add an additional pair of images, one of which will be inverted. The location of the folds in this sheet correspond just to the caustic lines, along which the magnification of the images will be divergent.

In the case in which the lenses are singular, this would make the lens mapping discontinuous at some points, what would be reflected as tears appearing in this sheet. When this happens, one of the new images can be lost, as we will illustrate further below, and Burke's theorem is no longer valid.

In practice, the mapping among these sheets can be performed by considering light rays which arrive to the observer along directions forming a regular grid (in $\vec{\theta}$) and following them back to the source plane. The original grid defines the two-dimensional observer's sky (θ_1, θ_2), and the image of this grid defines the sheet projected into the source plane (β_1, β_2). The folds in the projected surface will hence define the caustics, and these will be closed lines in the source plane which can be smooth or can eventually contain cusps where two folds merge.

To visualize these folds it is useful to assign a third coordinate, h , to the mapping (as was actually done in the one-dimensional example in Figure 3.10). A convenient choice is to take h as the difference in travel times between the actual path of the light corresponding to the image considered and some reference time, such as the one that would be associated to the straight path from a source located at $\vec{\beta} = 0$ in the absence of lenses. With this choice, for a given source position the image with smaller h will be the one with the shortest travel time to the observer, and the difference in height among the different images is proportional to their associated time

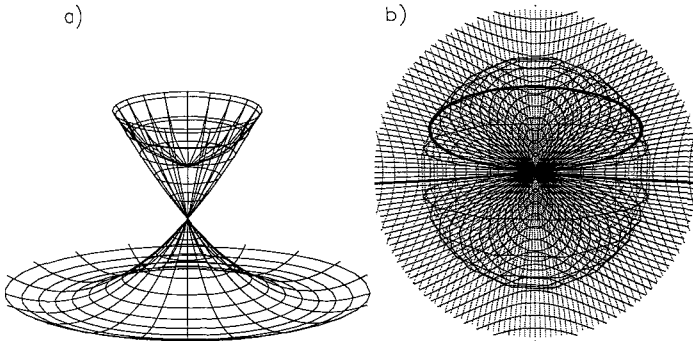


Fig. 3.11 The sky sheet for the softened isothermal sphere, displaying how the sky seen by an observer would look like if projected back into the source plane using the lens equation. The horizontal axes in panel a) are the coordinates in the source plane (β_1, β_2). The vertical axis is taken to be proportional to the time delay associated to each image. The number of images of a source is given by the number of times that a vertical line in the source location intersects the sky sheet. Panel b) shows a projection of case a) into the (β_1, β_2) plane. The thick solid line displays the points actually observed in the source plane when the direction of observation is moved along a particular straight line in the observer's plane.

delays. Let us now see how this surface looks for the different lens models.

Figure 3.11a shows a plot of the sky sheet for the smooth isothermal sphere lens model. Here, a circularly symmetric fold develops, producing some kind of blob connected to the lower surface at one point. The horizontal coordinates are (β_1, β_2) , so that the number of intersections of a vertical line with the surface gives the number of images in the observer's sky corresponding to that source location. Clearly for point sources inside the region covered by the blob, three images will be seen at three different positions in the sky, while for sources located outside the blob there will be just one image. The image in the lower surface in Figure 3.11.a corresponds to a minimum of the time delay function. The extra pair of images associated to the blob are a maximum (that in the upper cap) and a saddle point.

Figure 3.11b shows the projection of the sky sheet in the (β_1, β_2) plane, i.e. it shows how Figure 3.11a would appear when seen from above. Here, the amplification of a given image is related to how much this surface is stretched at the point corresponding to the image location. To visualize this stretching we started with a uniform rectangular grid in the observer's plane (while in Figure 3.11a a polar grid was used to respect the symmetry

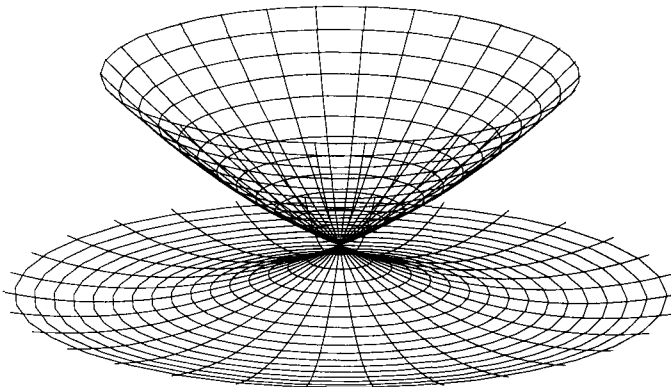


Fig. 3.12 The sky sheet for the singular isothermal sphere.

of the lens). If the surface is very stretched, this would mean that a given element of solid angle in the source would be seen through a much smaller solid angle in the observer's sky, and hence the magnification is very low. Instead, if the sheet appears contracted, the magnification will be high. The upper cap of the blob is very stretched and hence the image which is closer to the center is very demagnified. The circle corresponding to the border of the blob will have on the contrary a divergent magnification, since approaching it the projection of a surface element in the observer's plane degenerates into a segment into the source plane, so that the magnification is singular as expected for a caustic. The other singular point is the central one, corresponding to the place where the blob connects to the lower surface in Figure 3.11a. A source located there, i.e. perfectly aligned with the lens, will have as image all the circle which is contracted into that point (the Einstein ring). This corresponds to the point-like caustic associated to circularly symmetric lens configurations.

Figure 3.12 shows the equivalent of Figure 3.11a for the singular isothermal sphere lens model. In this case, the deflection angle is discontinuous at $\vec{\theta} = 0$, and this has the effect of removing the upper cap of the blob so that a hole appears in the sky sheet. This means that the very demagnified central image of the non-singular model is no longer present, and the blob is transformed into a conic surface. Thus, a source can have just one or two images in this case. The second image has its parity inverted and appears or disappears as the source crosses the border of the cone.

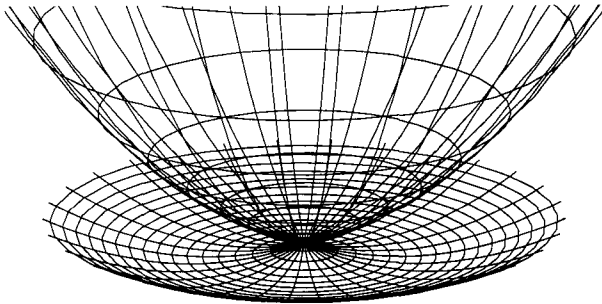


Fig. 3.13 Sky sheet for the point-like lens.

In this model, the deflection angle keeps a constant magnitude, even for light rays passing close to the center of the lensing distribution. On the contrary, for the point-like mass the deflection angle formally diverges as the light rays approach the lens direction. Thus, in this last case the border of the conic surface which appeared in Figure 3.12 will be stretched to infinity**, as shown in Figure 3.13. Hence, for the point-like lens there are always two images for any source position (except for perfect alignment, where the Einstein ring is the image). The principal image is always magnified, while the other one can become very demagnified, what is reflected here in that the conical surface becomes very stretched as we move away from the lens position.

The previous examples, corresponding to circularly symmetric lenses, all have a central point-like caustic. In more general models which do not have this symmetry, the point-like caustic is replaced by a caustic consisting of several folds merging in pairs at cusps, and forming a closed continuous line in the β plane. As an example, let us consider an elliptic potential lens. Figure 3.14 shows the sky sheet for a given ellipticity and several values of the potential at the center, in decreasing order. The first panel corresponds to the strongest potential and the sheet looks similar to the smoothed isothermal sphere one, with the difference that the central caustic is now given by a diamond shaped caustic with four cusps. The external caustic is still a single fold. A source outside this caustic has just one image,

**It has however no meaning to consider impact parameters smaller than the radius of the lens.

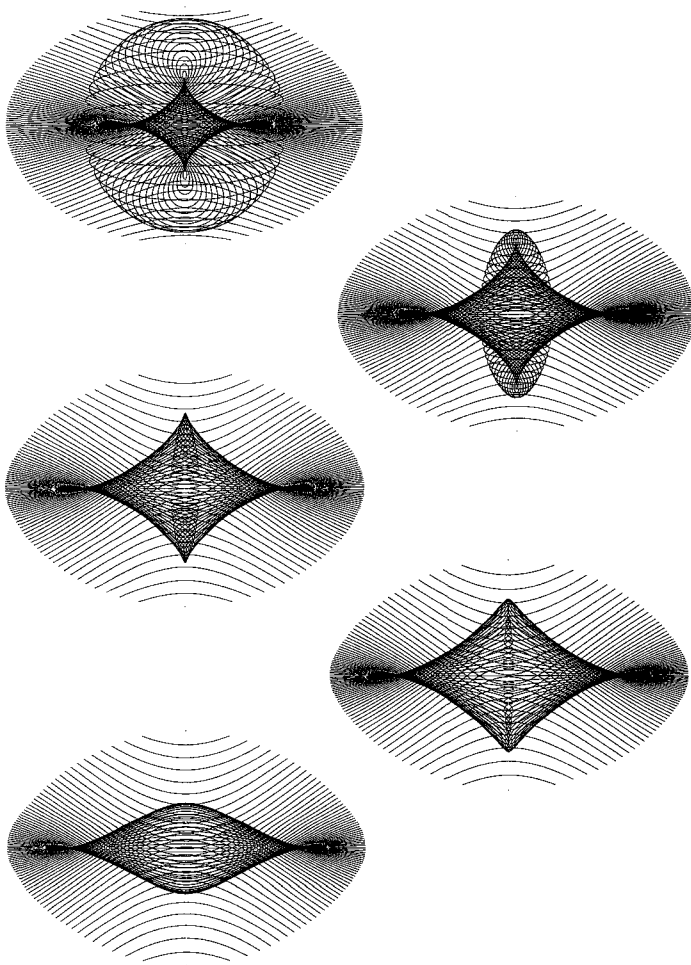


Fig. 3.14 Sky sheet for the elliptic potential lens. The different panels correspond to decreasing central potential values, for a fixed ellipticity.

one inside it but outside the diamond has three images, while one inside the diamond has five images. In the second panel the potential is weaker, and the radial caustic becomes smaller. Two of the cusps go outside the oblate fold (becoming ‘naked’), and they are now associated with transitions from one to three images. The formation of images in this case was exemplified in Figure 3.9. For even smaller central potential values the structure of

the caustics changes. The oblate fold shrinks inside the diamond, and in this process it takes with it the pair of cusps along the vertical direction, surviving as two folds which merge into two cusps, a structure which is known as a lip. In fact, two crossed lips (one in the vertical and the other in the horizontal directions) are present in the fourth panel. The vertical one then shrinks and disappears (unfolds), leaving just the horizontal lip in the fifth panel. In this case sources can have one or three images depending on whether they are outside or inside the lip.

The time delay structure of the images for the case in which a diamond caustic is present can be understood from Figure 3.15, where different vertical cuts of the sky sheet are displayed. The boxes show the surface profiles along the indicated cuts. The nature of the different images is indicated, i.e. whether they are minima (m), saddle points (s) or maxima (M) of the time delay function. These properties change at each fold of the sheet. As the pair of images created at a fold can be a maximum and a saddle point or a minimum and a saddle point, the vertical coordinate chosen allows a simple characterization of the extrema just by an inspection of these cuts and using the fact that far from the lens the single images are minima of the time delay.

3.8 Folds and cusps

In the last Section we have discussed some properties of the mapping from the image plane to the source plane, as determined by the lens equation, and shown some examples corresponding to commonly used lens models. A crucial role in the determination of the number of images was played by the caustics, which correspond to singularities in the amplification (i.e. the zeroes of the Jacobian of the mapping). A pair of very magnified images of a source appears or disappears whenever the source crosses a caustic. The caustics form closed lines, which can be understood in terms of folds of the sky sheet, in some cases joining in pairs at cusps.

These kind of mapping singularities are the subject of study of a branch of mathematics known as catastrophe theory, which has applications to many processes appearing in different fields of science, ranging from physics to biology and psychology [Po78]. This theory studies systems in which a continuous change in some input variable produces an abrupt change in the output effect. In the case of the gravitational lensing, a continuous

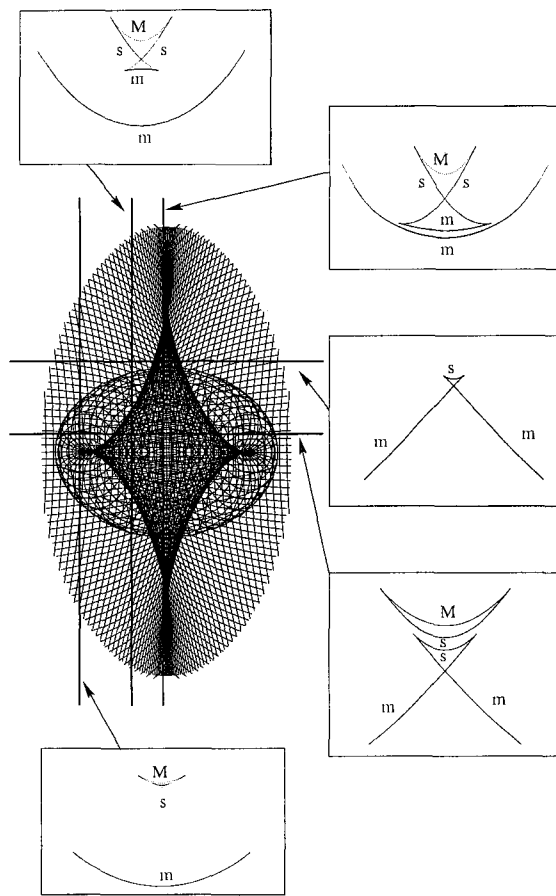


Fig. 3.15 Different cuts of the sky sheet for the elliptical lens. The vertical coordinate is proportional to the time delay associated to each image. In each line we indicate whether the images correspond to a minimum (m), a saddle point (s) or a maximum (M) of the time delay function.

change in the source position leads to a sudden change in the number of images when the source crosses a caustic. According to catastrophe theory, folds and cusps are the only catastrophes that appear for systems with two control variables. This is the case in gravitational lensing when we consider a model with fixed distances to the lens and the source, so that one is left with only two control parameters given by the position of the source

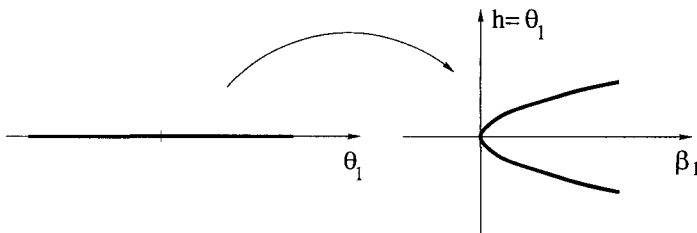


Fig. 3.16 Generic aspect of the lens mapping near a fold and in the direction orthogonal to it (fixed β_2).

(β_1, β_2) . We will now deduce some general properties of the magnification near folds and cusps by making a more detailed inspection of the sky sheet in their neighborhood.

3.8.1 Magnification near a fold

To understand the behavior of the magnification of a source very close to a fold we will adopt local coordinates in the source plane such that the origin $(\beta_1, \beta_2) = (0, 0)$ is a point in the fold and similarly its image, which is a point in the critical line, will be the origin $(\theta_1, \theta_2) = (0, 0)$ in the image plane. Let us also take the β_2 axis along the fold direction (i.e. the line $\beta_1 = 0$ describes locally the caustic), with the β_1 axis being orthogonal to it. We can also adopt the local coordinates in the image plane (θ_1, θ_2) such that the line $\beta_1 = 0$ is locally mapped to the line $\theta_1 = 0$ (i.e. the line $\theta_1 = 0$ describes the critical line locally) and the line $\beta_2 = 0$ is mapped to the line $\theta_2 = 0$. Notice that with this choice the coordinates (θ_1, θ_2) will in general be non-orthogonal. To visualize the fold we will also choose as vertical coordinate $h = \theta_1$. With this choice, the mapping in the neighborhood of the origin and in the direction orthogonal to the fold (i.e. for $\beta_2 = 0$) looks as depicted in Figure 3.16. The generic aspect of the two-dimensional folded sky near the caustic will be as illustrated in Figure 3.17 ††.

In a neighborhood of the origin we can describe the mapping by the first terms in its Taylor expansion,

$$\beta_1 \simeq a\theta_1^2, \quad (3.60)$$

††In the previous section, when using the time delay as vertical coordinate, the fold didn't look round as in Figure 3.17. This is because the behavior of δt near the caustic is quite peculiar, since images merge at inflection points of δt .

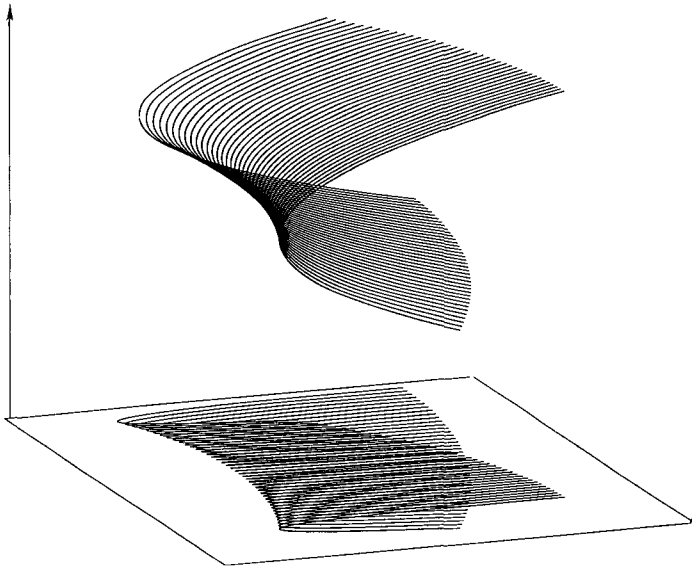


Fig. 3.17 The folded sky in the neighborhood of a caustic (bottom plane), corresponding to the observer's plane mapped into the source plane, and its deprojection to view it as a folded surface.

$$\beta_2 \simeq b\theta_2. \quad (3.61)$$

Hence, a solid angle in the source plane $d\Omega_\beta = d\beta_1 d\beta_2$ will be seen in the image plane as $d\Omega_\theta = \cos \eta d\theta_1 d\theta_2$, where $\cos \eta$ is the angle formed by the non-orthogonal axes θ_1 and θ_2 . The amplification of the source is then given by

$$A = \frac{d\Omega_\theta}{d\Omega_\beta} \simeq \frac{\cos \eta}{2ba\theta_1}, \quad (3.62)$$

Notice that one image has positive θ_1 ($\theta_1 \simeq +\sqrt{\beta_1/a}$) and the other has negative θ_1 ($\theta_1 \simeq -\sqrt{\beta_1/a}$), and hence they have opposite parities. The amplification in Eq. (3.62) grows as the inverse of θ_1 , which is the distance between the images and the critical line (and is also proportional to the separation among the images when these are merging). In terms of the distance from the source to the fold β_1 , one has

$$A \simeq \pm \frac{\cos \eta}{2b\sqrt{a\beta_1}}, \quad (3.63)$$

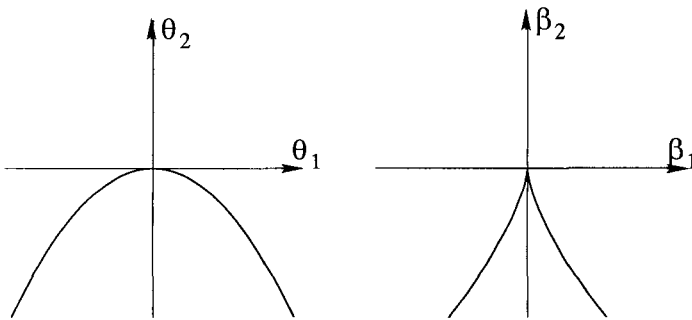


Fig. 3.18 Critical line and caustic for a cusp.

so that the amplification is inversely proportional to $\sqrt{\beta_1}$ [Ch79].

The magnification formally diverges when the source reaches the caustics and the images merge. This divergence is smoothed out when we consider the physical extension of a real source, since the apparent luminosity is obtained as a convolution of the magnification, weighted by the local surface brightness, across the source surface. This gives a finite result since the integral of $1/\sqrt{\beta_1}$ converges at the origin.

3.8.2 Magnification near a cusp

Two fold caustics can merge in a cusp, as was the case for the elliptical lens models. When a source crosses the caustic near a cusp, the new pair of images present inside the cusp will appear at the same place in the sky where the original image is, and the study of the analytic behavior of the magnification around the cusp is also of interest [Sc92; Za95].

To describe a neighborhood of a cusp, let us choose a coordinate system with the origin at the cusp location, the β_2 axis along the cusp direction and the β_1 axis orthogonal to it (as shown in the right panel of Figure 3.18). In the image plane we can choose θ_1 such that the line $\theta_1 = 0$ is the image of $\beta_1 = 0$ (the axis of symmetry of the cusp). Then, a cusp in the lens mapping can locally be described by a Taylor expansion as

$$\beta_1 \simeq a\theta_1^3 + b\theta_1\theta_2, \quad (3.64)$$

$$\beta_2 \simeq \frac{b}{2}\theta_1^2 + c\theta_2. \quad (3.65)$$

Notice from Eq. (3.64) that depending on the sign of θ_2 the mapping is

single valued or a region with three images appears. The absence of a quadratic term in θ_1 in Eq. (3.64) insures that the cusp looks symmetric about the axis $\beta_1 = 0$. The term proportional to θ_1^2 in Eq. (3.65) necessarily appears because, as the deflection angle is proportional to the gradient of a potential, we know that the lens equation has to verify $\partial\beta_1/\partial\theta_2 = \partial^2\Psi/\partial\theta_1\partial\theta_2 = \partial\beta_2/\partial\theta_1$.

The magnification near the cusp can then be computed as

$$A = \left(\det \frac{\partial\beta_i}{\partial\theta_j} \right)^{-1} = \frac{1}{(3ac - b^2)\theta_1^2 + bc\theta_2}. \quad (3.66)$$

The critical curve is then a parabola

$$\theta_2 = \frac{b^2 - 3ac}{bc}\theta_1^2, \quad (3.67)$$

as shown in the left panel of Figure 3.18. The corresponding line in the source plane, the caustic curve, is given by

$$\beta_2^3 = \frac{27c^2}{8b^3}(b^2 - 2ac)\beta_1^2. \quad (3.68)$$

The general properties of a cusp can be simply visualized if we adopt a vertical coordinate proportional to θ_1 , in which case the mapping will look as depicted in Figure 3.19. When the image plane is projected into the source plane, it develops two folds that merge at the cusp, where the surface unfolds.

Combining the expression obtained for the magnification in Eq. (3.66) with the mapping given in Eqs. (3.64) and (3.65) it can be seen that the amplification is also large outside the cusp. In Figure 3.20 we display the behavior of A along different directions, showing how the transition between the behavior of the point-like caustic ($A \propto \beta^{-1}$) and the fold caustic ($A \propto \beta^{-1/2}$) takes place around the cusp.

There is also an interesting relation among the magnification of the three images of a source located inside the cusp. To deduce it we need first to compute the position of the images for an arbitrary source location (β_1, β_2) . Substituting θ_2 from Eq. (3.65) into Eq. (3.64) we obtain a cubic equation for θ_1

$$\theta_1^3 \left(a - \frac{b^2}{2c} \right) + \theta_1 \frac{b\beta_2}{c} - \beta_1 = 0. \quad (3.69)$$

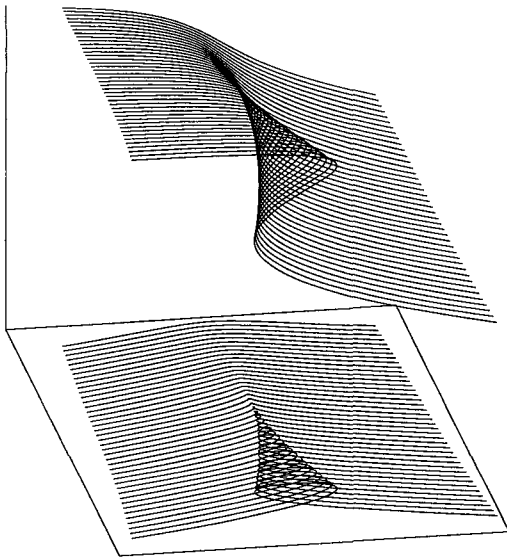


Fig. 3.19 Representation of the map $\vec{\theta} \rightarrow \vec{\beta}$ near a cusp. The lines correspond to fixed values of θ_2 in the image plane. Also shown is a deprojection of the mapping to view it as a folded surface.

The three solutions of this equation can be written as ($k = 0, 1, 2$)

$$\theta_1^{(k)} = \sqrt{\frac{8b\beta_2}{3(b^2 - 2ac)}} \cos\left(\frac{\alpha + 2k\pi}{3}\right), \quad (3.70)$$

where the angle α satisfies

$$\cos \alpha = -\frac{3c\beta_1}{2b\beta_2} \sqrt{\frac{3(b^2 - 2ac)}{2b\beta_2}}. \quad (3.71)$$

Replacing these in Eq. (3.65), the corresponding value of θ_2 is obtained. Inserting these solution for $\theta_{1,2}^{(k)}$ into Eq. (3.66), the magnification of a given image can then be written as

$$A^{(k)} = \frac{1}{b\beta_2 [1 - 4 \cos^2\left(\frac{\alpha+2k\pi}{3}\right)]}, \quad (3.72)$$

and if we develop the cosine of the sum in the denominator it is easy to see

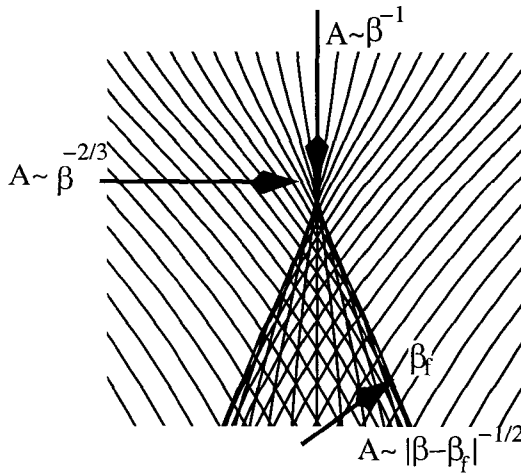


Fig. 3.20 Close view of a cusp: two folds meet and the surface unfolds. The behavior of the amplification along three different directions is also illustrated.

that

$$A^{(0)} + A^{(1)} + A^{(2)} = 0. \quad (3.73)$$

Taking into account that one of the images has a parity opposite to the other two, Eq. (3.73) means that the modulus of the sum of the amplifications of the images with the same parity is equal to the modulus of the amplification of the image with opposite parity. An application of this property is the so-called arc-length theorem [Ko90]. It states that when three giant arcs are formed around a cluster because a background galaxy is just inside a cusp (see e.g. the top panel of Figure 3.9), the sum of the lengths of the two smaller arcs should be equal to the length of the longer one (which is in between the other two and is inverted). This should hold because the length of the arcs is proportional to the tangential distortion of the solid angle subtended, and the radial distortion is not expected to differ much among the images. There are however not yet convincing examples of observed arcs having this property.

3.8.3 The binary lens

In many applications of interest, such as the study of microlensing by binary stars or planetary systems, the lens consists of two deflectors. In this case,

the deflection angle of the light rays is given by the superposition of the (vectorial) deflections produced by the two individual lenses. If lenses are point-like, with masses M_A and M_B , and are located in the lens plane forming angles $\vec{\theta}_A$ and $\vec{\theta}_B$ with respect to the chosen optical axis, the lens equation can be written as [Sc86]

$$\vec{\beta} = \vec{\theta} - \mu_A(\vec{\theta} - \vec{\theta}_A) \frac{\theta_E^2}{|\vec{\theta} - \vec{\theta}_A|^2} - \mu_B(\vec{\theta} - \vec{\theta}_B) \frac{\theta_E^2}{|\vec{\theta} - \vec{\theta}_B|^2}, \quad (3.74)$$

where $\mu_{A,B} = M_{A,B}/M$ with $M = M_A + M_B$ and θ_E is obtained from the expression for the Einstein angle, Eq. (3.6), using the total mass M .

In Figure 3.21 we show how the projection of the image plane into the source plane would appear for an asymmetric binary system, with reduced masses $\mu_A = 0.25$, $\mu_B = 0.75$, and for different values, in decreasing order, of the distance between the lenses. In the first panel, in which the separation among the lenses is large, there are two diamond shaped caustics with four cusps (wide binary topology), one associated to each lens and they can be interpreted as being the point-like caustics of each lens which have been distorted by the shear induced by the presence of the other lens. As the lenses are taken as point-like, the sky sheet has a hole associated to each lens, and this has been stretched to infinity as was the case for the single

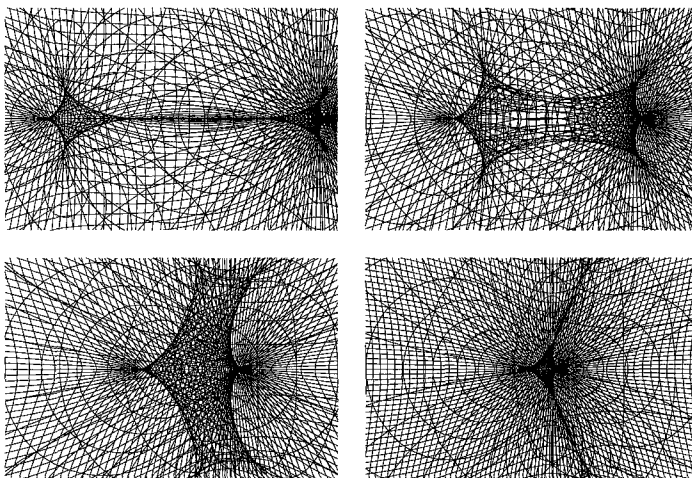


Fig. 3.21 Sky sheet for a point-mass binary lens for decreasing values of the distance between the lenses.

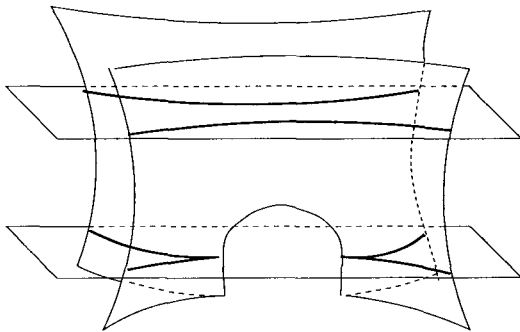


Fig. 3.22 Beak to beak transition.

point-like lens in Figure 3.13. Then, far from the lenses a source would have three images (two of them very demagnified) and inside the diamonds it would have five. When the lenses get closer, the two cusps which are closer to the center, one from each diamond, approach each other and merge, leading to a six cusp caustic (intermediate binary topology), as is shown in the second panel (top right). For smaller values of the lens separation, the six cusp caustic is stretched in the direction orthogonal to the lens separation, as displayed in the third panel. Finally, for even closer lenses, two pairs of fold caustics touch each other and break apart, so that the six cusp caustic separates into a four cusp caustic and two small triangular caustics (close binary topology), as shown in the last panel.

The changes in the caustic shapes which occur as the distance between the lenses changes can also be interpreted in the context of catastrophe theory [Er93]. For instance, the transition from two opposed cusps that merge leaving two folds, as happened between the first and second panels or between the third and fourth ones, is known as a beak-to-beak transition in this context. The lens separation is considered in this case as a third control parameter (in addition to the two source coordinates β_1 and β_2), and in this three dimensional space the fold caustics in Figure 3.21 will sweep a surface and the cusps will follow lines as the lens separation is varied. This is schematically illustrated in Figure 3.22, where the horizontal planes correspond to fixed lens separations and they are displaced vertically as this separation is varied.

In the case of the elliptical potential lens, discussed in Section 3.7, the topology of the caustic curves also suffers some transformations, as can be

seen in Figure 3.14. In this case the central value of the potential can be taken as the third control parameter. For large central potential values, there is an external pure fold caustics (without cusps) and an internal diamond shaped caustic (first panel). For a weaker potential, as was discussed before, first a pair of cusps goes outside of the fold and then, when the pair of cusps in the vertical touches the elliptical fold, the diamond loses the vertical cusps and becomes a horizontal lip, while the fold caustic acquires the two cusps and becomes a vertical lip. Each of these processes in which a cusp and a fold cross each other exchanging identities, i.e. the cuspy caustic loses the cusp and the smooth one acquires it, is a higher order catastrophe which can appear when three or more control parameters are considered, and is called an hyperbolic umbilic.

The transitions mentioned above are also called catastrophe metamorphoses, and they all share the property that cusps appear and disappear in pairs or their number is preserved. Hence, a general property of the caustics produced by a lens is that the total number of cusps has to be even.

Recommended reading

- P. Schneider, J. Ehlers and E. E. Falco (1992), “Gravitational lenses”, Springer-Verlag, New York.
- S. Refsdal and J. Surdej (1994), “Gravitational lenses”, Rep. Prog. Phys. **56**, 117.
- R. Narayan and M. Bartelmann (1998), “Lectures on gravitational lensing”, in *Formation of structure in the Universe*, Proceedings of the 1995 Jerusalem Winter School, Eds. A. Dekel and J. P. Ostriker, Cambridge University Press (preprint [astro-ph/9606001](#)).
- A. O. Petters, H. Levine and J. Wambsganss (2001), “Singularity theory and gravitational lensing”, Birkhäuser, Boston, Basel, Berlin.

Chapter 4

Macrolensing results

In this Chapter we will discuss the main examples and applications of gravitational lensing due to large mass distributions, including galaxies, clusters and the large scale structure of the Universe. These phenomena naturally split into the regimes of strong lensing, where multiple images of the sources are formed, and weak lensing, where images get only distorted and magnified (see Figure 4.1). In the first case the comparison of the location, intensity and structure of the different images can give very strong constraints on the lens mass, specially when the source is extended and its details can be recognized in the different images. When the source has a variable flux, the time delay between the images can be used to set the absolute length-scale of the lensing system, and together with the measured redshift of lens

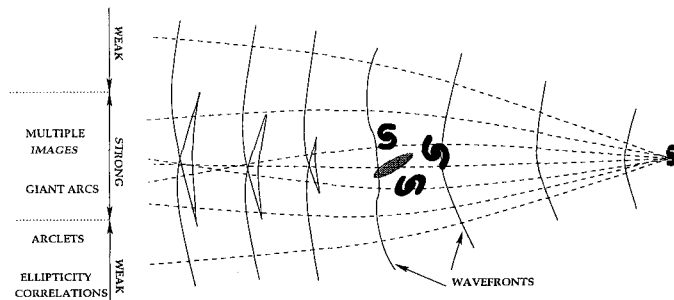


Fig. 4.1 Schematic picture of the different macrolensing regimes. The light wavefronts (orthogonal to the light rays) are displayed as they traverse the lensing distribution. In the central parts multiple images form (strong lensing), while farther out only coherent distortions of the image shapes are observed (weak lensing).

and source allows to infer the value of the Hubble constant. When the lensing effects are not strong enough to produce multiple images, anyhow the study of the shape distortion of the background objects or the change in the galaxy counts due to the lensing has precious information on the matter distribution at large scales. For instance, the coherent distortions of background faint blue galaxies around a cluster allows to reconstruct its mass distribution sometimes up to scales of the order of a Mpc, while in empty regions without clusters the correlations among galaxy ellipticities produced by the large scale structure inhomogeneities provides a test of the different scenarios of galaxy formation and of the overall matter content of the Universe.

4.1 Lensing of quasars

The gravitational lensing effect was first observed in the multiple imaging of quasars. This is understandable since quasars are the brightest objects at high redshift and the farther away is a source, the more likely it becomes to find a lensing galaxy near the line of sight to it, and also the smaller becomes the typical critical density required for an intervening galaxy to form multiple images. The frequency of multiple imaging of quasars is indeed only somewhat below 1%, with some 50 systems having been identified by now from out of $\sim 10^4$ observed quasars. The other great advantage of quasar systems is that they are easier to identify as multiply lensed candidates than galaxies, since to find two or more quasar images separated by less than a few arcsec, with the same measured redshift and similar color (so as to distinguish them from physically associated quasar pairs, a dozen of which have also been found) is not a common thing. Furthermore, if the lensing galaxy can also be identified near the line of sight, the case for a lensing system becomes very strong.

These basic features were all present in the binary quasar Q0957+561 when it was discovered in 1979 by Walsh et al. [Wa79], and were actually crucial to identify it as a lensing system. This quasar not only opened the observational era in gravitational lensing, but also became one of the most studied objects in astrophysics. Its two images were found to be at a redshift of $z_S = 1.41$, with the lensing galaxy being at $z_L = 0.36$. The image separation of $6''.1$ was actually somewhat large for being produced by a typical galaxy of mass $10^{11}\text{--}10^{12} M_\odot$, and also the two images were not

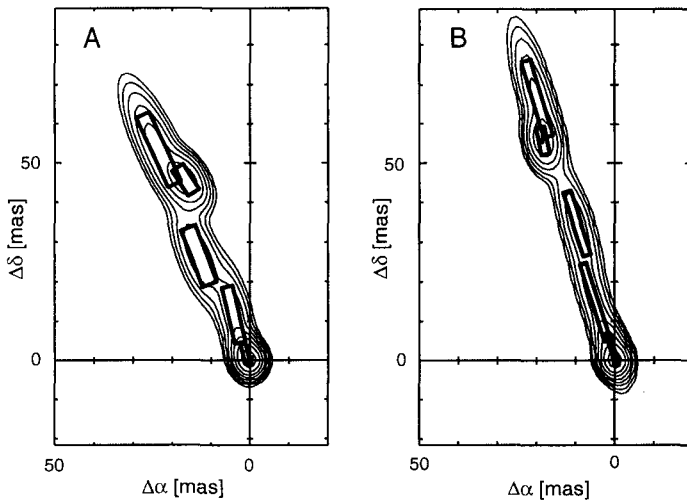


Fig. 4.2 VLBI radio map of Q0957+561. Images A and B show the central core of the radio source and a jet structure. The rectangles represent the axes and position angles of individual flux components, which are seen in both images and also show that their parities are different (courtesy of R. Barkana, reproduced from [Ba99] with permission from *The Astrophysical Journal*).

exactly aligned with the lens galaxy (see Figure 1.1). These two features became understood once it was realized that the lens belonged to a cluster of galaxies. The cluster convergence increased the image separation naturally and its shear displaced them outwards of the cluster center. High resolution VLBI observations later confirmed unequivocally the lensing interpretation by showing fine details of a jet structure in the images (see Figure 4.2). The core and several features of the jets, which extends for ~ 50 mas, can be indeed identified in both images. It is also clear that, as expected, the parities of the images are opposite, that the principal image A (the one farther out from the lens) is more magnified tangentially than image B, while B is somewhat longer radially, but as an overall effect the flux of B is a factor 0.8 smaller than the flux of A.

Detailed models of the lens predict that if a third image were present (as expected for non-singular lensing potentials) it should be located on top of the lensing galaxy and with a flux $< 3\%$ of that of the principal image, being then very hard to identify. A large jet extending $\sim 5''$ from image A outwards from the lens has also been seen in VLA observations,

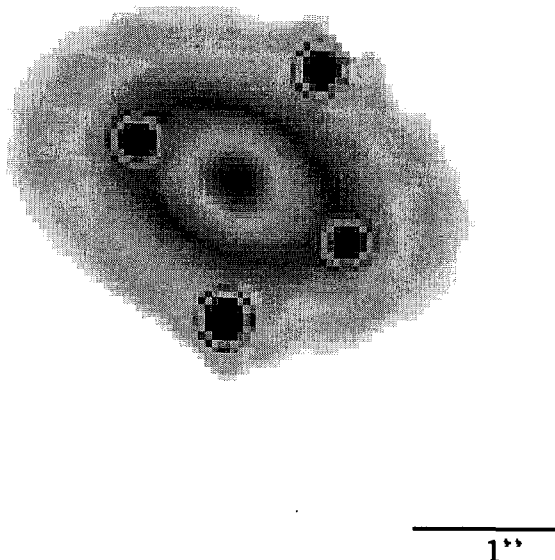


Fig. 4.3 HST picture of Q2237+0305 (from <http://cfa-www.harvard.edu/glensdata/> CfA/Arizona Space Telescope Lens Survey (CASTLES) website, credit of C. S. Kochanek, E. E. Falco, C. Impey, J. Lehar, B. Mc Leod and H. -W. Rix).

and the fact that it is not seen on image B is understood because it lies outside the radial caustic in the source plane and hence it is not multiply imaged. Finally, recently it has been possible to image with the HST the galaxy hosting the quasar [Ke00]. Part of the host galaxy was found to lie inside the astroid (tangential) caustic and is hence quadruply imaged, producing some arc structures. Clearly all these observations gave very strong constraints on the lensing mass distribution, and similar studies are generally attempted with the other lensing systems.

Approximately half of the multiply imaged quasars observed are doubly imaged while around one third are quadruply imaged, the rest having ring like images or more than one source being multiply imaged, like B1933+507 which has two ‘quads’ and one binary making a total of ten lensed images (also one system has six images of the same source). The first example of quadruply imaged quasar was found in 1985 by Huchra [Hu85], and is known as the Einstein cross (see Figure 4.3). In these kind of systems

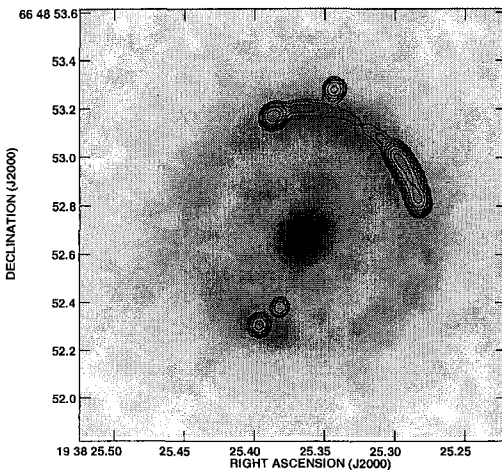


Fig. 4.4 Einstein ring image of the source B1938+666, in the NICMOS infrared picture in grey scale, and superimposed are the MERLIN 5-Ghz radio map contours (courtesy of L. J. King et al., reproduced from [Ki98] with permission from *MNRAS*).

the source lies inside the astroid caustic produced by the non-circular lens (the fifth image expected if the lens is non-singular being very faint and unobserved*). The four images are then very magnified, and this may explain the high frequency of quadruples observed as a very simple example of what is known as magnification bias, i.e. that in flux limited surveys the sources which are highly magnified are brought above threshold by the lensing effect more frequently than those which are less strongly magnified, as is generally the case for the binary quasars. Another effect that could help to increase the frequency of quadruples is the presence of strong shear near the location of the lensing galaxies (due to the cluster hosting the galaxy or to another galaxy nearby), since this would increase the size of the astroid caustic, and hence the probability of producing quadruples, with respect to the expectations based on the typical observed ellipticities of the lensing galaxies.

*The non-observation of triplets and fiveplets implies that the core radii of the galactic potentials should be quite small, $r_c < 200$ pc.

When the angular size of the source is comparable to the size of the astroid caustic (what is more likely at the wavelength in which the emission region in the source is more extended and when the lens is approximately symmetric so that the caustic tends to shrink to a point), ring-like images can be observed when the lens-source alignment is so accurate that the source covers all the astroid caustic, as shown in Figure 4.4. In general the rings break up into separate images in these systems at the wavelengths for which the source becomes more compact, as is the case in the radio image.

4.2 Time delays and H_0

Another important observation in multiply imaged quasars has been the measurement of time delays among the different images, which is possible due to the intrinsically variable nature of some of the quasars. In the case of Q0957+561, the measured time delay is $\Delta t = 417 \pm 3$ d. This is illustrated in Figure 4.5, where the light-curves are seen to agree very well once the B image is advanced temporally by an amount equal to Δt and its flux rescaled to compensate for their different magnifications. This kind of observations are not only a fundamental check of the lensing hypothesis of the system, but can be used to determine the Hubble constant, as first realized by Refsdal [Re64].

The expression for the time delay for an image located at an angle $\vec{\theta}_i$, measured with respect to the straight path in the absence of deflectors, is (see Eq. (3.37))

$$\Delta t_i = K \left[\frac{(\vec{\theta}_i - \vec{\beta})^2}{2} - \Psi(\vec{\theta}_i) \right], \quad (4.1)$$

with

$$K \equiv (1 + z_L) \frac{D_{OS} D_{OL}}{c D_{LS}} \equiv H_0^{-1} f(z_S, z_L, \Omega_m, \Omega_\Lambda), \quad (4.2)$$

where the function f is easily obtainable from the expressions in Appendix A. Clearly the time delay between the images will be the difference of the time delays of each of the images, $\Delta t \equiv \Delta t_2 - \Delta t_1$. Notice that the lens equation just states that the gradient of the term in square brackets in Eq. (4.1) vanishes. Hence, the determination of the lens mass distribution necessary to reproduce the observed position of the images and their

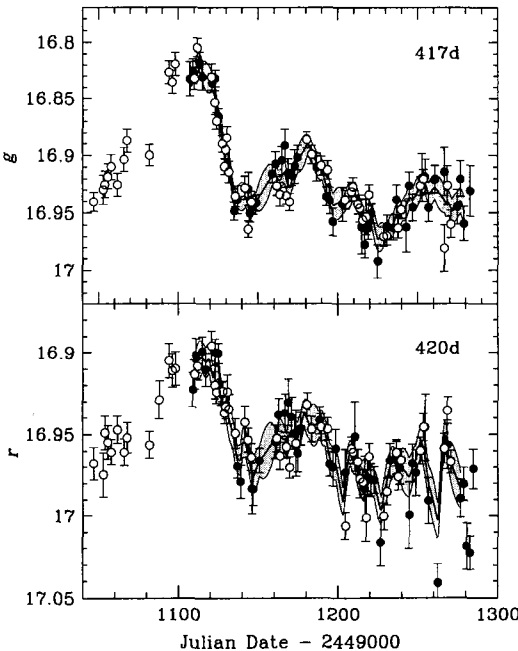


Fig. 4.5 Optical light curves in two bands of the two images of Q0957+561. The principal image A (black dots) is displaced temporally in order that the main features of the two images agree. The resulting time delay is ~ 417 d (courtesy of T. Kundic, reproduced from [Ku97] with permission from *The Astrophysical Journal*).

relative fluxes will fix the term in square brackets (up to some ambiguities which will be discussed below), but is independent of the overall factor K . Once the mass model is established, the measurement of the time delay can then be used to determine the factor K . In other words, the duration of the interval Δt fixes the overall length scale of the system, and hence from the knowledge of the redshift of the lens and source, the Hubble constant H_0 can be determined (see Figure 4.6). The dependence on the cosmological model, i.e. on Ω_m and Ω_Λ through Eq. (4.2), is in general not very large. For instance for Q0957+561 one has $K = 0.475H_0^{-1}$ for $(\Omega_m, \Omega_\Lambda) = (1, 0)$ while $K = 0.497H_0^{-1}$ for $(\Omega_m, \Omega_\Lambda) = (0.3, 0.7)$. The difference can however amount to a 10–20% effect for lenses at redshifts of order unity.

The main uncertainty in the determination of H_0 from the time delays

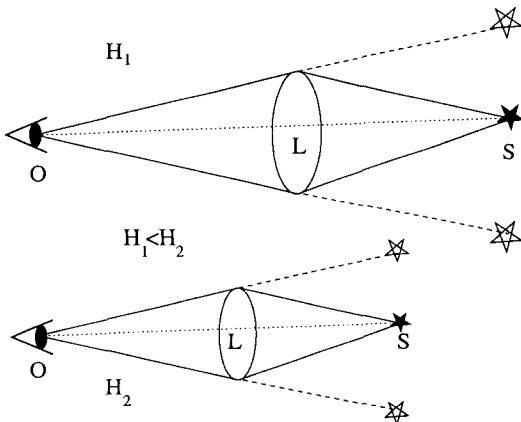


Fig. 4.6 Lensing configurations corresponding to some given observed image positions and measured redshift of lens and source. The two different values of the Hubble constant assumed in each case lead to different overall scale lengths, and hence to different time delays.

comes from the modeling of the lens. When fitting the observed image locations and fluxes to obtain a lens model, there are in general several parameters to determine, which are typically: the mass profile, the ellipticity and orientation of the lens galaxy, the shear induced by the tidal field of nearby objects and the amount of convergence contributed by the lensing galaxy environment (the hosting cluster). There are however in general not sufficient constraints to determine all these parameters unequivocally and hence some degeneracies can be present. The most important one is the so-called ‘mass-sheet degeneracy’ [Fa85], which reflects the fact that there are different possible ways of splitting the mass between the cluster and the galaxy, which to leading order are indistinguishable.

To see this suppose that a model is obtained which fits the data and has an associated projected gravitational potential $\Psi(\vec{\theta})$. Consider now a potential of the form

$$\Psi'(\vec{\theta}) = \frac{1}{2}\bar{\kappa}|\vec{\theta}|^2 + (1 - \bar{\kappa})\Psi(\theta), \quad (4.3)$$

which actually corresponds to rescaling the previous potential by $(1 - \bar{\kappa})$ and adding a sheet of constant surface density $\Sigma = \bar{\kappa}\Sigma_{cr}$ (for instance Ψ could be the potential obtained from a fit with the lensing galaxy alone, while $\bar{\kappa}$ could be the convergence associated to the cluster, whose introduction

reduces the required galaxy potential to $(1 - \bar{\kappa})\Psi$). If the lens equation was previously satisfied for a source located at the solutions of the lens equation $\vec{\beta} = \vec{\theta}_i - \nabla\Psi(\vec{\theta}_i)$, the new source position, satisfying $\vec{\beta}' = \vec{\theta}_i - \nabla\Psi'(\vec{\theta}_i)$, will just be $\vec{\beta}' = (1 - \bar{\kappa})\vec{\beta}$. Anyhow, the only observable change will be in the time delay, since one has

$$\begin{aligned}\Delta t'_i &= K \left[\frac{1}{2}(\vec{\theta}_i - \vec{\beta}')^2 - \Psi'(\vec{\theta}_i) \right] \\ &= (1 - \bar{\kappa})K \left[\frac{1}{2}(\vec{\theta}_i - \vec{\beta})^2 - \Psi(\vec{\theta}_i) - \bar{\kappa}\vec{\beta}^2 \right],\end{aligned}\quad (4.4)$$

and hence to leading order in $\bar{\kappa}$ one has $\Delta t' \equiv \Delta t'_2 - \Delta t'_1 = (1 - \bar{\kappa})\Delta t$. If we want to use the observed time delay to measure the Hubble constant, a change in the model will imply then a change in the inferred value, according to

$$H'_0 = (1 - \bar{\kappa})H_0. \quad (4.5)$$

To deduce the expansion rate accurately it is then necessary to break down this mass-sheet degeneracy. This can be done if the cluster convergence κ_{clust} can be measured directly (looking to its effect on background galaxies around the lens location) or by determining the normalization of the galaxy potential by measuring the velocity dispersion of the stars in the lens galaxy.

There are at present eight measured quasar time delays, and the typical resulting values of H_0 obtained are in the range 50–80 km/s/Mpc. For instance, for Q0957+561 a recent analysis [Ke00] obtains the value

$$H_0 = 68 \div 112 \left(\frac{1 - \kappa_{clust}}{0.8} \right) \frac{\text{km}}{\text{s Mpc}}, \quad (4.6)$$

assuming a flat Universe with $\Omega_m = 1$ (and 4.5% higher for $\Omega_m = 0.3$), with the convergence contributed by the cluster being estimated to be $\kappa_{clust} \simeq 0.2$.

There are several advantages of this method with respect to the other classical ways of determining the Hubble constant. In particular, it measures the expansion rate directly at very high redshifts, where peculiar velocities are negligible, and does not depend on any particular distance ladder nor standard candle, but clearly has the uncertainty arising from the indeterminacy in the lens models.

4.3 Statistical lensing and cosmological parameters

There are a few statistical studies which can be performed with the observed lensed quasars. These include the overall frequency of multiple imaging, its dependence with source and lens redshift, the distribution of angular splittings in binary images and the ratio of binary to quadruple configurations.

Probably the most important result from these studies is the possibility to obtain information on the cosmological parameters, including in particular a relevant upper bound on the cosmological constant from the observed frequency of multiple imaging of quasars [Tu84; Tu90; Fu90a]. This comes about essentially from the fact that the comoving volume per unit redshift interval is a sensitive function of the cosmological model and, being the number of galaxies per comoving volume essentially constant, this means that the amount of lensing galaxies along the line of sight to a high redshift source will depend on the cosmological parameters. For instance, for a QSO at redshift $z_S > 2$ in a flat Universe, there are an order of magnitude more lenses along the line of sight if $\Omega_\Lambda = 0.9$ than if $\Omega_\Lambda = 0$, and furthermore the action of the lenses is also more efficient in the former case.

Following the notation introduced in Appendix A, the comoving volume element near the location of a lens (i.e. the volume measured in comoving coordinates χ , θ and ϕ) is

$$dV = r^2(\chi) d\Omega d\chi \equiv \frac{dV}{d\Omega dz_L} d\Omega dz_L, \quad (4.7)$$

with

$$\frac{dV}{d\Omega dz_L} = D_{OL}^2 (1 + z_L)^2 \frac{c}{H_0} F(z_L), \quad (4.8)$$

and for a flat Universe $F(z) \simeq ((1 + z)^3 \Omega_m + \Omega_\Lambda)^{-1/2}$.

To proceed to compute the expected frequency of multiple lensing it is necessary to adopt a model for the mass distribution of the lenses. Let us consider first the simplest case in which we assume that the lensing objects are not galaxies but instead a cosmological distribution of compact point-like objects with comoving density distribution $d\eta/dM = (1/M)d\rho/dM$, giving an overall contribution to the density of the Universe $\rho = \int dM d\rho/dM \equiv \Omega_l \rho_c$, with $\rho_c = 3H_0^2/8\pi G$ the critical density and Ω_l the fraction of it contributed by the compact lenses. Since point-like lenses always produce two images of a background source, the probability

that a given source be multiply imaged would actually be unity in this case. However, one has to take into account that one of the images will be very faint and unobservable if the angular separation between lens and source is large. Hence, in order that the two images of the source be observable, one must require a minimum value for the demagnification of the fainter image or, equivalently, a maximum value for the ratio of magnifications. According to Eq. (3.20), this ratio is just

$$\frac{A_+}{A_-} = \frac{u^2 + 2 + u\sqrt{u^2 + 4}}{u^2 - 2 + u\sqrt{u^2 + 4}}, \quad (4.9)$$

where $u \equiv \beta/\theta_E$. Let us take for simplicity the threshold condition $u < 1$, corresponding to $A_+/|A_-| < 6.85$. This means that the probability that a given background source have multiple images under these conditions (which is called the optical depth τ) is just the expected number of lenses within an angular distance θ_E of the line of sight, and is

$$\begin{aligned} \tau &= \int dz_L \int dM \frac{dn}{dM} \pi \theta_E^2 \frac{dV}{d\Omega dz_L} \\ &= \frac{3}{2} \Omega_l \frac{H_0}{c} \int dz_L \frac{D_{OL} D_{LS}}{D_{OS}} (1+z_L)^2 F(z_L). \end{aligned} \quad (4.10)$$

Notice that in this simplified model the dependence on the mass distribution has disappeared because for a fixed value of Ω_l , the smaller the lens mass, the larger will be the number density of lenses but also the smaller will be their associated Einstein radii. These two competing effects (a larger number of less efficient lenses) then cancel each other. The integral in the last expression in Eq. (4.10) contains all the dependence on the cosmological model. Besides the factors from the comoving volume per unit redshift, there is also the factor involving the angular distances, and these two actually reinforce each other in giving an increased sensitivity to the cosmological parameters. In Figure 4.7 we plot the quantity τ/Ω_l for different values of Ω_Λ and assuming a flat Universe, showing the strong dependence of the results on the adopted parameters.

Going now to a more realistic description of galactic lenses, the simplest approach is to use the singular isothermal sphere model to parameterize the galaxies and their halos altogether, and hence the density profile will depend just on the lens characteristic velocity dispersion σ (see Eq. (3.41)). As was shown in Section 3.31, multiple images are formed in this model as long as $\beta < \theta_E$, and hence one can define the differential probability for the source

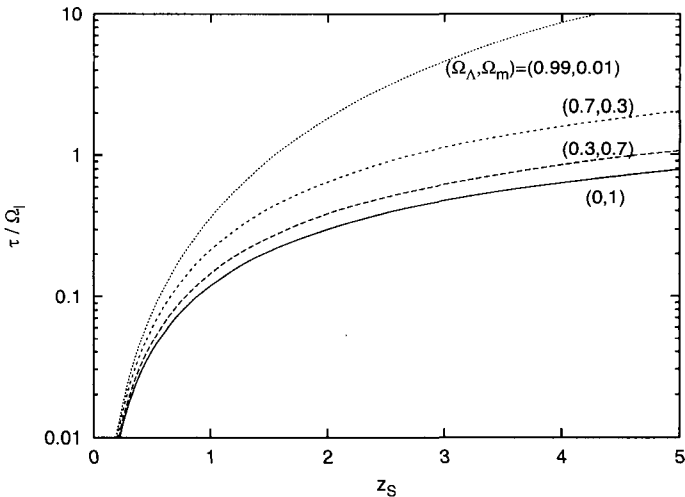


Fig. 4.7 Optical depth versus source redshift due to a cosmological distribution of compact lenses with overall density Ω_l , for different values of Ω_m and Ω_Λ .

to be multiple imaged as the number of lenses within an angular separation θ_E of the line of sight (a restriction to the possible strong demagnification of one of the images could easily be taken into account with a somewhat smaller threshold value for β). This gives

$$\frac{d\tau}{d\sigma} = \int dz_L \frac{dn}{d\sigma} \frac{dV}{d\Omega dz_L} \pi \theta_E^2. \quad (4.11)$$

Notice that isothermal spheres are much less efficient lenses than point-like objects, because all the mass lying outside the Einstein radius does not contribute to the optical depth, and it is important to keep in mind that an angular separation of $2''$, typical of the splittings produced by galactic lenses, corresponds to a scale of only 10 kpc in the lens plane for a lensing object at 1 Gpc.

A way to estimate the differential distribution of lenses is to use the so-called Schechter distribution of galaxy luminosities

$$\frac{dn}{dL} = \frac{n_0}{L_*} \left(\frac{L}{L_*} \right)^{-\nu} \exp(-L/L_*), \quad (4.12)$$

where fits to the observed galaxies give $\nu \simeq 1.1$, $L_* = 1.1 \times 10^{10} L_\odot$ and $n_0 \simeq 1.5 \times 10^{-2} h^3 \text{Mpc}^{-3}$. Approximately 40% of these are ellipticals and

the rest are spirals, but being the spirals less massive than the ellipticals for a given luminosity, their effect on the lensing is small and can be ignored. The distribution in luminosities can then be translated into a distribution with respect to velocity dispersions by using the Faber-Jackson relation valid for elliptical galaxies, which is $L/L_* = (\sigma/\sigma_*)^\alpha$, with $\alpha \simeq 4$ and $\sigma_* = 225 \text{ km/s}^\dagger$.

Finally, another effect which has to be taken into account in the comparison with observations is the possible magnification bias, which can bring lensed sources above the threshold of the survey and hence introduce a bias towards multiple imaged sources.

A thorough analysis of the data available in 1996 was performed by Kochanek [Ko96], leading to the conclusion that $\Omega_\Lambda < 0.66$ (95% CL) in a flat cosmology. The strong efforts devoted at present to complete large quasar surveys, such as JVAS/CLASS, 2dF and the Sloan Digital Sky Survey (this last containing $\sim 10^5$ quasars) will surely tighten the constraints obtained through this kind of analyses.

Besides the overall statistics of multiple imaging, also the distribution of angular separations in binary quasars contains important information. Indeed, cold dark matter scenarios predict the formation of structures in all the range from galaxy to cluster sizes and beyond, and hence in addition to the observed binary images due to galactic lenses, with typical arcsec splittings, there should also be systems with wider ($> 7''$) separations caused by more massive lenses. The lack of any observed large separation QSO pair then sets strong constraints on cosmological models for structure formation [Na88; Ce94; Ba98], in particular excluding the standard ($\Omega_m = 1$) COBE normalized CDM scenario, which is known to predict an excess number of clusters, and in the same way it also predicts an excess number of wide separation images.

4.4 Strong lensing by clusters

Background high redshift galaxies are certainly much more numerous than quasars, although they are also much fainter. This implies that it is practically impossible to establish if two close-by high-redshift galaxies which look similar are multiple images of the same galaxy or not, unless the lensing is

[†]For spirals one has analogously the Tully-Fisher relation $L/L_* = (v_c/v_c^*)^\alpha$, with $\alpha \simeq 2.6$ and the circular velocity $v_c^* \simeq 200 \text{ km/s}$.

so strong that it distorts the images to a shape which cannot be accounted for without invoking lensing. These distortions are actually what allowed to identify giant arcs around cluster cores as images of background galaxies laying on top of the caustics produced by the cluster potential and hence being strongly elongated along one direction.

The first arcs were identified in 1986 by Lynds and Petrosian [Ly86] and Soucail et al. [So87], and their interpretation in terms of lensed galaxies was suggested by Paczyński [Pa87]. Since then several arc systems have been found (in around $\sim 1/3$ of the rich X-ray emitting clusters, and $< 1/10$ of the optically selected clusters). Being the arcs extended objects, very strong constraints on the central cluster gravitational potential can be set from the requirement of reproducing the observed image shapes and locations. This has many important applications, such as measuring the amount of dark matter on cluster scales (and hence obtain the fraction of baryonic matter from the observed amount of hot gas and galaxy stars), or to measure the profile of the density distribution to compare it with the expectations from structure formation scenarios.

The arcs around a cluster will appear in the locations where the magnification ($A = [(1 - \kappa)^2 - \gamma^2]^{-1}$) is very large, i.e. for $\kappa \simeq 1 - \gamma$ (for the tangential arcs), which corresponds to a surface density somewhat smaller than critical in the presence of shear. For spherical lenses, the arcs follow approximately the Einstein ring of the mass distribution (i.e. they are the cluster analogue of the rings produced by galactic lenses). As we saw in the previous Chapter, Eq. (3.32), the total mass contained within the arcs will then be

$$M(\theta_{arc}) \simeq \pi(D_{OL}\theta_{arc})^2 \Sigma_{cr} \simeq 1.1 \times 10^{14} M_\odot \left(\frac{\theta_{arc}}{30''} \right)^2 \frac{D_{OL} D_{OS}}{\text{Gpc } D_{LS}}, \quad (4.13)$$

and this expression also gives a rough idea of the mass contained inside the arcs for more general lens models.

Figure 4.8 shows one of the most impressive examples of strong lensing in clusters. In this HST picture of CL0024+1654, eight elongated images of the same background galaxy are observed (one radial and seven tangentially aligned in an almost circular pattern). A very detailed study of this system, modeling the lens with more than a hundred mass distributions corresponding to the observed cluster galaxies, the gas distribution and the unobserved dark matter, allowed to reproduce accurately the observed features of the images [Ty98]. It was found that besides the galaxies, the

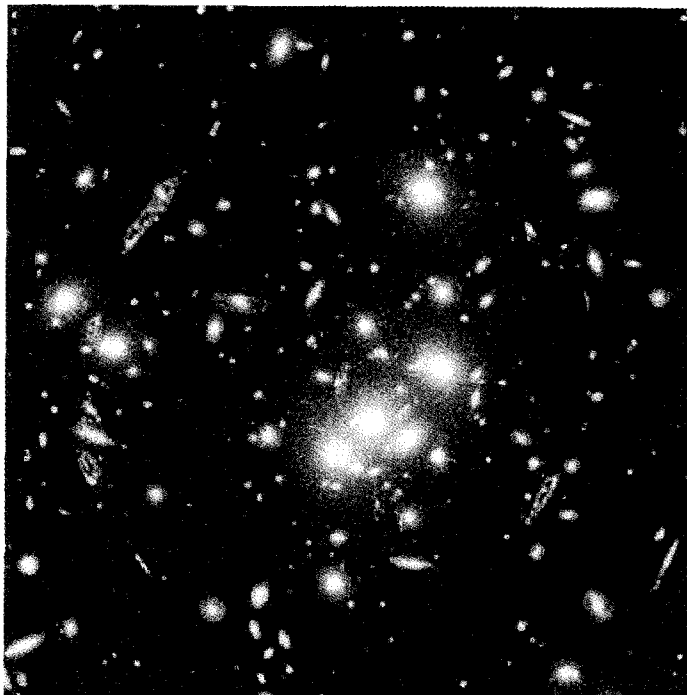


Fig. 4.8 Strong lensing of a background blue galaxy by cluster 0024+1654 (credit of W. N. Colley, E. Turner and J. A. Tyson). Eight images of the same galaxy are seen in this HST picture.

vast majority ($\sim 83\%$) of the mass forms a very smooth and spherically symmetric distribution of dark matter. The total mass within $107h^{-1}$ kpc of the cluster core (corresponding to the location of the arcs) is

$$M_{107} = 1.662 \pm 0.002 \times 10^{14} h^{-1} \left(\frac{D_{LS}/D_{OS}}{0.57} \right)^{-1} M_{\odot}. \quad (4.14)$$

The existence of a central radial arc requires that the density distribution must have a soft core with size $\sim 35h^{-1}$ kpc, in contradiction with the singular profiles resulting in some popular models of structure formation (e.g. the Navarro, Frenk and White profiles). A subsequent measurement [Br00] of the source galaxy redshift, $z_S = 1.675$, together with the known cluster redshift, $z_L = 0.39$, implies $D_{LS}/D_{OS} = 0.675$ assuming

$$(\Omega_m, \Omega_\Lambda) = (0.3, 0.7)^{\ddagger}.$$

Several other studies can be performed with the observed arc systems. For instance, the radial magnification of the tangential arcs (which may be guessed if the actual size of the source can be estimated) depends on the steepness of the density profile, since A_r depends on $\partial M/\partial\theta$ (see Eq. (3.33)). On the other hand, at the arc location one has $A_r \equiv [(1 - \kappa) + \gamma]^{-1} \simeq 0.5/(1 - \kappa)$. The minimum value of A_r is then 0.5, corresponding to a very compact lens for which $\kappa \simeq 0$ near the arc location. On the contrary, the flatter that the mass profile becomes, the closer to unity becomes κ near the arc location and hence the larger will be the radial magnification. The observation of very thin arcs in some clusters has then been interpreted as suggesting that their potential is steep, with $\kappa < 0.5$, and hence a significant amount of shear should be present near the arc locations [Ko89a; Ba94a].

4.5 Weak lensing in clusters

If the density of a cluster is under-critical or if we look into the region outside the giant arcs where $\kappa < 1 - \gamma$, so that no multiple images can be formed, we enter the regime of weak lensing. In this case it is not easy to measure directly the effects of the cluster convergence, but instead the effects of the shear can become observable. This is because the images are magnified by a factor $A_1 = (1 - \kappa + \gamma)^{-1}$ in one direction and $A_2 = (1 - \kappa - \gamma)^{-1}$ in the orthogonal one, and hence the shear induces tangential deformations of the images. Although the source galaxies are intrinsically elliptical, the huge number of background faint blue galaxies present at redshifts $z \sim 1$ (referred to as Tyson's population [Ty88]) with a density of ~ 50 per square arcmin down to 27 mag, allows to obtain the ellipticity induced by lensing in different directions around the clusters by averaging over many nearby background galaxies, whose intrinsic ellipticities are randomly oriented.

Considering that a circular source will be deformed into an ellipse with axis ratio $r \equiv A_1/A_2$, the average ellipticity produced will be $\langle \epsilon \rangle = (1 - r)/(1 + r) = \gamma/(1 - \kappa)$. Hence, when the convergence is small ($\kappa \ll 1$), the average ellipticity gives directly a measure of the shear. On the other hand, both the shear and the convergence are obtained from second derivatives of

[†]This later work also obtained a somewhat smaller total cluster mass inside the arcs, $M(< 100h^{-1} \text{ kpc}) = 1.11 \pm 0.03 \times 10^{14} M_\odot$.

the gravitational potential Ψ . There are inversion techniques to obtain then the convergence from the measured shear maps, and with this the surface mass density profile $\Sigma = \kappa \Sigma_{cr}$ can be reconstructed.

The main technique to perform this inversion is due to Kaiser and Squires [Ka93a] and was then refined and extended by several authors [Ka95; Se95; Sq96]. To see how it works let us write a complex shear

$$\Gamma \equiv \gamma_1 + i\gamma_2 = \left(\frac{\partial_1^2 - \partial_2^2}{2} + i\partial_1\partial_2 \right) \Psi, \quad (4.15)$$

where $\partial_i \equiv \partial/\partial\theta_i$. This shear will be related to a complex ellipticity $\varepsilon = \epsilon_1 + i\epsilon_2$. If we now write the potential in terms of the convergence (through the integral of the Poisson equation, see Eq. (2.66)), one has

$$\begin{aligned} \Gamma(\vec{\theta}) &= \frac{1}{\pi} \left(\frac{\partial_1^2 - \partial_2^2}{2} + i\partial_1\partial_2 \right) \int d^2\theta' \kappa(\vec{\theta}') \ln |\vec{\theta} - \vec{\theta}'| \\ &= \frac{1}{\pi} \int d^2\theta' \kappa(\vec{\theta}') D(\vec{\theta} - \vec{\theta}'). \end{aligned} \quad (4.16)$$

In this way the shear is expressed as a convolution of the convergence. The kernel D satisfies

$$D(\vec{\theta}) \equiv \left(\frac{\partial_1^2 - \partial_2^2}{2} + i\partial_1\partial_2 \right) \ln |\vec{\theta}| = \frac{-1}{(\theta_1 - i\theta_2)^2}. \quad (4.17)$$

To invert Eq. (4.16) it is convenient to go to the Fourier space and notice that the transform of D is

$$D(\vec{\ell}) \equiv \int d^2\theta D(\vec{\theta}) e^{i\vec{\theta} \cdot \vec{\ell}} = \pi \frac{\ell_1^2 - \ell_2^2 + 2i\ell_1\ell_2}{|\vec{\ell}|^2}. \quad (4.18)$$

It satisfies $D(\vec{\ell})D^*(\vec{\ell}) = \pi^2$, and since from Eq. (4.16) one has that $\Gamma(\vec{\ell}) = D(\vec{\ell})\kappa(\vec{\ell})/\pi$, this implies that $\kappa(\vec{\ell}) = D^*(\vec{\ell})\Gamma(\vec{\ell})/\pi$. This means that the convergence is obtained as

$$\kappa(\vec{\theta}) = \kappa_0 + \frac{1}{\pi} \int d^2\theta' D^*(\vec{\theta} - \vec{\theta}') \Gamma(\vec{\theta}'). \quad (4.19)$$

Notice that a constant convergence κ_0 appears here, reflecting the fact that the presence of a sheet of uniform density cannot be determined from the measurement of the shear alone, and hence this ambiguity corresponds to a ‘mass sheet degeneracy’.

When the convergence κ is not negligible, the complex shear is related to the complex ellipticity through $\Gamma = (1 - \kappa)\langle\varepsilon\rangle$, and Eq. (4.19) leads to an

integral equation for κ which has to be solved iteratively. To break the mass sheet degeneracy and determine κ_0 it is necessary to measure the effects of the cluster convergence, what can be done if the magnification of the images can also be determined. For this one would have to rely on the estimation of the change in the apparent size of the images with respect to expectations [Ba95a], or alternatively to measure the change in the background galaxy counts compared to the galaxy counts in unlensed fields far from the cluster [Br95]. For instance, if $N_0(< m)$ represents the number density (per unit solid angle) of sources brighter than a given apparent magnitude m in the absence of lensing effects[§], the actual number of sources brighter than m observed in a direction in which the amplification produced by the lensing effects is A , will be $N(< m) = N_0(< m + 2.5 \log A)/A$. Here we have taken into account that the solid angle under which some given sources are seen also increases by lensing, as dictated by Liouville theorem, and introduces the dilution factor A^{-1} in the densities. One has then $N(< m) \simeq N_0(< m)A^{2.5s-1}$, with $s \equiv d \log N_0/dm$. Hence, the change in the density of sources depends on the steepness of the luminosity distribution, i.e. on the reservoir of faint sources available to be brought above threshold by the magnification. The effect in general depends on the filter used in the observations, since for instance $s \simeq 0.4$ in blue (giving an almost vanishing change in the number counts with lensing due to a cancellation of the two effects), but in red $s \simeq 0.15$ and the density of sources diminishes in the presence of magnification due to the dominant effect of the change in the solid angle. Then, comparing $N(< m)$ with $N_0(< m)$ and knowing s for the filter used, an estimation of the amplification $A(\vec{\theta})$ is obtained, which combined with $\gamma(\vec{\theta})$ and $\kappa(\vec{\theta})$ can be used to determine κ_0 .

Figure 4.9 from [Na98] shows the reconstructed mass profile for the cluster 0024+1654 (right panel) from the measured shear (left panel), showing that the mass distribution is recovered up to distances ~ 1.5 Mpc from the center, and nicely complements the strong lensing studies of the central part of the cluster discussed in the previous Section.

Weak lensing surveys of several clusters show that the mass distribution follows in general the light distribution up to scales of ~ 3 Mpc, and allow to estimate the overall matter density of the Universe, which turns out to be $\Omega_m \simeq 0.2$ [Wi00b]. The weak lensing around field galaxies (probing

[§]The magnitude of an object in terms of its luminosity is just $m = 2.5 \log(\mathcal{L}_0/\mathcal{L})$, with \mathcal{L}_0 being the luminosity of an object with zero magnitude.

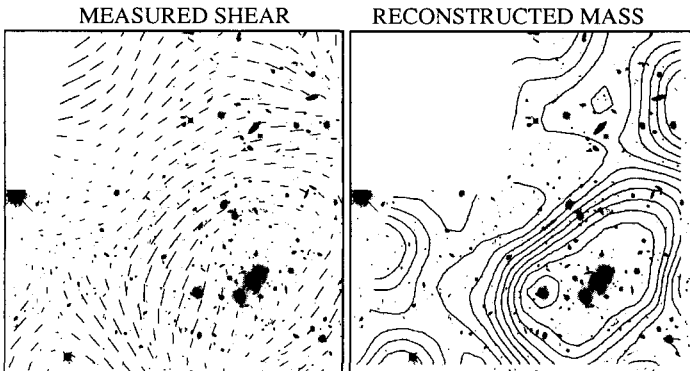


Fig. 4.9 Weak lensing around cluster 0024+1654. On the left is the measured shear field (Y. Mellier and B. Fort) overlaid in an HST picture, and on the right the reconstructed mass density (C. Seitz et al.), courtesy of M. Bartelmann and R. Narayan.

typical distances of ~ 200 kpc from the center of the lensing galaxies) has been measured recently [Fi00; Sm01], and this was used to set a lower limit of $42.7 \pm 0.6 \times 10^{12} M_{\odot}$ for the mass of an L_* galaxy halo, again suggesting an overall value $\Omega_m \simeq 0.2$.

4.6 Cosmic shear

When one looks far away from the line of sight to a cluster, i.e. in ‘empty regions’, the weak lensing effects are very small, but they are anyhow non-vanishing. Indeed, the gravitational effects of the large scale inhomogeneities in the density distribution of the Universe accumulate along the line of sight and induce correlations among the ellipticities of background galaxies [Bl91; Mi91; Ka92]. This effect, known as cosmic shear, is very difficult to observe due to its small amplitude and because of the different sources of contamination, but its detection by several groups has shown the feasibility of such measurements [Wi00a; Ka00; Ba00; va00; Ma01]. The induced galaxy ellipticities amount to only a few per cent, which is much smaller than the typical intrinsic random ellipticities of galaxies, and taking into account that there are artificial systematic sources of distortions of comparable amplitude, a careful statistical study of the shapes of hundreds of thousands of galaxies covering few degrees is needed to extract a signal. The importance of the cosmic shear measurements

is that its statistical properties are determined by the large scale matter distribution, and thus they can be used to constrain the power spectrum of density fluctuations, the cosmological parameters and the bias [Ja97b; Be97a; Ka98].

For the computation of the cosmic shear signal, one has to abandon the thin lens approximation, i.e. the assumption adopted up to now that the deflection can be considered to take place at a single plane, because the bending of light rays takes place all along the photon's path. By solving the geodesic equation in an inhomogeneous Universe, we can obtain the change in the angular position of photons during their trip, and this will turn out to depend on the transverse gradient of an integral of the gravitational potential along the photon path. This leads to a mapping matrix in which the convergence and shear are functions of the second derivatives of this 'projected potential'. The two point correlation function of the shear can then be written in terms of the power spectrum of the density perturbations, and this is used to compare model predictions with observations. In what follows, we present a sketch of this computation, which is somewhat more technical than the rest of the Chapter.

The effects of the density inhomogeneities of the Universe is studied by considering the trajectory of photons in a perturbed Friedmann-Robertson-Walker metric. As discussed in Appendix A, the line element in comoving coordinates can be written as

$$ds^2 = a^2(\tau) \left\{ \left(1 + 2\frac{\varphi}{c^2}\right) d\tau^2 - \left(1 - 2\frac{\varphi}{c^2}\right) [d\chi^2 + r^2(\chi)(d\theta^2 + \sin^2 \theta d\phi^2)] \right\}, \quad (4.20)$$

where τ is the conformal time, χ the comoving separation, $r(\chi)$ the comoving angular diameter distance and $\varphi(\vec{x}, \tau)$ the gravitational potential perturbation. Null geodesics in these coordinates are identical to those in a non-expanding Universe ($a = \text{const}$). In the absence of lenses ($\varphi = 0$), light rays arriving to an observer at the origin of coordinates travel along straight lines having constant θ and ϕ and the temporal evolution is just given by $\chi(\tau) = \tau_0 - \tau$.

The lensing effect of small inhomogeneities in the matter distribution can be taken into account by solving the geodesic equations with a non-vanishing $\varphi(\vec{x}, \tau)$ in the metric. These are

$$\frac{d^2 x^i}{d\lambda^2} = -g^{ik} \left(\frac{\partial g_{kl}}{\partial x^m} - \frac{1}{2} \frac{\partial g_{lm}}{\partial x^k} \right) \frac{dx^m}{d\lambda} \frac{dx^l}{d\lambda}, \quad (4.21)$$

and to the first perturbative order in φ , the affine parameter can be chosen as the comoving separation, i.e. $d\lambda = d\chi$. The solution to the geodesic equations will provide the change in the angular cross section of a light beam as it propagates, and this is the quantity required to compute the magnification effects. It is convenient to consider a fiducial direction along the beam and take angular coordinates θ_σ ($\sigma = x, y$) in the neighborhood of it, such that $d\theta_x^2 + d\theta_y^2 = d\theta^2 + \sin^2 \theta d\phi^2$. The geodesic equation can then be written to the first perturbative order in φ as

$$\frac{d^2\theta_\sigma}{d\chi^2} = -\frac{2}{r} \frac{\partial r}{\partial \chi} \frac{d\theta_\sigma}{d\chi} - \frac{2\varphi_{,\sigma}}{c^2 r^2}, \quad (4.22)$$

where we have denoted by a comma partial derivatives ($\varphi_{,\sigma} \equiv \partial\varphi/\partial\theta_\sigma$). The first term accounts for the effect of the curvature of space on the geodesic angular separation while the second accounts for the deflections due to the gravitational potential inhomogeneities along the photon's path and, as in the thin lens case, it depends on the transverse gradient of the potential. The solution of this equation for a light ray that reaches the observer with angular separation θ_σ^0 from the fiducial ray, is given by

$$\theta_\sigma(\chi) = \theta_\sigma^0 - \frac{2}{c^2} \int_0^\chi \frac{d\chi'}{r^2(\chi')} \int_0^{\chi'} d\chi'' \varphi_{,\sigma}(\vec{\theta}r(\chi''), \chi''). \quad (4.23)$$

Changing the order of integration and using the fact that for $r(\chi)$ given in Eq. (A.3) we have that $\int_{\chi'}^\chi d\chi''/r^2(\chi'') = r(\chi - \chi')/r(\chi)r(\chi')$, Eq. (4.23) can be written as

$$\theta_\sigma(\chi) = \theta_\sigma^0 - \frac{2}{c^2} \int_0^\chi d\chi' \varphi_{,\sigma}(\vec{\theta}r(\chi'), \chi') \frac{r(\chi - \chi')}{r(\chi)r(\chi')}. \quad (4.24)$$

Notice that the integral involves the orthogonal derivative of the gravitational potential along the perturbed photon path. Since this path is just the quantity that we want to compute, a solution can be obtained iteratively starting with the unperturbed solution inside the integral (with $\vec{\theta}r(\chi) \rightarrow \vec{\theta}^0 r(\chi)$), to get the solution to the first perturbative order in φ at which we are working. An expression for the mapping matrix can be obtained as

$$\mathcal{T}_{\sigma\alpha} = \frac{\partial\theta_\sigma(\chi)}{\partial\theta_\alpha^0} = \delta_{\sigma\alpha} - \frac{2}{c^2 r(\chi)} \int_0^\chi d\chi' \varphi_{,\sigma\alpha}(\vec{\theta}r(\chi'), \chi') \frac{r(\chi - \chi')}{r(\chi')}. \quad (4.25)$$

We see that the role of the rescaled gravitational potential Ψ in Eq. (3.24) is here played by the integral

$$\Psi = \frac{2}{c^2 r(\chi)} \int_0^\chi d\chi' \varphi(\vec{\theta}r(\chi'), \chi') \frac{r(\chi - \chi')}{r(\chi')}, \quad (4.26)$$

being $\mathcal{T}_{\sigma\alpha} = \delta_{\sigma\alpha} - \Psi_{,\sigma\alpha}$. The integral has to be performed along the line of sight up to the source position (with radial comoving coordinate χ). The isotropic focusing, represented by the convergence, is given by the trace of $\Psi_{,\sigma\alpha}$

$$\kappa(\vec{\theta}) = \frac{1}{2} \nabla_\theta^2 \Psi = \frac{1}{c^2} \int_0^\chi d\chi' \nabla_\perp^2 \varphi(\vec{x}_\perp, \chi') \frac{r(\chi - \chi') r(\chi')}{r(\chi)}, \quad (4.27)$$

where the derivatives ∇_\perp are with respect to the transverse coordinates $\vec{x}_\perp = \vec{\theta}r(\chi')$. The traceless part of $\Psi_{,\sigma\alpha}$ corresponds to the shear, responsible for the distortion of the image shapes, and it is obtained in terms of $\gamma_1 = (\Psi_{,xx} - \Psi_{,yy})/2$ and $\gamma_2 = \Psi_{,xy}$.

The transverse Laplacian in Eq. (4.27) can be written as $\nabla_\perp^2 = \nabla^2 - \nabla_\chi^2$, and it can be shown that upon integration the term proportional to the longitudinal Laplacian $\nabla_\chi^2 \varphi$ gives a vanishing contribution. Hence, in Eq. (4.27) $\nabla_\perp^2 \varphi$ can actually be replaced by $\nabla^2 \varphi$, and this last is related to the density perturbation $\delta(\vec{x}, \tau)$ through the Poisson equation (see Eq. (A.24)), i.e.

$$\nabla^2 \varphi(\vec{x}, \tau) = \frac{3H_0^2 \Omega_m}{2a(\tau)} \delta(\vec{x}, \tau). \quad (4.28)$$

Thus, the convergence can be expressed as an integral of the density inhomogeneities along the line of sight to the source.

If the sources are distributed in redshift, according to a normalized[¶] comoving density $n(\chi)$, the observed convergence will result from an integration of Eq. (4.27) over the source distribution. After a change in the integration order, this can be written as

$$\kappa(\vec{\theta}) = \frac{3H_0^2 \Omega_m}{2c^2} \int_0^{\chi_H} d\chi \delta(\vec{x}_\perp, \chi) \frac{g(\chi)}{a(\chi)}, \quad (4.29)$$

[¶]Such that $n(\chi) = N_{tot}^{-1}(dN/d\chi)$.

where χ_H corresponds to the horizon, the maximal visible distance, and

$$g(\chi) = r(\chi) \int_{\chi}^{\chi_H} d\chi' \frac{r(\chi - \chi') n(\chi')}{r(\chi')}.$$

Both the shear and the convergence are determined by the mass distribution along the path of the photons. Thus, the two point correlation function of the shear or the convergence (that is the mean value of the product of the function in all the pair of directions separated by a given angle θ , e.g. $C_\kappa(\theta) = \langle \kappa(\vec{\beta}) \kappa(\vec{\beta} + \vec{\theta}) \rangle$) encodes information on the amplitude of the density inhomogeneities at the different scales. To quantify this it is more convenient to go to the Fourier space. The Fourier transform of the convergence

$$\kappa(\vec{\ell}) = \int d^2\theta \kappa(\vec{\theta}) e^{i\vec{\ell}\cdot\vec{\theta}}$$

has power spectrum $P_\kappa(\vec{\ell})$ defined by

$$\langle \kappa(\vec{\ell}) \kappa(\vec{\ell}') \rangle = (2\pi)^2 \delta^{(2)}(\vec{\ell} - \vec{\ell}') P_\kappa(\ell), \quad (4.30)$$

which is the Fourier transform of $C_\kappa(\theta)$ (see Appendix A). Hence, it can be written as

$$\begin{aligned} P_\kappa(\ell) &= \int d^2\theta C_\kappa(\theta) e^{i\vec{\ell}\cdot\vec{\theta}} \\ &= \frac{9H_0^4 \Omega_m^2}{4c^4} \int d^2\theta e^{i\vec{\ell}\cdot\vec{\theta}} \int_0^{\chi_H} d\chi \frac{g^2(\chi)}{a^2(\chi)} \int_0^{\chi_H} d\chi' \int \frac{d^3k}{(2\pi)^3} P_\delta(k) e^{-i(k_\sigma r\theta^\sigma + k_\chi \chi')}, \end{aligned} \quad (4.31)$$

where the last integral, coming from the two point correlation function of the density perturbations, was written as the Fourier transform of the power spectrum $P_\delta(k)$. The angular integration in Eq. (4.31) gives a δ -function that picks out the modes $k_\sigma = \ell_\sigma / r(\chi)$, and assuming a slow variation of the factor $g(\chi)/a(\chi)$ with respect to the typical scale of the perturbations, the integral in χ gives another δ -function that selects $k_\chi = 0$. Then,

$$P_\kappa(\ell) = \frac{9H_0^4 \Omega_m^2}{4c^4} \int_0^{\chi_H} d\chi \frac{g^2(\chi)}{a^2(\chi)} P_\delta\left(\frac{\ell}{r(\chi)}, \chi\right), \quad (4.32)$$

where the second argument in P_δ , $\chi = \tau_0 - \tau$, indicates that the power spectrum may have a slow variation along the photon path due to the time evolution of the density inhomogeneities.

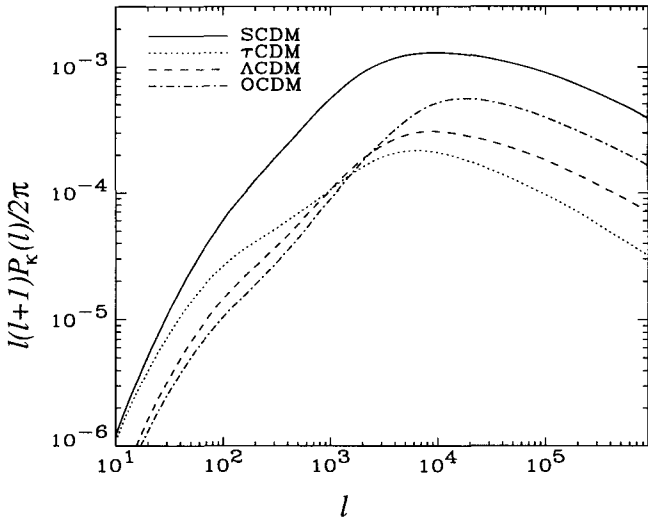


Fig. 4.10 The power spectrum of the convergence for different cosmological models: SCDM corresponding to $(\Omega_m, \Omega_\Lambda, \sigma_8) = (1, 0, 1)$, τ CDM to $(1, 0, 0.6)$, Λ CDM to $(0.3, 0.7, 1)$ and OCDM to $(0.3, 0, 1)$ (courtesy of R. Ellis, reproduced from [Ba00] with permission from *MNRAS*).

Analogously, the shear power spectrum can be defined as

$$\langle \gamma_1(\vec{\ell})\gamma_1(\vec{\ell}') + \gamma_2(\vec{\ell})\gamma_2(\vec{\ell}') \rangle = (2\pi)^2 \delta^{(2)}(\vec{\ell} - \vec{\ell}') P_\gamma(\ell) \quad (4.33)$$

in terms of the Fourier transform of the shear, $\gamma_i(\vec{\ell})$. It is easy to see using the relations between the Fourier transforms

$$\begin{aligned} \kappa(\vec{\ell}) &= \frac{1}{2}(\ell_x^2 + \ell_y^2)\Psi(\vec{\ell}), \\ \gamma_1(\vec{\ell}) &= -\frac{1}{2}(\ell_x^2 - \ell_y^2)\Psi(\vec{\ell}), \\ \gamma_2(\vec{\ell}) &= \ell_x\ell_y\Psi(\vec{\ell}), \end{aligned}$$

that the power spectrum of the shear is equal to the power spectrum of the convergence, i.e.

$$P_\gamma(\ell) = P_\kappa(\ell) = \frac{\ell^4}{4} P_\Psi(\ell).$$

Figure 4.10 shows a plot of the convergence power spectrum for differ-

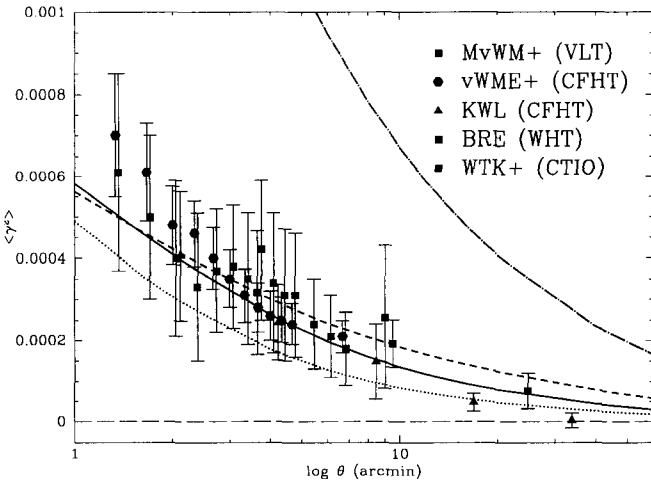


Fig. 4.11 Measured galactic ellipticity correlations in empty fields (cosmic shear) due to weak gravitational lensing by large scale structures. Also the predictions for different cosmological models are displayed: short dashes corresponds to $(\Omega_m, \Omega_\Lambda, \sigma_8) = (1, 0, 1)$, dot-dashes to $(0.3, 0, 1.2)$, dots to $(1, 0, 0.6)$ and the solid line to $(0.3, 0.7, 1.02)$ (courtesy of R. Maoli, reproduced from [Ma01] with permission from *Astronomy and Astrophysics*).

ent cosmological models. Notice that there is an inverse proportionality between the wavenumber ℓ and the associated angular scale $\theta = 2\pi/\ell$.

The quantity used in the comparison with observations is the variance of the shear averaged over a circular window of angular size θ . Denoting by $W(\theta)$ the window function and by $W(\ell)$ its Fourier transform, the shear of the smoothed field results

$$\langle \gamma^2(\theta) \rangle = 2\pi \int_0^\infty d\ell \ell W^2(\ell) J_0(\ell\theta) P_\gamma(\ell). \quad (4.34)$$

The results obtained by several groups are summarized in Figure 4.11 and they are compared with the predictions of some popular models for structure formation. It is expected that measurements with enlarged statistics and better control of the systematics involved will play an important role to discriminate among the models.

4.7 Quasar-galaxy correlations

The gravitational lensing by large scale structures can also induce correlations between the quasar and galaxy distributions [Na89; Ko89b; Sc89]. Indeed, due to the magnification bias effect, the observed density of quasars depends on the matter distribution along the line of sight. As was shown in Section 4.5, the density of quasars brighter than a certain magnitude m should satisfy $N_Q(< m) = N_Q^0(< m)A^{2.5s-1}$, where A is the amplification produced by the gravitational lensing along the direction being considered. This effect makes bright quasars (for which $s \sim 1$) to be more abundant behind dark matter lumps. On the other hand, galaxies are believed to be good tracers of the dark matter distribution and hence an enhancement in the density of bright quasars around foreground galaxies is expected.

For this weak lensing phenomenon, the amplification can be approximated by $A \simeq 1 + 2\kappa$, with κ given by Eq. (4.29). Then, the excess of quasars in a given direction will be $(N_Q - N_Q^0)/N_Q^0 \simeq (2.5s - 1)2\kappa(\vec{\theta})$. On the other hand, the galaxy number density is related to the density contrast δ through the bias parameter b , see Eq. (A.31). Thus, the quasar-galaxy angular two-point correlation will be proportional to $(2.5s - 1)b$ times an integral of P_δ along the line of sight [Ba95b], and hence carries information about the structure formation scenario and specially about the biasing. Several observations in the range from $1'$ to $25'$ have confirmed the existence of an excess number of galaxies around bright quasars (see e.g. [Fu90b; Ba94b; Be97b]), supporting the presence of a magnification bias effect. The precise amplitude is however still controversial, and wide field surveys like SDSS and 2dF will provide huge galaxy and quasar catalogues to settle this point.

4.8 Lensing of the Cosmic Microwave Background

The CMB photons arriving from the last scattering surface also suffer a gravitational bending of their trajectories as they travel through the large scale structure of the Universe, and this affects the temperature anisotropies detected today. In Appendix A we briefly described the CMB anisotropies and here we will discuss how that picture is modified by the gravitational lensing [Bl87b; Ca93; Se96a]. The basis of the effect is that, as a consequence of the deflections, the radiation detected from a direction $\vec{\theta}$ actually originated from an angular position on the last scattering surface

$\vec{\beta} = \vec{\theta} - \vec{\alpha}(\vec{\theta})$. This means that the temperature pattern is affected because

$$\tilde{T}(\vec{\theta}) = T(\vec{\theta} - \vec{\alpha}), \quad (4.35)$$

where the tilde refers to the actual quantity measured in the presence of lensing effects and $T(\vec{\beta})$ is the theoretical value that would result ignoring the lensing effects. Hence, by changing the correspondence between the points in the last scattering surface and the observed directions, gravitational lensing can distort the pattern of the observed anisotropies. However, it is important to keep in mind that gravitational lensing by itself cannot generate anisotropies, since as a consequence of the surface brightness conservation a perfectly isotropic background would remain isotropic after lensing. Indeed, gravitational lensing changes the position and the solid angle under which a patch of the last scattering surface is seen, but if the surface brightness were homogeneous on it, no anisotropies would result. Gravitational lensing hence only modifies already existing anisotropies.

To quantify this effect, let us study the two point correlation function of the lensed anisotropies

$$\tilde{C}(\theta) = \left\langle \frac{\Delta T}{T}(\vec{\theta}_1 - \vec{\alpha}_1) \frac{\Delta T}{T}(\vec{\theta}_2 - \vec{\alpha}_2) \right\rangle_{|\vec{\theta}_1 - \vec{\theta}_2|=\theta} \quad (4.36)$$

At small angular scales it is a good approximation to use a Fourier expansion for $\Delta T/T$. Then,

$$\tilde{C}(\theta) = \int \frac{d^2\ell}{(2\pi)^2} \frac{d^2\ell'}{(2\pi)^2} e^{-i\vec{\ell}\cdot\vec{\theta}_1 + i\vec{\ell}'\cdot\vec{\theta}_2} \left\langle e^{i\vec{\ell}\cdot\vec{\alpha}_1 - i\vec{\ell}'\cdot\vec{\alpha}_2} \frac{\Delta T}{T}(\vec{\ell}) \frac{\Delta T^*}{T}(\vec{\ell}') \right\rangle. \quad (4.37)$$

Two different stochastic processes enter in this problem, one is the temperature intrinsic anisotropies in the last scattering surface $\Delta T/T$ and the other is the angular displacement pattern $\vec{\alpha}$ produced by the fluctuations in the gravitational potential along the photon path from the last scattering surface to the observer. These vary for different realizations of the density inhomogeneities and ensemble averages over both of them have to be performed. The first average gives the angular spectrum

$$\left\langle \frac{\Delta T}{T}(\vec{\ell}) \frac{\Delta T^*}{T}(\vec{\ell}') \right\rangle = (2\pi)^2 \delta^{(2)}(\vec{\ell} - \vec{\ell}') C_\ell, \quad (4.38)$$

while the second one gives for a Gaussian field

$$\left\langle e^{i\vec{\ell}\cdot(\vec{\alpha}_1 - \vec{\alpha}_2)} \right\rangle = e^{-\frac{\ell^2 \sigma^2(\theta)}{2}}, \quad (4.39)$$

where $\sigma^2(\theta) \equiv \langle (\vec{\alpha}_1 - \vec{\alpha}_2)^2 \rangle$. Hence, we can write Eq. (4.37) as

$$\tilde{C}(\theta) = \int d\ell \frac{\ell}{2\pi} C_\ell J_0(\ell\theta) e^{-\frac{\ell^2 \sigma^2(\theta)}{2}}. \quad (4.40)$$

where the Bessel function $J_0(x)$ comes from the integration over the $\vec{\ell}$ direction (the 2D analogue of Eq. (A.29)). The two point correlation function differs from the unlensed expression by the appearance of the exponential factor, whose effect is to smear the anisotropies on angular scales smaller than the dispersion angle $\sigma(\theta)$. The dispersion can be computed in terms of the correlation function of the angular displacement $C_\alpha(\theta)$,

$$\sigma^2(\theta) = 2(\langle \vec{\alpha}^2 \rangle - \langle \vec{\alpha}_1 \cdot \vec{\alpha}_2 \rangle) = 2(C_\alpha(0) - C_\alpha(\theta)). \quad (4.41)$$

The computation of $C_\alpha(\theta)$ is similar to that followed to obtain the correlation of the convergence in Section 4.6. One has that $\vec{\alpha} = \vec{\nabla}\Psi$, with Ψ given by Eq. (4.26), where the integral over χ has now to be performed up to χ_{rec} (the last scattering surface). This gives

$$C_\alpha(\theta) = \frac{9H_0^4\Omega_m^2}{c^4} \int_0^{\chi_{rec}} \frac{d\chi}{r^2(\chi_{rec})a^2(\chi)} \int \frac{dk}{2\pi k} P_\delta(k, \chi) J_0(k\theta r(\chi)). \quad (4.42)$$

The resulting variance $\sigma(\theta)$ depends on the cosmological model and can be computed using Eqs. (4.41) and (4.42) once the power spectrum is given.

For most models $\sigma(\theta)/\theta$ results less than 20% on scales larger than $1'$ and less than 5% on scales larger than 1° . Hence, the effects on the anisotropies will not be significant at angular scales around the degree and larger, but can become relevant at smaller scales. The effect of lensing on the power spectrum can be obtained from the Legendre transform of Eq. (4.40)

$$\tilde{C}_\ell = 2\pi \int_0^\pi d\theta \sin \theta \tilde{C}(\theta) P_\ell(\cos \theta). \quad (4.43)$$

The result is that lensing smoothes somewhat the sharp features in the angular power spectrum, but leaves the overall shape unchanged. This is exemplified in Figure 4.12, where the lensed and unlensed power spectra are displayed for standard cold dark matter ($\Omega_m, \Omega_\Lambda = (1, 0)$) and lambda cold dark matter ($\Omega_m, \Omega_\Lambda = (0.3, 0.7)$), computed with the CMBFAST code [Se96b]. It is apparent that the effect of lensing is smaller for smaller values of Ω_m .

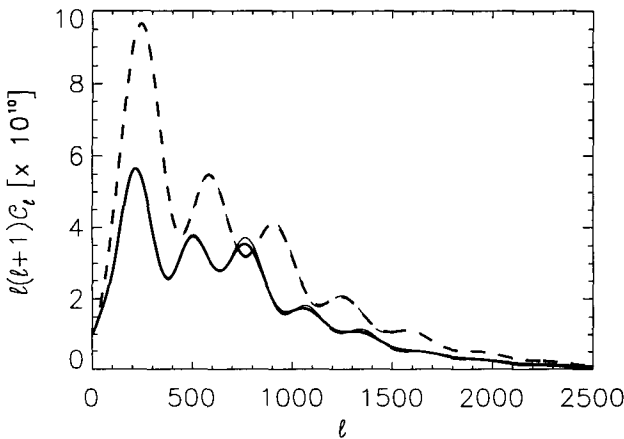


Fig. 4.12 Effect of gravitational lensing on the angular power spectrum for standard cold dark matter (solid line) and lambda cold dark matter (dashed lines). The thin lines correspond to the unlensed spectrum while the thick lines are for the lensed spectrum.

It has also been pointed out that lensing produces a transfer of power from lower to higher ℓ in the damping tail of the power spectrum. This leads to a power spectrum that falls less steeply with increasing ℓ , what could be used to distinguish otherwise degenerate model predictions [Me98].

Recommended reading

- R. D. Blandford and R. Narayan (1992) “Cosmological applications of gravitational lensing”, Annual Review of Astronomy and Astrophysics **30**, 311.
- B. Fort and Y. Mellier (1994), “Arc(let)s in clusters of galaxies”, The Astronomy and Astrophysics Review **5**, 239.
- Y. Mellier (1999) “Probing the Universe with weak lensing”, Annual Review of Astronomy and Astrophysics **37**, 127.
- M. Hattori, J. P. Kneib and N. Makino (1999), “Gravitational lensing in Cluster of Galaxies”, Progress of Theoretical Physics Supplement **133**, 1.
- M. Bartelmann and P. Schneider (2001), “Weak gravitational lensing”, Physics Reports **340**, 291.

This page is intentionally left blank

Chapter 5

Microlensing I: Basics

The gravitational lensing phenomena in which the multiple images of a source are unresolved, so that only an apparent brightness increase (and a tiny displacement of the light centroid) results, have become known under the name of microlensing. The origin of the name arose because the first observational search for this effects was in the context of the lensing of one of the images of a multiple imaged quasar by the individual stars belonging to the lensing galaxy, and the typical separation between the two images produced by the compact star in this case turns out to be of order *microarcsec*. On the other hand, the most active microlensing searches nowadays are those involving stars from our galaxy or nearby ones belonging to the Local Group of galaxies (in particular the Magellanic Clouds and the Andromeda galaxy), which are lensed by intervening stellar size dark objects. In this case the images are still unresolvable with present day telescopes, although the typical angular splittings are of order *milliarcsec* (see Eq. (3.9)).

The crucial fact which allows microlensing phenomena to be observed is that, due to the relative motion of the lens and the source, the amplification of the unresolved images is time dependent. The time dependence of a microlensing event should follow some very characteristic patterns, making possible the distinction between microlensed stars and just intrinsically variable stars (such as Cepheids), which constitute the main background for this kind of searches. Also, due to its gravitational origin the effect should be achromatic, looking the same at different wavelengths, and due to its small probability it should never repeat for the same star.

The main reason why microlensing searches in the Local Group gained

significant impetus in recent years was the realization [Pa86a] that by monitoring the light curves of several million stars in the LMC for a few years (something feasible with the advent of CCDs) it would be possible to establish whether the dark halo of our galaxy consists of compact dark objects such as dead stars, black holes, brown dwarfs or planets (generally named MACHOs, for Massive Astrophysical Compact Halo Objects). On the contrary, if the searches failed to find significant number of events, this would mean that the halo should consist of something of a more elusive nature, such as Weakly Interacting Massive Particles (WIMPS), for which the favored candidate would be the supersymmetric neutralino, or other elementary dark matter candidates such as the axions, or alternatively just cool ordinary baryonic gas clouds.

The microlensing searches towards the galactic bulge had also their own interest [Pa91; Gr91b], since the rates from known faint stellar populations were guaranteed to be significant (several hundred events have been observed by now) and they could also make possible the search for dark constituents near the galactic plane or around the central parts of the Galaxy. The large number of events observed in this direction also allows to study the more rare events which are produced by binary lenses and even to search for planetary systems at great distances from us.

Several groups undertook these kind of observations at the beginning of the nineties and significant advances have been done, although the final interpretation of the observations still remains uncertain and further results are hence eagerly awaited.

5.1 The Galaxy in brief

Before discussing the microlensing searches themselves it is useful to mention what are the main characteristics of the different stellar populations of the Galaxy, as well as the expected properties of the dark galactic halo.

5.1.1 *The thin and thick disks*

Most of the visible stars in our galaxy belong to a flat disk, usually assumed to be exponentially distributed in galactocentric cylindrical coordi-

nates (R, z)

$$\rho^D(R, z) = \rho_0^D \exp\left(-\frac{R - R_0}{h_R} - \frac{|z|}{h_z}\right), \quad (5.1)$$

with ρ_0^D the local disk density, $R_0 \simeq 8.5$ kpc the galactocentric distance, $h_R \simeq 3.5$ kpc the radial scale length and h_z is the scale height, which is ~ 100 pc for the young stars and gas, and ~ 325 pc for the older disk stars [Ba86b]. The disk has still significant amounts of gas, what gives rise to continued star formation and to the observed spiral pattern (which is actually not accounted for in the simplistic profile in Eq. (5.1)). The stars in the disk are relatively young and metal rich, they have small one-dimensional velocity dispersion ($\sigma^D \simeq 20$ km/s) and are supported by their rotation around the galactic center ($v_{rot}^D \simeq 220$ km/s).

In addition to this ‘thin’ disk, there is also a thicker disk [Gi83] with scale height $h_z \simeq 1$ kpc, with somewhat smaller rotation velocity ($v_{rot}^{TD} \simeq 180$ km/s) and higher velocity dispersion ($\sigma^{TD} \simeq 40$ km/s). Thick disk stars are more metal poor than typical thin disk stars and, although their origin is not definitively established yet, they are probably related to old disk stars which were ‘heated’ by the last big merger of a galactic satellite.

The visible thin disk local column density $\Sigma_0^D \equiv 2h_z\rho_0^D$ has been measured to be $\Sigma_0^D \simeq 40 M_\odot/\text{pc}^2$, with $\sim 13 M_\odot/\text{pc}^2$ in gas and the rest in luminous stars [Go96b]. The contribution from luminous stars to the thick disk column density is an order of magnitude smaller [Oj96]. On the other hand, studies of the vertical motion of stars [Ku91] imply that the total column density (disk + halo) within ± 1.1 kpc of the galactic plane is $\Sigma_0(|z| < 1.1 \text{ kpc}) = (71 \pm 6)M_\odot/\text{pc}^2$. Removing the halo contribution leads, for the disks alone, $\Sigma_0^{D+TD}(|z| < 1.1 \text{ kpc}) = (48 \pm 9)M_\odot/\text{pc}^2$, what leaves limited space for the presence of non-luminous matter in the disks.

5.1.2 Galactic spheroid and bulge

Another population of stars which is observed locally looking for high proper motion stars which cannot be bound to the disk, and also at large heights above the galactic plane, is the so-called spheroid (or stellar halo), made out of old metal poor stars formed in the first 1–2 Gyrs of the Galaxy’s life [Ca81; Ba83; Fr87]. These stars have an approximately spherical distribution with a radial profile $\rho^S \propto r^{-3.5}$ and have a large velocity dispersion ($\sigma^S \simeq 120$ km/s) with little rotation. The local density in luminous

spheroid stars has been estimated to be $\rho_0^S \simeq 10^{-4} M_\odot/\text{pc}^3$ [Go98b], and hence is almost three orders of magnitude smaller than the disk local density, although at heights of a few kpc from the galactic plane the spheroid is the dominant stellar component.

An important stellar population, known as the bulge, is present in the inner 2 kpc of the Galaxy. The oldest stars in the bulge are probably related to the central part of the spheroid, although there are also more metal rich stars from a different origin [va96]. Several studies, including infrared satellite observations [Dw95] and studies of gas motions [Bi91] have shown that the bulge is elongated, having the shape of a bar with its near side in the first quadrant. A model commonly adopted to describe its density distribution is [Dw95]

$$\rho^B(s) = \frac{M_0}{8\pi abc} \exp\left[-\frac{s^2}{2}\right], \quad (5.2)$$

where $s^4 \equiv [(x'/a)^2 + (y'/b)^2]^2 + (z'/c)^4$, with the primed axes being along the principal axes of the bar. These coordinates are related to the galactocentric coordinates in which x points opposite to the Sun's direction, y towards the direction of increasing longitudes and z towards the north galactic pole, by $x' = x \cos \alpha + y \sin \alpha$ and $y' = -x \sin \alpha + y \cos \alpha$, with $\alpha \simeq 20^\circ$ being the inclination of the major axis of the bar with respect to the line of sight. The scale lengths of this bar model are $a = 1.58$ kpc, $b = 0.62$ kpc and $c = 0.43$ kpc. The velocity dispersion of bulge stars along the principal axes of the bar has been estimated to be $\bar{\sigma} \simeq (116, 90, 79)$ km/s [Ha95]. The total mass of this bar is $M_{Bar} = 0.82M_0$, and dynamical estimates give $M_{Bar} \simeq 1-2 \times 10^{10} M_\odot$.

It is important to mention that the bulge density profile given here only aims to reproduce observations in the inner 2 kpc of the Galaxy, vanishing exponentially outside this region. There are also models of the Galaxy [Ca81] which fit the different dynamical observations and in which the bulge is related to the central part of the spheroid, eventually affected by a bar instability of the inner disk, and hence has the power-law decline $r^{-3.5}$ outside the central bulge region. These models predict that the ‘outer’ spheroid should be an order of magnitude more massive than what is inferred from the luminous observed spheroid stars. If this were the case there should be a dominant contribution to the spheroid density from stellar remnants such as faint white dwarfs, neutron stars or brown dwarfs, something of potential interest for microlensing searches.

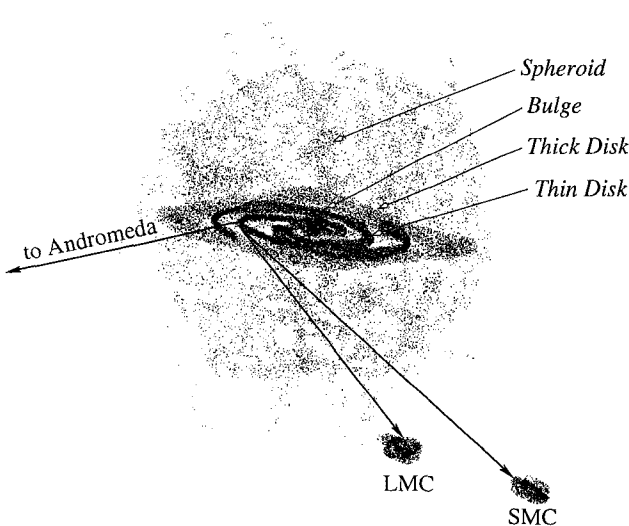


Fig. 5.1 Pictorial view of the different stellar populations in the Galaxy. Also illustrated are the Magellanic Clouds and the direction to the Andromeda galaxy. Their galactic longitude and latitude as measured from the Earth are $(\ell, b)_{LMC} = (281^\circ, -33^\circ)$, $(\ell, b)_{SMC} = (303^\circ, -44^\circ)$ and $(\ell, b)_{M31} = (121^\circ, -22^\circ)$. In addition to these stellar components there is the dark halo (not shown), extending well beyond the Magellanic Clouds.

The different stellar galactic populations are pictorially illustrated in Figure 5.1, together with the main targets of microlensing searches: the Large and Small Magellanic Clouds, (at ~ 50 and 65 kpc respectively), the bulge (at ~ 8.5 kpc from us) and the Andromeda galaxy (at ~ 725 kpc). Notice that since the bulge is obscured by significant amounts of gas, optical observations have to be performed only in some clear windows, such as Baade's Window.

5.1.3 *The dark halo*

Besides the stellar components discussed previously, there are many indications that the mass of the Galaxy is dominated by an extended, in first approximation spherical, distribution of dark matter [Fi91]. This evidence comes for instance from the measured rotation curves in spiral galaxies, which remain flat well beyond the region where the luminous matter is present, or from the motion of satellite galaxies in the Local Group. The

flatness of the rotation curve of the Galaxy, with $v_c \simeq 220$ km/s, implies that the halo density should vary as $\rho^H \propto r^{-2}$, and hence a simple parameterization used for it is

$$\rho^H(r) = \rho_0^H \frac{R_0^2 + r_c^2}{r^2 + r_c^2}, \quad (5.3)$$

where r_c is the halo core radius, typically a few kpc. The local halo density is $\rho_0^H \simeq 10^{-2} M_\odot/\text{pc}^3$. The velocity dispersion of halo objects is usually adopted as constant and isotropic (i.e. an isothermal sphere) with $\sigma^H = v_c/\sqrt{2} \simeq 155$ km/s. Clearly the density profile in Eq. (5.3) has to be truncated at some large radius since otherwise the total mass would be divergent.

No stellar population has been observed with the distribution and kinematical properties of the halo objects, and hence this component should be essentially dark. Since the dark halo provides the dominant contribution to the overall mass of the Galaxy, the fact that the nature of its constituents is unknown represents a fundamental problem, and the clarification of this is still one of the main challenges for the microlensing searches.

A crucial question regards whether the haloes are baryonic or non-baryonic. Since the overall contribution to the density of the Universe of luminous matter has been estimated to be less than one percent of the critical density ($\Omega_{lum} \simeq 0.007$), while the baryon density inferred from the theory of primordial nucleosynthesis in order to get agreement with the observed abundances of light elements (such as Deuterium and Lithium) corresponds to $\Omega_b \simeq 0.04(h/0.7)^{-2}$, it is clear that a sizeable fraction of the baryons in the Universe should be non-luminous. These dark baryons could be as cold gas clouds or instead in the form of compact objects (MACHOs), and if the halo were made of the later, microlensing would be the ideal tool to search for them. On the other hand the dark haloes could also be non-baryonic (e.g. made out of WIMPS), and actually the favored cosmological model at present [Tu01] requires that the matter density of the Universe be an order of magnitude larger than what is believed to be present in the form of baryons ($\Omega_m \simeq 0.3$, a result supported in particular by the macrolensing observations discussed in the previous Chapter). This matter should naturally fall in the galactic potential wells, actually having a crucial role in the process of galaxy formation itself, and the natural place to find it would then be in the galactic haloes. Hence, the failure to find MACHOs with microlensing would just strengthen the case for non-baryonic dark haloes.

5.2 Basic microlensing theoretical tools

5.2.1 The light curve

As was shown in Section 3.3, when a compact object lenses a background star it leads to the formation of two images, and the total magnification of the light from the source results

$$A = \frac{u^2 + 2}{u\sqrt{u^2 + 4}}, \quad (5.4)$$

where $u \equiv \beta/\theta_E$ is the angular separation between the lens and the source measured in units of the Einstein angle of the lens. Assuming that the lens moves with constant velocity with respect to the line of sight (l.o.s.) during the duration of the microlensing event, one has

$$u^2(t) = \frac{b^2 + [v^\perp(t - t_0)]^2}{r_E^2} \equiv u_0^2 + \left[\frac{(t - t_0)}{t_E} \right]^2, \quad (5.5)$$

where b is the minimum distance between the lens trajectory and the l.o.s. to the star, the Einstein radius $r_E \equiv \theta_E D_{OL}$ is the distance subtended by θ_E in the lens plane, $u_0 \equiv b/r_E$ is the normalized impact parameter, t_0 is the time of closest approach ($u(t_0) = u_0$) and v^\perp is the component of the lens velocity relative to the l.o.s. in the direction perpendicular to this same line. The characteristic time

$$t_E \equiv \frac{r_E}{v^\perp}, \quad (5.6)$$

is usually adopted as the definition of the event duration*, and corresponds to the time it takes to the lens to cross an Einstein radius. Numerically one has

$$t_E = 39 \text{ days} \left(\frac{200 \text{ km/s}}{v^\perp} \right) \sqrt{\frac{D_{OS}}{10 \text{ kpc}}} \frac{m}{M_\odot} 4x(1-x), \quad (5.7)$$

where we introduced $x \equiv D_{OL}/D_{OS}$ as the normalized distance to the lens in units of the distance to the source.

Combining the expression for $u(t)$ with Eq. (5.4) leads to a time dependent amplification of the luminosity of the source described by a very characteristic light curve, plotted in Figure 5.2 for $u_0 = 1, 0.5, 0.2$ and 0 .

*The MACHO group uses instead the Einstein's diameter crossing time $\hat{t} \equiv 2t_E$ in their analyses.

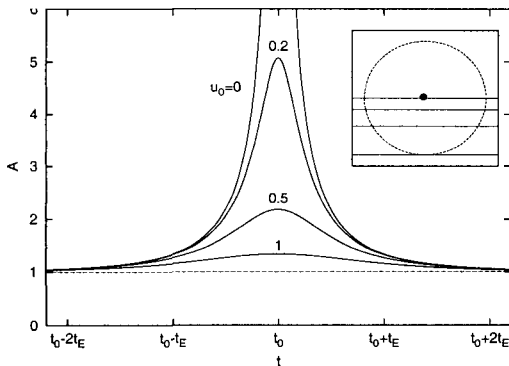


Fig. 5.2 Light curves, i.e. time evolution of the light amplification, for different values of the normalized impact parameter u_0 . The insert shows the different source trajectories with respect to the lens position (the central dot), with the circle having a radius r_E .

The amplification reaches its maximum value A_{max} at the time t_0 as $u(t)$ approaches u_0 . In particular, we have $A_{max} = 3/\sqrt{5} \simeq 1.34$ for $u_0 = 1$, and A_{max} diverges (in the point-like source approximation considered in this Chapter) for $u_0 \rightarrow 0$. The curves are, of course, symmetric about t_0 .

The event duration t_E is determined, together with u_0 (or equivalently A_{max}) and t_0 , by fitting the theoretical light-curve to the observed star luminosities plotted as a function of time. There is clearly no useful information contained in t_0 , and the distribution of A_{max} values for different microlensing events tests only the expected uniform distribution of impact parameters b . The interesting information lies then in the event duration distribution and in the rates of microlensing events. However, these observables depend in a convoluted way on the lens and source spatial distributions and motions, as well as on the lens mass function, so that it is actually quite hard to extract clean information about the lens properties from these measurements alone, and this can only be done in a statistical way rather than on an event basis.

In the next Chapter we will discuss how for some particular events involving finite source size effects, the measurement of parallax, or an astrometric measurement of the image centroid shift, it is possible to get additional information about the lens. This information will be crucial to identify the lensing populations and to ultimately measure their mass function.

5.2.2 Optical depth

A quantity which turns out to be useful in the discussion of microlensing is the optical depth τ [Vi83], which is defined as the probability that at a given time a source star is being microlensed with an amplification larger than 1.34, i.e. having $u_0 < 1$. This quantity is then just the probability to find a lens inside the so-called ‘microlensing tube’, i.e. a tube around the l.o.s. to the source of radius equal to the Einstein radius of the lens r_E , and hence is given by

$$\begin{aligned}\tau(D_{OS}) &= \int_0^{D_{OS}} dD_{OL} \int_0^{\infty} dm \frac{dn_L}{dm} \pi r_E^2 \\ &= \frac{4\pi G D_{OS}^2}{c^2} \int_0^1 dx x(1-x) \rho_L(x).\end{aligned}\quad (5.8)$$

The mass function of the lenses dn_L/dm describes the distribution of lens masses, and it is related to the lens mass density through

$$\rho_L = \int_0^{\infty} dm m \frac{dn_L}{dm}.\quad (5.9)$$

Notice that the optical depth turns out to be independent of the assumed lens mass distribution, depending only on the total density ρ_L . This is so because lighter lenses imply smaller Einstein radii but also, for a given mass density, larger number densities, and these two effects actually cancel each other in the expression for τ .

When performing observations in a given direction, one may have to take into account, especially for observations towards the bulge of the Galaxy, that the sources can be distributed with a non-negligible spread along the l.o.s.. In this case, one has to perform an average over the source distribution [Ki94] to obtain the actual optical depth

$$\tau = \frac{1}{N_S} \int dD_{OS} \frac{dn_S}{dD_{OS}} \tau(D_{OS}),\quad (5.10)$$

where the normalization factor is $N_S = \int dD_{OS} dn_S / dD_{OS}$ and dn_S/dD_{OS} describes the number density profile of detectable sources along the l.o.s.. For observations towards the bulge, it can be parameterized as $dn_S/dD_{OS} \propto \rho_S D_{OS}^{2-2\beta}$. The factor D_{OS}^2 is due to the change of the volume element with distance. The parameter β arises because the observations are magnitude

limited and the fraction of sources with luminosities larger than L is assumed to scale as $L^{-\beta}$. This implies that the fraction of stars which remain detectable behave as $D_{OS}^{-2\beta}$. Hence,

$$\tau = \frac{\int dD_{OS} D_{OS}^{2(1-\beta)} \rho_S \tau(D_{OS})}{\int dD_{OS} D_{OS}^{2(1-\beta)} \rho_S}. \quad (5.11)$$

A reasonable range for β has been estimated to be $\beta = 1 \pm 0.5$ in Baade's Window [Zh95], so that $\beta = 1$ is usually adopted in the discussion of microlensing in the bulge, although if one restricts to bright sources which are always above threshold, such as the red clump stars, $\beta = 0$ is appropriate.

The typical values of the optical depth for microlensing of stars in different targets in the Local Group are quite small. For instance, assuming that the halo wholly consists of compact objects, one has for sources in the LMC that $\tau \simeq 5 \times 10^{-7}$, and this is why millions of stars need to be monitored to search for microlensing. This very small lensing probability also implies that microlensing should essentially never repeat for the same star.

5.2.3 Event duration distribution

Due to its simplicity and the property of being independent of the lens motion and mass distribution, the optical depth is often used in the discussions of microlensing observations. However, since the experiments measure the number of events and their durations, there is more information contained in the microlensing rate, and in particular in its distribution as a function of the event durations.

To obtain the event duration distribution, one starts from the expression for the differential rate in terms of the variables depicted in Figure 5.3. The rate of events with amplification above the threshold value, i.e. with $A_{max} > 1.34$, is the flux of lenses across the microlensing tube [Gr91a]. One then has

$$\frac{d\Gamma}{dm} = \frac{dn_L}{dm} v^\perp \cos \omega f(v^\perp) d^2 v^\perp dS, \quad (5.12)$$

where $dS = r_E da dD_{OL}$ is a surface element of the microlensing tube, ω is the angle between the normal to the surface element and the lens relative velocity vector v^\perp (orthogonal to the l.o.s.). The function f in Eq. (5.12) describes the distribution of relative velocities. Due to the motion

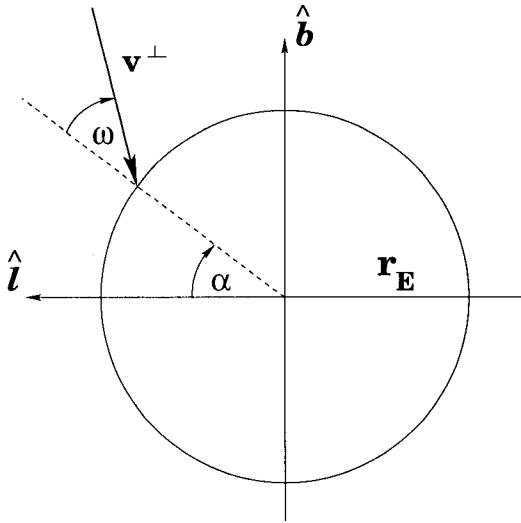


Fig. 5.3 Microlensing tube section in a plane orthogonal to the l.o.s. to the star. The tube radius is r_E , and we show the angular variables entering the computation of the flux of lenses (moving with relative velocity v^\perp in this plane) through this tube.

of the observer and the source, with velocities \mathbf{v}_O and \mathbf{v}_S respectively, the microlensing tube will be moving with a speed

$$\mathbf{v}_t = x\mathbf{v}_S + (1-x)\mathbf{v}_O. \quad (5.13)$$

If \mathbf{v}_L is the lens velocity in the same reference frame, the lens relative velocity with respect to the microlensing tube is

$$\mathbf{v} = \mathbf{v}_L - \mathbf{v}_t. \quad (5.14)$$

It is convenient to decompose all velocities as $\mathbf{V} = \mathbf{V}_{bulk} + \mathbf{V}_{dis}$, where \mathbf{V}_{bulk} accounts for a bulk global motion[†] and \mathbf{V}_{dis} is the component that will be assumed to be Gaussian distributed with the characteristic velocity dispersion of the lens/source population considered. From the previous expressions one then has

$$\mathbf{v}_{bulk} = \mathbf{v}_{L,bulk} - x\mathbf{v}_{S,bulk} - (1-x)\mathbf{v}_O$$

[†]The bulk motion of the Sun is $\mathbf{v}_\odot = (9, 231, 16)$ km/s (in the (x, y, z) coordinate system introduced after Eq. (5.2)). The LMC bulk motion $\mathbf{v}_{LMC} = (53, -160, 162)$ km/s [Gr91a]. For the disk lensing populations there is a bulk rotational motion while halo and spheroid populations are not expected to have significant bulk motions.

$$\mathbf{v}_{dis} = \mathbf{v}_{L,dis} - x\mathbf{v}_{S,dis}. \quad (5.15)$$

The orthogonal component of \mathbf{v} can be projected onto axes along the directions of increasing longitudes, $\hat{\ell}$, and latitudes, \hat{b} , i.e. $\mathbf{v}^\perp = v^\ell \hat{\ell} + v^b \hat{b}$. The velocity distribution function can then be obtained from the assumed Gaussian distribution $G(v_{dis}^i)$ of the dispersive components ($i = \ell, b$)

$$G(v_{dis}^i) = \frac{1}{\sqrt{2\pi}\sigma^i} \exp\left[-\frac{(v_{dis}^i)^2}{2(\sigma^i)^2}\right], \quad (5.16)$$

where σ^i are the corresponding velocity dispersions. If both lenses and sources have non-vanishing dispersions, σ_L^i and σ_S^i respectively, the relative velocity dispersion is just the quadratic sum (see Eq. (5.15))

$$\sigma^i = \sqrt{(\sigma_L^i)^2 + (x\sigma_S^i)^2}. \quad (5.17)$$

In terms of the modulus of the orthogonal relative velocity v^\perp , which is the quantity related to the event duration $t_E = r_E/v^\perp$, one can write (see Figure 5.3)

$$\begin{aligned} v_{dis}^\ell &= -v_{bulk}^\ell - v^\perp \cos \gamma \\ v_{dis}^b &= -v_{bulk}^b - v^\perp \sin \gamma, \end{aligned} \quad (5.18)$$

where $\gamma \equiv \omega + \alpha$. We can now substitute in Eq. (5.12)

$$f(\mathbf{v}^\perp) d^2\mathbf{v}^\perp = G(v_{dis}^\ell)G(v_{dis}^b) dv_{dis}^\ell dv_{dis}^b, \quad (5.19)$$

and use that $d^2\mathbf{v}^\perp = v^\perp dv^\perp d\omega$, to end up with

$$\frac{d\Gamma}{dm} = \frac{dn_L}{dm} r_E v^{\perp 2} \cos \omega G(v_{dis}^\ell)G(v_{dis}^b) dv^\perp d\omega d\gamma dD_{OL}. \quad (5.20)$$

The integral in $\omega \in [-\pi/2, \pi/2]$ (only lenses entering the microlensing tube) is now trivial. The distribution in terms of the event duration is then

$$\frac{d\Gamma}{dt_E dm} = 2 \int_0^{2\pi} d\gamma \int_0^{D_{OL}} dD_{OL} \frac{dn_L}{dm} \left(\frac{r_E}{t_E}\right)^4 G(v_{dis}^\ell)G(v_{dis}^b). \quad (5.21)$$

This expression for the differential rate is quite general, including an arbitrary lens mass function, the effect of bulk velocities of observer, lens and source as well as the (eventually anisotropic) velocity dispersions of lenses and sources. In order to apply it to a particular observational case, one needs just to construct the appropriate $G(v_{dis}^i)$ using Eqs. (5.16), (5.17)

and (5.18), with the replacement $v^\perp = r_E/t_E$. The source velocity dispersion is important for bulge observations or for LMC self-lensing, but can be neglected for LMC stars lensed by galactic objects. In this last case, a further integral can be performed analytically if the lens dispersion is isotropic. The effect of the bulk motions is small for lensing of LMC stars by halo objects, but becomes important when considering the rotating disk populations or for the discussion of bulge observations. Finally, if the spread in source distances is non-negligible, an average over the source locations similar to the one in Eq. (5.11) should also be performed.

The ultimate goal of microlensing observations is the determination of the lens mass function $dn_L(x)/dm$, about which very little is known a priori. A common assumption regarding its spatial dependence is the so-called factorization hypothesis, i.e. that the mass function only changes with position by an overall normalization

$$\frac{dn_L(x)}{dm} = \frac{\rho_L(x)}{\rho_0} \frac{dn_0}{dm}, \quad (5.22)$$

where the subscript 0 stands for the local value of the lens densities. It is also useful as a first step to discuss microlensing predictions under the simplifying assumption of having a common lens mass M , so that

$$\frac{dn_L}{dm} = \frac{\rho_L}{m} \delta(m - M). \quad (5.23)$$

In this case, one has

$$\frac{d\Gamma}{dt_E} = \frac{2}{M} \int_0^{2\pi} d\gamma \int_0^{D_{OL}} dD_{OL} \rho_L(D_{OL}) v^{\perp 4} G(v_{dis}^\ell) G(v_{dis}^b). \quad (5.24)$$

Since t_E only enters in this equation through $v^\perp \propto \sqrt{M}/t_E$, it is easy to see that the differential rate distributions for two lens models with masses M_1 and M_2 are related through

$$\frac{d\Gamma}{dt_E}(t_{E1}, M_1) = \frac{M_2}{M_1} \frac{d\Gamma}{dt_E}(t_{E2} = t_{E1}\sqrt{M_2/M_1}, M_2). \quad (5.25)$$

This implies that the total ‘theoretical’ rate

$$\Gamma_{th} = \int_0^\infty dt_E \frac{d\Gamma}{dt_E} \quad (5.26)$$

scales with the assumed lens mass as

$$\Gamma_{th} \propto 1/\sqrt{M}. \quad (5.27)$$

Similarly, the average event duration is

$$\langle t_E \rangle_{th} = \int_0^\infty dt_E t_E \frac{d\Gamma}{dt_E}, \quad (5.28)$$

and there is a useful relation expressing the fact that the probability of microlensing τ is just proportional to the total rate times the average event duration, which is

$$\Gamma_{th} = \frac{2}{\pi} \frac{\tau}{\langle t_E \rangle_{th}}, \quad (5.29)$$

with the geometrical factor $2/\pi$ being related to the particular definition of event duration adopted[‡].

From this relation it is also clear that, in the case in which the lenses are assumed to have a common mass M , the average event duration scales with M as

$$\langle t_E \rangle_{th} \propto \sqrt{M}, \quad (5.30)$$

just due to the fact that the associated Einstein radii scale as \sqrt{M} .

The event rate distribution for observations towards the LMC is plotted in Figure 5.4 assuming that the whole halo density consists of compact objects and for two different values of the lens mass, $M = 0.1$ and $1 M_\odot$. The behavior just discussed is apparent. Also notice that the distributions have power-law (and not exponential) tails [Ma96], with $d\Gamma/dt_E \propto t_E^{-4}$ for large event durations and $\propto t_E^2$ for small durations. The long event durations correspond to lenses moving almost parallel to the l.o.s. (i.e. with small v^\perp although not necessarily small v), while the short duration event tail corresponds to lenses close to the observer or to the source, where the Einstein radius of the lens is small ($r_E \propto \sqrt{D_{OL} D_{LS}}$).

In order to actually predict the total event rate for a given experiment, one has to take into account that the observational efficiencies are generally smaller than unity and, moreover, that they are a function of the event

[‡]One has $\tau = \Gamma_{th} \langle t_{ev} \rangle$, where $\langle t_{ev} \rangle$ is the average time during which $A > 1.34$. Since t_E is the time it takes for the lens to move a distance r_E orthogonally to the l.o.s., one has, for a given event, $t_{ev} = 2t_E \sqrt{1 - u_0^2}$. Making the average with a uniform u_0 distribution leads to Eq. (5.29).

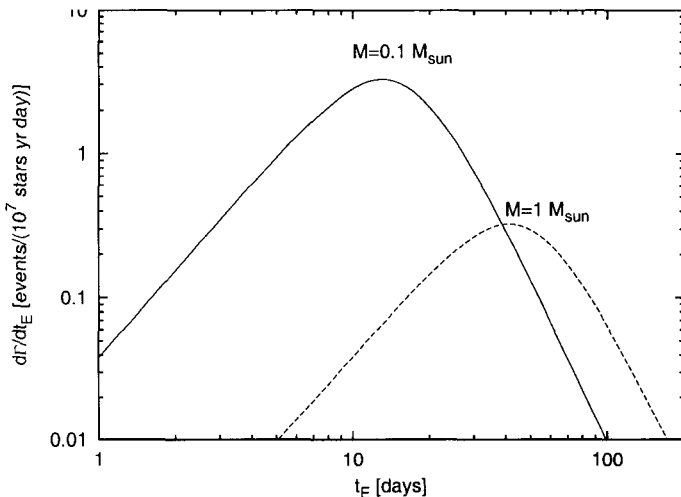


Fig. 5.4 Differential rate distribution for LMC stars lensed by a standard halo population consisting of objects with a common mass of $M = 0.1M_\odot$ (solid line) and $M = 1M_\odot$ (dashed line).

duration, mainly due to the poor sampling of the short duration events and the incomplete coverage of the very long duration ones. Hence, the predicted total rate for a given experiment is a convolution of the differential rate with the experimental efficiency $\epsilon(t_E)$, i.e.

$$\Gamma = \int_0^\infty dt_E \epsilon(t_E) \frac{d\Gamma}{dt_E}. \quad (5.31)$$

The efficiency $\epsilon(t_E)$ actually also takes into account the fact that the observational threshold could be different from $A_{max} > 1.34$. In the same way, one may define the expected time moments

$$\langle t_E^n \rangle = \frac{1}{\Gamma} \int_0^\infty dt_E \epsilon(t_E) \frac{d\Gamma}{dt_E} t_E^n, \quad (5.32)$$

where $n = 1$ gives just the average event duration $\langle t_E \rangle$ and the dispersion of event durations can be characterized by $\Delta t_E \equiv \sqrt{\langle t_E^2 \rangle - \langle t_E \rangle^2}$ (notice that for $\epsilon = 1$ the higher moments with $n > 2$ are all divergent) [de91; de95]. Clearly the more spreaded is the mass function (rather than being a delta function), the larger will be Δt_E , and the same trend is expected if different lensing populations contribute simultaneously to the rates. On the other hand, the dispersions could be reduced if the lens motions are

dominated by a bulk motion, e.g. if they belong to a rotating disk, since in this case the spread in values of v^\perp is reduced.

One may go beyond the approximation in which the lenses have a unique common mass by for instance parameterizing the mass function as a power law within a certain mass range, and the parameters involved may then be fitted through a comparison with the observed event rate distribution. However, for this to be meaningful the kinematics of the underlying lensing distribution has to be known (and hence one has to be confident about the correct identification of the lensing population). Moreover, a significant number of events (more than 10^2) would be required in order to be able to learn something more than just the average mass of the lenses from these studies.

5.3 Microlensing of unresolved sources

The classical way to search for microlensing consists in the study of the light curves of ‘individual’ stars, which are followed employing the traditional photometric technique. Since the microlensing of a star is a very unlikely event, in order to observe this phenomenon at a non-negligible rate one needs to monitor the largest possible number of stars, and hence searches have been performed towards dense stellar fields like the bulge or the Magellanic Clouds. However, due to the effect of seeing, there is a limiting magnitude, which is set by the crowding limit, in order that the source stars could be resolved. Hence, the maximum number of sources which can be followed is constrained by this limiting magnitude.

To extend the microlensing searches to targets farther away, like the Andromeda galaxy (M31) which is some ~ 725 kpc from us, a different approach had to be devised since in this case the stellar fields are very crowded and the sources cannot be individually resolved. The idea proposed by Crotts [Cr92] and Baillon et al. [Ba93] consists in monitoring the flux of light received by every CCD pixel in the picture of a galaxy, rather than looking just to the flux from the individual stars. This makes possible the detection of the amplification due to the lensing of one of the many stars contributing to the flux received by the pixels. The number of monitored stars is then greatly enhanced with this method (e.g. by three orders of magnitude when going from the LMC to M31). However, since each of the unresolved stars contributes only a small fraction of the light reaching a

pixel, the microlensing events will be harder to detect, so that only lensing of bright stars or very high magnifications of faint stars will be observable.

The basic idea of the method [Go96a] is that if a star of flux F_* is lensed in a crowded field, by subtracting from the actual images a reference one (obtained for instance by averaging several images of the same field taken under optimal seeing conditions), one should just get a stellar image with flux equal to $\Delta F \equiv (A - 1)F_*$ on top of the photon noise. Hence, for a desired signal to noise ratio, there will be a minimum amplification, which depends on F_* , for the event to be observable, with fainter stars requiring to be more magnified.

There are of course sources of fluctuations which have to be controlled for a successful observation. These include limited precision in the telescope pointing (requiring a geometric realignment of the different images), changes in the background sky light and the transparency of the atmosphere (requiring a photometric realignment of the images) and last but not least, to take into account that the images are taken under different seeing conditions. The seeing conditions determine the point spread function (PSF), which characterizes the extent of the stellar images, and if a change in the PSF is not properly taken into account it can generate a spurious variability in the difference image.

A simple strategy to deal with seeing variations is to analyze the light reaching superpixels, i.e. groups of neighboring pixels chosen in a number so as to approximately match the size of the PSF under bad seeing conditions, since this minimizes seeing variations. This is the approach pioneered by the AGAPE group [An97]. The other solution is to make the convolution of the reference image with the PSF corresponding to the actual seeing conditions of each image, so as to match the PSFs of the images to be subtracted, as advocated by the VATT/Columbia Collaboration [To96]. An optimization of this convolution procedure was developed in Refs. [Al98; Al00a]. This technique is now generally known as difference image analysis (DIA), and using it the fluctuations can be reduced essentially down to the photon noise level.

Pixel lensing is being applied by the groups searching for microlensing in M31 (POINT-AGAPE using superpixels [Ke01] and MEGA using the DIA technique [Cr00]). These collaborations have already seen some microlensing events and are expected to obtain a significant number of them in a few years. These searches are sensitive to compact dark objects belonging to Andromeda itself besides those from our galaxy. The interest

of these observations lies in that it is possible to explore many different lines of sight towards Andromeda and, since the disk of this galaxy is quite inclined with respect to the line of sight, looking at the rates on the far side of M31 and comparing them with those from the near side provides an important signature to identify the lensing population.

The DIA technique has also been applied to microlensing events which had been previously studied with the traditional photometric analyses, with the result that twice as many events could be identified employing this technique. This was possible thanks to the improved quality of the DIA data and also because sources fainter than the limiting magnitude of the survey become observable when lensed, due to an ‘amplification bias’ effect [Ne94b]. These magnified faint sources would go unnoticed in a traditional photometric search but are detected with the DIA technique, so that this last has now become the standard tool for microlensing studies.

The pixel lensing light curves retain many of the features of the classical microlensing light curves, such as their symmetric shapes (for non-binary lenses), their non-repetitive nature and their achromaticity, since

$$\frac{[\Delta F(t)]_{red}}{[\Delta F(t)]_{blue}} = \frac{[F_*]_{red}}{[F_*]_{blue}}. \quad (5.33)$$

An important problem with the pixel lensing technique is that due to the fact that the baseline flux of the lensed star F_* is unknown, there is a large degeneracy in fitting the lens parameters. In particular, since for crowded fields the required magnifications are large, in this limit one has $A \simeq u^{-1}$ and hence

$$\Delta F(t) \simeq \frac{F_*}{\sqrt{u_0^2 + \left[\frac{t-t_0}{t_E} \right]^2}} \simeq \frac{A_{max} F_*}{\sqrt{1 + \left(\frac{A_{max}}{t_E} \right)^2 (t - t_0)^2}}, \quad A_{max} \gg 1. \quad (5.34)$$

It is then clear that the light curve will remain the same under the changes $F_* \rightarrow F_*/\xi$, $A_{max} \rightarrow \xi A_{max}$ and $t_E \rightarrow \xi t_E$. Hence, without knowing the baseline flux there is an indeterminacy between the lensing due to a bright star magnified by a lens with a certain mass or that of a fainter star which is more magnified by a heavier lens, since both cases can give rise to similar light curves [Wo97]. This also implies that if one neglects the effect of source blending in the traditional microlensing searches, i.e. one overestimates the baseline fluxes, one is underestimating the event durations, and hence also the inferred lens masses ($m \propto t_E^2$). This would introduce a bi-

asing in the reconstruction of the lens mass function towards lower masses. The impossibility to accurately determine the event duration t_E with pixel lensing in very crowded fields requires also a new approach to estimate the optical depth from the observations [Go99a].

In order to deal with the blending problem in ‘classical’ microlensing, one may fit the traditional light curves with an extra parameter allowing for blending, but this parameter can be usefully determined only in special cases, such as for binary lenses. If the two blended sources are significantly displaced among each other, it may be possible to astrometrically detect the movement of the image centroid during the lensing event and hence determine the blending [Go98a]. Alternatively, knowing the source luminosity function the blending effects could be corrected statistically on the event sample. Finally, one may use color information during the microlensing event to identify the amount of blending [Bu96; Ha97a].

Some of the potential applications of the DIA technique include also the massive search of very high magnification events looking at the whole region of the bulge with poor angular resolution [Go98a] or to a smaller region with high sampling rate [Bo01a], or the search for binary events in faraway galaxies like M31 or M87, taking profit of the fact that the fraction of binary events with respect to the single lens events which can be detected with pixel lensing searches is enhanced due to the large magnifications achieved in caustic crossing events [Ba01] (see next Chapter).

5.4 Observational searches of microlensing

Since the beginning of the nineties, several groups initiated the search for microlensing signals looking to stars in the Magellanic Clouds (EROS and MACHO) and the galactic bulge (MACHO, OGLE and DUO). More recently these searches have also been extended towards the Andromeda galaxy, in the direction of several spiral arm directions and towards globular clusters. Furthermore, collaborations among several telescopes around the Earth have been established to form networks to study in detail the events which are observed in real time by the major teams and are then immediately alerted to the microlensing community for follow-up. Table 5.1 summarizes the different Collaborations involved in these studies, their main targets, the event statistics gathered (circa mid 2001) as well as their run-

<i>Experiment</i>	<i>Target</i>	<i>Events</i>	<i>Years</i>
MACHO	Bulge	~ 350	92–99
	LMC	~ 25	
	SMC	2	
OGLE I	Bulge	20	92–95
	OGLE II	~ 520	97–00
	LMC	1	
	SMC	1	
OGLE III			01–
EROS I	LMC	1	91–95
	EROS II	4	97–
		1	
	Bulge		
	Spiral arms	~ 7	
DUO	Bulge	13	94–94
MOA	Bulge	20	00–
<i>Follow up networks</i>			
PLANET, MPS, GMAN, MOA			
<i>Andromeda searches</i>			
AGAPE	M31	2	94–99
	M31	11	94–99
VATT/Columbia	M31	1	99–
	M31		99–
POINT-AGAPE			
MEGA			

Table 5.1 Main experiments looking for microlensing, their targets and the approximate number of events observed in the different directions, as well as their running periods.

ning periods.

5.4.1 *Searches towards the Magellanic Clouds*

The basic reason to look for microlensing towards the Magellanic Clouds has been to establish whether the galactic halo consists of compact objects [Pa96]. Several events have actually been observed, but the results are still affected by poor statistics (~ 20 events analyzed so far) since the rates have been significantly smaller than those expected from a halo wholly consisting of lenses. This allowed to constrain the contribution to the halo density from compact objects in the mass range between $10^{-7} M_{\odot}$ and $30 M_{\odot}$, as

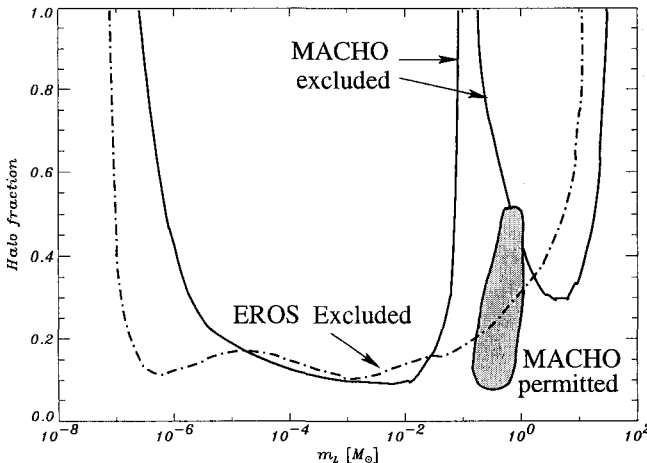


Fig. 5.5 Bounds on the fraction of a ‘standard’ halo as a function of the assumed lens mass from searches towards the LMC. The grey region is the one suggested to account for the events observed by the MACHO Collaboration (for references see text).

is shown in Figure 5.5. This Figure depicts the constraints on the fraction of a ‘standard’ halo (adopting $\rho_0^H \simeq 7.9 \times 10^{-3} M_\odot/\text{pc}^3$) which can be in the form of compact objects, for different assumed common lens masses.

The low mass range ($m < 10^{-2} M_\odot$) was constrained by searching for short duration events with $t_E <$ few days [Al96; Re98], while the large masses ($m > 1 M_\odot$) by the non-observation of very long events [Al01c]. The events actually observed have typical durations of $t_E \sim 2$ weeks to 4 months, pointing towards the existence of lenses with masses in the ballpark of 0.1 to $1 M_\odot$. The optical depth reported by the MACHO Collaboration from their 13 event sample towards the LMC is [Al00c]

$$\tau_{LMC}^{MACHO} = 1.1_{-0.3}^{+0.4} \times 10^{-7} \quad (13 \text{ events}). \quad (5.35)$$

These results are usually presented by stating that $\sim 20\%$ of a standard halo could be due to lenses in the mass range $0.1-1 M_\odot$, as is shown in the dashed region in Figure 5.5. The EROS Collaboration, having observed 5 events towards the LMC [La00], reports only an upper-bound on the halo contribution from compact lenses, which is depicted in Figure 5.5 and which excludes the upper part of the MACHO allowed region.

The final interpretation of the observed events is complicated by the

fact that the statistics is low and also because the known stellar populations should be contributing some (or possibly all?) background events.

One important background is that of self-lensing by LMC stars. It was even suggested after the first LMC results were obtained that the bulk of the LMC events could be due to stars belonging to the LMC central bar [Sa94], whose contribution to the optical depth was estimated to be $\tau \simeq 5 \times 10^{-8}$. However several events are found outside the bar, where the optical depth for self-lensing by the LMC disk stars is much smaller. Realistic estimates of the average optical depth for lensing due to the known stellar LMC populations suggest a value $\tau_{LMC}^{stars} \simeq 2.4 \times 10^{-8}$ [Gy00]. The LMC self-lensing, although below the reported value in Eq. (5.35), is still significant, and this implies that for the accumulated statistics some of the observed events should actually arise from it. Moreover, as will be discussed in the next Chapter, for some events (being of very long duration or involving binary lenses) it is possible to infer the location of the lenses. This was the case for one of the LMC events and for the two events observed towards the SMC, and in all three cases the interpretation that the lenses belonged to the Magellanic Clouds was favored. In the case of the SMC, it is actually expected that the self-lensing rate be enhanced, since this galaxy has a cigar shape and is elongated along the l.o.s..

If the dark halo of the LMC were composed of compact objects, it would contribute an additional $\tau \simeq 10^{-7}$ to the optical depth [Go93; Wu94], which added to the galactic halo expectations ($\tau^H \simeq 5 \times 10^{-7}$) will further increase the discrepancy with observations. Although the LMC halo contribution alone is of the order of the observed depth, there is no stellar population known with the spatial distribution and kinematics expected for LMC halo constituents, and it would be unnatural that the LMC halo wholly consists of dark compact objects, with at the same time the halo of our galaxy having a negligible amount of them.

The stars in the thin disk of our galaxy are on the other hand very inefficient lenses, due to their proximity to the observation point. Indeed, the optical depth towards the LMC associated to an exponential galactic disk is just

$$\tau_{LMC}^D \simeq 10^{-8} \left(\frac{\Sigma_0}{30 M_\odot/\text{pc}^2} \right) \left(\frac{h_z}{300 \text{ pc}} \right). \quad (5.36)$$

Hence, the known thin disk stars contribute $\tau < 10^{-8}$ (taking into account that a significant amount of them would be too bright to not be directly

detected).

A thick disk population would be more efficient to lens LMC stars [Go94c], due to its larger associated scale height, and although the contribution from the observed thick disk stars is small, a larger thick disk column density ($\Sigma \leq 30 M_\odot/\text{pc}^2$) is dynamically allowed and could add a sizeable contribution to the LMC rates.

The known spheroid stars also give a contribution much smaller than the observed depth, with

$$\tau_{LMC}^S \simeq 0.3 \left(\frac{\rho_0^S}{10^{-4} M_\odot/\text{pc}^3} \right) \times 10^{-8}, \quad (5.37)$$

but if a dominant fraction of its constituents were stellar remnants, with a total density closer to the one obtained in some dynamical galactic models ($\rho_0^S \simeq 10^{-3} M_\odot/\text{pc}^3$ [Ca81]), its contribution could be sizeable [Gi94]. Hence, either a ‘heavy’ spheroid or a ‘heavy’ thick disk, added to the LMC self-lensing rates, would give rise to a theoretical prediction not too far from the observations.

It is noteworthy that all the different galactic populations described predict approximately similar relations between the event durations and the lens masses, since populations with larger scale heights (and hence larger average r_E) also have larger associated lens velocity dispersions. The event durations observed then suggest that the lenses could be faint white dwarfs ($m \simeq 0.5 M_\odot$), with possibly some neutron stars[§] ($m \simeq 1.4 M_\odot$) or brown dwarfs near the hydrogen burning limit ($m \simeq 0.1 M_\odot$) also present. There are actually other observations giving the hint that a significant population of old high velocity white dwarfs has been found [Op01], although it is not clear if they belong to the halo, the spheroid or are just a tail of the disk population. In the case of LMC self-lensing, the lenses are most likely just light main sequence stars.

Finally, there have also been suggestions that the LMC events could be due to an intervening very faint dwarf galaxy or to LMC debris resulting from its disruption by the tidal gravitational effects from our galaxy [Zh98].

An important signature to identify the lensing population is the distribution of microlensing events across the different fields monitored towards the LMC, since lensing due to the stellar LMC populations would imply

[§]Neutron stars may also be expelled from the disk towards positions more favorable for LMC microlensing in the supernova explosions producing them [Mo97].

an enhanced optical depth towards the LMC center, while galactic lenses would give rise to a more uniform distribution. With the present (limited) statistics there is however no marked excess of events towards the central part of the LMC [Al00a].

5.4.2 *Searches towards the bulge*

Microlensing searches towards the center of the Galaxy were originally suggested as a sure way to observe microlensing [Gr91b; Pa91], since at least faint disk stars would act as lenses. The optical depth for bulge sources lensed by disk stars was estimated to be $\tau_B^D \simeq (0.29 \div 0.96) \times 10^{-6}$ [Gr91b], and hence the associated event rates would be observable. On the other hand, these searches could also be useful to constrain the amount of dark compact objects in the region of the galactic plane.

Several hundreds of events have indeed been found towards the bulge, and furthermore the optical depth inferred is significantly higher than those initial expectations. The MACHO Collaboration reported $\tau = 2.43^{+0.39}_{-0.38} \times 10^{-6}$ from an analysis of 99 microlensing candidates [Al00d]. Assuming that a fraction f_{Disk} of the monitored stars are actually foreground disk stars and using the fact that the optical depth for lensing of these foreground stars is much smaller than that for bulge stars [Mo96], they infer that the optical depth restricted to bulge sources should be

$$\tau_B \simeq 3.23^{+0.52}_{-0.50} \left(\frac{0.75}{1 - f_{Disk}} \right) \times 10^{-6}. \quad (5.38)$$

On the other hand, an analysis of 52 events associated to clump giant stars, which are known to belong to the bulge and being bright are less affected by blending effects, gives

$$\tau_B \simeq 2.0 \pm 0.4 \times 10^{-6}. \quad (5.39)$$

The OGLE Collaboration has found by now already 520 events towards the bulge [Wo01], but only the optical depth from the 9 events found by the OGLE I campaign has been reported, amounting to $\tau_B = 3.3 \pm 1.2 \times 10^{-6}$ [Ud94].

An increase in the optical depth beyond the one predicted from faint disk stars results when self-lensing by bulge stars is included. An indication in this direction was obtained from the predictions of the heavy spheroid models for observations towards Baade's Window, which amount to $\tau_B^S \simeq$

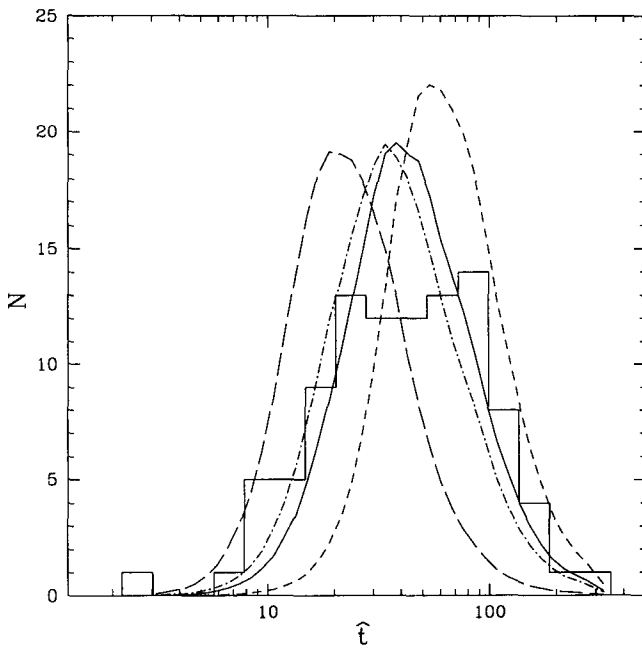


Fig. 5.6 Histogram of event duration distribution ($\hat{t} \equiv 2t_E$) observed by the MACHO Collaboration towards the galactic bulge, as well as predictions from different models for the mass function of the lenses. Long dashes correspond to $m = 0.1 M_\odot$, short dashes to $m = 1 M_\odot$ while the solid line is for a Scalo main sequence present day mass function and the dot-dashed line for a power law model mass function in the range $m = 0.1\text{--}1.4 M_\odot$ (courtesy of C. Alcock, reproduced from [Al00d] with permission from *The Astrophysical Journal*).

0.7×10^{-6} [Gi94], arising mainly from lenses near the galactic center where this model describes the bulge. Using an axisymmetric bulge model and including the effect of the spatial distribution of the sources (according to Eq. (5.10), what increases τ by $\sim 50\%$) leads to $\tau_B \simeq 1 \times 10^{-6}$ [Ki94]. A further increase in the bulge self-lensing is obtained by taking into account the barred shape of the bulge. For instance, for an adopted inclination of the bar axis with respect to the l.o.s. of $\alpha = 13^\circ.4$, one has [Zh95]

$$\tau_B^{Bar} \simeq 1.7 \left(\frac{M_{Bar}}{2 \times 10^{10} M_\odot} \right) \times 10^{-6}, \quad (5.40)$$

so that one may say that the large optical depth measured has led to a rediscovery of the existence of the bar in the center of our Galaxy.

A crucial signature to identify the different possible populations of lenses and sources responsible for the microlensing events towards the bulge is to map the event rates (and event durations) along many different directions. The resulting maps are expected to differ significantly according to which population is producing the events, with for instance disk lenses having strong latitude dependence but little longitude dependence, while bulge lenses depending sizeably on both coordinates, and a bar population being asymmetric with respect to positive and negative longitudes.

Regarding the event duration distribution, Figure 5.6 from Ref. [Al00d] shows an histogram of the events analyzed by the MACHO Collaboration as a function of their duration, together with the predictions from a bar+disk model under several assumptions regarding the lens mass function. Lenses with masses distributed in the interval $m = 0.1\text{--}1 M_\odot$ provide a reasonable agreement with observations, so that the lenses are most probably just faint ordinary stars.

Recommended reading

- E. Roulet and S. Mollerach (1997), “Microlensing”, Physics Reports **279**, 67.
- B. Paczyński (1996), “Gravitational microlensing in the Local Group”, Annual Review of Astronomy and Astrophysics **34**, 419.

Chapter 6

Microlensing II: Beyond the simplest light curve

In the previous Chapter we have described the simplest microlensing light curve, that corresponding to a point-like source, being lensed by a point-like lens, and assuming a uniform relative velocity between them. This light curve has a symmetric shape, as was depicted in Figure 5.2, is achromatic and does not repeat. Of the three parameters describing it (u_0 , t_0 and t_E , see Eq. (5.4) and (5.5)), only the event duration, t_E , contains information about the lens physical properties. This is hence the most important observable in a typical microlensing event, but it has the problem that from it only a convoluted relation between the mass of the lens, the distance to the lens (and the source) and the relative velocity between the lens and the source can be determined. This makes quite difficult the identification of the lensing population and the determination of its mass function, since only statistical comparisons between the observed event durations and the expected values for different assumptions about the lensing distributions can be made.

The approximations mentioned above are good for the majority of the events. However, sources or lenses often form part of binary systems, sources are extended objects and the relative motion between the lens and the source may depart from the rectilinear and uniform one. Each of these facts introduces modifications in the light curve which become observable for a fraction of the events. The resulting light curves need extra parameters for their description, what makes their analysis more complicated, but they also contain additional information about the lens parameters which can help to break the degeneracy among them.

The most remarkable departures from the simplest light curve are found

in the presence of multiple lenses. We will then start describing in some detail the microlensing produced by binary systems. The analysis of events caused by binary lenses allows the study of the distribution of binary mass ratios and projected separations, and also to search for signals due to planets even as small as the Earth.

We will then continue with a discussion of the different observations which can provide additional information about the lens parameters. These include the observation of finite source size effects (in particular exploiting the huge magnifications achieved in binary caustic crossings), the observation of parallax effects associated to the Earth motion around the Sun (which is observable for long duration events), or from future simultaneous observation of events from the Earth and from a satellite in solar orbit. We will also discuss the direct determination of the Einstein angle of the lens through the observation of the image centroid shift during the event, what is known as astrometric microlensing. This is expected to become feasible in the near future, and will greatly help in breaking the degeneracy among the lens parameters for most of the events.

We will conclude with a discussion of quasar microlensing, which is another case in which very peculiar light curves are expected since the effects can be due to the simultaneous action of several stars in the lensing galaxy and also finite source effects can be of paramount importance.

6.1 Binary lenses

It is a well established fact that most stars in the Galaxy are binaries [Ab83] and hence it is reasonable to expect that a sizeable fraction of the lenses will form part of binary systems. Therefore, lensing by two point-like masses has been studied in great detail. We will now review the formalism used to describe it and the main observable characteristics of binary microlensing events, discussing how these can be exploited to determine the lens parameters, the source properties or to search for planets orbiting the lens.

6.1.1 *The complex lens equation*

In order to extend the results from the single point-like lens to a system with two point-like lenses, it is useful to work with angular variables defined in the complex plane and normalized in terms of the Einstein angle θ_E

associated to the total mass $M = M_A + M_B$ [Wi90]. Let us then introduce source coordinates

$$\zeta \equiv \frac{\beta_x + i\beta_y}{\theta_E}, \quad (6.1)$$

and image coordinates

$$z \equiv \frac{\theta_x + i\theta_y}{\theta_E}. \quad (6.2)$$

Then, the lens equation (3.74) can be rewritten as

$$\zeta = z - \frac{\mu_A}{\bar{z} - \bar{z}_A} - \frac{\mu_B}{\bar{z} - \bar{z}_B}, \quad (6.3)$$

with $\mu_j \equiv M_j/M$ and z_j are the locations of the lenses, with $j = A, B$. As discussed in Section 3.3, the amplification of an image is given by

$$A_i = J^{-1}|_{z_i}, \quad (6.4)$$

where z_i is the position of the image and J is the Jacobian of the mapping from the image to the source plane, i.e.

$$J(z, \bar{z}) = \det \begin{pmatrix} \partial\zeta/\partial z & \partial\zeta/\partial\bar{z} \\ \partial\zeta/\partial\bar{z} & \partial\zeta/\partial\bar{z} \end{pmatrix} = \left| \frac{\partial\zeta}{\partial z} \right|^2 - \left| \frac{\partial\zeta}{\partial\bar{z}} \right|^2. \quad (6.5)$$

For the binary lens, one gets from Eq. (6.3) that $\partial\zeta/\partial z = 1$, and hence

$$J = 1 - \left| \frac{\partial\zeta}{\partial\bar{z}} \right|^2, \quad (6.6)$$

with

$$\frac{\partial\zeta}{\partial\bar{z}} = \frac{\mu_A}{(\bar{z} - \bar{z}_A)^2} + \frac{\mu_B}{(\bar{z} - \bar{z}_B)^2}. \quad (6.7)$$

The critical curves, corresponding to the points where infinitely magnified images could appear, are determined by the vanishing of J . This condition can be written from Eq. (6.6) as

$$\frac{\partial\zeta}{\partial\bar{z}} = e^{i\varphi}. \quad (6.8)$$

Combining the last two equations, we obtain a quartic equation for the points defining the critical lines

$$z^4 - z^2 (2\bar{z}_A^2 + e^{i\varphi}) - z\bar{z}_A 2(\mu_A - \mu_B)e^{i\varphi} + \bar{z}_A^2 (\bar{z}_A^2 - e^{i\varphi}) = 0, \quad (6.9)$$

where for simplicity the origin of coordinates has been taken at the midpoint between the two lenses ($z_A = -z_B$) and the real axis lies along the line joining the lenses. The critical lines are then obtained from the four solutions of this equation as φ is allowed to vary from 0 to 2π .

The caustics, formed by the points in the source plane with infinite magnification, can be obtained from the critical lines directly applying the lens equation, Eq. (6.3). The shape of these curves depends on the mass ratio $q \equiv \mu_A/\mu_B$ and on the lens separation in units of the Einstein angle, $d \equiv |z_A - z_B| = 2|z_A|$. They can be classified according to their topologies into three different regimes, known as wide, intermediate and close binary systems, as shown in Figure 6.1 (see also the discussion in Section 3.8.3 for a different view of these issues). A wide binary system has two separate four-cusp caustics, corresponding to the point-like caustics associated to each individual lens which are deformed by the presence of the other lens. As the lenses are brought closer, two cusps approach each other and merge, giving rise to a single six-cusp caustic, characteristic of intermediate binaries. For even closer lens positions, the caustic separates into two triangles and one four-cusp diamond, corresponding to the close binary topology.

The transition between the different regimes occurs when two critical lines merge at a point, as it can be seen in the left panel of Figure 6.1. As the critical lines are the set of points where $J = 0$, at the merging points also the gradient of J has to vanish [Er93; Rh00b]. Solving the system of equations $J = 0$ and $\partial J/\partial \bar{z} = 0$, the relation between the critical lens separation and the associated mass ratio can be obtained. As $|\partial\zeta/\partial\bar{z}| = 1$ (from the condition $J = 0$), the condition $\partial J/\partial \bar{z} = 0$ implies $\partial^2\zeta/\partial\bar{z}^2 = 0$. This fixes the relation between the critical value of \bar{z} and μ_A, μ_B and z_A

$$\bar{z} + z_A = 2z_A \left[1 - \left(-\frac{\mu_A}{\mu_B} \right)^{1/3} \right]^{-1}. \quad (6.10)$$

This expression gives rise to three different values for \bar{z} , according to which of the three cubic roots of -1 is chosen. Inserting these solutions into Eq. (6.7) and requiring that $J = 0$, one gets the final expression for the lens separation at the transition points. The transition from wide to intermediate lens systems (corresponding to the -1 root) occurs at a separation

$$d_{WI} = 2z_{A(WI)} = \left(\mu_A^{1/3} + \mu_B^{1/3} \right)^{3/2}. \quad (6.11)$$

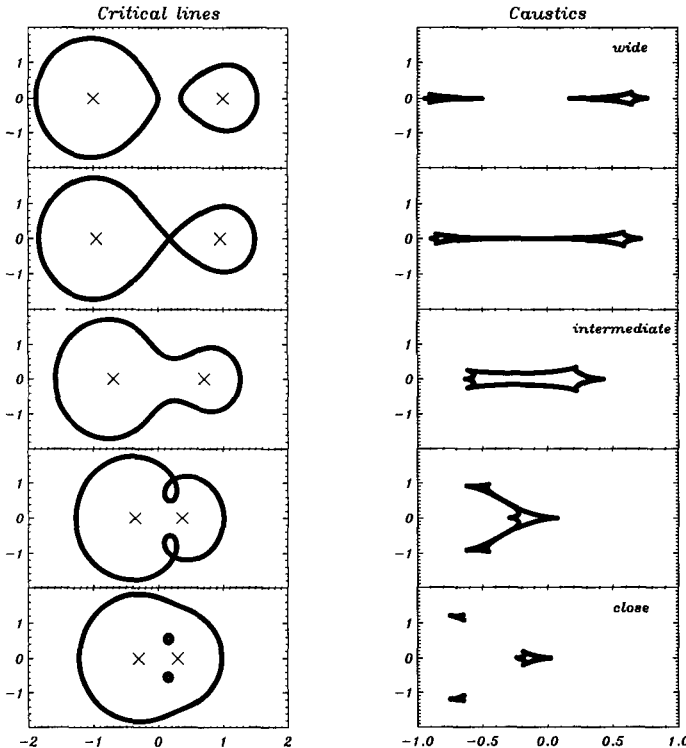


Fig. 6.1 The critical lines (left) and caustics (right) for a binary lens system with mass parameter $\mu_A = 0.25$. The crosses indicate the position of the lenses, with the heavier one being to the left. The lens separations are taken in decreasing value from top to bottom, with the second panels corresponding to $d = d_{WI}$ and the fourth ones to $d = d_{IC}$.

The other two roots, $e^{\pm i\pi/3}$, correspond to the two critical points in the transition from the intermediate to close binary systems taking place when the separation is

$$d_{IC} = 2z_{A(IC)} = \left(\mu_A^{1/3} + \mu_B^{1/3} \right)^{-3/4}. \quad (6.12)$$

Notice that in the limit of small mass ratios, i.e. for $q = \mu_A/\mu_B \ll 1$ as would be the case for planetary systems, one has $d_{WI} \simeq 1 + 1.5 q^{1/3}$ and $d_{IC} \simeq 1 - 0.75 q^{1/3}$, and hence both transitions occur for angular separations among the binary lenses very close to θ_E .

Turning now to the image positions for a given source location ζ , these

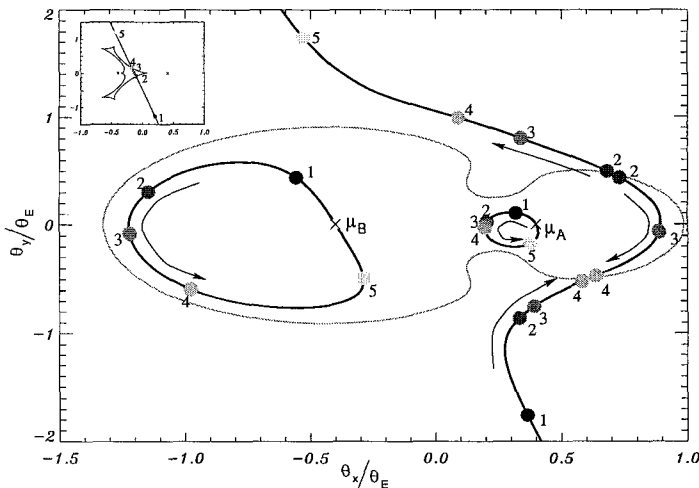


Fig. 6.2 Images of a source moving across the sky along the line shown in the insert in the upper left corner, where the closed line depicts the caustic of an intermediate binary lens system with mass fraction $\mu_A = 0.2$ and angular separation between the lenses equal to $0.8 \theta_E$. The solid lines in the main plot show the location of the images. Points 1 through 5 highlight the images corresponding to the five source positions marked in the insert. When the source is outside the caustic it has three images. A couple of new images appears at a point along the critical line (marked in the plot as a grey line) when the source crosses the caustic, and another pair disappears also along the critical line when the source crosses to the outside of the caustic.

can be determined by solving the lens equation (6.3). It is actually convenient to rewrite it as a fifth order equation in z , replacing \bar{z} from the conjugate of the lens equation [Wi90; Wi95b], so that it takes the form

$$g(z) \equiv (z^2 - z_A^2) [z + z_A(\mu_A - \mu_B) + (z^2 - z_A^2)(\bar{\zeta} + z_A(\mu_A - \mu_B))] - \\ (z - \bar{\zeta}) \left[(\bar{\zeta}(z^2 - z_A^2) + z + z_A(\mu_A - \mu_B))^2 - z_A^2(z^2 - z_A^2)^2 \right] = 0. \quad (6.13)$$

When the source is located inside the caustics, the five solutions of this equation correspond to the five images of the source. A source outside the caustics has only three images, meaning that two solutions of Eq. (6.13) will be spurious. These two solutions correspond to complex values of θ_x and θ_y and they have to be removed using Eq. (6.3) as a check.

Figure 6.2 shows the position of the images of a source which moves along the sky crossing the caustic twice (entering and leaving it), as is

shown in the small insert in the upper corner. A source far away from the lenses (point 1) has three images, one close to the source position (with positive parity) and the other two near the lenses (with negative parities). When the source enters the caustic (point 2) a pair of new images with opposite parities appears along the critical line, leading to a total of five images. When the source reaches the opposite border of the caustic (point 4), one of the two recently created images, the one with negative parity, merges with one of the original ones, the one of positive parity, and they disappear, leaving again three images.

6.1.2 Microlensing by binaries

As we have discussed, when the angular separation of the images is too small to be resolved the lensing effect manifests as a modification of the total flux received from the source. This is given by the total amplification, which corresponds to the sum of the absolute values of the magnifications of all the images. For binary lenses, the resulting light curves have very characteristic shapes, with pronounced spikes associated to every caustic crossing. This can be appreciated in Figure 6.3, which corresponds to a binary system with $\mu_A = 0.2$ and lens separation $d = 0.8$, and for which the light curve for three different possible trajectories of the source are plotted. Whenever the source crosses towards the inside region of the caustic through a fold, there is a sharp discontinuous rise in the amplification which is then followed by a smooth fall down. When it exits the caustic, the opposite behavior takes place, with a smooth rise followed by a discontinuous drop in the magnification. The light curve rise or fall near the inner side of the fold caustic reflects the $1/\sqrt{\beta}$ behavior of the amplification found in Eq. (3.63), with β being the transverse distance to the caustic. In the trajectory A , the source enters the caustic through a cusp and hence on both sides of the caustic the light curve shows the $\sim \beta^{-1}$ behavior obtained in Eq. (3.72). More symmetric peaks are then found when the source crosses the caustic close to a cusp.

The complete shape of the light curve has to be computed by numerically solving for the image positions and then summing the amplifications of all of them. There are also some interesting relations among the image magnifications which can be obtained without the need to compute the image positions [Wi95b; Rh97]. One of these is that the sum of the amplification of the five images of a source which lies inside the caustic (re-

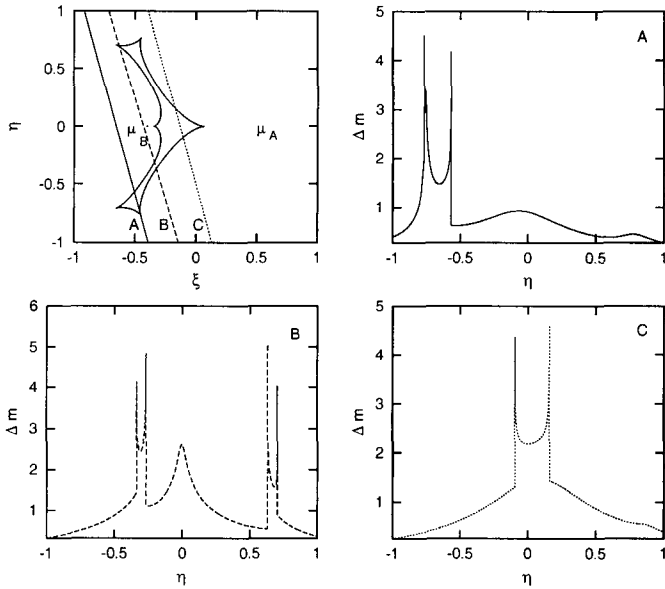


Fig. 6.3 Light curves of a source crossing the caustic region of a binary system with a mass fraction $\mu_A = 0.2$ and angular separation between lenses equal to $d = 0.8$. The first panel displays the caustic curve (in angular coordinates $\xi \equiv \beta_x/\theta_E$ and $\eta \equiv \beta_y/\theta_E$) and the three trajectories labeled A , B and C , for which the light curves are shown in the following three panels. In these plots the change in the apparent magnification is shown as a function of the angular coordinate η .

remembering that the amplification is negative for inverted images, according to the definitions in Chapter 3) has to be unity, i.e.

$$\sum_{i=1}^5 A_i = \sum_{i=1}^5 J^{-1}|_{z_i} = 1, \quad (6.14)$$

where z_i denote the positions of the images. To demonstrate this identity, notice that the transformation matrix for the inverse mapping can be written (directly inverting the matrix \mathcal{T}) as

$$\mathcal{T}^{-1} = \begin{pmatrix} \partial z / \partial \zeta & \partial z / \partial \bar{\zeta} \\ \partial \bar{z} / \partial \zeta & \partial \bar{z} / \partial \bar{\zeta} \end{pmatrix} = \frac{1}{\det \mathcal{T}} \begin{pmatrix} \partial \bar{\zeta} / \partial \bar{z} & -\partial \zeta / \partial \bar{z} \\ -\partial \bar{\zeta} / \partial z & \partial \zeta / \partial z \end{pmatrix}. \quad (6.15)$$

Equating the first entry of these matrices and using that from the conjugate

of the lens equation $\partial\bar{\zeta}/\partial\bar{z} = 1$, one has that

$$J^{-1} = \det \mathcal{T}^{-1} = \frac{\partial z}{\partial \bar{\zeta}}, \quad (6.16)$$

so that the sum of the signed amplifications reads

$$\sum_{i=1}^5 A_i = \frac{\partial}{\partial \zeta} \sum_{i=1}^5 z_i \quad (6.17)$$

On the other hand, being Eq. (6.13) a fifth order polynomial in z , it can be expressed as

$$g(z, \zeta, \bar{\zeta}) = \sum_{j=0}^5 a_j(\zeta, \bar{\zeta}) z^j = a_5 \prod_{i=1}^5 (z - z_i(\zeta, \bar{\zeta})) = 0, \quad (6.18)$$

where z_i are the five roots of the equation (the position of the five images). From this one gets that $a_4 = -a_5 \sum z_i$, implying then that

$$\sum_{i=1}^5 A_i = -\frac{\partial}{\partial \zeta} \left(\frac{a_4}{a_5} \right). \quad (6.19)$$

Using now the explicit form of the coefficients a_4 and a_5 , which can be read from Eq. (6.13), one finds $\partial_\zeta a_4 = -a_5$ and $\partial_\zeta a_5 = 0$, what proves the result anticipated in Eq. (6.14).

This means that inside the caustic region the absolute value of the sum of the amplification of the negative parity images $|A_-|$ is one unit less than the sum of the amplifications of the positive parity images A_+ , i.e. $|A_-| = A_+ - 1^*$. This property has an interesting corollary [Wi95b; Rh97], because the total amplification can then be written as $A_{tot} = A_+ + |A_-| = 2A_+ - 1$, and since there are two positive parity images and the amplification of each of them has to be larger than or equal to one (see discussion in Section 3.3), this implies that the total amplification of a source inside the binary caustic has to be larger than three, i.e. $A_{tot} \geq 3$. This fact can be appreciated in Fig. (6.3), where the increment in the apparent magnitude of the source in the region between the caustic crossing spikes has to be larger than $2.5 \log_{10} 3 = 1.19$. Actually some observed binary events do not satisfy this constraint (in particular the first binary event observed by OGLE),

*Notice that a similar relation also holds for the two images produced by a single lens, as can be seen from Eq. (3.20).

but this is explained by the presence of significant blending with another source which is not lensed.

Since the binary lens light curves have significant additional structure with respect to the single lens light curves, they clearly contain also more information about the lenses. However, the problem of fitting a binary lens model to the light curve data is much more complex than for the single lens, as the number of parameters needed to describe the system is larger. To the three parameters characterizing a single lens event, t_E (time in which the source crosses the Einstein angle associated to the total mass), t_0 (time of closest approach to the center of the lensing system) and u_0 (impact parameter of the source trajectory), one has to add the mass ratio μ_A/μ_B , the projected separation of the lenses in terms of θ_E and the angle between the axis joining the lenses and the direction of the source trajectory. In addition, the angular size of the source θ_* has to be specified. This last is very relevant for caustic crossing events, because the infinite magnification associated to the caustic is smeared out by the effects of the finite size of the source. Sometimes also the rotation of the binary system has to be included (see e.g. [Al00b]).

The difficulty of fitting the binary lens light curves comes in part from the large size of the parameter space, combined with the sensitivity of the χ^2 to subtle changes in the parameters. Different strategies have been proposed to tackle this problem. Mao and di Stefano [Ma95b] developed a densely sampled library of events and characterized them by their gross features, like the number of peaks, height and intervals between them. Comparing the observed features of an event with this library allows to reduce the region of the parameter space to be explored. A similar idea was proposed by di Stefano and Perna [di97] using instead of the light curve features, the coefficients of the expansion of the light curves in a given basis of functions to select the viable regions in the parameter space. Another approach, advanced by Albrow et al. [Al99b], uses that for light curves with a well sampled caustic crossing an analytical fit to the behavior of the amplification near the caustic ($A \propto 1/\sqrt{\beta}$) can be performed. The parameters extracted from this preliminary fit can then be used to constrain the region of the parameter space to be explored in the subsequent fit to the full light curve.

Unfortunately, degeneracies exists between different binary configurations, and in particular between close and wide binary systems, and sometimes the light curves can be well fitted by quite different lensing systems

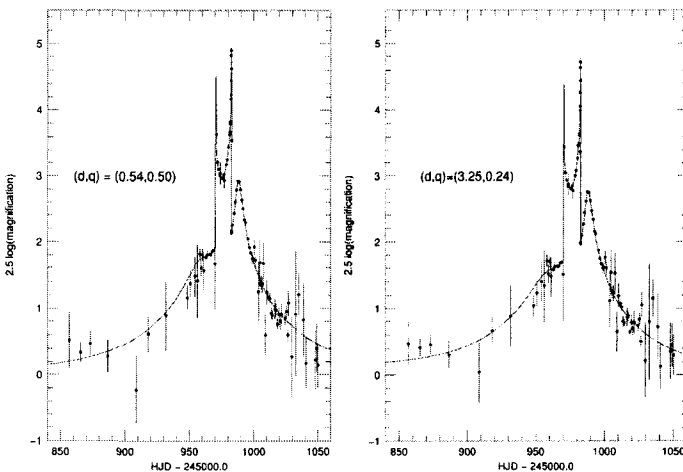


Fig. 6.4 Light curve of the binary event MACHO 98-SMC-1 and two different fits to the data corresponding to the close binary solution (left) and wide binary solution (right) (courtesy of C. Alcock, reproduced from [Af00] with permission from *The Astrophysical Journal*).

[Al99b; Do99]. In some cases, this photometric degeneracy between radically different binary geometries may be broken through observations of astrometric deviations, as will be discussed further below.

Even if most stars are believed to be in binaries, it is estimated that only about 5 – 10% of microlensing events will show clear signatures of binarity. This is due to the fact that when the projected separation of the lenses is much smaller or much larger than θ_E , the size of the caustics are too small to be relevant and hence for most source trajectories the magnification pattern closely resembles that produced by single lenses.

One of the nicest binary lensing examples detected to date is that observed towards the Small Magellanic Cloud in 1998 (MACHO 98-SMC-1 [Al99a]). It has been followed by five different Collaborations and the combined data provides a very good coverage of the event. It shows two fold caustic crossings and the source also approaches a cusp. The data points from the five groups are plotted together in Figure 6.4, where also the fitted light curves obtained by Afonso et al. [Af00] are shown. They find two different sets of values for the lens separation d and mass ratio q which are compatible with all the data points, given by $(d, q) = (0.54, 0.50)$ and $(d, q) = (3.65, 0.36)$, showing the close-wide binary degeneracy mentioned

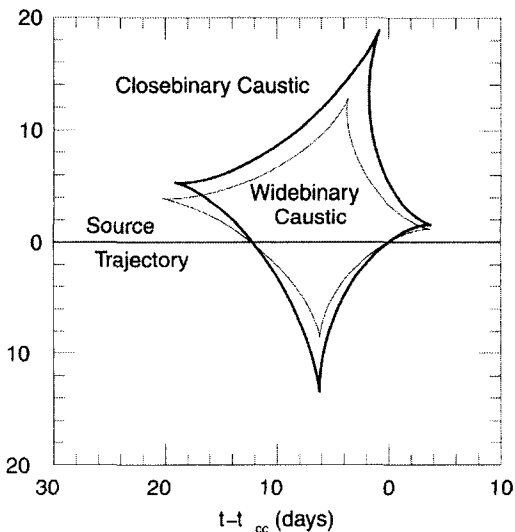


Fig. 6.5 Caustic structures for the two different fits to light curve data shown in Figure 6.4 (courtesy of C. Alcock, reproduced from [Af00] with permission from *The Astrophysical Journal*).

before. The structure of the caustic corresponding to both fits is shown in Figure 6.5, and looking at them the extreme resemblance of both light curves can be understood. Another interesting feature is that the wide binary solution requires that the binary be rotating in order to be consistent with all the data.

6.1.3 Planetary searches

Gravitational microlensing provides also a method to look for distant planetary systems. This consists in intensively monitoring microlensing events towards the galactic bulge looking for possible deviations in the light curve, with respect to the expectations from individual lenses, which can be produced by planets orbiting the foreground lens star.

Mao and Paczyński [Ma91] first noted that for microlensing observations towards the bulge, the typical size of the Einstein ring in the lens plane,

which is

$$r_E \simeq 1.9 \text{ AU} \sqrt{\frac{m_L}{0.3M_\odot} \frac{D_{OL}}{6 \text{ kpc}} \frac{D_{LS}}{2 \text{ kpc}} \frac{8 \text{ kpc}}{D_{OS}}}, \quad (6.20)$$

is of the same order of magnitude as the expected size of the planetary orbits. This means that it is not unlikely that light rays arriving from one of the images have passed close to the planet and have been affected by its gravitational field, resulting in an observable variation in the light curve. These deviations in the light curve are expected to be short bumps (lasting from hours to a day) superimposed on the single lens light curve. The duration of the perturbation ($\simeq (\theta_p/\theta_E)t_E \simeq \sqrt{q}t_E$, with θ_p being the Einstein angle associated to the planet) is clearly shorter for smaller mass planets.

Figure 6.6 shows two typical examples of light curves for a planet with mass ratio $q = 10^{-3}$ (similar to that between Jupiter and the Sun). The first panel corresponds to the case when the distance from the planet to the star is larger than the Einstein ring (corresponding to a wide binary system) and it shows a characteristic bump in the light curve. In the second panel the planet orbits the star at a distance smaller than the Einstein ring (close binary system) and the light curve shows a dip.

Further studies by Gould and Loeb [Go92] showed that star lenses containing Jupiter-like planets should leave a noticeable signature on gravitationally lensed bulge stars in 20% of the microlensing events associated to them (with this probability becoming smaller for lighter planets). Based on this high probability, they proposed to set a network of telescopes around the globe for follow-up observations of alerted events in order to search for planets. These ideas have been put in practice by different Collaborations, and their combined data have provided accurate photometry of many microlensing events. The microlensing Collaborations (EROS, MACHO and OGLE) have routinely monitored millions of stars each night, checking them for variations in their light-curves. When a candidate event is detected, an alert is sent to the interested community that can start the follow-up of the event. The PLANET Collaboration has observing time at four southern locations (Tasmania, Western Australia, South Africa and Chile), GMAN at Australia, Chile and Israel, MOA at New Zealand and MPS at Australia. Using data from about fifty microlensing events with very good sensitivity to planets (they have a median sampling time of about an hour and typi-

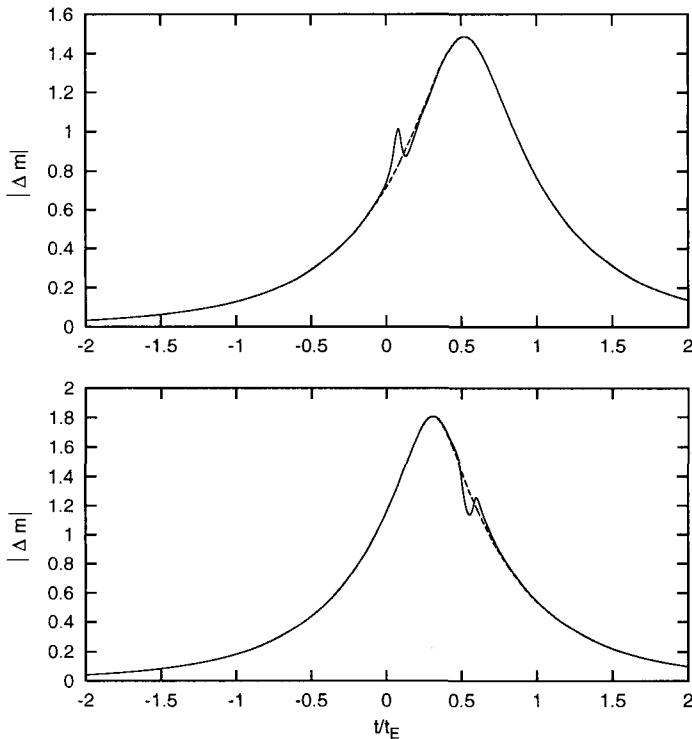


Fig. 6.6 Light curves showing characteristic planetary perturbations for a mass ratio $q = 10^{-3}$. In the first panel the distance between the planet and the star is $1.2r_E$ and in the second panel is $0.8r_E$.

cal photometric precision of 1–2 % near the peaks of the events and a bit poorer in the tails) the PLANET collaboration has put an upper limit on the abundance of Jupiter-like planets ($m \sim 10^{-3}M_\odot$) of order 30 % from the non-observation of anomalies in the light curves [Al01b].

A slightly different strategy has been proposed by Griest and Safizadeh [Gr98], who noticed that in high magnification events, in which the source transits very close to the lens location ($u_0 \ll 1$), the Jupiter mass planet detection probability rises to 100% and even smaller mass planets have a high detection probability. If the planet is present, the light curve would differ from the single lens one because the caustic is diamond shaped instead of point-like, due to the distortion produced by the planet. This gives rise to a deviation in the light curve near its maximum, and as the time of the occur-

rence of the peak can be predicted in advance, the follow-up of high magnification events requires the use of a relatively small amount of telescope time. The first evidence for a planetary companion has been discovered in the MACHO 98-BLG-35 event, which reached a peak magnification factor of almost 80. It was found by the MACHO alert system and followed by the MOA and MPS Collaborations. Two analyses of this event have found some evidence for a low mass planet orbiting the lens star [Rh00a; Bo01b] and excluded the presence of giant planets from the region between 0.4 to 2.5 r_E .

6.2 Further determinations of the lensing parameters

As we have mentioned in the introduction of this Chapter, for the simplest and most common microlensing events only the event duration can be used to obtain information about the intrinsic lens properties. However, t_E depends in a convoluted way on the lens mass, distance and velocity, so that these quantities cannot be separately determined. Fortunately, for a fraction of the events it is possible to extract additional information about the lens parameters. The two observables which become relevant for this task, besides the event duration, are the Einstein angle θ_E and the Einstein radius projected onto the observer's plane \tilde{r}_E , which are shown in Figure 6.7. The first can be measured when finite source size effects can be detected, while the second can be obtained through parallax measurements. Also, in a nearby future astrometric microlensing observations will be used to determine θ_E . Thus, much work has been devoted to exploit these observations to further constrain the lens masses, distances and velocities for individual events so as to get a better knowledge about the lensing populations.

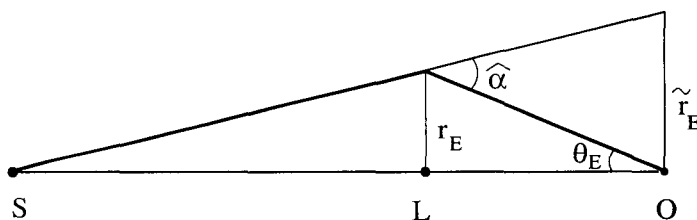


Fig. 6.7 Microlensing observables: the Einstein angle θ_E and the Einstein radius projected onto the observer's plane \tilde{r}_E .

If both \tilde{r}_E and θ_E were measured for the same event, the lens mass would be directly determined, since noting from Figure 6.7 that

$$\tilde{r}_E = r_E \frac{D_{OS}}{D_{LS}} = \theta_E \frac{D_{OL} D_{OS}}{D_{LS}}, \quad (6.21)$$

and recalling the definition of the Einstein angle:

$$\theta_E^2 = \frac{4GM}{c^2} \frac{D_{LS}}{D_{OL} D_{OS}}, \quad (6.22)$$

one obtains that

$$\tilde{r}_E \theta_E = \frac{4GM}{c^2}. \quad (6.23)$$

If \tilde{r}_E and θ_E are known, also the distance to the lens can be obtained from Eq. (6.21) and the lens relative velocity v^\perp results from the angular velocity of the lens relative to the source, i.e. the so called proper motion

$$\mu = \frac{\theta_E}{t_E} = \frac{v^\perp}{D_{OL}}. \quad (6.24)$$

Hence, all the physical lens parameters can be recovered if t_E, θ_E and \tilde{r}_E can be determined.

In order to measure θ_E , a known angular scale in the sky is needed to be used as ‘ruler’, the natural candidate being the angular size of the source θ_* . The source size can be inferred from the star’s magnitude and dereddened color, using the color/surface brightness relation. A few determinations of θ_E have been performed to date using some caustic crossing events due to binary lenses or some very high magnification events associated to single lenses with tiny impact parameters. The knowledge of θ_E directly provides a one to one relation between the distance to the lens and the lens mass.

For the measurement of \tilde{r}_E , a reference scale in the observer’s plane is needed, and in this case the natural scale is just the size of the orbit of the Earth. For few events, those lasting more than three months so that the deviation of the Earth’s trajectory from rectilinear and uniform motion is important, \tilde{r}_E has been determined by measuring the deviation of the light curve induced by the motion of the Earth around the Sun. The effect is proportional to the parallax $\pi_E \equiv AU/\tilde{r}_E$ and is hence observable if π_E is not much smaller than unity. Also, if a telescope on a satellite in heliocentric orbit were available for microlensing observations, the comparison of the

light curves obtained from the Earth and from the satellite could provide a parallax determination (without requiring the event duration to be long).

Many ideas have been proposed to measure θ_E and \tilde{r}_E (see [Go96c] for a review), and we will discuss some of them in the following Sections. To date, their measurement has only been possible for very special classes of events, such as caustic crossings in the case of θ_E and very long duration events in the case of \tilde{r}_E . Moreover, since these two classes of events have little overlap, no simultaneous determination of them has yet been possible. However, it is expected that determinations of both θ_E and \tilde{r}_E for a large number of events will become possible with the precision measurements of the shift of the centroid of the image occurring during a microlensing event, what is known as astrometric microlensing, together with the simultaneous measurement of the parallax. These kind of measurements are expected to become feasible in a near future using high accuracy space interferometers.

6.2.1 Proper motion

The angular velocity of the lens relative to the source, or proper motion μ , can be measured when the lens caustic passes over the face of the source star, so that the effects associated to the finite source size become observable [Ne94a; Go94a]. In these cases, the actual amplification is obtained from the convolution of the theoretical point-like source amplification with the actual surface brightness of the star. This procedure modifies the predicted light curve, suppressing the divergence near the caustic and giving it a smoother shape. By modeling this deviation, it is possible to determine the time t_* that it takes the lens to cross the source radius, and from the estimated angular source size θ_* the proper motion can be determined as

$$\mu = \frac{\theta_*}{t_*}. \quad (6.25)$$

For a point-like lens, the magnification of a circular source with surface brightness $I(\rho, \varphi)$ is given by the two-dimensional convolution integral

$$A_{ext}(u) = \frac{1}{F_*} \int_0^{2\pi} \int_0^{\rho_*} d\varphi d\rho \rho I(\rho, \varphi) A(\sqrt{u^2 - 2u\rho \cos \varphi + \rho^2}), \quad (6.26)$$

where $u \equiv \beta/\theta_E$ is the angular distance between the lens and the center of the source in units of the Einstein angle, $\rho_* \equiv \theta_*/\theta_E$ is the angular size of the source similarly normalized, the angle φ is measured with respect to

the direction from the source center to the lens, $A(u)$ is the point source amplification given by Eq. (5.4), and F_* is the unlensed flux from the source.

In the particular case of a source with uniform surface brightness, expression (6.26) can be integrated analytically [Wi94] and the final result can be expressed in terms of elliptical functions[†]. The deviation from the point-like source light curve depends on the relation between the size of the minimal angular distance of the lens to the center of the source, $\beta_0 \equiv u_0\theta_E$, and the angular size of the source, θ_* . When β_0 is larger than $\theta_*/2$, the peak magnification is larger than that found for the point-like source case, while for β_0 smaller than $\theta_*/2$, the peak amplification is smaller than in the point-like source case. In particular, when the alignment is perfect ($\beta_0 = 0$) the amplification does not diverge, but instead reaches a maximum value given by

$$A_{max}(u=0) = \frac{2}{\rho_*^2} \int_0^{\rho_*} d\rho \rho A(\rho) = \sqrt{1 + \frac{4\theta_E^2}{\theta_*^2}}. \quad (6.27)$$

The first proper motion measurement obtained using this method is shown in Figure 6.8, and involved a high magnification event observed towards the bulge, the MACHO 95-BLG-30 event [Al97]. Since this event was alerted well before the maximum amplification was reached, it could be studied in detail by follow-up networks. The measurements near the peak are shown in Figure 6.9, and clearly display the effects of the finite source size (and of limb darkening, as will be explained below). A fit to the light curve shape provides a measurement of ρ_* , i.e. of the ratio between the source angular size and the Einstein angle, which combined with the estimated source size provides a measure of θ_E . The resulting proper motion of the lens for this event is $\mu = \theta_E/t_E = 21.5 \pm 2.9$ km/s/kpc, and its small value favors that the lens be located near the bulge.

However, for events due to single lenses, the probability that the point-like caustic crosses the source face is very small. A better chance to measure proper motions results for events produced by binary lenses with masses of comparable magnitude. For them the caustics are closed curves with a characteristic size of the order of the Einstein angle, and then they have a higher probability to give rise to events with caustic crossings. Several proper motions have indeed been measured studying these kind of events [Al99a; Af00; Al00b; Al01a].

[†]An extension to other surface brightness profiles has been done in Ref. [Wi95a].

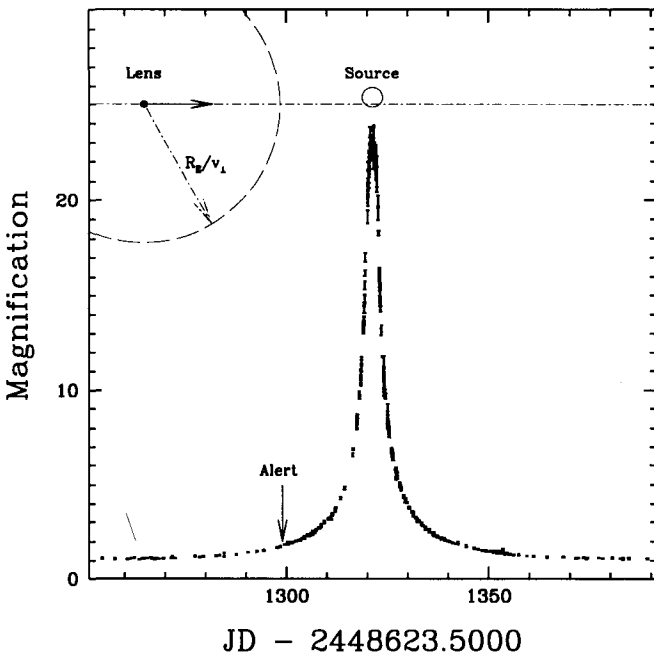


Fig. 6.8 Light curve of the MACHO 95-BLG-30 event. Also illustrated is the size of the Einstein ring (i.e. the event duration $t_E = r_E/v^\perp$) and the source size, with the lens trajectory traversing the face of it near the maximum in the light curve. The arrow indicates the time at which the event was alerted to the follow-up networks (courtesy of C. Alcock, reproduced from [Al97] with permission from *The Astrophysical Journal*).

The amplification of a source in the neighborhood of a fold can be written as

$$A(u) \simeq A' + A_{div}(u), \quad (6.28)$$

where A_{div} is the contribution associated to the pair of images created when the source enters the caustics (and hence A_{div} has the $1/\sqrt{\beta}$ divergence in the point-like source limit), while A' is the piece associated to the remaining images, having a smooth behavior and hence being unsensitive to finite source effects.

According to Eq. (3.63), the amplification of the new image pair of a

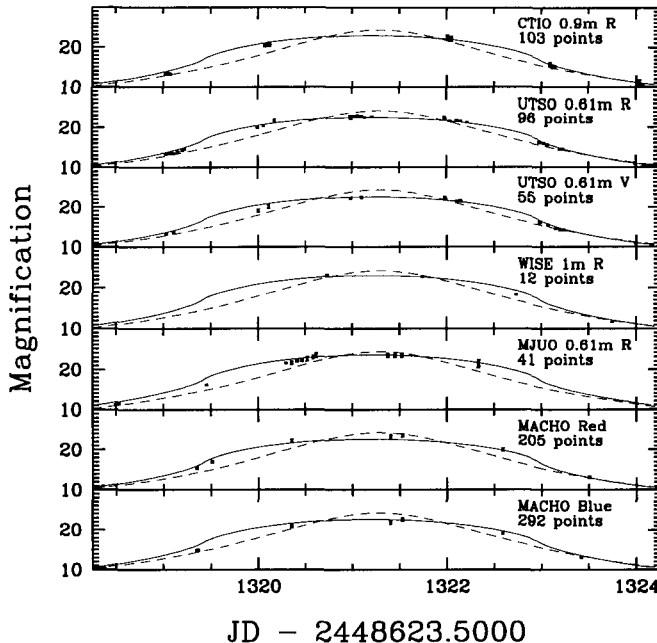


Fig. 6.9 Light curves near the peak for event MACHO 95-BLG-30, obtained with telescopes at different locations. The dashed line indicates the fit of the whole light curve without including finite source effects, the solid line takes into account the finite source size and the limb darkening (courtesy of C. Alcock, reproduced from [Al97] with permission from *The Astrophysical Journal*).

point-like source can be written in a neighborhood of the fold as

$$A_{div}(\mathbf{u}) = \frac{A_f}{\sqrt{\Delta u^\perp}} \Theta(\Delta u^\perp), \quad (6.29)$$

where Δu^\perp is the distance from the source center to the fold (taken positive for a source inside the caustic and negative if it lies outside).

For an extended source, this expression has to be convolved with the star's surface brightness. This can be written, using Cartesian coordinates centered on the source and scaled to the source radius (as depicted in Fig-

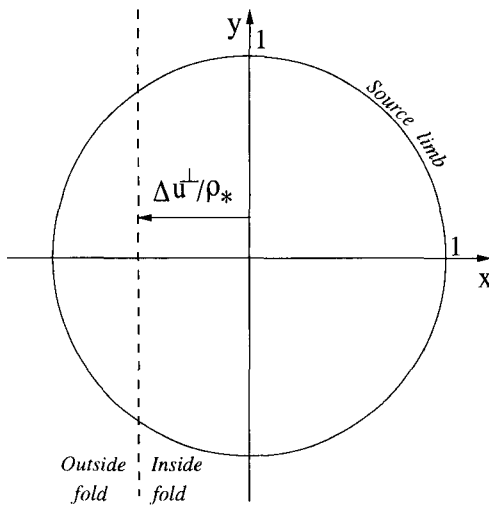


Fig. 6.10 Normalized coordinates to describe the source (as a circle of unit radius), with the x axis being orthogonal to the fold caustic. The distance from the origin to the fold is $\Delta u^\perp/\rho_*$.

ure 6.10) as

$$A_{div}^{ext}(\mathbf{u}) = \frac{A_f \rho_*^{3/2}}{F_*} \int_{\max(-1, -\frac{\Delta u^\perp}{\rho_*})}^1 \frac{dx}{\sqrt{x + \frac{\Delta u^\perp}{\rho_*}}} \int_{-\sqrt{1-x^2}}^{\sqrt{1-x^2}} dy I(x, y) \Theta \left(1 + \frac{\Delta u^\perp}{\rho_*} \right). \quad (6.30)$$

Using now that

$$F_* = \rho_*^2 \int_{-1}^1 dx \int_{-\sqrt{1-x^2}}^{\sqrt{1-x^2}} dy I(x, y), \quad (6.31)$$

one arrives to the general form

$$A_{div}^{ext}(\mathbf{u}) = \frac{A_f}{\sqrt{\rho_*}} G \left(-\frac{\Delta u^\perp}{\rho_*} \right), \quad (6.32)$$

where G is a function which depends on the shape of the surface brightness profile. The source radius only affects the width of the caustic crossing through the argument of G , which is $\eta \equiv -\Delta u^\perp/\rho_*$. For a uniform surface

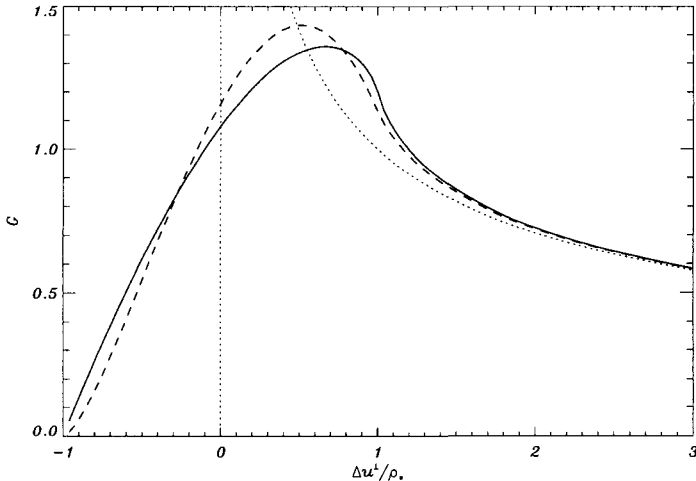


Fig. 6.11 Amplification of an extended source crossing a fold caustic. The solid line corresponds to a uniform surface brightness and the dashed line to a linear limb darkening with $c_1 = 1$. For reference we show with a dotted line the amplification corresponding to a point-like source. Notice that the limb darkened source looks more similar to the point-like source limit than the uniform brightness one, as expected.

brightness, this function reads

$$G_0(\eta) = \frac{2}{\pi} \int_{\max(-1, \eta)}^1 dx \left(\frac{1-x^2}{x-\eta} \right)^{1/2} \Theta(1-\eta). \quad (6.33)$$

The function G_0 is plotted in Figure 6.11 (solid line), showing how the fold amplification divergence is smeared for a uniform surface brightness source.

In the case of a fold crossing, what can be measured by fitting the observed light curve to the theoretical expression is the time Δt needed for the caustic (and not just the center of mass of the lens) to cross the source radius. To determine the relative lens-source proper motion it is then necessary to know also the angle ϕ between the source trajectory and the fold direction, since

$$\mu = \frac{\theta_*}{\Delta t \sin \phi}. \quad (6.34)$$

This angle can be inferred from a detailed modeling of the whole binary event, what allows the caustic geometry to be reconstructed.

The measurement of the proper motion for the LMC (or SMC) microlensing events is particularly interesting as it allows to distinguish between lenses belonging to the Magellanic Clouds and galactic lenses. For instance, LMC lenses are typically ~ 50 kpc away and have relative speeds characterized by the LMC rotation velocity ~ 80 km/s, and hence they are expected to have $\mu \leq 2$ km/s/kpc. Galactic lenses have larger velocities (~ 200 km/s) and are at smaller distances (~ 10 kpc), leading then to larger typical proper motions, $\mu \geq 20$ km/s/kpc. For observations towards the bulge, the expected values are instead not so different for the different lensing populations.

For the binary SMC event discussed in Section 6.1.2, it has been possible to measure its proper motion using the intensive coverage of the second caustic crossing. The value obtained for the two possible fits to the overall event (the wide and close binary configurations), are $\mu = 1.30 \pm 0.08$ km/s/kpc (close binary) and $\mu = 1.76 \pm 0.11$ km/s/kpc (wide binary) [Af00], both indicating that the lens should belong to the SMC rather than to the galactic halo.

6.2.2 Limb darkening

By detailed monitoring of the events in which a caustic crosses the face of the source, not only more information about the lens can be obtained, but it is also possible to study the surface brightness profile of the source star [Wi95a]. Observations of the Sun show a falloff of the brightness near the edge of the stellar disk with respect to the center. This should be a general phenomenon according to stellar atmosphere theories, and it is known as limb darkening. However, the traditional measurements using eclipsing binaries have proved extremely difficult, and have been performed only for nearby stars.

On the other hand, microlensing can provide limb darkening measurements of distant stars with reasonable accuracy for well-sampled caustic crossing events. Despite the small angular size under which the source stars are seen, as the caustic crosses the star's surface different parts of the star are amplified at different times, and in this way the surface brightness profile can be recovered. Fold caustic crossing events scan a 1-dimensional luminosity function corresponding to the surface brightness integrated along the caustic direction, while point-like caustics or cusps test the 2-dimensional surface brightness profile, providing in principle more accurate results.

However, point-like caustic and cusp crossings are less likely to occur than fold crossings [Ga99].

The limb darkened surface brightness profile of the source is usually parameterized as

$$I_\lambda(\vartheta) = I_\lambda(0) \left(1 - \sum_n c_n(\lambda) (1 - \cos^n \vartheta) \right), \quad (6.35)$$

where $\sin \vartheta \equiv \theta/\theta_*$. The so-called linear model corresponds to taking $c_n = 0$ for $n \neq 1$. More general non-linear models may include also the quadratic term, c_2 , or the square root one, $c_{0.5}$. Convoluting the surface brightness with the caustic point-like source amplification (e.g. the inverse square root singularity for fold caustics, Eq. (6.30)) the shape of the light curve can be obtained for different values of the limb darkening parameters, and these can then be used to fit the observations. As an example, we show in Figure 6.11 the function G introduced in Eq. (6.32), describing the smoothing of the fold amplification by a linear limb darkened source with $c_1 = 1$ ($I = I(0)\sqrt{1 - x^2 - y^2}$), which is given by

$$G_1(\eta) = \frac{3}{4} \int_{\max(\eta, -1)}^1 dx \frac{1 - x^2}{\sqrt{x - \eta}} \Theta(1 - \eta). \quad (6.36)$$

A quite precise limb darkening measurement was obtained by the PLANET Collaboration [Al99a] for a K giant in the galactic bulge, the MACHO 97-BLG-28 event. The event had a cusp crossing that was accurately and intensively monitored. This allowed to fit both the linear and the square root limb darkening coefficients in the I and V bands. Other events for which limb darkening measurements have been obtained involved fold caustic crossings due to binary lenses [Af00; Al00b; Al01a], for which a determination of the linear coefficients has been possible.

6.2.3 Parallax measurements

The original proposal for measuring the Einstein ring projection into the observer's plane, \tilde{r}_E , was based in exploiting the differences in the light curve of a microlensing event observed from two faraway points [Re66]. These differences arise because the apparent trajectory of the source relative to the lens position will look different from the two observing positions. In particular, if the relative motion between the telescopes can be neglected,

the trajectories will look like parallel lines with different impact parameters u_0 and different times of closest approach to the source t_0 . Since the typical values of \tilde{r}_E are given by

$$\tilde{r}_E \simeq 4 \text{ AU} \sqrt{\left(\frac{M}{0.3 M_\odot}\right) \left(\frac{D_{OL}}{D_{LS}}\right) \left(\frac{D_{OS}}{8 \text{ kpc}}\right)}, \quad (6.37)$$

in order to have significant differences between the light curves the second telescope should be located at a distance $\mathcal{O}(\text{AU})$ from the Earth [Go94b; Go95], and hence should be on board of a satellite in heliocentric orbit.

From the light curves it is possible to obtain the values of u_0 and t_0 as seen from the Earth (u_0^\oplus, t_0^\oplus) and from the satellite (u_0^{sat}, t_0^{sat}). At any given time, the separation between the trajectories in the lens plane, measured in units of the Einstein radius, will be given by

$$\Delta u_\pm \equiv |\mathbf{u}^\oplus(t) - \mathbf{u}_\pm^{sat}(t)| = \sqrt{(u_0^\oplus \pm u_0^{sat})^2 + (t_0^\oplus - t_0^{sat})^2 / t_E^2}. \quad (6.38)$$

The two results corresponding to the plus and minus signs reflect the fact that from the values of u_0 and t_0 alone it is not possible to know if the source trajectory as seen from the Earth and from the satellite passed on the same side or on opposite sides of the lens. The two possible situations are exemplified in Figure 6.12.

From the measurement of Δu and the knowledge of the Earth–satellite separation d_{sat} measured orthogonally to the l.o.s., one can determine \tilde{r}_E , since $\tilde{r}_E \Delta u = d_{sat}$, as it can be seen from Figure 6.12. Then,

$$\tilde{r}_E = \frac{d_{sat}}{\Delta u}. \quad (6.39)$$

The main problem of this approach is the degeneracy in the determination of Δu . Fortunately, this degeneracy can in principle be broken using the tiny difference in the time scales measured from the Earth and from the satellite, which arises due to the relative motion among them and is proportional to Δu [Go95].

Up to the present time, no parallax determinations have however been performed using this technique, since no telescope on a satellite in heliocentric orbit has been available. On the other hand, for some microlensing events, those lasting several months, it has been possible to measure the parallax directly from the ground, exploiting the fact that the orbital motion of the Earth around the Sun implies that the lens veloc-

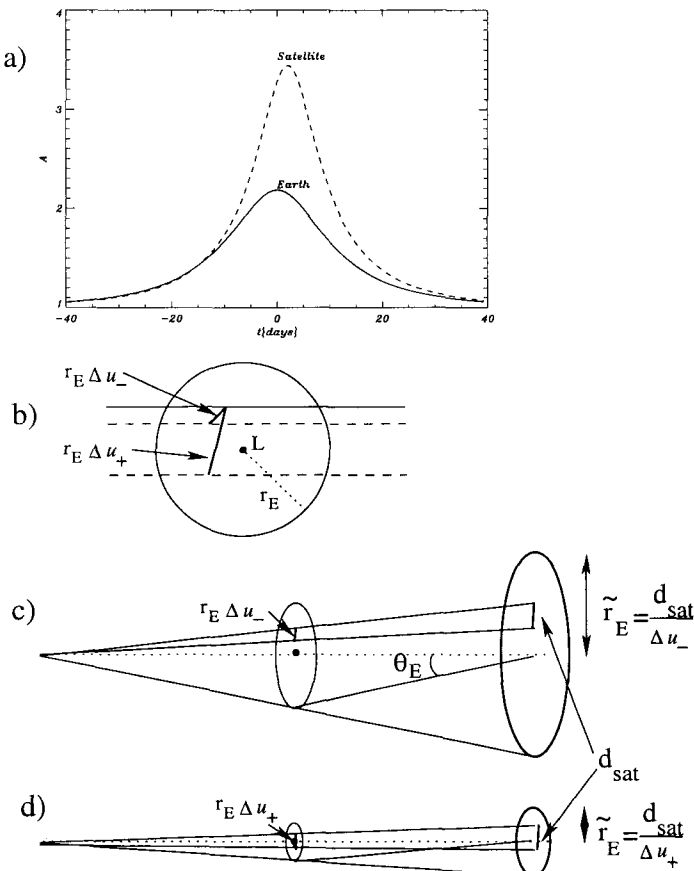


Fig. 6.12 Measurement of \tilde{r}_E using parallax from the Earth and a satellite at a distance d_{sat} . a) Light curves as measured from the Earth ($u_0^{\oplus} = 0.5$) and the satellite ($u_0^{sat} = 0.3$) with $\Delta t_0 = 2$ days. b) Two possible values of Δu corresponding to the source trajectory as seen from the Earth (solid line) and the satellite (dashed lines) and passing through the same (Δu_-) or opposite (Δu_+) sides of the lens. c) and d) The two different determinations of $\tilde{r}_E = d_{sat}/\Delta u$ resulting from the two possible values of Δu . The value of \tilde{r}_E obtained from Δu_+ is significantly smaller than that obtained from Δu_- .

ity with respect to the line of sight to the source, \mathbf{v}^\perp , is non uniform, giving rise to a predictable correction to the light curve. This has actually been observed for a few events towards the bulge [Al95; Be97c; So01] and towards the Carina spiral arm [Ma99]. Figure 6.13 shows the

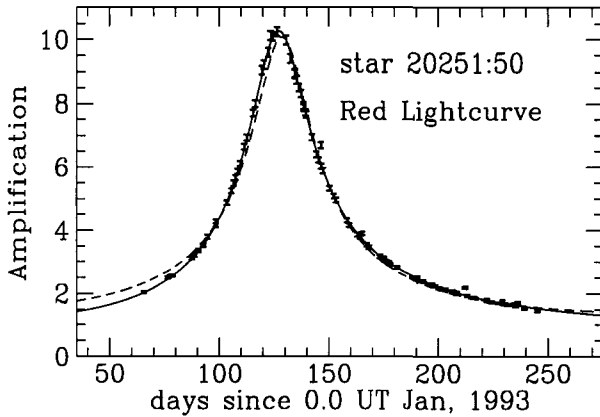


Fig. 6.13 First observation of parallax in a microlensing event by the MACHO collaboration. The dashed line is the fit without taking into account the Earth motion while the solid line does include it (courtesy of C. Alcock, reproduced from [Al95] with permission from *The Astrophysical Journal*).

light curve fit for the first event for which parallax was measured [Al95].

Parallax measurements are more feasible when the lens is closer to the observer, as \hat{r}_E is smaller in this case. Then, the non observation of parallax in long duration events can be interpreted as evidence for a lens close to the source. This was the case for example for the EROS2 SMC event, which lasted 123 days but had no observable parallax, favoring the interpretation that the lens is in the SMC [Pa98b].

Another effect related to the parallax can occur when the source belongs to a binary system. The light curve due to the binary star should be just a superposition (weighted by each source luminosity) of the individual source light curves [Gr92]. However, if the binary orbital period is comparable or shorter than the microlensing event duration, it can give rise to a measurable correction to the light curve with respect to the static case [Ha97b]. This effect is somehow the inverse of the parallax associated to the Earth motion which was discussed above. For the correction to be significant, it is necessary that the separation between the sources be not much smaller than the Einstein radius projected onto the source plane, \hat{r}_E . The observation of this effect also allows a better determination of the physical parameters.

From the light curve fit, the ratio of \hat{r}_E to the semi-major axis of the binary orbit can be measured, as well as the binary period. The total mass of the source system can be determined from the color-magnitude relation. The semi-major axis is then obtained from the mass and period according to Kepler's laws, and this provides a reference scale in the source plane which fixes the value of \hat{r}_E . The proper motion can then be determined as

$$\mu = \frac{v^\perp}{D_{OL}} = \frac{\hat{r}_E}{D_{OST_E}}. \quad (6.40)$$

This effect has been observed in the MACHO 96-LMC-2 event, for which relatively small values of μ are preferred, favoring the interpretation that the lens belongs to the LMC [Al01d].

6.3 Astrometric microlensing

In the previous Sections we have discussed the microlensing searches and the methods used to extract information about the lenses and sources by studying the light curve observations. These studies, based only on the measurement of flux variations as a function of time, are known as photometric microlensing. The angular separation of the multiple images formed by microlensing events within the Galaxy or towards the Magellanic Clouds are ~ 1 mas, and thus they are unresolvable for existing detectors. However, during a microlensing event also the centroid of the combined images is expected to move around by ~ 1 mas, and it turns out to be easier to accurately position an image than to resolve an angular separation. The accuracy needed to follow the centroid shift during a microlensing event will actually be reached in a near future using the space based interferometers *SIM* and *GAIA* (for instance, the *Space Interferometry Mission* will have an angular resolution ~ 10 mas and a positional accuracy ~ 4 μ as for stars as faint as 20 mag), and also ground based ones using 8-10 m class telescopes could be helpful for these measurements.

For a point-like lens, the location of the centroid of the combined images can be obtained from Eqs. (3.7) and (3.20) as

$$\vec{\vartheta} \equiv \frac{A_+ \vec{\theta}_+ + |A_-| \vec{\theta}_-}{A_+ + |A_-|} = \theta_E \frac{\mathbf{u}(3 + u^2)}{2 + u^2}, \quad (6.41)$$

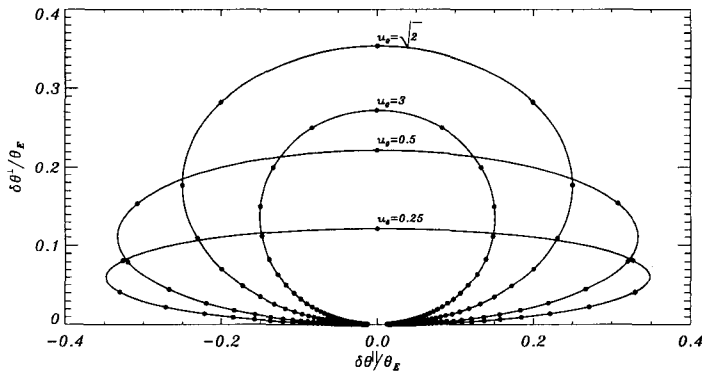


Fig. 6.14 Shifts of the image centroid in units of the Einstein angle for a source moving in the horizontal direction for different values of the impact parameter u_0 . The dots along the trajectories correspond to the positions at times separated by t_E .

and the centroid shift relative to the source position results

$$\delta\vec{\vartheta} \equiv \vec{\vartheta} - \vec{\beta} = \theta_E \frac{\mathbf{u}}{2 + u^2}. \quad (6.42)$$

The maximum shift occurs for $u = \sqrt{2}$ and is given by $\delta\vartheta_{max} = \theta_E/\sqrt{8}$. Hence, the centroid shift turns out to be proportional to the Einstein angle, and thus astrometric measurements of ongoing microlensing events can be used to determine θ_E and to better characterize the lens parameters [Wa95; Ho95; Mi95].

If the motion of the source relative to the lens is approximated as rectilinear and uniform, adopting coordinates in the directions parallel and perpendicular to the source motion, one has $\mathbf{u} = (\Delta t/t_E, u_0)$, with $\Delta t = t - t_0$. This gives for the centroid shift

$$\begin{aligned} \delta\vartheta^{\parallel}(\Delta t) &= \theta_E \frac{\Delta t/t_E}{2 + u_0^2 + (\Delta t/t_E)^2}, \\ \delta\vartheta^{\perp}(\Delta t) &= \theta_E \frac{u_0}{2 + u_0^2 + (\Delta t/t_E)^2}. \end{aligned} \quad (6.43)$$

The trajectory of the centroid is shown in Figure 6.14 for different values of u_0 . These are ellipses with semi-major axis (in the direction of motion) given by

$$a = \frac{\theta_E}{2\sqrt{2 + u_0^2}}, \quad (6.44)$$

and semi-minor axis (in the orthogonal direction) given by

$$b = \frac{\theta_E u_0}{2(2 + u_0^2)}. \quad (6.45)$$

Then, the measurement of the ellipse allows the determination of θ_E . Combining this with the photometrically determined t_E , the proper motion can be obtained[†]. These measurements also allow to infer the source direction of motion relative to the lens as well as the impact parameter u_0 .

One important advantage of astrometric microlensing is that, for large values of u_0 , the size of the centroid shift falls off rather slowly with the impact parameter ($\delta\vartheta \propto u_0^{-1}$) compared to the behavior of the amplification ($A - 1 \propto u_0^{-4}$). Hence, for large impact parameter events the photometric effect is negligible, while the astrometric effect may remain observable.

One can define, in analogy with the ‘amplification’ optical depth associated to a photometric event, Eq. (5.8), a ‘deflection’ optical depth which would be the fraction of the sky for which the centroid shift is larger than a given threshold value θ_T . Noting that for $u_0 \gg 1$ the centroid shift describes a circle of diameter θ_E/u_0 (see Eqs. (6.44) and (6.45)), one has that in order that this diameter be larger than θ_T the impact parameter has to be smaller than $u_T = \theta_E/\theta_T$. Then, the deflection optical depth is

$$\begin{aligned} \tau_d &= \int_0^{D_{OS}} dD_{OL} \int_0^\infty dm \frac{dn_L}{dm} \pi(r_E u_T)^2 \\ &= \frac{16\pi G^2 D_{OS}}{c^4 \theta_T^2} \int_0^1 dx (1-x)^2 \int_0^\infty dm \frac{dn_L}{dm} m^2. \end{aligned} \quad (6.46)$$

From this expression one can see that the contribution to τ_d from nearby lenses ($x \ll 1$) is enhanced, contrary to the photometric case where the enhancement was in the contribution from lenses at half way to the source. Hence, self-lensing events (from LMC stars in LMC observations, or from bulge stars when looking to the galactic center) will be harder to detect astrometrically.

For the expected accuracy of next generation space interferometers, the deflection optical depth is typically much larger than the amplification one, being for instance $\tau_d \simeq (\theta_T/\mu\text{as})^{-2}$ for bulge stars. This means that in a

[†]The speed of the centroid motion along the astrometric ellipse can also provide a determination of t_E , although the accuracy in the reconstruction of the lens parameters is much poorer using astrometry alone.

survey mode, astrometric observations can provide a large number of microlensing events not detectable by photometric means. On the other hand, the duration of an astrometric event is a factor θ_E/θ_T longer than that of a photometric event, so that they typically last 1–10 yrs, and some events may even be too long for the planned duration of the satellite missions. This also indicates that there is a lot of time available to perform astrometric follow-ups of photometrically observed events.

As the astrometric shift dies off very slowly ($\propto u^{-1}$), lenses close to the l.o.s. but not directly associated to a photometric microlensing event can also cause significant shifts in the apparent position of the source. However, this additional shift should have a much slower variation in time than the one produced by the lens responsible for the photometric event, and hence it should not interfere with the determination of the associated θ_E [Do00].

If a microlensing event is observed photometrically and astrometrically, both t_E and θ_E will be determined. To completely characterize the lens parameters it would then be necessary to also have a parallax measurement. One proposal to obtain the parallax consists in measuring the distortions in the astrometric ellipse arising from the fact that the orbital motion of the Earth (or the satellite) makes that the motion of the source relative to the line of sight to the lens, $\mathbf{u}(t)$, deviates from a rectilinear and uniform one [Pa98a; Bo98]. When this distortion can be measured it is possible to determine \tilde{r}_E , and hence obtain the lens mass. Notice that since the duration of the astrometric event is much longer than t_E , one is not restricted to very long duration events as in the case of photometric parallaxes. However, it was noticed that the relative errors in the astrometric measurement of \tilde{r}_E are much larger than those for θ_E , and that the parallax distortion of the ellipse will be unmeasurably small for a large fraction of the microlensing events [Go99b]. Alternatively, since *SIM* does astrometry by counting photons as a function of the fringe position, it can simultaneously do photometry and it was hence proposed that it could be used (combined with ground-based photometry) to measure \tilde{r}_E through the photometric parallax method described in Section 6.2.3 [Go99b]. Moreover, since from the orientation of the astrometric ellipse it is possible to infer in which side of the lens was the source trajectory, the degeneracy in the parallax determination may be broken.

Then, precision astrometry at few μas will open the window to a systematic determination of the mass, distance and velocity of the lens for individual events, and this will be a very significant step to accurately

characterize the lensing populations.

Astrometric measurements can also play a relevant role in the study of events produced by binary lenses, since signals of binarity can be observed in a larger fraction of these events with this technique. Furthermore, astrometry helps to break the degeneracies present in binary events, since e.g. in close/wide binary fits of a photometric binary event the centroid trajectory is generally very different [Ha99].

Another application of astrometric microlensing could be to determine the masses of nearby stars by measuring the variation of the positions of background stars induced by the transit of the nearby star [Re66; Mi96; Pa96]. In the case of nearby high proper motion stars, both the lens and the source are bright objects so that their proper motion and parallax may be measured. If the astrometric measurement of θ_E can be performed looking to the centroid displacement, the lens parameters will be completely determined. Pairs of lens and source stars for which measurements will be possible can be determined well in advance, and this is actually the only practical method to accurately measure masses of single stars.

6.4 Quasar microlensing

Just after the first observation of a multiple imaged quasar, i.e. the double image of Q0957+561 discovered in 1979, Chang and Refsdal [Ch79] considered the possibility that individual stars in the lensing galaxy could produce an additional lensing effect leading to a change in the luminosity of one of the quasar images as the star moved with respect to the line of sight. Since the Einstein radius associated to this microlensing effect is

$$r_E \simeq 4.26 \times 10^{16} \text{ cm} \sqrt{\frac{M}{M_\odot}} \sqrt{\frac{D_{OS} D_{LS}}{\text{Gpc } D_{OS}}}, \quad (6.47)$$

the associated Einstein radius crossing time will be

$$t_E = \frac{r_E}{v^\perp} \simeq 22.4 \text{ yr} \left(\frac{v^\perp}{600 \text{ km/s}} \right)^{-1} \sqrt{\frac{M}{M_\odot}} \sqrt{\frac{D_{OS} D_{LS}}{\text{Gpc } D_{OS}}}, \quad (6.48)$$

with v^\perp the transverse velocity of the lens with respect to the line of sight. This duration is then quite long for stellar mass lenses with the velocities arising from typical galaxy peculiar velocities or from stellar velocity

dispersions. However, the light curves will not be due to the effect of individual stars, but rather to the collective effects of many of them [Yo81; Pa86b; Ka86]. This can be understood by noting that if one assumes that the mass along the line of sight is dominated by the column density Σ of the lensing galaxy and that most of the column density is due to compact stellar objects (what seems reasonable since multiple images are often close to the central parts of the lensing galaxy, although non-compact dark matter could also be contributing to Σ), the optical depth for microlensing of the quasar images is

$$\tau = \frac{4\pi G}{c^2} \int dD_{OL} \frac{D_{OL} D_{LS}}{D_{OS}} \rho_L \simeq \frac{\Sigma}{\Sigma_{cr}}, \quad (6.49)$$

where Σ_{cr} is the critical density introduced in Eq. (3.26). Hence, we see that in the thin lens approximation the optical depth is just the convergence associated to the macrolens, and this has to be of order unity near the location of the multiple images of a quasar. This means that the light beam trajectory will most likely be affected by several lenses simultaneously.

In the presence of multiple lenses, the number of images and their positions cannot be found analytically. Hence, to compute the magnification of a source, the inverse ray-shooting technique is used [Ka86; Sc87; Wa92]. This method consists in back tracing a very large number of isotropically distributed light rays from the observer's to the source plane, and the amplification is obtained from the density of rays arriving to the source location.

As a result of the combined action of the many lenses, actually a dense and complex structure of caustics will be generated. These caustics are also further affected by the shear produced by the lensing galaxy and its hosting cluster (recall that even a single isolated lens has a non-trivial caustic in the presence of external shear [Ch79]). For instance, Figure 6.15 from Ref. [Wa98] shows the caustic structure associated to a dense stellar field with the convergence $\kappa = 0.36$ and shear $\gamma = 0.44$ corresponding to image A of the quadruply imaged quasar Q2237+0305 (the Einstein cross).

The typical intercaustic separation in the lens plane is set by the Einstein radii of the lenses, and as the source traverses the caustics (near cusps or across folds) large magnification peaks will result in the light curves. The typical duration Δt_c of such caustic crossing peaks will be a sizeable fraction of the Einstein radius crossing time, i.e. $\Delta t_c \simeq (0.1 \div 1)t_E$.

There is another relevant characteristic time, Δt_S , which is related to

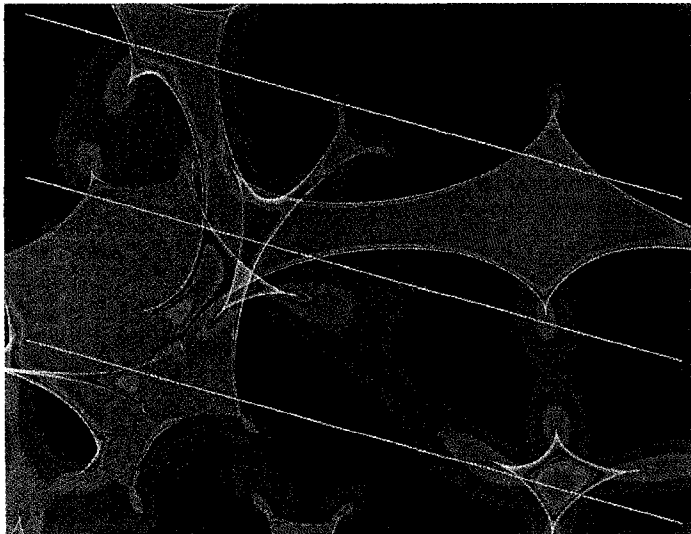


Fig. 6.15 Caustic structure produced by a dense field of stars in the lensing galaxy. The brighter regions correspond to larger magnifications. The lensing parameters are taken according to a model of image *A* of the quasar Q2237+0305: $\kappa = 0.36$ and $\gamma = 0.44$ (courtesy of J. Wambsganss, reproduced from [Wa98]).

the time it takes to the source of radius r_S to cross a fold caustic,

$$\Delta t_S = \frac{r_S}{v^\perp} \frac{D_{OL}}{D_{OS}} \simeq 19 \text{ days} \left(\frac{600 \text{ km/s}}{v^\perp} \right) \left(\frac{r_S}{10^{15} \text{ cm}} \right) \left(\frac{10 D_{OL}}{D_{OS}} \right). \quad (6.50)$$

In the limit $\Delta t_S \ll \Delta t_c$, i.e. if the source is sufficiently compact, the effect of the finite size of the source will be that the discontinuous rise in the magnification produced when the source enters a caustic through a fold (or the discontinuous drop produced when it exits through a fold) will be smoothed out with a characteristic rise time $\sim \Delta t_S$, and also the divergent magnification associated to the fold in the point-like source case will become finite. In the other limit, i.e. for $\Delta t_S \gg \Delta t_c$, all the peaks associated with the caustic crossings are averaged out due to the finite source size effects, leaving only a smooth light curve with variations on the scale of t_E . These behaviors are illustrated in Figure 6.16, where the light curves for the source trajectories corresponding to the three straight lines shown in Figure 6.15 are displayed for the two regimes (small and large source radii).

Hence, if the source is sufficiently compact and the lens is relatively

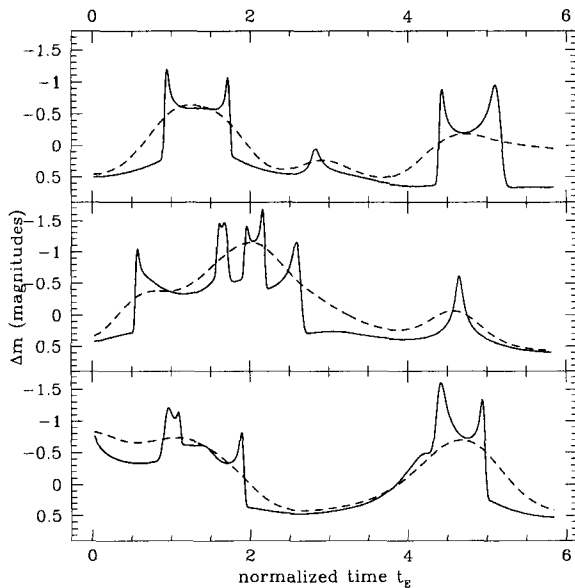


Fig. 6.16 Microlensing light curves for the tracks shown in white in Figure 6.15. The solid and dashed lines indicate the cases of small and large source sizes respectively (courtesy of J. Wambsganss, reproduced from [Wa98]).

closeby ($D_{OL} \ll D_{OS}$), it is possible to have significantly fast changes in the light curve without the need to invoke the presence of large amounts of brown dwarf or planetary lenses. Reversing this line of reasoning, if a rapid non-intrinsic[§] variation in the luminosity of one image is observed, it is possible to infer an upper bound on the source size.

The first microlensing variability observed was that of image *A* of Q2237 +561, reported in 1989 by Irwin et al. [Ir89], which raised by 0.5 mag on a time scale of a few months. Detailed modeling of the typical caustic structures expected from stellar mass lenses (with $m_L \simeq 0.1\text{--}1 M_\odot$) allowed to constrain the optical continuum quasar size to be smaller than 2×10^{15} cm [Wa90]. This quasar is very well suited for microlensing studies, because the very symmetric configuration of the four images implies that the time delay has to be less than a few days, and it is hence easy to know if the

[§]The non-intrinsic character of a luminosity change is established by comparing the light curves of the different images, taking into account their expected time delays.

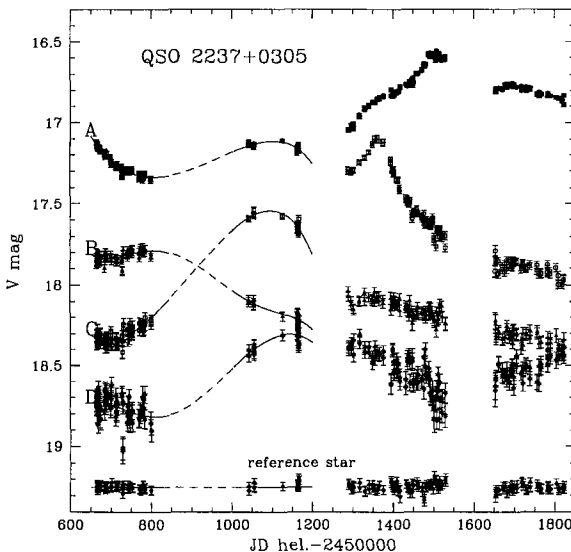


Fig. 6.17 Light curves of the four images of Q2237+0305, from OGLE web page (<http://www.astro.princeton.edu/~ogle/ogle2/huchra.html>, courtesy of P. Woźniak).

light curve variations are not intrinsic. Also, the proximity of the lens ($z_L \simeq 0.04$, while $z_S \simeq 1.7$) attenuates significantly the finite source size effects, allowing for faster luminosity changes to be observed. The most spectacular observations of this quasar have been done in the last years by the OGLE collaboration using Difference Image Analysis, and have shown that significant flux variations occur in all four images, as is shown in Figure 6.17 [Wo00].

Recommended reading

- A. Gould (1996), “Microlensing and the Stellar Mass Function”, Publication of the Astronomical Society of the Pacific **108**, 465.
- A. Gould (2001), “Applications of microlensing to stellar astrophysics”, [astro-ph/0103516](http://arxiv.org/abs/astro-ph/0103516).

Appendix A

Cosmology tools

A.1 The Friedmann-Robertson-Walker Universe

On very large scales the Universe is to a good approximation homogeneous and isotropic. This property, known as the cosmological principle, was initially postulated as a simplifying assumption to obtain cosmological solutions in General Relativity. However, there is now observational evidence that it holds, coming essentially from the fact that the cosmic microwave background is nearly isotropic and from the distribution of galaxies at the largest scales observed. If we consider the matter as being a fluid, clearly the isotropy will only be realized in a coordinate system in which the fluid is at rest (for instance we know that the Earth is not exactly at rest with respect to that system because of the non-zero dipole component of the cosmic microwave background temperature anisotropies). In these so-called comoving coordinates, the general metric describing the Universe is the Friedmann-Robertson-Walker one, which is given by

$$ds^2 = c^2 dt^2 - a^2(t) d\ell^2, \quad (\text{A.1})$$

where $a(t)$ is called the scale factor and takes into account the expansion of the Universe, and the spatial metric can be written as

$$d\ell^2 = d\chi^2 + r^2(\chi) (d\theta^2 + \sin^2 \theta d\phi^2), \quad (\text{A.2})$$

where χ , θ and ϕ are the comoving coordinates, which are constant for observers moving with the fluid, and the time measured by their clocks, t , is called the proper time.

This form of the metric clearly enforces the isotropy, while homogeneity can be shown to require that the function $r(\chi)$ be

$$r(\chi) = \begin{cases} \frac{1}{\sqrt{k}} \sin(\sqrt{k}\chi) & \text{for } k > 0 \\ \chi & \text{for } k = 0 \\ \frac{1}{\sqrt{-k}} \sinh(\sqrt{-k}\chi) & \text{for } k < 0 \end{cases} \quad (\text{A.3})$$

The parameter k describes the curvature of the spatial sections and hence determines whether the Universe is closed, flat or open. Notice that a particular choice which is often adopted is to take as radial coordinate directly r rather than χ , and in this case the spatial part of the metric becomes

$$d\ell^2 = \frac{dr^2}{1 - kr^2} + r^2 (d\theta^2 + \sin^2 \theta d\phi^2). \quad (\text{A.4})$$

Assuming that the matter consists of a perfect fluid with energy momentum tensor $T_{ij} = \text{diag}(\rho, p, p, p)$, with ρ the energy density and p the pressure, one can show (computing the Christoffel symbols associated to this metric) that the (0,0) component of the Einstein equations leads to the so-called Friedmann equation

$$\left(\frac{\dot{a}}{a}\right)^2 + \frac{kc^2}{a^2} = \frac{8\pi G}{3} \rho_{tot}, \quad (\text{A.5})$$

where $\rho_{tot} = \rho_r + \rho_m + \rho_\Lambda$ is the sum of the radiation, non-relativistic matter and vacuum energy densities, with $\rho_\Lambda \equiv \Lambda/8\pi G$.

The Hubble constant measures the rate of expansion of the scale factor, and is defined as

$$H \equiv \frac{\dot{a}}{a}. \quad (\text{A.6})$$

Its present value is conventionally parameterized as $H_0 \equiv h$ 100 km/s/Mpc, with different observations giving $0.5 < h < 0.8$.

There is a second independent equation which comes from the spatial part of the Einstein equation, or alternatively from the energy momentum conservation relation (which as we have seen is not independent from the Einstein equation). This last is actually simpler, and leads to

$$\frac{d}{dt}(\rho a^3) = -p \frac{d}{dt} a^3. \quad (\text{A.7})$$

It can readily be solved if we know the equation of state of the fluid, which in general will be of the form $p = \alpha\rho$, with $\alpha = 0$ for non-relativistic matter, $\alpha = 1/3$ for radiation and $\alpha = -1$ for vacuum energy (Λ). Hence, one gets $\rho \propto a^{-3(1+\alpha)}$, so that the corresponding energy density evolves as

$$\rho_r = \rho_r^0 \left(\frac{a(t_0)}{a(t)} \right)^4, \quad \rho_m = \rho_m^0 \left(\frac{a(t_0)}{a(t)} \right)^3, \quad \rho_\Lambda = \rho_\Lambda^0, \quad (\text{A.8})$$

where ρ_i^0 denotes the present values and the usual convention is to take $a(t_0) = 1$.

It is also convenient to introduce the critical density as

$$\rho_{crit} = \frac{3H_0^2}{8\pi G}, \quad (\text{A.9})$$

and define the density parameters $\Omega_i \equiv \rho_i^0 / \rho_{crit}$. According to observational determinations

$$\Omega_r h^2 = 3.6 \times 10^{-5}, \quad \Omega_m = 0.35 \pm 0.1. \quad (\text{A.10})$$

As the energy density in relativistic matter (CMB photons and relic neutrinos) evolves as a^{-4} and that in non-relativistic matter as a^{-3} , at a sufficiently early time the density in radiation should have equalled that in matter. This happened when the scale factor was $a_{eq} = 2.7 \times 10^{-4}(0.16/\Omega_m h^2)$. Before that the Universe was radiation dominated, and during that period $a(t) \propto t^{1/2}$, while for $a > a_{eq}$ the Universe became matter dominated, with $a(t) \propto t^{2/3}$.

Recent observations indicate that $\Omega_\Lambda = 0.65 \pm 0.1$ [Ri98; Pe99]. This would mean that the Universe became cosmological constant dominated for $a > a_\Lambda = (\Omega_m/\Omega_\Lambda)^{1/3} \simeq 0.8$.

A.2 The distance scales

If we consider light emitted at a certain time t_e and arriving to an observer at time t_o , the comoving (or coordinate) distance between the emission and observation points is, setting the origin at the observer's position,

$$\chi(t_e, t_o) = \int_o^e d\chi. \quad (\text{A.11})$$

In terms of the time traveled by the photon, one has (since $ds = 0$) that $d\chi = -c dt/a$, with the minus sign due to the fact that as the photon travels

towards the observer, its coordinate distance is reduced as time increases. Hence,

$$\chi(t_e, t_o) = c \int_{t_e}^{t_o(t_e)} \frac{dt}{a}. \quad (\text{A.12})$$

By definition the comoving distance for a given source at rest will not change if we change the particular emission time t_e considered, and this leads to

$$0 = \frac{d}{dt_e} \chi(t_e, t_o) = \frac{c}{a(t_o)} \frac{dt_o}{dt_e} - \frac{c}{a(t_e)}. \quad (\text{A.13})$$

Notice that the fact that the Universe is expanding changes the proper time interval measured by the observer with respect to that at the emission point. Since the photon frequencies at the emission and observation points have to satisfy $\nu_e/\nu_o = dt_o/dt_e$, one has

$$\frac{a(t_o)}{a(t_e)} = \frac{dt_o}{dt_e} = \frac{\nu_e}{\nu_o} = \frac{\lambda_o}{\lambda_e} = 1 + z, \quad (\text{A.14})$$

where the redshift of the emitter z is defined as the relative change in the photons wavelength, i.e. $z \equiv (\lambda_o - \lambda_e)/\lambda_e$. The redshift is then a direct measure of the amount of expansion since a given event, and it is then often used to measure times in the expanding Universe.

It is convenient to write down the comoving distance in terms of the redshift, using that

$$H = \frac{\dot{a}}{a} = \frac{d}{dt} \log \left(\frac{a(t)}{a(t_o)} \right) = \frac{d}{dt} \log \left(\frac{1}{1+z} \right) = -\frac{1}{1+z} \frac{dz}{dt}. \quad (\text{A.15})$$

We have then

$$\chi(z_e, z_o) = \frac{c}{H_0} \int_{z_o}^{z_e} dz F(z), \quad (\text{A.16})$$

with $F(z) \equiv H_0 / ((1+z)aH)$, i.e.

$$F(z) = [(1+z)^4 \Omega_r + (1+z)^3 \Omega_m + (1+z)^2 (1 - \Omega_{tot}) + \Omega_\Lambda]^{-1/2}, \quad (\text{A.17})$$

where using the Friedmann equation we wrote $kc^2/a^2(t_o) = H_0^2(\Omega_{tot} - 1)$. Notice that since the density in radiation at present is very small, $\Omega_r < 10^{-4}$, the function $F(z)$ depends essentially only on Ω_m and Ω_Λ .

In cosmological applications of gravitational lensing, we have seen that the physical distance involved is always the angular distance, defined as the ratio between a length in the direction transverse to the line of sight (i.e. with $d\chi = 0$), measured at the time t_e , and the angle it subtends, being then

$$D_{ang}(z_e, z_o) = a(z_e)r(\chi(z_e, z_o)). \quad (\text{A.18})$$

With this notation, one has for instance $D_{LS} = D_{ang}(z_S, z_L)$. The other distance measure often encountered is the luminosity distance, defined such that the flux received from a source with intrinsic luminosity \mathcal{L} is

$$\mathcal{S} = \frac{\mathcal{L}}{4\pi D_{\mathcal{L}}^2}. \quad (\text{A.19})$$

If the source is at coordinate distance $\chi(z_e, z_o)$, the photons will be distributed at the time of observation on a surface of area

$$A = 4\pi \left(a(z_o)r(\chi(z_e, z_o)) \right)^2, \quad (\text{A.20})$$

but their energy is redshifted by a factor $a(z_e)/a(z_o)$ and also photons emitted in an interval dt will be received over a longer interval $a(z_o)/a(z_e)dt$. Putting all these factors together one has

$$\mathcal{S} = \frac{\mathcal{L}}{4\pi (a(z_o)r(\chi(z_e, z_o)))^2} \left(\frac{a(z_e)}{a(z_o)} \right)^2, \quad (\text{A.21})$$

and hence

$$D_{\mathcal{L}}(z_e, z_o) = \frac{a(z_o)^2}{a(z_e)} r(\chi(z_e, z_o)) = \left(\frac{a(z_o)}{a(z_e)} \right)^2 D_{ang}(z_e, z_o). \quad (\text{A.22})$$

Figure A.1 shows the angular distances as a function of the redshift for different cosmological models and for an observer at $z = 0$. The corresponding luminosity distances can be obtained just by multiplying them by a factor $(1+z)^2$. For instance, for the Einstein-de Sitter Universe, corresponding to a flat matter dominated Universe (dashed line in Figure A.1), a source at $z = 2$ will be at an angular distance $D_{ang}(2, 0) \simeq 0.28c/H_0 \simeq 0.85 \text{ Gpc}/h$, while its luminosity distance will be a factor of nine larger.

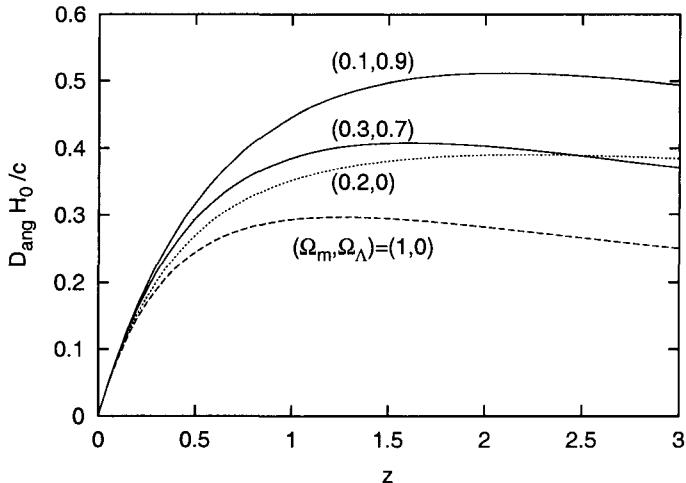


Fig. A.1 Angular diameter distance versus redshift for four different cosmological models, corresponding to flat Universes with $(\Omega_m, \Omega_\Lambda) = (1, 0)$, $(0.3, 0.7)$ and $(0.1, 0.9)$, and an open Universe with $\Omega_m = 0.2$ and $\Omega_\Lambda = 0$.

A.3 Large scale structures

The distribution of matter in the Universe can be taken as homogeneous only when the average over large volumes is considered ($\gg (100 \text{ Mpc})^3$), but at smaller scales we know that matter forms galaxies, which are distributed forming clusters, superclusters, voids, etc.. The formation of these large scale structures has been one of the most active fields of research in cosmology during the last years. We present in this Section just a brief account of the concepts appearing in our discussion of the weak lensing phenomena in Chapter 4. The interested reader can find a deep coverage of these topics in the recommended readings at the end of the Appendix.

Large scale structures are believed to have grown by gravitational instability from initially small inhomogeneities in the matter distribution. In this scheme the structure of spacetime is perturbed by small amplitude fluctuations in the gravitational potential $\varphi(\vec{x}, t)$. The line element, using comoving coordinates and the conformal time $d\tau \equiv dt/a(t)$, can be written

as

$$ds^2 = a^2(\tau) \left\{ \left(1 + 2\frac{\varphi}{c^2}\right) d\tau^2 - \left(1 - 2\frac{\varphi}{c^2}\right) [d\chi^2 + r^2(\chi)(d\theta^2 + \sin^2 \theta d\phi^2)] \right\}. \quad (\text{A.23})$$

The presence of $\varphi(\vec{x}, t)$ accounts for the variations in the spacetime geometry caused by density fluctuations. The perturbed Einstein's field equations imply a cosmological version of the classical Poisson equation of Newtonian gravity

$$\nabla^2 \varphi = a^2 4\pi G \delta \rho, \quad (\text{A.24})$$

where the source term is proportional to the density fluctuation, given by the difference between the actual total mass density and its mean value $\bar{\rho}$, $\delta\rho(\vec{x}, t) \equiv \rho(\vec{x}, t) - \bar{\rho}(t)$. Instead of $\delta\rho$, the density contrast $\delta \equiv \delta\rho/\bar{\rho}$ is often used and is usually decomposed in Fourier modes[¶],

$$\delta(\vec{x}) = \int \frac{d^3 k}{(2\pi)^3} e^{-i\vec{k}\cdot\vec{x}} \delta(\vec{k}). \quad (\text{A.25})$$

This is very convenient as each mode evolves independently while perturbations are small (linear regime).

There are different physical mechanisms to explain the origin of the fluctuations in the Early Universe. These are in general stochastic processes which predict the root mean square amplitude of the fluctuations and other statistical properties, rather than a particular value of the density at each spacetime point. One of the most relevant quantities to describe the perturbations is the two point correlation function, defined as

$$\xi(\vec{r}) = \langle \delta(\vec{x}) \delta(\vec{x} + \vec{r}) \rangle, \quad (\text{A.26})$$

where the angle brackets denote an ensemble average over realizations of the stochastic process, that under the ergodic hypothesis is equivalent to an average in a large volume over all the pairs of points separated by \vec{r} . Using Eq. (A.25) we can write (A.26) as

$$\xi(\vec{r}) = \int \frac{d^3 k}{(2\pi)^3} e^{-i\vec{k}\cdot\vec{r}} |\delta(\vec{k})|^2. \quad (\text{A.27})$$

[¶]This is a correct approach for a flat spatial geometry. For curved spatial sections, plane waves are not an appropriate basis, but in the study of many problems this complication can be neglected, as long as the distances involved are much smaller than the Universe curvature radius size.

A usual assumption is that perturbations are statistically homogeneous, which means that there are no preferred directions in space. Then, ξ is only function of the modulus of the distance between the two points entering in the product, r ; and its Fourier transform, the power spectrum $P_\delta(k) \equiv |\delta(k)|^2$, depends only on k , the modulus of the wave number, i.e.

$$\langle \delta(\vec{k})\delta(\vec{k}') \rangle = (2\pi)^3 \delta^{(3)}(\vec{k} - \vec{k}') P_\delta(k). \quad (\text{A.28})$$

The angular integration can then be performed, leading to

$$\xi(r) = \int dk \frac{k^2}{2\pi^2} \frac{\sin(kr)}{kr} P_\delta(k). \quad (\text{A.29})$$

Several models for the primordial perturbations lead to power spectra of the power law type, $P_\delta(k) \propto k^n$. The $n = 1$ case, known as Harrison Zeldovich spectrum, is favored by several observational results and also most inflationary models predict initial perturbations with n close to unity.

At later times, the gravitational evolution of the perturbations modifies the primordial power spectrum. The linear perturbation theory shows that in an Einstein-de Sitter Universe the gravitational potential remains constant with time. Then, according to Eq. (A.24) the density contrast δ should grow like a^2 during the radiation era and linearly with a during the matter era. If $\Omega_\Lambda \neq 0$ or if the Universe is not flat, the growth of perturbations is suppressed at the late times when the effect of the cosmological constant or the curvature becomes non-negligible (an accurate fit for the suppression of growth is given in [Ca92]). Combining these different evolutions, a growth factor $D(a)$ is usually defined, which gives the overall scale relating the amplitude of the late time fluctuations to the primordial ones. However, also the shape of the power spectrum is modified at late times, as different modes have evolved differently. A complete computation of these effects, which strength depend on the cosmological model, involves solving a system of Boltzmann equations for the evolution of the phase space distribution of the different components, taking into account the interactions among them (see e.g. [Bo87; Ma95a]). These components include a mixture of matter (collisionless dark matter particles and baryons) and relativistic particles (photons and collisionless neutrinos), and the Boltzmann equations have to be solved numerically [Se96b].

The result for the present day power spectrum is usually summarized in the so-called transfer function $T(k)$, giving the ratio of the late time

amplitude of each mode to its initial value. The late time power spectrum $P_\delta(k, a)$ is in this way related to the primordial one $P_\delta(k, a_i)$ through

$$P_\delta(k, a) = \left(\frac{D(a)}{D(a_i)} \right)^2 T^2(k, a) P_\delta(k, a_i). \quad (\text{A.30})$$

There is in general a relative suppression of the strength of the small wavelength modes, because before matter radiation equality modes with wavelengths smaller than the horizon size are prevented from growing by radiation pressure^{||}. In an Einstein-de Sitter Universe, this leads to a spectrum $P_\delta \propto k$ for the large wavelength modes entering the horizon during matter domination and $P_\delta \propto k^{-3}$ for the small wavelength modes that entered the horizon during the radiation era. The transition between these two behaviors takes place at scale $\lambda \simeq 12(\Omega_m h^2)^{-1}$ Mpc, corresponding to the Hubble radius at matter-radiation equality. Figure A.2 shows the shape of the transfer function for an $(\Omega_\Lambda, \Omega_m, \Omega_b) = (0.65, 0.3, 0.05)$ Universe. A complete expression for the transfer function is usually obtained by fitting an appropriate functional form to the numerical results as a function of the cosmological parameters [Ba86a; Pe94; Su95]. A further point to be taken into account for small scales is that when at late times perturbations depart from the linear behavior, a transfer of power to the smaller scales results. An analytic procedure to take into account this effect has been proposed by Hamilton [Ha91] and a fitting formula for the non linear power spectrum has been obtained by Peacock and Dodds [Pe96].

The procedure just discussed provides a description of the overall shape of the power spectrum, but the global amplitude is still free and has to be fixed to match observations. The two standard procedures to achieve this are either to fit the amplitude of the gravitational potential perturbations at very large scales using the CMB anisotropy data, or to fit the root mean square density fluctuations when smoothed on spheres of $8h^{-1}\text{Mpc}$ (the scale associated to rich clusters, which are the largest non-linear systems at present), known as σ_8 , which is observed to be very close to unity.

^{||}Notice that the physical wavelength associated to a given wavenumber k grows as $a(t)$ as the Universe expands. The horizon size, corresponding to the causal contact region within which microphysics can affect the evolution of the perturbations, is proportional to the inverse of the Hubble expansion rate H^{-1} and grows as a^2 during the radiation era and as $a^{3/2}$ in the matter dominated one. Thus, different modes enter the horizon ($\lambda = a(t)/k = cH^{-1}$) at different times.

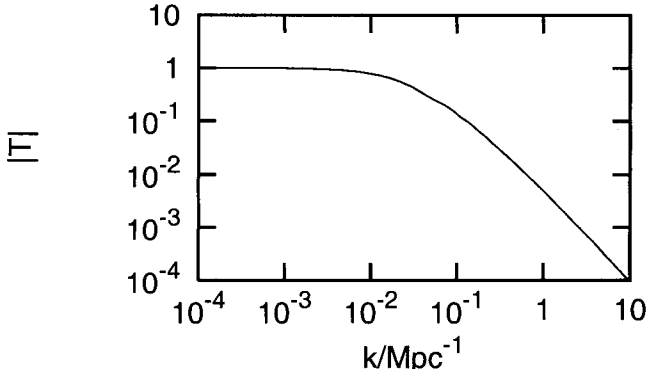


Fig. A.2 Transfer function for a lambda cold dark matter Universe with $h = 0.6$.

Let us finally point out that the distribution of galaxies (and other luminous objects) need not necessarily follow the distribution of mass. The galaxy formation process is still not fully understood and there are arguments supporting the idea that the efficiency of galaxy formation was enhanced in dense environments. This phenomenon is called bias and is generally described introducing a bias parameter b defined through

$$\delta_{gal} = b\delta_{mass}. \quad (\text{A.31})$$

A.4 Cosmic Microwave Background anisotropies

Since its discovery by Penzias and Wilson in 1965 [Pe65] the Cosmic Microwave Background (CMB) has played a major role in cosmology. The existence of this background is a necessary consequence of a hot phase in the early Universe, when the temperature was large enough for atoms to stay ionized, and thus it became one of the strongest evidences in favor of the hot Big Bang model. Its spectrum is that of a black body with temperature $T_0 \simeq 2.726^\circ\text{K}$.

The other important property of the CMB is that it is nearly isotropic. The CMB photons have freely traveled through the Universe since the recombination time, when electrons combined with protons to form hydrogen and the Universe became transparent to photons. This happened at a redshift $z_{rec} \sim 1100$, during the matter dominated era, and thus the CMB

contains information about the conditions of the Universe at that time. The temperature anisotropy for a given direction of observation $\vec{\gamma}$ is measured by the quantity

$$\frac{\Delta T}{T}(\vec{\gamma}) = \frac{T(\vec{\gamma}) - \bar{T}}{\bar{T}}, \quad (\text{A.32})$$

where \bar{T} is the mean value of the temperature. An anisotropy at the level of 10^{-3} with dipole angular dependence ($\propto \cos \theta$) has been detected and it reflects the motion of our reference system with respect to the ‘CMB rest frame’. After subtracting this, a much more isotropic background remains, which is an important piece of evidence for the large scale homogeneity of the Universe. Anisotropies with amplitudes $\Delta T/T \sim 10^{-5}$ have been detected by the COBE satellite in 1992 [Sm92], and they encode valuable information about the primordial inhomogeneities in the energy density that gave rise to the observed structures. Different physical effects are responsible for the anisotropies observed. At large angular scales ($\theta > 1.7^\circ (\Omega_m + \Omega_\Lambda)^{1/2} (z_{rec}/1100)^{-1/2}$, the size of the horizon at the recombination time) temperature anisotropies arise through the Sachs-Wolfe effect [Sa67]. This is due to the fact that photons coming from different directions suffer different redshift because of the fluctuations in the gravitational potential φ at the last scattering surface (a spherical shell around us with radius $\chi_{rec} = \tau_0 - \tau_{rec}$, from where the CMB photons we detect today started their trip at the recombination time).

At smaller angular scales, fluctuations were inside the horizon at the recombination time, and the anisotropies reflect the dynamical evolution of the inhomogeneities in the photon fluid. Before recombination, photons were tightly coupled to baryons through electromagnetic interactions in the plasma. Two competing effects were relevant at that time: on one side gravity pulled the fluid towards the gravitational potential wells, and on the other side the radiation pressure was opposing to the fluid compression. As a result, acoustic oscillations developed. These started at the time when the wavelength of the mode considered entered the horizon, and hence the recombination time catches the different wavelength modes at different phases of their oscillation cycle, leading to a series of peaks and troughs in the anisotropy amplitude.

The anisotropies in the celestial sphere are described through an expansion

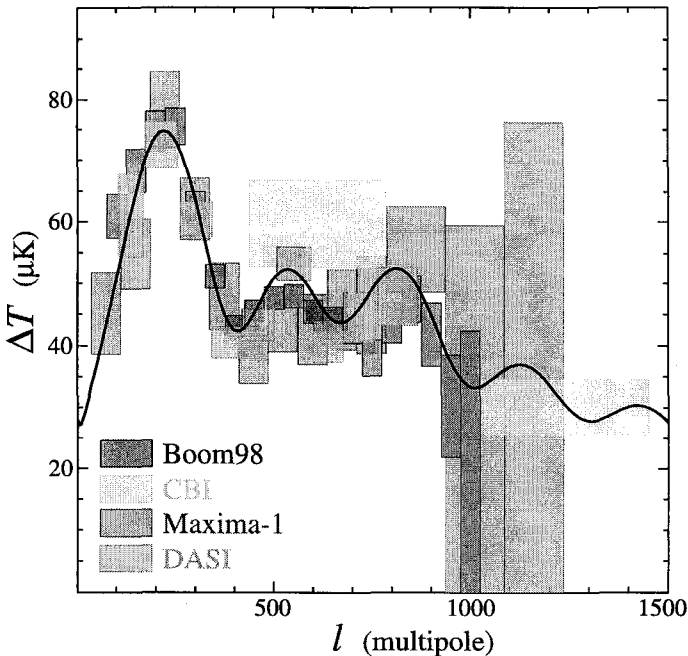


Fig. A.3 Angular power of CMB anisotropies and summary of measurements from different groups (courtesy of W. Hu).

sion in spherical harmonics, i.e.

$$\frac{\Delta T}{T}(\vec{\gamma}) = \sum_{\ell,m} a_{\ell m} Y_{\ell m}(\vec{\gamma}). \quad (\text{A.33})$$

The correlation function is defined as

$$\mathcal{C}(\theta) \equiv \left\langle \frac{\Delta T}{T}(\vec{\gamma}_1) \frac{\Delta T}{T}(\vec{\gamma}_2) \right\rangle_{\vec{\gamma}_1, \vec{\gamma}_2 = \cos \theta}, \quad (\text{A.34})$$

where the mean over all the pair of directions separated by an angle θ has to be taken. Furthermore, an ensemble average over realizations of the fluctuations has to be done. Using Eq. (A.33) and simple properties of the spherical harmonics, the correlation function can be rewritten as

$$\mathcal{C}(\theta) = \frac{1}{4\pi} \sum_{\ell} (2\ell + 1) C_{\ell} P_{\ell}(\cos \theta), \quad (\text{A.35})$$

where we have defined the angular power spectrum

$$C_\ell = \frac{1}{2\ell + 1} \sum_m \langle |a_{\ell m}|^2 \rangle,$$

and P_ℓ are the Legendre polynomials.

The power spectrum contains information about many cosmological parameters, including the geometry of the Universe, the contribution to Ω from baryons, dark matter and cosmological constant, the Hubble constant, the amplitude and spectral index of primordial fluctuations, the ionization history, etc.. The computation of the C_ℓ for a given set of parameters is complex, but fortunately there is a public code available for this task [Se96b]. On the other hand, much observational effort is being devoted to accurately measure the power spectrum and put constraints on these parameters. The COBE satellite studied the large angular scales (corresponding to small values of ℓ) where the Sachs Wolfe effect is dominant. Figure A.3 summarizes the present observational results at larger values of ℓ , and shows some model fit to the data. The peaks here arise from the acoustic oscillations and the balloon missions BOOMERANG [Ne01], MAXIMA [Le01] and DASI [Ha01] already provide a determination of the location and heights of the first three peaks. Two new satellites (MAP and PLANCK) will produce full sky CMB maps with small scale resolution, obtaining precision measurements of the cosmological parameters involved.

Recommended reading

- E. Kolb and M. Turner (1990), “The Early Universe”, Addison-Wesley, Redwood City, California, U.S.A..
- P. J. E. Peebles (1993), “Principles of Physical Cosmology”, Princeton University Press, Princeton, U.S.A..
- T. Padmanabhan (1993), “The Large Scale Structure of the Universe”, Cambridge University Press, Cambridge, U.K..
- P. Coles and F. Lucchin (1995), “Cosmology: The Formation and Evolution of Cosmic Structure”, Wiley, Chichester, U.K..
- J. Peacock (1999), “Cosmological Physics”, Cambridge University Press, Cambridge, U.K..
- L. Bergström and A. Goobar (1999), “Cosmology and particle astrophysics”, J. Wiley and Sons, Chichester.

This page is intentionally left blank

Bibliography

- [Ab83] Abt H. A. (1983), “Normal and abnormal binary frequencies”, *Annu. Rev. Astron. and Astrophys.* **21**, 343.
- [Af00] Afonso C. *et al.* (2000), “Combined analysis of the binary lens caustic-crossing event MACHO 98-SMC-1”, *Astrophys. J.* **532**, 340.
- [Al93] Alcock C. *et al.* (1993), “Possible gravitational microlensing of a star in the Large Magellanic Cloud”, *Nature* **365**, 621.
- [Al95] Alcock C. *et al.* (1995), “First observation of parallax in Gravitational Microlensing Event”, *Astrophys. J.* **454**, L125.
- [Al96] Alcock C. *et al.* (1996), “The MACHO Project: Limits on planetary mass dark matter in the Galactic halo from gravitational microlensing”, *Astrophys. J.* **471**, 774.
- [Al97] Alcock C. *et al.* (1997), “MACHO alert 95-30: First real-time observation of extended source effects in gravitational microlensing”, *Astrophys. J.* **491**, 436.
- [Al98] Alard C. and Lupton R. (1998), “A method for optimal image subtraction”, *Astrophys. J.* **503**, 325.
- [Al99a] Albrow M. *et al.* (1999), “Limb darkening of a K giant in the Galactic bulge: planet photometry of MACHO 97-BLG-28”, *Astrophys. J.* **522**, 1011.
- [Al99b] Albrow M. *et al.* (1999), “A complete set of solutions for caustic crossing binary microlensing events”, *Astrophys. J.* **522**, 1022.
- [Al00a] Alard C. (2000), “Image subtraction using a space-varying kernel”, *Astron. and Astrophys. Suppl.* **144**, 363.
- [Al00b] Albrow M. *et al.* (2000), “Detection of rotation in a binary microlens: PLANET photometry of MACHO 97-BLG-41”, *Astrophys. J.* **534**, 894.
- [Al00c] Alcock C. *et al.* (2000), “The MACHO Project: Microlensing results from 5.7 years of Large Magellanic Cloud observations”, *Astrophys. J.* **542**, 281.
- [Al00d] Alcock C. *et al.* (2000), “The MACHO Project: Microlensing optical

- depth towards the Galactic bulge from difference image analysis”, *Astrophys. J.* **541**, 734.
- [Al01a] Albrow M. *et al.* (2001), “PLANET observations of microlensing event OGLE-1999-BUL-23: Limb Darkening measurement of the source star”, *Astrophys. J.* **549**, 759.
- [Al01b] Albrow *et al.* (2001), “Limits on the abundance of Galactic planets from five years of PLANET observations”, *Astrophys. J.* **556**, L113.
- [Al01c] Alcock C. *et al.* (2001), “MACHO Project limits on black hole dark matter in the $1\text{--}30 M_\odot$ range”, *Astrophys. J.* **550**, L169.
- [Al01d] Alcock C. *et al.* (2001), “MACHO 96-LMC-2: Lensing of a binary source in the Large Magellanic Cloud and constraints on the lensing object”, *Astrophys. J.* **552**, 259.
- [An97] Ansari R. *et al.* (1997), “AGAPE: a search for dark matter towards M31 by microlensing effects of unresolved stars”, *Astron. and Astrophys.* **324**, 843.
- [Au93] Aubourg E. *et al.* (1993), “Evidence for gravitational microlensing by dark objects in the Galactic halo”, *Nature* **365**, 623.
- [Ba83] Bahcall J., Schmidt M. and Soneira R. (1983), “The Galactic spheroid”, *Astrophys. J.* **265**, 730.
- [Ba86a] Bardeen J. *et al.* (1986), “The statistics of peaks of Gaussian random fields”, *Astrophys. J.* **304**, 15.
- [Ba86b] Bahcall J. (1986), “Star counts and Galactic structure”, *Annu. Rev. Astron. and Astrophys.* **24**, 577.
- [Ba93] Baillon P. *et al.* (1993), “Detection of brown dwarfs by the microlensing of unresolved stars”, *Astron. and Astrophys.* **277**, 1.
- [Ba94a] Bartelmann M. and Weiss A (1994), “Arc statistics with realistic cluster potentials I. Method and first results”, *Astron. and Astrophys.* **287**, 1.
- [Ba94b] Bartelmann M. and Schneider P. (1994), “Large-scale correlations between QSOs and IRAS galaxies”, *Astron. and Astrophys.* **284**, 1 (Erratum: (1995), *Astron. and Astrophys.* **295**, 565).
- [Ba95a] Bartelmann M. and Narayan R. (1995), “The lens parallax method: determining redshifts of faint blue galaxies through gravitational lensing”, *Astrophys. J.* **451**, 60.
- [Ba95b] Bartelmann M. (1995), “Cosmological parameters from angular correlations between QSOs and galaxies”, *Astron. and Astrophys.* **298**, 661.
- [Ba98] Bartelmann M. *et al.* (1998), “Arc statistics with realistic cluster potentials. IV. Clusters in different cosmologies”, *Astron. and Astrophys.* **330**, 1.
- [Ba99] Barkana R. *et al.* (1999), “A reassessment of the data and models of the gravitational lens Q0957+561”, *Astrophys. J.* **520**, 479.
- [Ba00] Bacon D., Réfrégier A. and Ellis R. (2000), “Detection of weak gravitational lensing by large scale structure”, *Month. Not. R. Astron. Soc.* **318**, 625.
- [Ba01] Baltz E. A. and Gondolo P. (2001), “Binary events and extragalactic

- planets in pixel microlensing”, [astro-ph/9909509](#).
- [Be95] Bennett, D. P. *et al.* (1995), “Recent developments in Gravitational Microlensing and the latest MACHO results: Microlensing towards the galactic bulge”, in AIP Conference Proceedings 334: *Dark Matter*, Eds. S. S. Holt and C. L. Bennett.
- [Be97a] Bernardeau F., Van Waerbeke L. and Mellier Y. (1997), “Weak lensing statistics as a probe of Ω and power spectrum”, *Astron. and Astrophys.* **322**, 1.
- [Be97b] Benítez N., Martínez-González E. and Martín-Mirones J. M. (1997), “Statistical excess of foreground galaxies around high-z radiogalaxies”, *Astron. and Astrophys. Lett.* **321**, L1.
- [Be97c] Bennett D. P. *et al.* (1997), “The MACHO Project: Parallax and binary source microlensing events”, *Bulletin of the American Astron. Soc.*, **191**, 83.03.
- [Bi91] Binney J. *et al.* (1991), “Understanding the kinematics of Galactic Centre gas”, *Month. Not. R. Astron. Soc.* **252**, 210.
- [Bl86] Blandford R. D. and Narayan R. (1986), “Fermat’s principle, caustics, and the classification of gravitational lens images”, *Astrophys. J.* **310**, 568.
- [Bl87a] Blandford R. D. and Kochanek C. (1987), “Gravitational imaging by isolated elliptical potential lens I: cross sections”, *Astrophys. J.* **321**, 658.
- [Bl87b] Blanchard A. and Schneider J. (1987), “Gravitational lensing effect on the fluctuations of the cosmic background radiation”, *Astron. and Astrophys.* **184**, 1.
- [Bl91] Blandford R. D. *et al.* (1991), “The distortion of distant galaxy images by large scale structure”, *Month. Not. R. Astron. Soc.* **251**, 600.
- [Bo75] Bourassa R. R. and Kantowski R. (1975), “The theory of transparent gravitational lenses”, *Astrophys. J.* **195**, 13.
- [Bo87] Bond J. R. and Efstathiou G. (1987), “The statistics of cosmic background radiation fluctuations”, *Month. Not. R. Astron. Soc.* **226**, 655.
- [Bo98] Boden A. F., Shao M. and Van Buren D. (1998), “Astrometric observation of MACHO gravitational lensing”, *Astrophys. J.* **502**, 538.
- [Bo01a] Bond I. *et al.* (2001), “Real-time difference image analysis of MOA galactic bulge observations during 2000”, [astro-ph/0102181](#).
- [Bo01b] Bond I. A. *et al.* (2001), “Study by MOA of extra-solar planets in gravitational microlensing events of high magnification”, [astro-ph/0102184](#).
- [Br95] Broadhurst T. J., Taylor A. N. and Peacock J. (1995), “Mapping cluster mass distributions via gravitational lensing of background galaxies”, *Astrophys. J.* **438**, 49.
- [Br00] Broadhurst T. J. *et al.* (2000), “A spectroscopic redshift of the Cl 0024+16 multiple arc system: implications for the central mass distribution”, *Astrophys. J.* **534**, L15.
- [Bu81] Burke W. (1981), “Multiple gravitational imaging by distributed

- masses”, *Astrophys. J.* **244**, L1.
- [Bu96] Buchalter A., Kamionkowski M. and Rich R. M. (1996), “Rates of color-shifted microlensing events”, *Astrophys. J.* **469**, 676.
- [Ca81] Caldwell J. A. R. and Ostriker J. P. (1981), “The mass distribution within our galaxy: a three component model”, *Astrophys. J.* **251**, 61.
- [Ca92] Carroll S. M., Press W. H. and Turner E. L. (1992), “The cosmological constant”, *Annu. Rev. Astron. and Astrophys.* **30**, 499.
- [Ca93] Cayón L. *et al.* (1993), “Gravitational lensing and the cosmic microwave background”, *Astrophys. J.* **403**, 471.
- [Ce94] Cen R. *et al.* (1994), “Strong gravitational lensing statistics as a test of cosmogonic scenarios”, *Astrophys. J.* **423**, 1.
- [Ch24] Chwolson O. (1924), “Über eine mögliche Form fiktiver Doppelsterne”, *Astr. Nachrichten* **221**, 329.
- [Ch79] Chang K. and Refsdal S. (1979), “Flux variations of QSO 0957+561 A, B and image splitting by stars near the light path”, *Nature* **282**, 561.
- [Cr92] Croots A. P. S. (1992), “M31 - A unique laboratory for gravitational microlensing”, *Astrophys. J.* **399**, L43.
- [Cr00] Croots A. *et al.* (2000), “Microlensing in M31 - The MEGA survey’s prospects and initial results”, in *Microlensing 2000: a new era of microlensing astrophysics*, ASP Conf. Proc., Eds. Menzies J. W. and Sackett P. D..
- [de91] de Rújula A., Jetzer P. and Massó E. (1991), “Dark mass moments”, *Month. Not. R. Astron. Soc.* **250**, 348.
- [de95] de Rújula A. *et al.* (1995), “Wither do the microlensing agents rove?”, *Month. Not. R. Astron. Soc.* **275**, 545.
- [di97] di Stefano R. and Perna R. (1997), “Identifying microlensing by binaries”, *Astrophys. J.* **488**, 55.
- [Do99] Dominik M. (1999), “The binary gravitational lens and its extreme cases”, *Astron. and Astrophys.* **349**, 108.
- [Do00] Dominik M. and Sahu K. (2000), “Astrometric microlensing of stars”, *Astrophys. J.* **534**, 213.
- [Dw95] Dwek E. *et al.* (1995), “Morphology, near-infrared luminosity, and mass of the Galactic bulge from COBE DIRBE observations”, *Astrophys. J.* **445**, 716.
- [Dy20] Dyson F. W., Eddington A. S. and Davidson C. R. (1920) “A determination of the deflection of light by the Sun’s gravitational field from observations made at the total eclipse of May 29, 1919”, *Mem. Roy. Astron. Soc.* **62**, 291.
- [Ed20] Eddington A. S. (1920), *Space, Time and Gravitation* (Cambridge University Press, Cambridge).
- [Ei36] Einstein A. (1936), “Lens-like action of a star by the deviation of light in the gravitational field”, *Science* **84**, 506.
- [Er93] Erdl H. and Schneider P. (1993), “Classification of the multiple deflection two point-mass gravitational lens models and application of catastrophe

- theory in lensing”, *Astron. and Astrophys.* **268**, 453.
- [Fa85] Falco E. E., Gorenstein M. V. and Shapiro, I. I. (1985), “On model dependent bounds on H_0 from gravitational images: application to Q 0957+561 A, B”, *Astrophys. J.* **289**, L1.
- [Fi91] Fich M. and Tremaine S. (1991), “The mass of the Galaxy”, *Annu. Rev. Astron. and Astrophys.* **29**, 409.
- [Fi00] Fischer P. et al. (2000), “Weak lensing with SDSS commissioning data: The Galaxy-Mass correlation function to $1h^{-1}$ Mpc”, *Astron. J.* **120**, 1198.
- [Fr87] Freeman K. C. (1987), “The galactic spheroid and old disk”, *Annu. Rev. Astron. and Astrophys.* **25**, 603.
- [Fu90a] Fukugita M., Futamase T. and Kasai M. (1990), “A possible test for the cosmological constant with gravitational lenses”, *Month. Not. R. Astron. Soc.* **246**, 24P.
- [Fu90b] Fugmann W. (1990), “Statistical gravitational lensing and the Lick catalogue of galaxies”, *Astron. and Astrophys.* **240**, 11.
- [Ga99] Gaudi B. S. and Gould A. (1999), “Spectrophotometric resolution of stellar surfaces with microlensing”, *Astrophys. J.* **513**, 619.
- [Gi83] Gilmore G. and Reid N. (1983), “New light on faint stars. III – Galactic structure towards the South Pole and the Galactic thick disk”, *Month. Not. R. Astron. Soc.* **202**, 1025.
- [Gi94] Giudice G. F., Mollerach S. and Roulet E. (1994), “Can EROS and MACHO be detecting the Galactic spheroid instead of the Galactic halo?”, *Phys. Rev. D* **50**, 2406.
- [Go81] Gott J. R. (1981), “Are heavy halos made of low mass stars? A gravitational lens test”, *Astrophys. J.* **243**, 140.
- [Go92] Gould A. and Loeb A. (1992), “Discovering planetary systems through gravitational microlenses”, *Astrophys. J.* **396**, 104.
- [Go93] Gould A. (1993), “Probing the Large Magellanic Cloud halo for MACHOS”, *Astrophys. J.* **404**, 451.
- [Go94a] Gould A. (1994), “Proper motions of MACHOs”, *Astrophys. J.* **421**, L71.
- [Go94b] Gould A. (1994), “MACHO velocities from satellite-based microlensing”, *Astrophys. J.* **421**, L75.
- [Go94c] Gould A., Miralda-Escudé J. and Bahcall J. (1994), “Microlensing events: thin disk, thick disk or halo”, *Astrophys. J.* **423**, L105.
- [Go95] Gould A. (1995), “MACHO parallaxes from a single satellite”, *Astrophys. J.* **441**, 77.
- [Go96a] Gould A. (1996), “Theory of pixel lensing”, *Astrophys. J.* **470**, 201.
- [Go96b] Gould A., Bahcall J. and Flynn C. (1996), “Disk M dwarf luminosity function from Hubble space telescope star counts”, *Astrophys. J.* **465**, 759.
- [Go96c] Gould A. (1996), “Microlensing and the stellar mass function”, *Pub. Astron. Soc. of the Pacific* **108**, 465.

- [Go98a] Gould A. and Depoy D. L. (1998), “Pixel lensing search for bright microlensing events and variables in the Galactic bulge”, *Astrophys. J.* **497**, 62.
- [Go98b] Gould A., Flynn C. and Bahcall J. (1998), “Spheroid luminosity and mass functions from Hubble space telescope star counts”. *Astrophys. J.* **503**, 798.
- [Go99a] Gondolo P. (1999), “Optical depth evaluation in pixel microlensing”, *Astrophys. J.* **510**, L29.
- [Go99b] Gould A. and Salim S. (1999), “Photometric microlens parallaxes with the *Space Interferometry Mission*”, *Astrophys. J.* **524**, 794.
- [Gr91a] Griest K. (1991), “Galactic microlensing as a method of detecting massive compact halo objects”, *Astrophys. J.* **366**, 412.
- [Gr91b] Griest K. *et al.* (1991), “Galactic microlensing as a method of detecting disk dark matter and faint disk stars”, *Astrophys. J.* **372**, L79.
- [Gr92] Griest K. and Hu W. (1992), “Effect of binary sources on the search for massive astrophysical compact halo objects via microlensing”, *Astrophys. J.* **397**, 362; *Erratum:* (1993) *Astrophys. J.* **407**, 440.
- [Gr98] Griest K. and Safizadeh N. (1998), “The use of high magnification events in discovering extrasolar planets”, *Astrophys. J.* **500**, 37.
- [Gy00] Gyuk G., Dalal N. and Griest K. (2000), “Self-lensing models of the Large Magellanic Cloud”, *Astrophys. J.* **535**, 90.
- [Ha91] Hamilton A. J. S. *et al.* (1991), “Reconstructing the primordial spectrum of fluctuations of the universe from the observed nonlinear clustering of galaxies”, *Astrophys. J.* **374**, L1.
- [Ha95] Han C. and Gould A. (1995), “Statistics of microlensing optical depth”, *Astrophys. J.* **449**, 521.
- [Ha97a] Han C. (1997), “Correcting for blending problem in gravitational microlensing events by using the Hubble Space Telescope”, *Astrophys. J.* **490**, 51.
- [Ha97b] Han C. and Gould A. (1997), “Einstein radii from binary-source lensing events”, *Astrophys. J.* **480**, 196.
- [Ha99] Han C., Chun M. and Chang K. (1999), “Astrometric properties of gravitational binary-microlens events and their applications”, *Astrophys. J.* **526**, 405.
- [Ha00] Hanany S. *et al.* (2000), “MAXIMA-I: A measurement of the Cosmic Microwave Background anisotropy on angular scales of $10'$ to $5''$ ”, *Astrophys. J.* **545**, L5.
- [Ha01] Halverson N. W. *et al.* (2001), “DASI First Results: A measurement of the Cosmic Microwave Background angular power spectrum”, *astro-ph/0104489*.
- [Ho95] Hog E., Novikov I. D. and Polnarev A. G. (1995), “MACHO photometry and astrometry”, *Astron. and Astrophys.* **294**, 287.
- [Hu85] Huchra J. *et al.* (1985), “2237+0305 – A new and unusual gravitational lens”, *Astron. J.* **90**, 691.

- [Ir89] Irwin M. J. *et al.* (1989), "Photometric variations in the Q2237+0305 system: first detection of a microlensing event", *Astron. J.* **98**, 1989.
- [Ja97a] Jaroszyński M. and Paczyński B. (1997), "Global energy conservation in gravitational lensing", *Acta Astron.* **46**, 361.
- [Ja97b] Jain B. and Seljak U. (1997), "Cosmological model predictions for weak lensing: linear and nonlinear regimes", *Astrophys. J.* **484**, 560.
- [Ka86] Kayser R., Refsdal S. and Stabell R. (1986), "Astrophysical applications of gravitational microlensing", *Astron. and Astrophys.* **166**, 36.
- [Ka92] Kaiser N. (1992), "Weak gravitational lensing of distant galaxies", *Astrophys. J.* **388**, 272.
- [Ka93a] Kaiser N. and Squires G. (1993), "Mapping the dark matter with weak gravitational lensing", *Astrophys. J.* **404**, 441.
- [Ka93b] Kassiola A. and Kovner I. (1993), "Elliptic mass distributions versus elliptic potentials in gravitational lenses", *Astrophys. J.* **417**, 450.
- [Ka95] Kaiser N. *et al.* (1995), "A method for weak lensing observations", *Astrophys. J.* **449**, 460.
- [Ka98] Kaiser N. (1998), "Weak lensing and cosmology", *Astrophys. J.* **498**, 26.
- [Ka00] Kaiser N., Wilson G. and Luppino G. (2000), "Large scale cosmic shear measurements", [astro-ph/0003338](#).
- [Ke00] Keeton C. R. *et al.* (2000), "The host galaxy of the lensed quasar Q0957+561", *Astrophys. J.* **542**, 74.
- [Ke01] Kerins E. *et al.* (2001), "Theory of pixel lensing towards M31 - I. The density contribution and mass of MACHOs", *Month. Not. R. Astron. Soc.* **323**, 13.
- [Ki94] Kiraga M. and Paczyński B. (1994), "Gravitational microlensing of the galactic bulge stars", *Astrophys. J.* **430**, L101.
- [Ki98] King L. J. *et al.* (1998), "A complete infrared Einstein ring in the gravitational lens system B1938+666", *Month. Not. R. Astron. Soc.* **295**, L41.
- [Ko87] Kovner I. (1987), "The quadrupole gravitational lens", *Astrophys. J.* **312**, 22.
- [Ko89a] Kovner I. (1989), "Diagnostics of compact clusters of galaxies by giant luminous arcs", *Astrophys. J.* **337**, 621.
- [Ko89b] Kovner, I. (1989), "Maximal lens bounds on QSO-galaxy association", *Astrophys. J.* **341**, L1.
- [Ko90] Kovner I. (1990), "Cosmic gravitational diagnostics", in *Gravitational Lensing*, Eds. Mellier Y., Fort B. and Soucail G., Springer-Verlag, 16.
- [Ko96] Kochanek C. S. (1996), "Is there a cosmological constant?", *Astrophys. J.* **466**, 638.
- [Ku91] Kuijken K. and Gilmore G. (1991), "The galactic disk surface mass density and the galactic force K_z at $z = 1.1$ kiloparsecs", *Astrophys. J.* **367**, L9.
- [Ku97] Kundic T. *et al.* (1997), "A robust determination of the time delay in 0957+561A,B and a measurement of a global value of Hubble's con-

- stant”, *Astrophys. J.* **482**, 75.
- [La75] Landau L. and Lifchitz E., Vol. II (1975), *The classical theory of fields*, (Pergamon, Oxford).
- [La00] Laserre T. et al. (2000), “Not enough stellar mass Machos in the Galactic halo”, *Astron. and Astrophys.* **355**, L39; and [astro-ph/0011375](#).
- [Le95] Lebach D. E. et al. (1995), “Measurement of the solar gravitational deflection of radio waves using Very Long Baseline Interferometry”, *Phys. Rev. Lett.* **75**, 1439.
- [Le01] Lee A. T. et al. (2001), “A high resolution analysis of the MAXIMA-1 Cosmic Microwave Background anisotropy data”, [astro-ph/0104459](#).
- [Li64] Liebes S. (1964), “Gravitational lenses”, *Phys. Rev.* **133B**, 835.
- [Ly86] Lynds R. and Petrosian V. (1986), “Giant luminous arcs in galaxy clusters”, *Bull. Am. Astron. Soc.* **18**, 1014.
- [Ma91] Mao S. and Paczyński B. (1991), “Gravitational microlensing by double stars and planetary systems”, *Astrophys. J.* **374**, L37.
- [Ma95a] Ma C.-P. and Bertschinger G. (1995), “Cosmological perturbation theory in the synchronous and conformal Newtonian gauges”, *Astrophys. J.* **455**, 7.
- [Ma95b] Mao S. and di Stefano R. (1995), “Interpretation of gravitational microlensing by binary systems”, *Astrophys. J.* **440**, 22.
- [Ma96] Mao S. and Paczyński B. (1996), “Mass determination with gravitational microlensing”, *Astrophys. J.* **473**, 57.
- [Ma99] Mao S. (1999), “An ongoing parallax microlensing event OGLE-1999-CAR-1 toward Carina”, *Astron. and Astrophys.* **350**, L19.
- [Ma01] Maoli R. et al. (2001), “Cosmic shear analysis in 50 uncorrelated VLT fields. Implications for Ω_0 and σ_8 ”, *Astron. and Astrophys.* **368**, 766.
- [Me98] Metcalf R. B. and Silk J. (1998), “On breaking cosmic degeneracy”, *Astrophys. J.* **492**, L1.
- [Mi73] Misner C. W., Thorne K. S. and Wheeler J. A. (1973), *Gravitation*, W. H. Freeman and Co., San Francisco.
- [Mi91] Miralda-Escudé J. (1991), “The correlation function of galaxy ellipticities produced by gravitational lensing”, *Astrophys. J.* **380**, 1.
- [Mi95] Miyamoto M. and Yoshii Y. (1995), “Astrometry for determining the MACHO mass and trajectory”, *Astron. J.* **110**, 1427.
- [Mi96] Miralda-Escudé J. (1996), “Microlensing events from measurements of the deflection”, *Astrophys. J.* **470**, L113.
- [Mo96] Mollerach S. and Roulet E. (1996), “Microlensing of disk sources”, *Astrophys. J.* **458**, L9.
- [Mo97] Mollerach S. and Roulet E. (1997), “Kicked neutron stars and microlensing”, *Astrophys. J.* **479**, 147.
- [Mo00] Mollerach S. and Roulet E. (2000), “Gravitational lensing as folds in the sky”, *Int. J. of Mod. Phys.* **A15**, 4083.
- [Na88] Narayan R. and White D.M. (1988), “Gravitational lensing in a cold dark matter universe”, *Month. Not. R. Astron. Soc.* **231**, 97.

- [Na89] Narayan, R. (1989), "Gravitational lensing and quasar-galaxy correlations", *Astrophys. J.* **339**, L53.
- [Na97] Navarro J., Frenk C. and White S. (1997), "A universal density profile from hierarchical clustering", *Astrophys. J.* **490**, 493.
- [Na98] R. Narayan and M. Bartelmann (1998), "Lectures on gravitational lensing", in *Formation of structure in the Universe*, Proceedings of the 1995 Jerusalem Winter School, Eds. A. Dekel and J. P. Ostriker, Cambridge University Press (preprint [astro-ph/9606001](#)).
- [Ne94a] Nemiroff R. J. and Wickramasinghe W. A. D. T. (1994), "Finite source sizes and the information content of MACHO-type lens search light curves", *Astrophys. J.* **424**, L21.
- [Ne94b] Nemiroff R. J. (1994), "Magnification bias in galactic microlensing searches", *Astrophys. J.* **435**, 682.
- [Ne01] Netterfield C. B. *et al.* (2001), "A measurement by BOOMERANG of multiple peaks in the angular power spectrum of the cosmic microwave background", [astro-ph/0104460](#).
- [Oj96] Ojha D. K. *et al.* (1996), "Structure and kinematical properties of the Galaxy at intermediate Galactic latitudes", *Astron. and Astrophys.* **311**, 456.
- [Op01] Oppenheimer B. R. *et al.* (2001), "Direct detection of Galactic halo dark matter", *Science* **292**, 698.
- [Pa86a] Paczyński B. (1986), "Gravitational microlensing by the galactic halo", *Astrophys. J.* **304**, 1.
- [Pa86b] Paczyński B. (1986), "Gravitational microlensing at large optical depth", *Astrophys. J.* **301**, 503.
- [Pa87] Paczyński B. (1987), "Giant luminous arcs discovered in two clusters of galaxies" *Nature* **325**, 572.
- [Pa91] Paczyński B. (1991), "Gravitational microlensing of the galactic bulge stars", *Astrophys. J.* **371**, L63.
- [Pa96] Paczyński B. (1996), "The masses of nearby dwarfs and brown dwarfs with the *HST*", *Acta Astron.* **46**, 291.
- [Pa98a] Paczyński B. (1998), "Gravitational microlensing with the *Space Interferometry Mission*", *Astrophys. J.* **494**, L23.
- [Pa98b] Palanque-Delabrouille N. *et al.* (1998), "Microlensing towards the Small Magellanic Cloud. EROS 2 first year survey", *Astron. and Astrophys.* **332**, 1.
- [Pe65] Penzias A. A. and Wilson R. W. (1965), "A measurement of excess antenna temperature at 4080 Mc/s", *Astrophys. J.* **142**, 419.
- [Pe94] Peacock J. A. and Dodds S. J. (1994), "Reconstructing the Linear Power Spectrum of Cosmological Mass Fluctuations", *Month. Not. R. Astron. Soc.* **267**, 1020.
- [Pe96] Peacock J. A. and Dodds S. J. (1996), "Non-linear evolution of cosmological power spectra", *Month. Not. R. Astron. Soc.* **280**, L19.
- [Pe99] Perlmutter S. *et al.* (1999), "Measurements of Omega and Lambda for

- 42 high redshift supernovae”, *Astrophys. J.* **517**, 565.
- [Po78] Poston T. and Steward I. (1978), *Catastrophe theory and its applications*, Pitman, New York.
- [Po00] Popowski P. et al. (2000), “Galactic bulge microlensing events with clump giants as sources”, *Astron. Soc. of the Pacific Conf. Series* **197**, 04.17, Eds. Menzies J. W. and Sackett P. D..
- [Pr73] Press W. H. and Gunn J. E. (1973), “Method for detecting a cosmological density of condensed objects”, *Astrophys. J.* **185**, 397.
- [Re64] Refsdal S. (1964), “The gravitational lens effect” *Month. Not. R. Astron. Soc.* **128**, 295.
- [Re66] Refsdal, S. (1996), “On the possibility of determining the distances and masses of stars from the gravitational lens effect”, *Month. Not. R. Astron. Soc.* **134**, 315.
- [Re79] Reasenberg R. D. et al. (1979), “Verification of signal retardation by solar gravity”, *Astrophys. J.* **234**, L219.
- [Re98] Renault C. et al. (1998), “Search for planetary mass objects in the Galactic halo through microlensing”, *Astron. and Astrophys.* **329**, 522.
- [Rh97] Rhie S. H. (1997), “Infimum microlensing amplification of the maximum number of images of n-point lens systems”, *Astrophys. J.* **484**, 63.
- [Rh00a] Rhie S. H. et al. (2000), “On planetary companions to the MACHO 98-BLG-35 microlens star”, *Astrophys. J.* **533**, 378.
- [Rh00b] Rhie S. H. and Bennett D. P. (2000), “Line Caustic crossing microlensing and limb darkening”, *astro-ph/9912050*.
- [Ri98] Riess A. G. et al. (1998), “Observational evidence from Supernovae for an accelerating universe and a cosmological constant”, *Astron. J.* **116**, 1009.
- [Sa67] Sachs R. K. and Wolfe A. M. (1967), “Perturbation of a cosmological model and angular variations of a microwave background”, *Astrophys. J.* **147**, 73.
- [Sa94] Sahu K. (1994), “Stars within the Large Magellanic Cloud as potential lenses for observed microlensing events”, *Nature* **370**, 275.
- [Sc84] Schneider P. (1984), “The amplification caused by gravitational bending of light”, *Astron. and Astrophys.* **140**, 119.
- [Sc85] Schneider P. (1985), “A new formulation of gravitational lens theory, time-delay, and Fermat’s principle”, *Astron. and Astrophys.* **143**, 413.
- [Sc86] Schneider P. and Weiss A. (1986), “The two-point-mass lens - Detailed investigation of a special asymmetric gravitational lens”, *Astron. and Astrophys.* **164**, 237.
- [Sc87] Schneider P. and Weiss A. (1987), “Gravitational lens origin for AGN variability? Consequences of microlensing”, *Astron. and Astrophys.* **171**, 49.
- [Sc89] Schneider P. (1989), “The number excess of galaxies around high redshift quasars”, *Astron. and Astrophys.* **221**, 221.
- [Sc92] Schneider P. and Weiss A. (1992), “The gravitational lens equation near

- cusps”, *Astron. and Astrophys.* **260**, 1.
- [Se95] Seitz S. and Schneider P. (1995), “Steps towards nonlinear cluster inversion through gravitational distortions. II. Generalization of the Kaiser and Squires method”, *Astron. and Astrophys.* **297**, 287.
- [Se96a] Seljak U. (1996), “Gravitational lensing effects on the cosmic microwave background anisotropies: a power spectrum approach”, *Astrophys. J.* **463**, 1.
- [Se96b] Seljak U. and Zaldarriaga M. (1996), “A line of sight integration approach to Cosmic Microwave Background anisotropies”, *Astrophys. J.* **469**, 437.
- [Sh64] Shapiro I. I. (1964), “Fourth test of General Relativity”, *Phys. Rev. Lett.* **13**, 789.
- [Sm92] Smoot G. *et al.* (1992), “Structure in the COBE differential microwave radiometer first year maps”, *Astrophys. J.* **396**, L1.
- [Sm01] Smith D. R. *et al.* (2001), “Weak lensing determination of the mass in galaxy halos”, *Astrophys. J.* **551**, 643.
- [So04] Soldner J. (1804), “Über die Ablenkung eines Lichtstrahls von seiner geradlinigen Bewegung durch die Attraktion eines Weltkörpers, an welchem er nahe vorbeigeht”, *Berliner Astron. Jahrb.* **1804**, 161.
- [So87] Soucail G. *et al.* (1987), “A blue ring-like structure in the center of the A370 cluster of galaxies”, *Astron. and Astrophys. Lett.* **172**, L14.
- [So01] Soszynski I. *et al.* (2001), “Optical Gravitational Lensing Experiment: Difference Image Analysis of OGLE-2000-BUL-43, a spectacular ongoing parallax microlensig event”, *Astrophys. J.* **552**, 731.
- [Sq96] Squires G. and Kaiser N. (1996), “Unbiased cluster lens reconstruction”, *Astrophys. J.* **473**, 65.
- [Su86] Subramanian K. and Cowling S. (1986), “On local conditions for multiple imaging by bounded, smooth gravitational lenses”, *Month. Not. R. Astron. Soc.* **219**, 333.
- [Su95] Sugiyama N. (1995), “Cosmic Background anisotropies in Cold Dark Matter cosmology”, *Astrophys. J. Suppl.* **100**, 281.
- [To96] Tomaney A. B. and Croots A. P. S. (1996), “Expanding the realm of microlensing surveys with difference image photometry”, *Astron. J.* **112**, 2872.
- [Tu84] Turner E. L., Ostriker J. P. and Gott J. R. III (1984), “The statistics of gravitational lenses: the distributions of image separations and lens redshifts”, *Astrophys. J.* **284**, 1.
- [Tu90] Turner E. L. (1990), “Gravitational lensing limits on the gravitational constant in a flat universe”, *Astrophys. J.* **365**, L43.
- [Tu01] Turner M. S. (2001), “A new era in determining the matter density”, [astro-ph/ 0106035](http://arxiv.org/abs/astro-ph/0106035).
- [Ty88] Tyson J. A., (1988), “Deep CCD survey: galaxy luminosity and color evolution”, *Astron. J.* **96**, 1.
- [Ty95] Tyson J. A. and Fischer P. (1995), “Measurement of the mass profile of

- Abell 1689”, *Astrophys. J.* **446**, L55.
- [Ty98] Tyson J. A. *et al.* (1998), “Detailed mass map of CL0024+1654 from strong lensing”, *Astrophys. J.* **498**, L107.
- [Ud93] Udalski A. *et al.* (1993), “The Optical Gravitational Lensing Experiment. Discovery of the first candidate microlensing event towards the direction of the galactic bulge”, *Acta Astron.* **43**, 289.
- [Ud94] Udalski A. *et al.* (1994), “The Optical Gravitational Lensing Experiment. The optical depth to gravitational microlensing in the direction of the Galactic bulge”, *Acta Astron.* **44**, 165.
- [va96] Van den Bergh S. (1996), “Formation of the Galaxy”, *Pub. Astron. Soc. of the Pacific* **108**, 986.
- [va00] Van Waerbeke L. *et al.* (2000), “Detection of correlated galaxy ellipticities from CFHT data: first evidence for gravitational lensing by large scale structures”, *Astron. and Astrophys.* **358**, 30.
- [Vi83] Vietri M. and Ostriker J. (1983), “The statistics of gravitational lenses: apparent changes in the luminosity function of distant sources due to passage of light through a single galaxy”, *Astrophys. J.* **267**, 488.
- [Wa79] Walsh D., Carswell R. F. and Weymann R. J. (1979), “0957+561 A, B: twin quasistellar objects or gravitational lens?”, *Nature* **279**, 381.
- [Wa90] Wambsganss J., Paczyński B. and Schneider P. (1990), “Interpretation of the microlensing event in QSO 2237+0305”, *Astrophys. J.* **358**, L33.
- [Wa92] Wambsganss J., Witt H. J. and Schneider P. (1992), “Gravitational microlensing: powerful combination of ray-shooting and parametric representation of caustics”, *Astron. and Astrophys.* **258**, 591.
- [Wa95] Walker M. A. (1995), “Microlensed image motions”, *Astrophys. J.* **453**, 37.
- [Wa98] Wambsganss J. (1998), “Gravitational lensing in astronomy”, *Living Reviews in Relativity* **1**, 1998–12, <http://www.livingreviews.org>.
- [Wi90] Witt H. J. (1990), “Investigation of high amplification events in light curves of gravitationally lensed quasars”, *Astron. and Astrophys.* **236**, 311.
- [Wi94] Witt H. J. and Mao S. (1994), “Can lensed stars be regarded as pointlike for microlensing by MACHOs?”, *Astrophys. J.* **430**, 505.
- [Wi95a] Witt H. J. (1995), “The Effect of the stellar size on microlensing at the Baade Window”, *Astrophys. J.* **449**, 42.
- [Wi95b] Witt H. J. and Mao S. (1995), “On the minimum magnification between caustic crossings for microlensing by binary and multiple stars”, *Astrophys. J.* **447**, 105.
- [Wi00a] Wittman D. M. *et al.* (2000), “Detection of weak gravitational lensing distortions of distant galaxies by cosmic dark matter at large scales”, *Nature* **405**, 143.
- [Wi00b] Wittman D. M. *et al.* (2000) “The normal cluster weak lensing survey: mass profiles and M/L ratios of eight clusters at $z = 0.2$ ”, in *Constructing the Universe with clusters of galaxies*, IAP2000 Meeting, Paris, Eds.

- Durret F. and Gerbal D..
- [Wo97] Woźniak P. and Paczyński B. (1997), “Microlensing of blended stellar images”, *Astrophys. J.* **487**, 55.
- [Wo00] Woźniak P. *et al.* (2000), “The Optical Gravitational Lensing Experiment: A hunt for caustic crossings in QSO 2237+0305”, *Astrophys. J.* **540**, L65.
- [Wo01] Woźniak P. *et al.* (2001), “Difference image analysis of the OGLE-II bulge data. II. Microlensing events”, [astro-ph/0106474](#).
- [Wu94] Wu W. P. (1994), “Gravitational microlensing by the MACHOs of the LMC”, *Astrophys. J.* **435**, 66.
- [Yo81] Young P. (1981), “Q0957+561: Effects of random stars on the gravitational lens”, *Astrophys. J.* **244**, 756.
- [Za95] Zakharov, A. F. (1995), “On the magnification of gravitational lens images near cusps”, *Astron. and Astrophys.* **293**, 1.
- [Zh95] Zhao H., Spergel D. N. and Rich, R. M. (1995), “Microlensing by the Galactic bar”, *Astrophys. J.* **440**, L13.
- [Zh98] Zhao H. (1998), “Microlensing of tidal debris on the Magellanic great circle”, *Month. Not. R. Astron. Soc.* **294**, 139.
- [Zw37a] Zwicky F. (1937), “Nebulae as gravitational lenses”, *Phys. Rev.* **51**, 290.
- [Zw37b] Zwicky F. (1937), “On the probability of detecting nebulae which act as gravitational lenses”, *Phys. Rev.* **51**, 679.

This page is intentionally left blank

Index

- amplification, 36–38, 55
 - radial, 40
 - tangential, 40
- amplification bias, 116
- Andromeda microlensing, 115
- angular diameter distance, 34, 165
- arc-length theorem, 65
- astrometric microlensing, 152
- bar, 102
 - optical depth, 124
- Bianchi identity, 16
- bias, 94
- binary lenses, 126
 - caustic curves, 128
 - complex lens equation, 126
 - critical curves, 127
 - microlensing, 131
 - sky sheet, 66
- binary source, 151
- blending, 117
- bulge, 102
- bulge microlensing, 122
- Burke’s theorem, 41, 48, 52
- catastrophe theory, 58, 67
- caustics, 41, 53
 - point-like, 41
- centroid shift, 152
- Christoffel symbols, 12
- clusters mass determination, 82
- comoving distance, 164
- convergence, 38
 - power spectrum, 91
- Cosmic Microwave Background
 - anisotropies, 171
 - angular spectrum, 95
 - lensing of, 95
 - cosmic shear, 87
- cosmological constant, 18, 163
 - lensing constraint, 78, 81
- covariant derivative, 11
- critical lines, 41
- critical surface density, 38, 39
- curvature of spacetime, 16
- curvature scalar, 17
- cusps, 53
 - magnification, 63
 - sum of the image amplifications, 65
- dark matter, 4, 104
- deflection angle, 23
- difference image analysis (DIA), 115
- disk of the Galaxy, 101
- Einstein angle, 30, 139
- Einstein equation, 17, 18
- Einstein radius, 139
- Einstein ring, 31
- elliptical lenses, 50

- caustic, 57
- sky sheet, 56
- event duration, 106
- event rate, 108
- extended lenses, 25, 33
- Fermat's principle, 42
- finite source effects, 141, 158
- fold caustics, 53, 143
 - magnification, 62
- follow-up networks, 137
- Friedmann equation, 162
- Friedmann-Robertson-Walker Universe, 161
- Galaxy, stellar populations, 103
- geodesic equation, 14
- giant arcs, 3, 82
- halo, 103
- high magnification events, 138
- Hubble constant determination, 2, 75
- image parity, 36, 39, 44
- impact parameter, 105
- interval, 8
- Jacobian of the mapping, 37
- lens equation, 30
- light curve, 105
- limb darkening, 147
- limiting magnitude, 114
- lips, 58
- LMC microlensing, 118
- LMC self-lensing, 120
- luminosity distance, 165
- mapping matrix, 37, 43
- mass function, 111
- mass sheet degeneracy, 76, 85
- maximum magnification, 106
- metric, 8
- microlensing, 4, 99, 125
 - microlensing experiments, 117
 - microlensing tube, 108
 - optical depth, 79, 107, 112
 - parallax, 140, 148
 - parallel transport, 11, 15
 - pixel lensing, 114
 - planetary microlensing, 136
 - point spread function, 115
 - point-like lens, 30
 - sky sheet, 56
 - Poisson equation, 167
 - power spectrum, 168
 - proper motion, 140, 141, 152
 - quasar lensing, 2, 70
 - quasar microlensing, 156
 - quasar-galaxy correlations, 94
 - redshift, 164
 - Ricci tensor, 17
 - Riemann tensor, 16
 - satellite parallax, 149
 - Schwarzschild metric, 20
 - Schwarzschild radius, 20
 - shear, 38, 84
 - power spectrum, 92
 - singular isothermal sphere, 45
 - sky sheet, 55
 - singular lenses, 42, 53
 - sky sheet, 51
 - softened isothermal sphere, 46
 - sky sheet, 54
 - spherically symmetric lens, 26
 - spheroid, 101
 - strong equivalence principle, 9
 - strong lensing, 33
 - surface brightness, 34
 - surface brightness conservation, 35
 - tensors, covariant and contravariant, 10

- thick disk, 101
- thin lens approximation, 25
- time delay, 43, 54, 73
 - geometric, 42
 - gravitational, 24
- time moments, 113
- transfer function, 168

- unresolved sources, 114

- weak equivalence principle, 8
- weak field approximation, 14
- weak lensing, 3, 84
 - cluster profile reconstruction, 85

Gravitational Lensing and Microlensing

This book provides a comprehensive and self-contained exposition of gravitational lensing phenomena. It presents the up-to-date status of gravitational lensing and microlensing, covering the cosmological applications of the observed lensing by galaxies, clusters and the large scale structures, as well as the microlensing searches in the Local Group and its applications to unveil the nature of the galactic dark matter, the search for planetary objects and the distribution of faint stars in our galaxy.

Gravitational Lensing and Microlensing is pitched at the level of the graduate student interested in the issues of astrophysics and cosmology, and should be useful for specialist researchers as well.

